



HAL
open science

Modeling and Optimal Control of a Multi-Active Bridge (MAB) Converter

Rebecca Tarraf

► **To cite this version:**

Rebecca Tarraf. Modeling and Optimal Control of a Multi-Active Bridge (MAB) Converter. Electric power. Université Grenoble Alpes [2020-..], 2024. English. NNT : 2024GRALT048 . tel-04729530

HAL Id: tel-04729530

<https://theses.hal.science/tel-04729530v1>

Submitted on 10 Oct 2024

HAL is a multi-disciplinary open access archive for the deposit and dissemination of scientific research documents, whether they are published or not. The documents may come from teaching and research institutions in France or abroad, or from public or private research centers.

L'archive ouverte pluridisciplinaire **HAL**, est destinée au dépôt et à la diffusion de documents scientifiques de niveau recherche, publiés ou non, émanant des établissements d'enseignement et de recherche français ou étrangers, des laboratoires publics ou privés.

THÈSE

Pour obtenir le grade de

DOCTEUR DE L'UNIVERSITÉ GRENOBLE ALPES



École doctorale : EEATS - Electronique, Electrotechnique, Automatique, Traitement du Signal (EEATS)

Spécialité : Génie électrique

Unité de recherche : Laboratoire d'Electronique et de Technologie de l'Information (LETI)

Modélisation et Commande Optimale d'un Convertisseur Multi-Active Bridge (MAB)

Modeling and Optimal Control of a Multi-Active Bridge (MAB) Converter

Présentée par :

Rebecca TARRAF

Direction de thèse :

Yves LEMBEYE

Professeur des universités, Université Grenoble Alpes

Directeur de thèse

David FREY

Maitre de Conférences, Université Grenoble Alpes

Co-encadrant de thèse

Sylvain LEIRENS

CEA Grenoble

Co-encadrant de thèse

Sébastien CARCOUET

CEA Grenoble L2EP

Co-encadrant de thèse

Rapporteurs :

Guillaume GATEAU

PROFESSEUR DES UNIVERSITES, TOULOUSE INP

Marc HILLER

FULL PROFESSOR, Karlsruhe Institute of Technology

Thèse soutenue publiquement le **10 juillet 2024**, devant le jury composé de :

Jean-Paul GAUBERT,

PROFESSEUR DES UNIVERSITES, Université de Poitiers

Président

Yves LEMBEYE,

PROFESSEUR DES UNIVERSITES, UNIVERSITE GRENOBLE ALPES

Directeur de thèse

Guillaume GATEAU,

PROFESSEUR DES UNIVERSITES, TOULOUSE INP

Rapporteur

Marc HILLER,

FULL PROFESSOR, Karlsruhe Institute of Technology

Rapporteur

Vincent DEBUSSCHERE,

MAITRE DE CONFERENCE HDR, GRENOBLE INP

Examinateur

Henk HUISMAN,

ASSOCIATE PROFESSOR, Eindhoven University of Technology

Examinateur

Invités :

Xavier MAYNARD

INGENIEUR, CEA Grenoble



Remerciements

Ce projet de thèse a été réalisé au sein du laboratoire L2EP du CEA Grenoble, en collaboration avec le G2Elab. J'aimerais exprimer ma gratitude pour toutes les personnes qui ont contribué directement ou indirectement à l'avancement de cette thèse et qui ont rendu ce travail possible.

Je tiens tout d'abord à remercier énormément Yves Lembeye, le directeur de ma thèse, ainsi que Sébastien Carcouet, David Frey, Sylvain Leirens et Xavier Maynard, mes encadrants de thèse, pour tout le temps et les efforts qu'ils m'ont consacrés au cours de ces trois dernières années. Chacun d'entre eux a influencé et enrichi mon travail à sa manière et m'a apporté des compétences et des connaissances précieuses et différentes dans le domaine de l'électronique de puissance. Je me considère très chanceuse d'avoir été accompagnée et guidée par ces cinq personnes passionnées et professionnelles.

Je remercie également toute l'équipe du L2EP pour les précieux conseils, les discussions intéressantes et les moments conviviaux que nous avons partagés. C'était un véritable plaisir d'intégrer cette équipe et d'effectuer ma thèse parmi ses membres.

Un grand merci à mes parents, Nadia et Nabil, ainsi que mon frère Elie pour leur soutien constant, leur confiance et leur amour inconditionnel, qui m'ont toujours permis de progresser dans ma vie professionnelle et personnelle.

Finalement, je remercie mes amis qui ont été une source inépuisable de motivation et d'encouragement durant ces trois années de thèse.

Abstract

A Multi-Active Bridge (MAB) converter is an interesting energy hub topology that has emerged in recent years. In an energy hub, the production, consumption and storage of electrical energy all take place within the same structure. In addition, MAB converters are multiport converters with intrinsic galvanic isolation. This is achieved by connecting the ports of this topology through a high-frequency (HF) transformer. Galvanic isolation is crucial for applications where different power sources/loads with important voltage dissimilarities and power ratings need to be connected together. Consequently, a MAB converter can connect several energy sources, loads and energy storage systems together, allowing multidirectional power flow between them. For these reasons, MAB converters are attracting great attention in many applications, especially those requiring energy storage and/or integration of renewable energy sources.

In general, the main objective of controlling a MAB converter is to manage the active power flows between its ports based on each port's requirements. However, optimizing the control of this converter can be achieved by adding another constraint, aiming to minimize the system's losses for example.

In this thesis, the mathematical modelling of a selected MAB converter topology is first developed to represent its steady-state and dynamic behaviour. The coupling between the ports is explained and existing decoupling techniques are detailed and discussed. The interaction between the MAB converter's ports with an externally connected LC circuit is also studied in the first part of this manuscript and an active solution to its effect on the ports is proposed.

The developed mathematical model is then used to elaborate a method for calculating the conduction and switching losses of the MAB converter at any operating point and for any combination of its control parameters. After that, an optimized control strategy is proposed with the aim of minimizing the total system losses over the entire operating range of the MAB converter. Conduction losses are minimized by eliminating the exchange of reactive energy between the different ports. Switching losses are minimized by achieving a soft switching at each of the system's switches. The proposed control strategy uses the developed mathematical model and the loss calculation method to predict the optimal combination of the control parameters resulting in minimum losses, and therefore an increased efficiency for any desired operating point.

A four-port $4 \times 500 \text{ W}$ prototype of a MAB converter (Quadruple Active Bridge) is built and experimental results are presented to demonstrate the reliability of the mathematical model and to prove the effectiveness of the proposed control strategy. The potential presence of DC bias in the multi-winding transformer of the MAB converter is also discussed and an active solution is presented and tested experimentally.

In general, MAB structures are based on voltage converters. However, in some applications, it may be useful to have a current-fed input port due to load characteristics or operational constraints. This leads to a hybrid MAB structure that mixes both current and voltage-fed bridges. In the final part of this manuscript, a novel hybrid-fed MAB converter topology is presented and evaluated. Its mathematical model is developed and a control strategy is proposed. Simulation results are provided in order to validate the presented theoretical study. The advantages and disadvantages of this topology are listed in order to compare it with the classical voltage-fed MAB converter studied in the first part of this thesis.

Résumé

Un convertisseur à multiples ponts actifs, appelé aussi convertisseur MAB (pour Multi-Active Bridge convertir en anglais), est une topologie intéressante de « Hub Energétique » qui a apparu récemment. Dans un Hub Energétique, la production, la consommation et le stockage de l'énergie électrique ont lieu au sein de la même structure. De plus, les convertisseurs MAB sont des convertisseurs multiports dotés d'une isolation galvanique intrinsèque. Celle-ci est obtenue en connectant les ports de cette topologie par l'intermédiaire d'un transformateur haute fréquence (HF). L'isolation galvanique est nécessaire pour les applications où différentes sources d'alimentation/charges présentant d'importantes dissimilarités de tensions et de puissances nominales doivent être connectées ensemble. Par conséquent, un convertisseur MAB peut connecter plusieurs sources d'énergie, charges et systèmes de stockage d'énergie électrique ensemble, permettant un flux d'énergie multidirectionnel entre eux. Pour toutes ces raisons, les convertisseurs MAB ont dernièrement attiré beaucoup l'attention, notamment pour les applications sollicitant des sources d'énergie renouvelables et des systèmes de stockage d'énergie.

En général, l'objectif principal du contrôle d'un convertisseur MAB est de gérer les flux de puissance active entre ses ports en fonction des besoins de chacun d'entre eux. Cependant, l'optimisation du contrôle de ce convertisseur peut être réalisée en ajoutant une contrainte, visant à minimiser les pertes du système par exemple.

Tout d'abord, dans cette thèse, le modèle mathématique d'un convertisseur MAB est développé pour représenter son comportement en régime transitoire et en régime permanent. Le couplage entre les ports est ensuite expliqué et les techniques de découplage existantes dans la littérature sont détaillées et discutées. L'interaction entre les ports du convertisseur MAB et un circuit LC connecté à l'un de ses ports est également étudiée dans la première partie de ce manuscrit, et une solution active visant l'atténuation des instabilités causées par cette connexion est proposée.

Le modèle mathématique développé est ensuite utilisé pour élaborer une méthode de calcul des pertes de conduction et de commutation du convertisseur MAB à n'importe quel point de fonctionnement et pour n'importe quelle combinaison de ses paramètres de contrôle. Ensuite, une stratégie de commande optimisée est proposée dans le but de minimiser les pertes totales du système sur toute sa plage de fonctionnement. Les pertes par conduction sont minimisées en éliminant l'échange d'énergie réactive entre les différents ports. Les pertes de commutation sont minimisées en réalisant une commutation douce à chacun des interrupteurs du système. La stratégie de commande proposée utilise le modèle mathématique et la méthode de calcul des pertes développés pour prédire la combinaison optimale des paramètres de contrôle aboutissant à des pertes minimales pour tout point de fonctionnement désiré.

Un prototype d'un convertisseur MAB à quatre ports (Quadruple Active Bridge) est construit et des résultats expérimentaux sont présentés dans ce manuscrit pour démontrer la fiabilité du modèle mathématique et l'efficacité de la stratégie de commande proposée dans cette thèse. La présence potentielle d'un courant continu dans le transformateur à enroulements multiples est également discutée et une solution active est présentée et testée expérimentalement.

En général, les structures MAB sont basées sur des convertisseurs alimentés en tension. Cependant, dans certaines applications, il peut être utile d'avoir un port alimenté en courant en raison des caractéristiques de la charge ou des contraintes opérationnelles. Cela conduit à une

structure MAB hybride qui mélange à la fois des ponts alimentés en courant et des ponts alimentés en tension. Dans la dernière partie de ce manuscrit, une nouvelle topologie de convertisseur MAB à alimentation hybride est présentée et étudiée. Son modèle mathématique est développé et une stratégie de commande est proposée. Des résultats de simulation sont fournis afin de valider l'étude théorique présentée. Les avantages et les inconvénients de cette topologie sont énumérés afin de la comparer avec le convertisseur MAB classique alimenté en tension qui est étudié dans la première partie de cette thèse.

Table of Content

INTRODUCTION	12
1. CHAPTER 1: TOPOLOGY AND MODELLING OF A MAB CONVERTER	20
1.1. Introduction	20
1.2. Considered MAB Converter Topology	20
1.3. Steady-State Modelling of a MAB Converter	24
1.3.1. First Harmonic Approximation	28
1.3.2. Generalized Harmonic Approximation (GHA)	31
1.3.3. Cross Coupling Between the Ports of a MAB Converter	32
1.4. Dynamic Modelling of a MAB Converter	37
1.4.1. Generalized Average Model of a TAB Converter	39
1.4.2. Simulation Results and Validation of the Dynamic Model	44
1.5. Interaction of a MAB Converter with an Externally Connected LC filter	47
1.5.1. Simulation Results of the Proposed Active Damping Method	52
1.6. Conclusion	55
2. CHAPTER 2: LOSS CALCULATION AND EFFICIENCY OPTIMIZATION OF A MAB CONVERTER	56
2.1. Introduction	56
2.2. Power Flow Control of a MAB Converter	56
2.3. Calculation of the Conduction Losses	60
2.4. Soft Switching Evaluation and Calculation of Switching Losses	61
2.4.1. Elaboration of the ZVS Criteria	62
2.4.2. Calculation of the Switching Losses	76
2.5. Efficiency Optimization	78
2.5.1. Minimization of the Exchanged Reactive Power	78
2.5.2. Minimization of Total System Losses	80
2.6. Conclusion	89
3. CHAPTER 3: EXPERIMENTAL RESULTS AND VALIDATION	90
3.1. Introduction	90
3.2. QAB Converter Prototype Sizing	90
3.2.1. Series Inductances	91
3.2.2. Multi-winding Transformer Design	91
3.3. Optimization Algorithm Implementation and Results	98
3.4. DC Bias in Transformer Windings and Magnetic Core Saturation	106
3.5. Conclusion	116

4. CHAPTER 4: MODELLING AND CONTROL OF A HYBRID-FED MAB CONVERTER	
117	
4.1. Introduction	117
4.2. The Proposed Converter	119
4.2.1. Topology of the Hybrid-Fed TAB Converter	119
4.2.2. Working Principle	121
4.2.3. Operating Conditions	125
4.3. Full-Order Generalized Average Model of the Hybrid-Fed TAB Converter	126
4.4. Reduced-Order Model of the Hybrid-Fed TAB Converter	128
4.5. Proposed Control Strategy	132
4.5.1. Input DC Current Control of Port 1	133
4.5.2. Output DC Voltage Control of Port 3	134
4.6. Simulated Results and Discussion	134
4.7. Conclusion	138
GENERAL CONCLUSION	140
REFERENCES	143

Table of Figures

Figure 0.1: Classical centralized and unidirectional energy system [4].	12
Figure 0.2: World population growth between 1700 and 2100 [5].	13
Figure 0.3: Renewable energy generation in the world between 1965 and 2019 [7].	13
Figure 0.4: Decentralized energy system with renewable energy integration [4].	14
Figure 0.5: Multiport system structure [10].	15
Figure 0.6: Example of a three-port converter combining dc-link and magnetic-coupling [10].	16
Figure 0.7: A four-port MAB converter application example.	17
Figure 0.8: Fully isolated coupling of different electrical sources and loads using: (a) Classical solution with multiple isolated Single-Input Single-Output (SISO) converters connected together through a DC bus, (b) a MAB converter [12].	17
Figure 1.1: Considered topology of a Multi-Active Bridge converter with n ports.	21
Figure 1.2: Star-delta transformation of the MAB converter's transformer model: (a) Star model, (b) Delta model.	21
Figure 1.3: AC voltages of port #1 and port # i referred to the reference port #1 with their corresponding external and internal phase shifts.	23
Figure 1.4: Command signals of the H-bridge switches of a port # i .	24
Figure 1.5: The 12 basic working modes generated by the H-bridges of a DAB converter [19].	26
Figure 1.6: Ideal voltages and current waveforms of the DAB converter using the modulation proposed in [21]: (a) $\alpha_2 = 0$, (b) $\alpha_1 = 0$.	27
Figure 1.7: Non-linear increase of current in an active bridge of a MAB converter as the power transfer gets closer to its maximum value [9].	30
Figure 1.8: The cross-coupling degree in function of the MAB's number of ports [23].	34
Figure 1.9: Inverse matrix decoupling method for a MIMO system with two inputs (w_1 and w_2) and two outputs (y_1 and y_2) [29].	36
Figure 1.10 : Time-sharing control of a QAB converter (a grey area indicates an activated port).	37
Figure 1.11: TAB converter topology considered for the dynamic modelling.	39
Figure 1.12: Equivalent models of the considered TAB converter: (a) Star equivalent model; (b) Delta equivalent model.	39
Figure 1.13: Switching functions of the TAB converter's ports if an EPS modulation is applied.	40
Figure 1.14: Control loops of the proposed TAB converter for the control of the DC current of port #2 and the DC voltage of port #3.	45
Figure 1.15: Closed loop response comparison of the mathematical model and the simulated model of the proposed TAB converter: (a) DC current i_2 of port #2; (b) Output DC voltage V_3 of port #3.	46
Figure 1.16: Waveforms of the AC and DC currents at a port of a MAB converter.	47
Figure 1.17: Bode plot of transfer function $G_{i2s} = I_2(s)/\varphi_{2s}$.	48
Figure 1.18: Active damping method proposed in [46] based on the shaping of the LC filter's output impedance.	50
Figure 1.19: Power circuit of grid-connected voltage source with LC-filter considered in [47]. The red arrows illustrate the parasitic oscillations addressed in this paper between the filter's capacitors and the grid's inductances.	51
Figure 1.20: Active damping block diagram proposed in [47].	51
Figure 1.21: Block diagram of the proposed active damping method for a MAB converter with a port # i connected to an LC filter.	52
Figure 1.22: Bode plot of the designed BPF for the active damping control.	53
Figure 1.23: Root locus of open-loop transfer function $GVCfs \times GBPF(s)$.	54
Figure 1.24: Application of the proposed active damping method and its effects on the active power control of the system: (a) DC current i_2 of port #2; (b) Output DC voltage V_3 of port #3.	55
Figure 2.1: Hierarchical representation of the three levels of control of a MAB converter.	57
Figure 2.2: AC waveforms of a DAB converter when EPS modulation is applied: (a) at nominal power with no voltage mismatch; (b) at nominal power with +5% DC voltage at port 2; (c) at 10% of nominal power with no voltage mismatch; (d) at 10% of nominal power with +5% DC voltage at port 2.	59

Figure 2.3: Losses and efficiency in function of the switching frequency in a MAB converter [49].	59
Figure 2.4: Switch symbol showing the drain-source capacitance and drain current.	62
Figure 2.5: Generic port-equivalent circuit of a MAB converter.	62
Figure 2.6: Representation of the switching instants of a port #i.	63
Figure 2.7: Current circulation at port #i during switching instant τ_{i1} when $\alpha_i > 0$.	64
Figure 2.8: Port current i_L, i and voltage v_x waveforms during the dead time of switching instant τ_{i1} when $\alpha_i > 0$, considering that i_L, i is equal to its minimum required value for a ZVS at the beginning of τ_{i1} .	67
Figure 2.9: Current circulation at port #i during switching instant τ_{i2} when $\alpha_i > 0$.	68
Figure 2.10: Current circulation at port #i during the dead time of the switching instant τ_{i1} when $\alpha_i = 0$.	71
Figure 2.11: Port current i_L, i and voltage v_x waveforms during the dead time of switching instant τ_{i1} when $\alpha_i > 0$, considering that i_L, i is smaller than its minimum required value for a ZVS at the beginning of τ_{i1} .	75
Figure 2.12: Switching cycle and associated losses of a switch.	77
Figure 2.13: Reactive power flow between port #i and port #j, as considered in expressions (2.68) and (2.69).	78
Figure 2.14: Accuracy percentage of the calculated total RMS current in a QAB converter using the developed GHA model and the proposed MPS modulation for $\alpha_1 = 1.5$ in function of the considered order of harmonics.	80
Figure 2.15: a) Total losses; b) total number of switches operating at ZVS; c) separated total conduction and total switching losses; d) Ports' RMS currents: as a function of the reference internal phase shift α_1 in a QAB converter using the proposed MPS modulation technique at 60% of nominal power and with a maximum of $\pm 20\%$ distortion on the DC voltage sources.	82
Figure 2.16: Total loss percentage of the proposed MPS modulation as a function of the reference internal phase shift α_1 compared to the conventional EPS modulation applied in a QAB converter at different power levels and with $\pm 20\%$ distortion on the DC voltage sources.	83
Figure 2.17: Total number of ZVS switches percentage of the proposed MPS modulation as a function of the reference internal phase shift α_1 compared to the conventional EPS modulation applied in a QAB converter at different power levels and with $\pm 20\%$ distortion on the DC voltage sources.	83
Figure 2.18: Total RMS current in the transformer windings of a MAB converter in function of the total power percentage from nominal power flowing through the system using the conventional EPS modulation and the proposed MPS modulation for two different values of the reference internal phase shift α_1 . A perturbation of $\pm 20\%$ is considered at the DC voltage source of each port.	85
Figure 2.19: Total loss percentage of the proposed MPS modulation as a function of the reference internal phase shift α_1 compared to the conventional EPS modulation applied in a different QAB converter at different power levels and with $\pm 20\%$ distortion on the DC voltage sources.	85
Figure 2.20: Flow chart of the proposed optimization algorithm where the main objective is: (a) minimizing the total system losses at any cost; (b) maximizing the number of satisfied ZVS conditions while decreasing the system losses.	88
Figure 2.21: Block diagram of the proposed control system of a MAB converter.	89
Figure 3.1: Ferrite material operating frequency ranges [54].	92
Figure 3.2: Magnetic core of the transformer.	92
Figure 3.3: Magnetic flux variation in the magnetic core of the transformer during a switching period.	93
Figure 3.4: Copper wire diameter and skin depth representation.	94
Figure 3.5: Dimensions of the coil former of the selected ETD54 magnetic core.	95
Figure 3.6: Transformer built for the 500W QAB prototype.	96
Figure 3.7: Built QAB prototype.	97
Figure 3.8: Control interface PCB.	97
Figure 3.9: Block diagram representing the control algorithm implemented in the microcontroller.	99
Figure 3.10: Comparison of the AC current waveforms obtained experimentally to the waveforms predicted by the GHA model developed in Chapter 1: (a) port #1; (b) port #2; (c) port #3; port #4.	100
Figure 3.11: Experimental results showing the AC current and voltage waveforms of each port at 40W (8% of P_{nom}) when: (a) EPS modulation is applied; (b) the proposed MPS modulation is applied.	101
Figure 3.12: Experimental results showing the AC current and voltage waveforms of each port at 130W (26% of P_{nom}) when: (a) EPS modulation is applied; (b) the proposed MPS modulation is applied.	102
Figure 3.13: Experimental results showing the AC current and voltage waveforms of each port at 380W (76% of P_{nom}) when: (a) EPS modulation is applied; (b) the proposed MPS modulation is applied.	102

Figure 3.14: Experimentally measured efficiency and total losses of the QAB prototype in function of the average port power when using the classical EPS modulation compared to using the proposed MPS modulation.	103
Figure 3.15: Calculated efficiency of the QAB prototype in function of the average port power using the developed mathematical model that only considers the conduction and switching losses of the system.	104
Figure 3.16: Efficiency curve of the QAB prototype obtained by adding the measured iron losses of the transformer to the conduction and switching losses calculated from the developed mathematical model.	105
Figure 3.17: Closed-loop responses of DC currents at different ports after the occurrence of an active power reference change: (a) uncontrolled reference port #1; (b) port #2; (c) port #3; (d) port #4.	106
Figure 3.18: Effect of the DC bias on the hysteresis loop of the transformer's core.	107
Figure 3.19: Resonant MAB converter topology.	108
Figure 3.20: Comparison of hysteresis loops of a ferrite core with and without an air gap [59].	108
Figure 3.21: Waveforms of the AC voltages of a DAB converter with EPS modulation when an external phase shift change occurs: (a) without DC current bias elimination (unbalanced waveforms) b) with two-step phase shift method for transient DC bias elimination (balanced waveforms).	109
Figure 3.22: Flux density measurement using a magnetic ear [58].	111
Figure 3.23: DC component measuring of the MAB's transformer current [9].	111
Figure 3.24: Developed circuit for the DC current component measurement.	112
Figure 3.25: Duty cycles representation of the positive and negative half-cycles of the AC voltage of a port #i with their corresponding switch commands' waveforms.	113
Figure 3.26: Block diagram of the developed DC current component cancellation technique at a port #i.	114
Figure 3.27: Closed-loop response of the proposed DC bias cancellation control method on port #4.	116
Figure 4.1: Proposed current-fed DAB converter topology in [65].	117
Figure 4.2: Proposed current-fed TAB topology in [66].	118
Figure 4.3: Coupled hybrid-fed TAB converter topology.	119
Figure 4.4: AC waveforms of the hybrid-fed TAB converter.	120
Figure 4.5: Star-delta transformation of the transformer windings referred to port #1.	121
Figure 4.6: Equivalent circuits of the converter at: (a) $0 < t < t_0$; (b) $t_0 < t < t_1$; (c) $t_1 < t < t_2$; (d) $t_2 < t < Ts_2$; (e) $Ts_2 < t < t_3$ (switches in grey are OFF).	124
Figure 4.7: Comparison of the Bode plots of the full-order model and the reduced-order model transfer functions of the hybrid-fed TAB converter: (a) Input current I_1 of port #1 controlled by D_1 ; (b) Output voltage V_3 of port #3 controlled by ϕ_{13}	131
Figure 4.8: Comparison of the Bode plots of the full-order model and the two reduced-order models of the DC current control of port #1.	131
Figure 4.9: Control block diagrams of the hybrid-fed TAB converter: (a) DC current control of port #1; (b) DC voltage control of port #3.	133
Figure 4.10: Simulation results of the current closed-loop control of port #1 of the hybrid-fed TAB converter.	135
Figure 4.11: Simulation results of the voltage closed-loop control of port #3 of the hybrid-fed TAB converter.	135
Figure 4.12: Waveforms of the hybrid-fed TAB converter: (a) Input current i_1 of port #1; (b) Duty cycle D_1 of command signal of port #1; (c) Uncontrolled input current i_2 of port #2; (d) Phase shift ϕ_{12} of command signal of port #2; (e) Output voltage V_3 of port #3; (f) Phase shift ϕ_{13} of command signal of port #3.	137
Figure 4.13: Waveforms of the AC voltages of the three ports and the AC current of port #1.	138

List of Tables

<i>Table 1.1: Parameter values of the considered TAB converter in Chapter 1 Section 4.....</i>	<i>49</i>
<i>Table 2.1: Considered parameter values of the equivalent port.</i>	<i>68</i>
<i>Table 2.2: ZVS conditions of a port #i.</i>	<i>73</i>
<i>Table 2.3: Parameter values of the two considered QAB converters.</i>	<i>86</i>
<i>Table 3.1: Parameter values for the prototype's transformer design.</i>	<i>94</i>
<i>Table 3.2: Summary of the QAB prototype's parameter values.</i>	<i>96</i>
<i>Table 3.3: Parameter values of considered operating point.....</i>	<i>100</i>
<i>Table 4.1: Parameter values of the simulated hybrid-fed TAB converter.....</i>	<i>136</i>

INTRODUCTION

In the late 1800s, the invention of high-voltage alternating current made it possible to transmit electricity over long distances using electrical cables. This has progressively led to the classical and modern AC grid system which is centralized around large-scale thermal power plants that usually use fossil fuels (coal, oil and gas) to produce energy [1], [2], [3]. This conventional electrification model is unidirectional, as electricity is delivered from these plants to consumers via transmission systems (Figure 0.1). In the 20th century, this great invention spread widely and rapidly around the world, aiming to deliver electricity to the residential, industrial and commercial energy consumers.

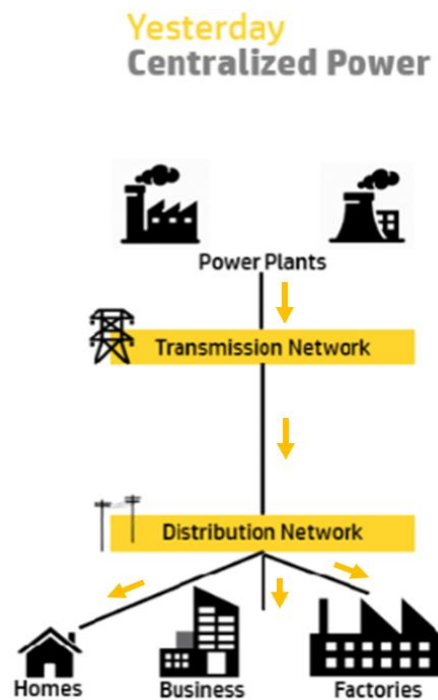


Figure 0.1: Classical centralized and unidirectional energy system [4].

Over the course of the 20th century, the world's population almost quadrupled [5] (Figure 0.2). This is largely due to medical and scientific advances that have increased human life expectancy and reduced infant mortality. This population growth has enormously increased global energy demand, leading to concerns about climate change and the depletion of available non-renewable fossil fuels, which take hundreds of millions of years to form. In fact, burning fossil fuels for energy produces harmful greenhouse gas emissions such as carbon dioxide. For all these reasons, one of the most important challenges facing humanity today is energy security. Energy security means providing consumers with energy services that are affordable, reliable, efficient and environmentally friendly [6].

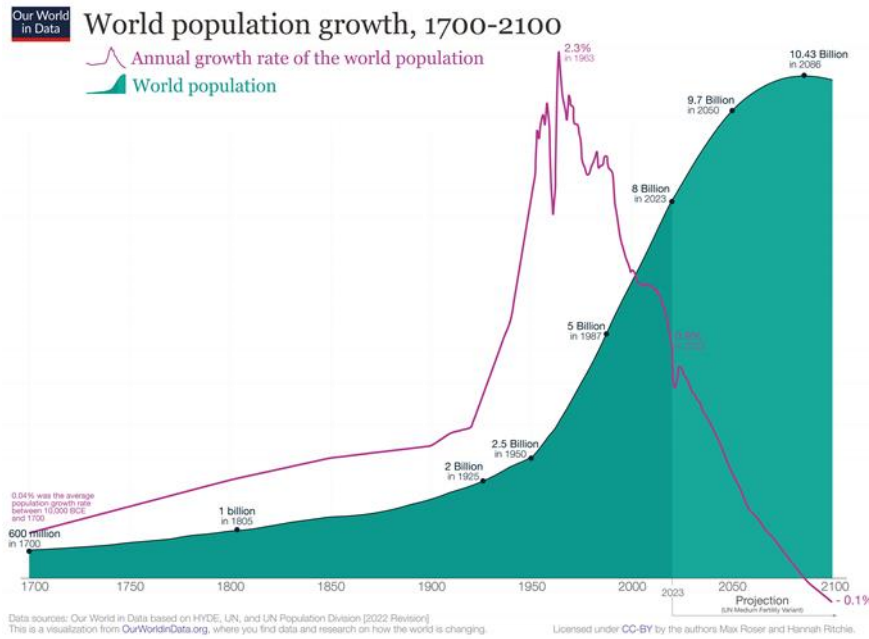


Figure 0.2: World population growth between 1700 and 2100 [5].

The use of renewable energy sources to produce energy is a proposed solution to this critical issue. Over the past 60 years, more research have been conducted in this field and the production of energy using renewables has increased, as shown in Figure 0.3 [7]. Renewable energy is derived from natural sources that are replenished on a human timescale, at a higher rate than they are consumed, such as sunlight and wind [8]. Producing renewable energy is far less polluting than burning fossil fuels, as it produces fewer emissions. In addition, renewable energy is cheaper in the majority of countries. Therefore, transitioning from fossil fuels to renewables is key to addressing both the climate crisis and the energy security issue.

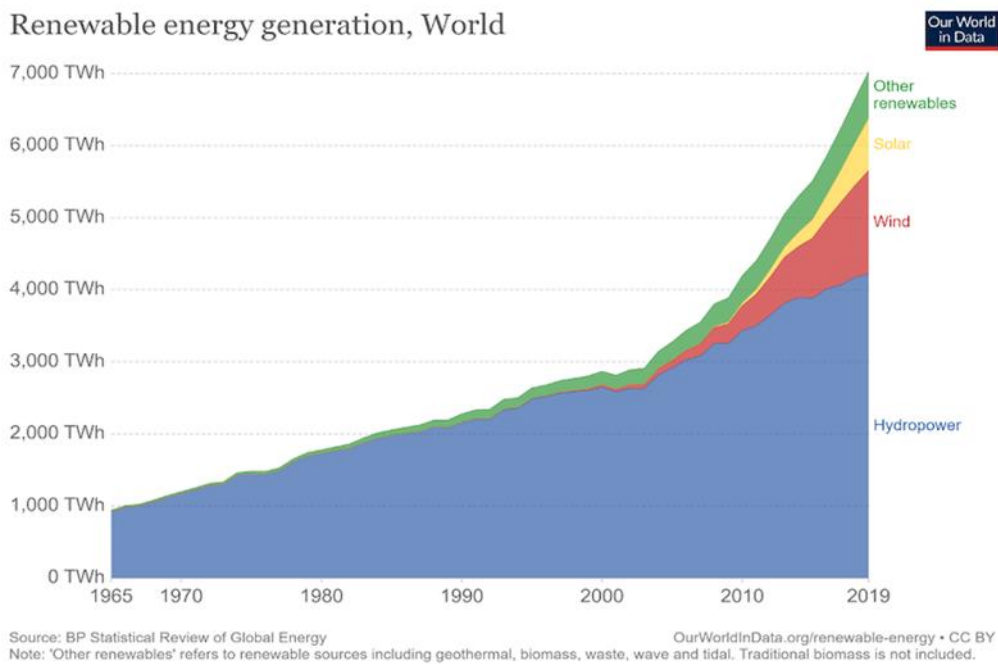


Figure 0.3: Renewable energy generation in the world between 1965 and 2019 [7].

Although the classical centralised and unidirectional energy paradigm has become mature, it is a bottleneck for the integration of renewable energy sources. Consequently, an alternative architecture for energy production and distribution is required. The new alternative architecture should be decentralized and multidirectional, allowing the insertion of renewables (Figure 0.4). This will offer a clean and sustainable substitute with the ability to produce electricity with low carbon emissions. In addition, decentralising the grid will increase its security by adding diversity, and reduce transmission costs and losses by generating energy locally. This would be a very helpful way of keeping up with the growing energy demand while reducing the variability of energy generation costs.

To reduce the stress caused by intermittent energy sources such as photovoltaics and wind turbines, energy storage is required in such a system. Batteries are very commonly used for this purpose. Energy Storage Systems (ESS) are bidirectional in terms of power, as they can act as energy sources or energy loads. In a decentralized power grid, the flow direction of electrical power between different parts of the grid depends on the instantaneous values of the consumers’ power demand on the one hand, and the available power from the different renewable sources and ESS on the other. Therefore, the grid should be able to provide multidirectional power exchange.

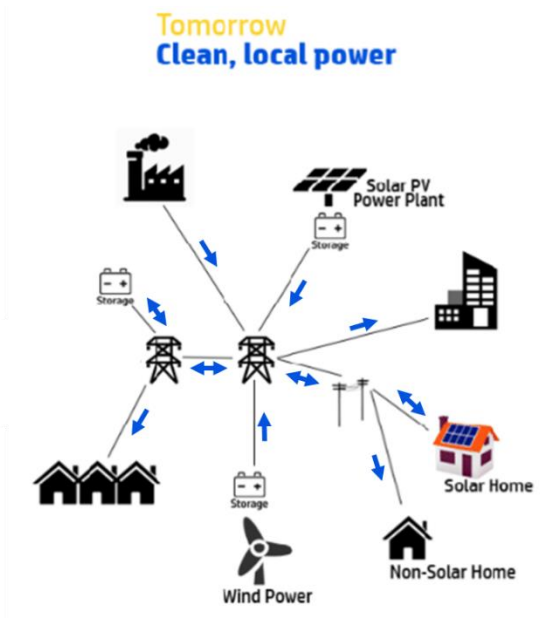


Figure 0.4: Decentralized energy system with renewable energy integration [4].

In order to interconnect the different energy sources, loads and ESS present in a decentralized and multidirectional grid, an intermediate level is required. The objective of this level is to correctly convert the power between these units, aiming to match their different electrical specifications, such as types of current (alternative current AC or direct current DC), voltage levels, frequencies, power ratings... For this purpose, power converters are usually sought, as they achieve a conversion stage between two electrical units by using different types of semiconductor devices.

A significant proportion of the emerging sources exhibit a DC character, with solar panels and batteries representing a particularly prominent example. Consequently, research is being

conducted to develop new DC grids in addition to the traditional AC grid, with the objective of collecting this energy and directly providing DC consumers with less power conversion stages.

A classic solution for interconnecting the various sources and loads would be to connect each unit separately to the main AC grid by using several stages of DC/DC and DC/AC converters [9]. This results in a chain of converters that reduces the overall efficiency. However, replacing these numerous converters with a single mutual multiport converter that connects all the units together (renewable energy sources, ESS, AC and DC grids) has many benefits over using the classic solution. Multiport electrical converters have attracted a lot of attention in recent years as a promising solution for the integration of renewable energy sources and the implementation of a decentralized energy system. These structures form an Energy Hub where the production, consumption and storage of electrical energy can be done in one place (Figure 0.5) [3]. In general, a multiport converter has the following advantages over the classical solution:

- Decreasing the overall amount of material needed for the manufacturing of the converter
- Reducing the total system volume and cost
- Increasing the overall efficiency, as the system will be working in a more adequate operation area, where it is less likely to operate at low power levels
- Allowing the implementation of several energy routing possibilities in order to reduce the impact of failures, optimize the power flows and enhance the grid’s efficiency

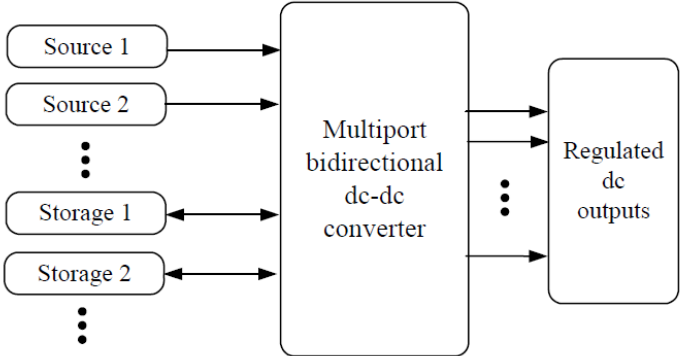


Figure 0.5: Multiport system structure [10].

The existing basic bidirectional switching cells (e.g. boost, buck, half-bridge, full-bridge...) offer a number of possibilities to create the ports of a multiport converter [10]. Another specification of a multiport converter is the type of coupling it uses to connect its different ports. In fact, there are two main types of coupling: DC-link coupling and magnetic coupling. Both types allow bidirectional power flow. DC-link coupling involves connecting several ports together via a DC bus. The main drawbacks of this method are the inability to connect ports with large voltage differences and the fact that it does not provide any isolation between ports. Magnetic coupling involves connecting the different ports via a multi-winding transformer. This method permits the interconnection of ports with quite different voltage levels, while simultaneously providing galvanic isolation between them. This simplifies earthing procedures, thereby enhancing safety. A combination of these two types of coupling can also be done in a multiport bidirectional converter, as shown in Figure 0.6 [10].

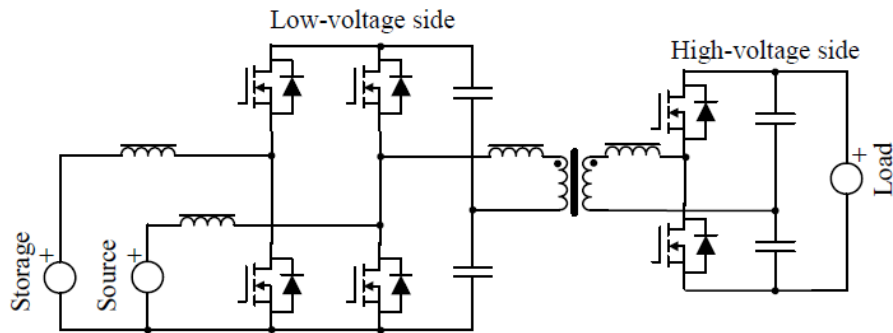


Figure 0.6: Example of a three-port converter combining dc-link and magnetic-coupling [10].

A Multi-Active Bridge (MAB) converter is one of the existing multiport converter topologies that has emerged in recent years. A MAB converter consists of any number of ports, all connected together through a high-frequency (HF) multi-winding transformer. This means that magnetic coupling is applied to all ports of the converter, providing full galvanic isolation between them. Galvanic isolation is crucial for applications where different power sources/loads with significant voltage dissimilarities and power ratings need to be connected together.

The MAB converter topology has many advantages, such as [11]:

- Full intrinsic galvanic isolation between all ports
- Multi-directional power flow
- Matching of port voltage levels due to the transformer windings and turn ratio
- Easy realisation of soft switching
- High system efficiency and power density
- Fast dynamic response

For these reasons, MAB converters represent an interesting topology that can be used in many applications leading to the achievement of a decentralized and sustainable energy system, such as:

- a) *Smart homes and buildings:* In future homes and buildings, renewable energy sources such as photovoltaic panels or wind turbines are likely to be installed to provide local and clean energy. Therefore, a MAB converter can be an interesting topology for connecting these renewable energy sources to the main AC grid, an ESS and the electrical loads of the building [12], [13]. Figure 0.7 shows an example of a four-port MAB converter used in a domestic application, such as a residential building equipped with photovoltaic panels and an ESS consisting of batteries. It is this type of application that this thesis is mainly focused on.

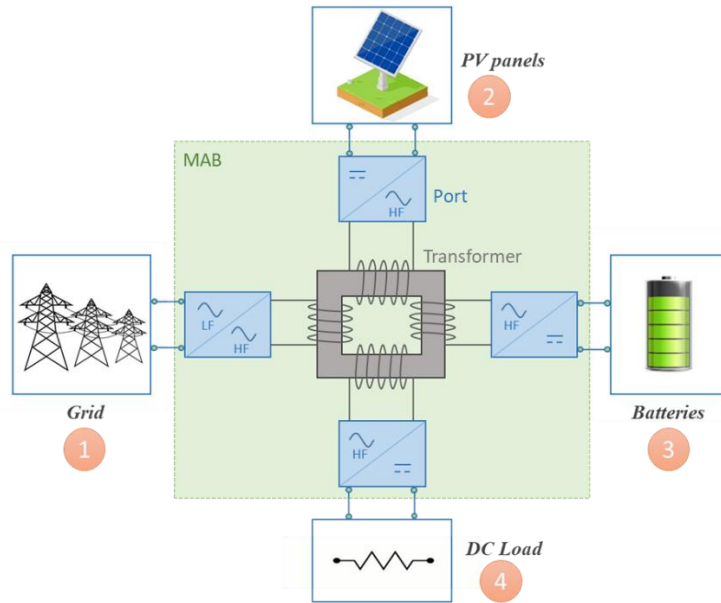


Figure 0.7: A four-port MAB converter application example.

- b) *Micro-grids:* Reference [9] proposes employing a cluster of MAB converters in micro-grids to interconnect their different parts, instead of the classical solution of installing one converter per function (Figure 0.8). This study has also shown the advantages that this cluster solution brings to the energy system, such as improving efficiency, reliability, and flexibility.
- c) *Electric vehicles:* Many previous studies have proposed using MAB converters for the fast charging of electrical vehicles [14], [15]. This multiport converter allows the vehicle's batteries to be charged from multiple sources, such as renewable energy sources and the grid, without the need for an intermediate DC bus. It also provides full galvanic isolation and allows the different sources to be connected to the batteries, even if they have different voltage levels.
- d) *Battery Management Systems (BMS):* MAB converters can also be interesting to use in BMSs to balance the voltages and charges of different cells by allowing an energy exchange between them. This increases the life expectancy of the cells by preventing them from being over-charged or over-discharged [16].

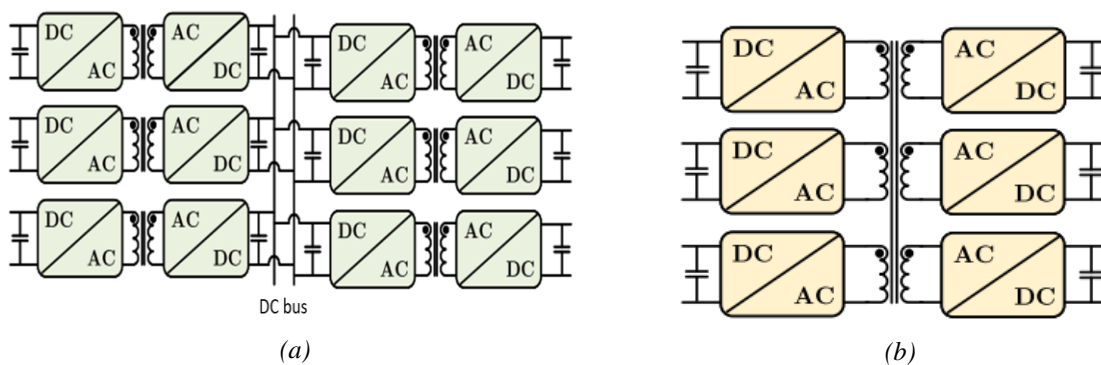


Figure 0.8: Fully isolated coupling of different electrical sources and loads using: (a) Classical solution with multiple isolated Single-Input Single-Output (SISO) converters connected together through a DC bus, (b) a MAB converter [12].

The main objective of this thesis is to develop a generic mathematical model of a MAB converter and then use it to develop an optimized control strategy for this multiport converter. The majority of this work focuses on the topology of a MAB converter consisting of full-bridges on all its ports, for simplicity and in order to fully explore this topology.

Controlling a MAB converter generally involves managing the power exchange between its ports in order to provide the required power at each port. However, many other challenges are associated with this. Therefore, the objectives of the developed control strategy can be summarized as follows:

- Maximize the system's efficiency across the entire operating range
- Decouple the control of the cross-coupled ports to avoid instability issues
- Prevent saturation of the transformer's magnetic core
- Compensate for interactions with externally connected systems to maintain the stability of the MAB converter

A $4 \times 500\text{ W}$ prototype was built during this thesis for experimental validation.

Finally, a new topology of a hybrid-fed MAB converter is also proposed and investigated during this thesis. A mathematical model is developed and a control strategy is elaborated for this topology to prove the feasibility of such a converter.

This thesis has led to the following contributions:

- Conference paper: R. Tarraf *et al.*, "Modeling and Control of a Decoupled Hybrid-Fed Multi-Active Bridge (MAB) Converter," in *PCIM Europe 2023; International Exhibition and Conference for Power Electronics, Intelligent Motion, Renewable Energy and Energy Management*, May 2023, pp. 1–9. doi: 10.30420/566091242.
- Conference paper (in progress): R. Tarraf *et al.*, "An Optimized Control Strategy Using Multivariable Modulation and Reactive Power Exchange Cancellation for a Multi-Active Bridge (MAB) Converter", in *PEMD 2024; Power Electronics, Machines and Drives 13th International Conference*, June 2024.
- Journal: Tarraf, R.; Frey, D.; Leirens, S.; Carcouet, S.; Maynard, X.; Lembeye, Y., "Modelling and Control of a Hybrid-Fed Triple-Active Bridge Converter", *Energies* 16, no. 16: 6007, <https://doi.org/10.3390/en16166007>.
- Patent: Tarraf, R.; Frey, D.; Leirens, S.; Carcouet, S.; Maynard, X. (2023), "Système de multiples ponts actifs à alimentation hybride, procédé et dispositif associés", FR2304696.
- Patent (in progress): Tarraf, R.; Frey, D.; Leirens, S.; Carcouet, S.; Maynard, X. (2024), "Une stratégie de commande optimisée utilisant une modulation multi-variable et l'annulation de l'échange de puissance réactive pour un convertisseur à multiples ponts actifs".

This manuscript is structured as follows:

Chapter 1 introduces the considered MAB converter topology and details its steady-state and dynamic modelling. Steady-state models represent a system at a certain operating point while dynamic models represent it between two operating points. The coupling between the ports of this topology is also explained in this chapter and existing decoupling strategies are described. Finally, the interaction between the MAB converter and an externally connected LC filter is

investigated, and an active solution is proposed to compensate for the instabilities caused by this connection.

Chapter 2 proposes a loss calculation technique based on the steady-state mathematical model developed in Chapter 1. Conduction and switching losses are considered in this study. An optimization control strategy is then elaborated, aiming to provide each port with its required power while minimizing the total system losses.

Chapter 3 provides the experimental results obtained from a built $4 \times 500 \text{ W}$ MAB converter prototype in order to validate the theoretical study presented in the first two chapters. The prototype design is first detailed and the mathematical model is then validated along with the proposed optimization control strategy. The possible presence of DC bias in the transformer is also addressed in this chapter, and an active solution is proposed to eliminate this bias and prevent transformer saturation.

Finally, in Chapter 4, a new topology of a hybrid-fed MAB converter mixing both voltage-fed and current-fed ports is investigated and modelled. A control strategy is also proposed for this topology, knowing that the presence of a current-fed port imposes strict constraints on the control system of the MAB converter.

Conclusions and perspectives for future works are presented at the final part of this manuscript.

CHAPTER 1: TOPOLOGY AND MODELLING OF A MAB CONVERTER

1.1. Introduction

The primary objective of this chapter is to introduce and describe the MAB converter topology on which most of the work in this thesis has been focused. After that, the mathematical model of this converter is established. The mathematical modelling of a system makes the study of its behaviour easier as it gives valuable insights into its operation and stability margins. Furthermore, it helps with the closed-loop controllers' design. Two types of mathematical models are addressed in this thesis: the steady-state model and the dynamic model. A steady-state model should precisely depict the behaviour of the system at a certain operating point A or B, after the steady state's establishment. This model will be useful to build the optimal multi-variable control strategy of the MAB converter in the next chapter. Conversely, a dynamic model portrays the system when the steady-state model fails to do so, during its transition between two operating points A and B, or when disturbances arise at a particular operating point. The dynamic model is valuable in designing the closed-loop controllers of the system.

1.2. Considered MAB Converter Topology

A MAB converter is a multiport, multidirectional DC-DC converter consisting of any number of ports tied together through a HF multi-winding transformer. It is the extension of the well-known Dual Active Bridge (DAB) converter that has been used in many power electronic applications since the 90's. Actually, a DAB converter is a MAB converter consisting of only two ports.

Generally, at each input port of a MAB converter, a DC voltage source is connected to a DC/AC inverter that allows the HF power supply of the multi-winding transformer. This inverter should also act like a rectifier (AC/DC converter) when the power is reversed, if the connected source is bidirectional (ESS or the grid), allowing bidirectional power exchange [17]. Output ports usually connect the transformer to DC loads of capacitive nature through a rectifier. In this thesis, H-bridges were considered at all the ports of the MAB converter in order to keep it symmetrical and generic by allowing bidirectional power flow on all its ports.

The considered topology for this thesis is shown in Figure 1.1. Each port consists of a DC voltage source (representing either a real power source or a load with the behaviour of a voltage source) and a classical H-bridge. All ports are connected through a HF multi-winding transformer. L_i represents the leakage inductance of the transformer winding of a port #i, which can be connected to an additional external series inductance. These inductances work as the main power transfer elements between the ports. R_i represents the total series resistance at the transformer winding of a port #i. Voltage $v_{ac,i}$ of a port #i is a HF square voltage created by the H-bridge by inverting the DC voltage V_i at the switching frequency f_s .

Figure 1.2 illustrates the star-delta equivalent circuits of the transformer (neglecting the transformer's series resistances). Each port is replaced by a square voltage source $v_{ac,i}$ in these

models. The star equivalent model is closer to the real physical converter, but the delta equivalent model helps in visualizing and modelling the power exchanges between the ports.

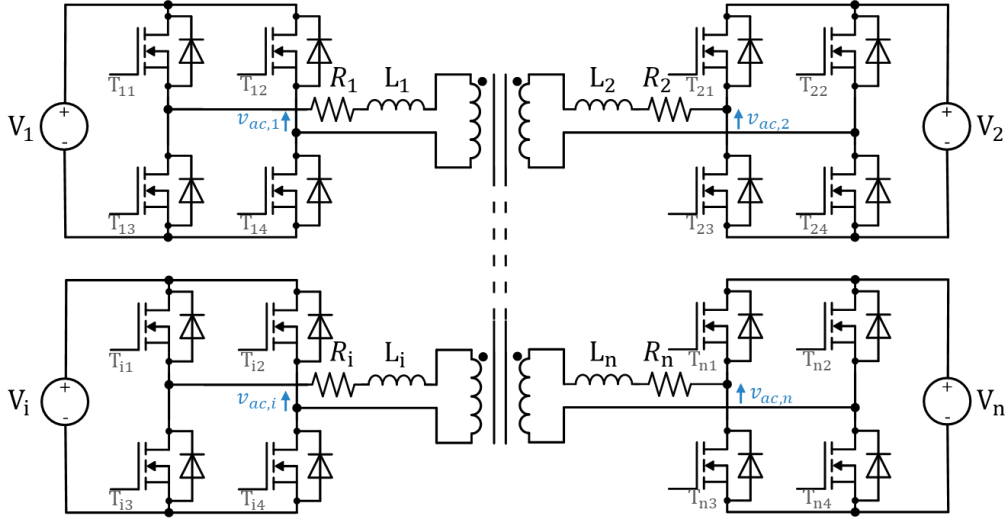


Figure 1.1: Considered topology of a Multi-Active Bridge converter with n ports.

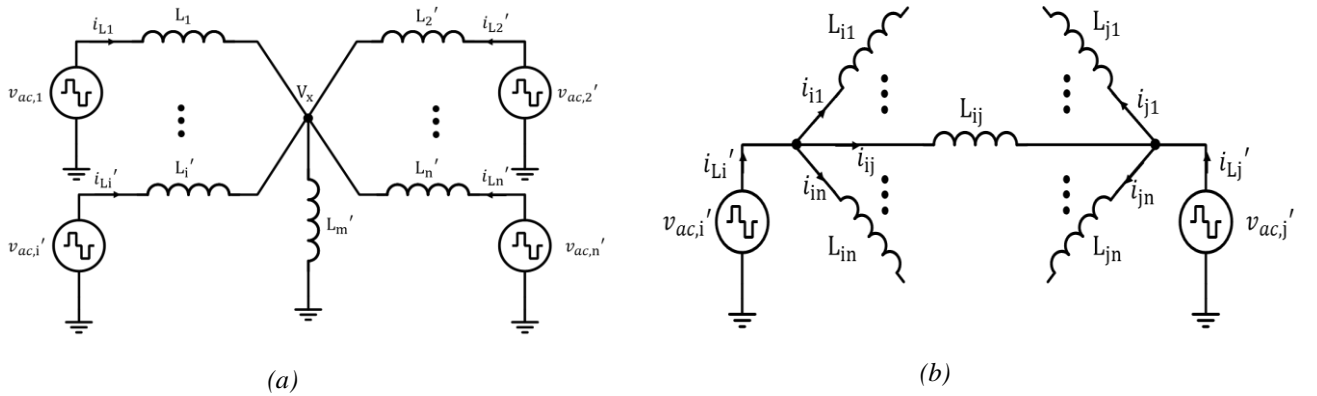


Figure 1.2: Star-delta transformation of the MAB converter's transformer model: (a) Star model, (b) Delta model.

The voltages, the delivered currents, the leakage inductances and the magnetizing inductance in Figure 1.2 are all referred to the reference port of this converter, which will be port #1:

$$v'_{ac,i} = \frac{n_1}{n_i} v_{ac,i} \quad ; \quad i'_{Li} = \frac{n_i}{n_1} i_{Li} \quad ; \quad L'_i = \left(\frac{n_1}{n_i}\right)^2 L_i$$

n_i is the turn number of the transformer winding corresponding to port # i . The magnetizing inductance will be neglected from now on in this study, as its value is usually significantly greater than that of the leakage inductances.

The effective inductance between two ports is represented in the delta equivalent model, which is developed by applying the theory of superposition to the star model [18]. This inductance,

also called the “link inductance” L_{ij} between a port #i and a port #j, can be calculated as follows, referred to the reference port #1:

$$L_{ij} = \begin{cases} NA, & \forall i = j \\ L'_i + L'_j + L'_i L'_j \left(\sum_{k \neq i, j}^n \frac{1}{L'_k} \right), & \forall i \neq j \end{cases} \quad (1.1)$$

The link inductance value needs to be calculated in order to get the average power flow between two ports.

The series link resistances R_{ij} can be calculated in a similar way to the link inductances, from (1.1).

In order to get the transformer windings' currents as represented in the star-equivalent model of Figure 1.2, we integrate the following expression over a switching period:

$$\frac{di'_{Li}}{dt} = \frac{v'_{ac,i} - V_x}{L'_i} \quad (1.2)$$

V_x is the voltage at the star-point referred to port #1, which is obtained by applying the theory of superposition to estimate the Thevenin voltage contribution of all ports [18]:

$$V_x(t) = \sum_{i=1}^n \frac{\left(\sum_{j=1, j \neq i}^n \frac{1}{L'_j} \right)^{-1}}{L'_i + \left(\sum_{j=1, j \neq i}^n \frac{1}{L'_j} \right)^{-1}} \times v'_{ac,i}(t) \quad (1.3)$$

The waveform of the AC voltage $v'_{ac,i}$ of a port #i is shown in Figure 1.3, along with the AC voltage of the reference port #1. The turn ratios of a MAB's transformer windings are chosen such that all the AC voltages have equal maximum values once referred to the same port:

$$\frac{n_i}{n_j} = \frac{V_i}{V_j} \quad (1.4)$$

This is what makes the connection of ports with different voltage levels possible in a MAB converter. In Figure 1.3, T_s is the switching period of the MAB, which is equal to $1/f_s$.

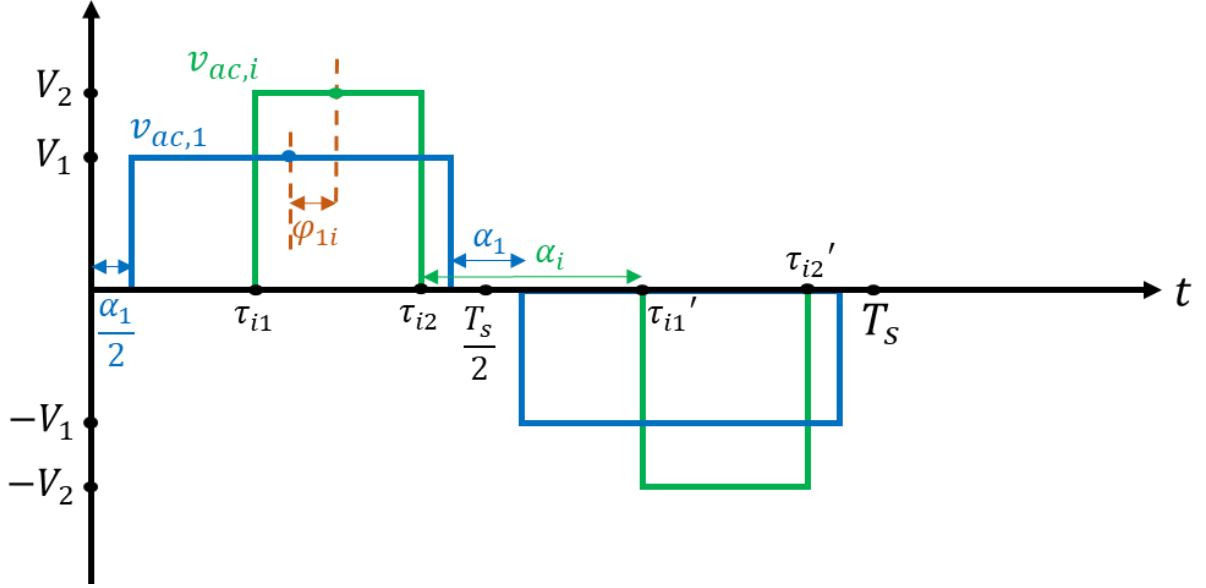


Figure 1.3: AC voltages of port #1 and port #i referred to the reference port #1 with their corresponding external and internal phase shifts.

The command phase shift between the legs of each H-bridge of this topology is called “internal phase shift” and is noted by α_i for a port #i, with $0 \leq \alpha_i \leq \pi$. When the internal phase shift of a port #i is different from zero, its AC voltage $v_{ac,i}$ will have three levels (Figure 1.3). However, if $\alpha_i = 0$, $v_{ac,i}$ will be two-leveled. Internal phase shifts are also called “duty cycles” in other references because they control the duty cycles of the ports’ AC voltages.

We call $\varphi_{1i} = (\varphi_1 - \varphi_i)$ the “external phase shift” of a port #i (Figure 1.3). Since port #1 is the reference port, its external phase shift is considered equal to zero ($\varphi_1 = 0$). Therefore, the AC voltages of all the other ports are shifted with respect to the reference port. More generally, we denote by $\varphi_{ij} = (\varphi_i - \varphi_j)$ the external phase shift between a port #i and a port #j. In this manuscript, the external phase shift between two ports #i and #j corresponds to the phase shift between the middle points of the two positive parts or the two negative parts of their AC voltages, as represented in Figure 1.3. The value of each external phase shift is limited between $-\pi$ and π in radians. External phase shifts mainly determine the energy flow values and directions between ports.

The command signals of the H-bridge’s switches of a port #i (as referred to in Figure 1.1) are displayed in Figure 1.4.

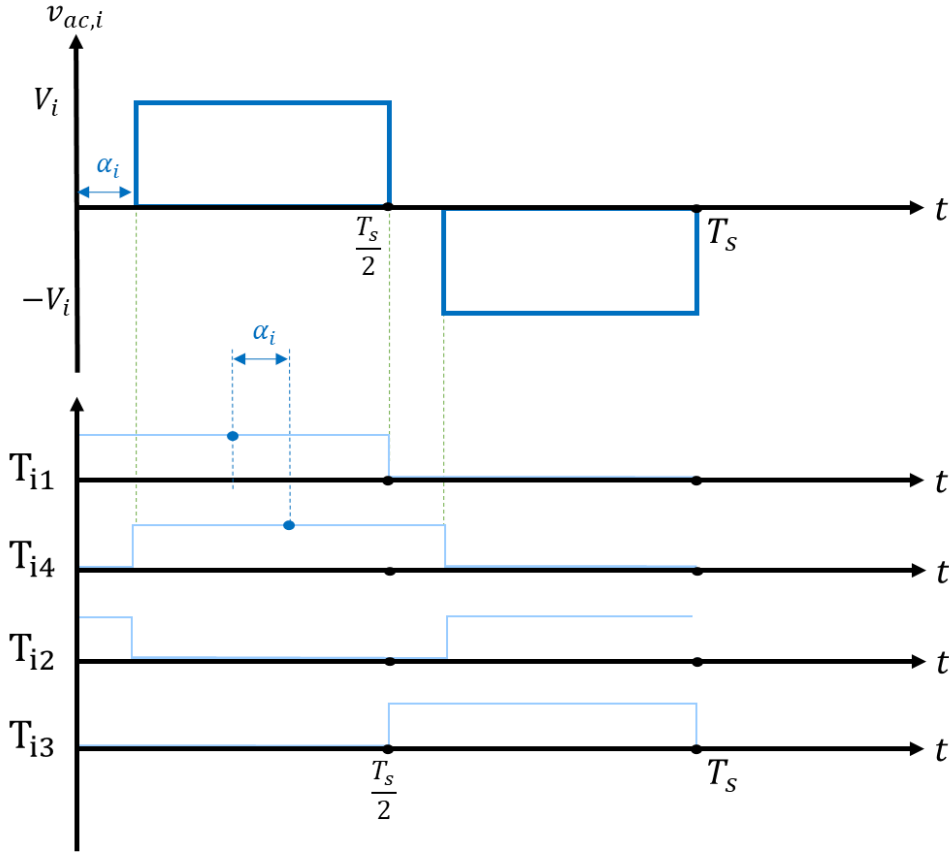


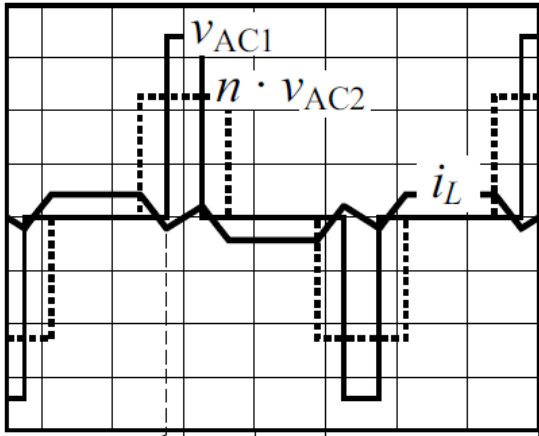
Figure 1.4: Command signals of the H-bridge switches of a port #i.

Controlling the power flows between the ports of a MAB converter can be achieved by varying its external and internal phase shifts. The switching frequency of the ports can also be changed for this purpose. However, varying the switching frequency can lead to many problems like passive component sizing complexities and electromagnetic compatibility (EMC) issues. Therefore, in this thesis, the only control parameters that are used are the internal and external phase shifts of the MAB converter.

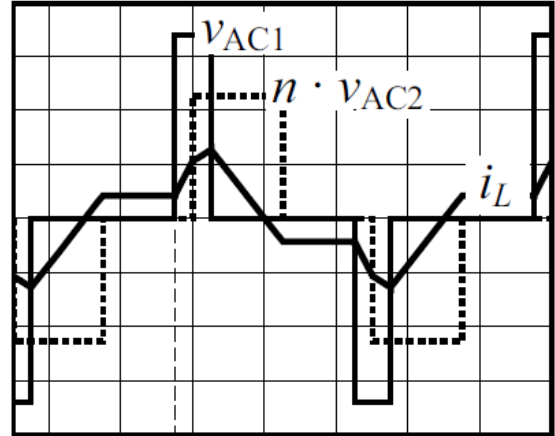
Each port of a MAB converter has an internal phase shift and an external phase shift, except for the reference port, which only has an internal phase shift (since $\varphi_1 = 0$). This means that a MAB converter with n ports has a total of $(2n - 1)$ control parameters, with n internal phase shifts and $(n - 1)$ external phase shifts. In other words, its control has $(2n - 1)$ degrees of freedom.

1.3. Steady-State Modelling of a MAB Converter

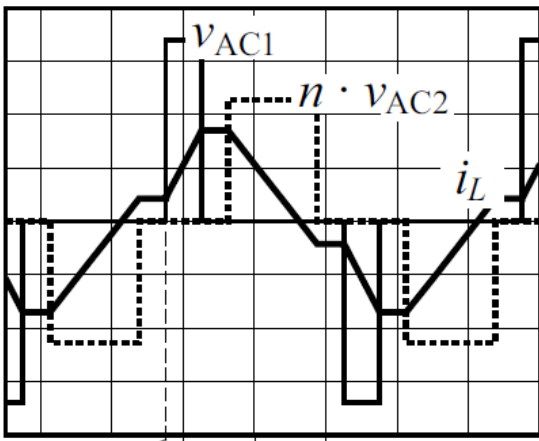
The time domain analysis is the most accurate way to model a MAB converter. In literature, many works have proposed a time-domain-based model of a DAB converter. When all three control parameters of a DAB converter are used to control the power flow between its two ports (two internal phase shifts and one external phase shift), twelve working modes can be distinguished [19]. These working modes are based on the different sequences of the rising and falling edges of the AC voltages at the transformer windings and are shown in Figure 1.5. In general, some of these working modes are not considered when studying a DAB converter, as they lead to increased circulating currents and losses in the converter [19], [20].



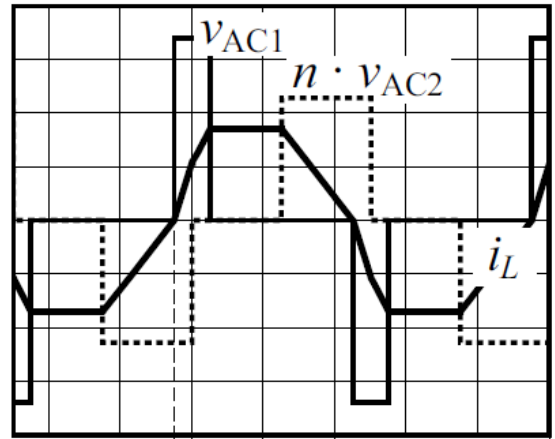
(a)



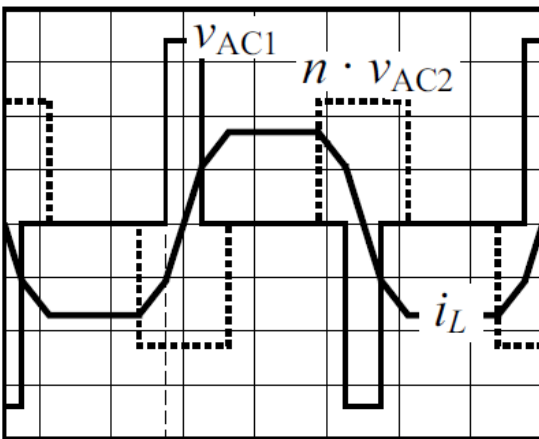
(b)



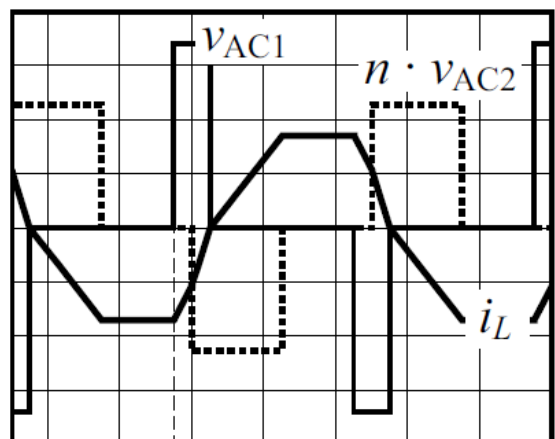
(c)



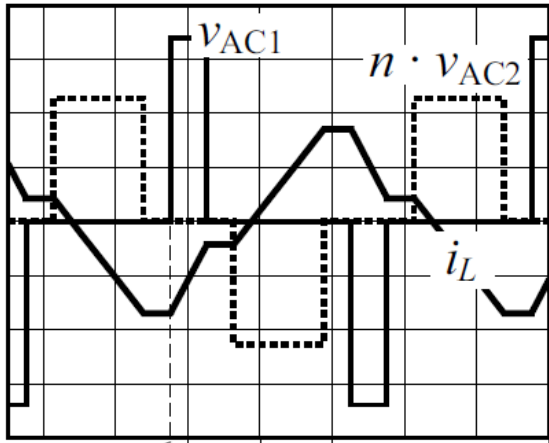
(d)



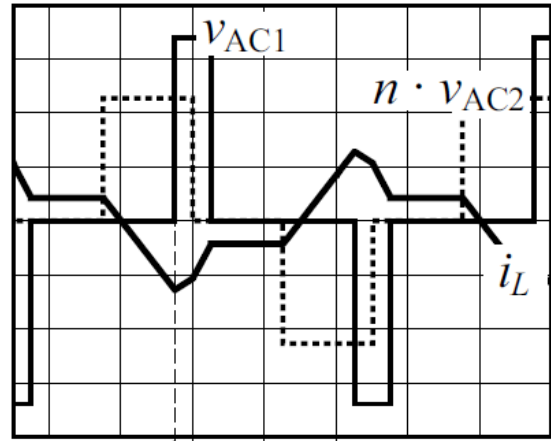
(e)



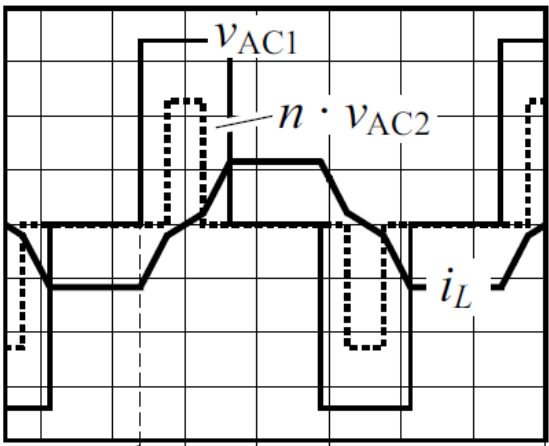
(f)



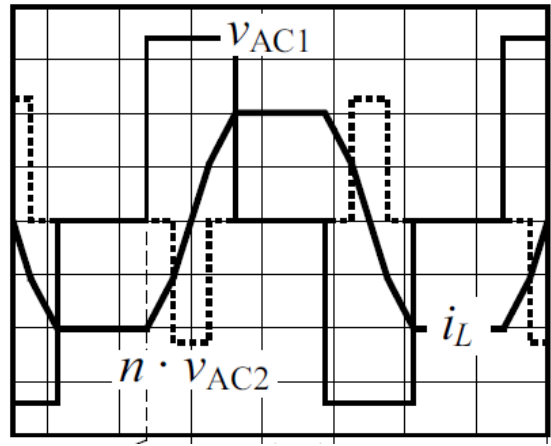
(g)



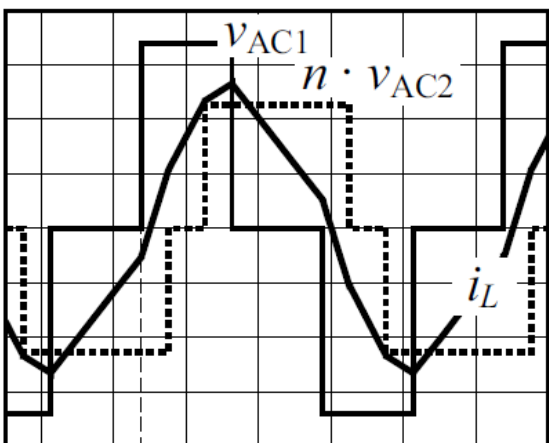
(h)



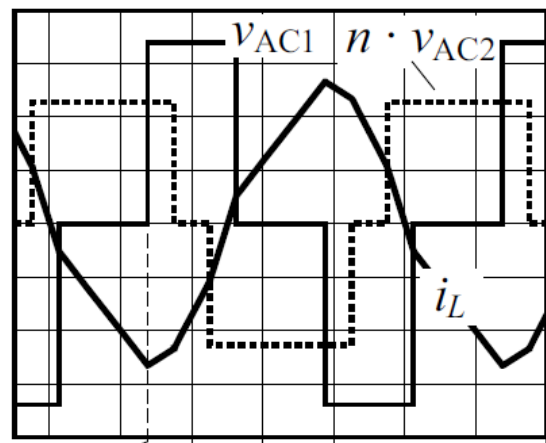
(i)



(j)



(k)



(l)

Figure 1.5: The 12 basic working modes generated by the H-bridges of a DAB converter [19].

In each working mode, the expression of the AC current is calculated using Figure 1.5 and the following expression, which is a particular case of expression (1.2), integrated on a switching period T_s :

$$\frac{di_L}{dt} = \frac{v_{ac,1} - v'_{ac,2}}{L} \quad (1.5)$$

where L is the total transformer series inductance of the DAB converter referred to port #1 and i_L is the AC current flowing in the transformer winding of port #1.

The average power flowing between the two ports can therefore be calculated as follows:

$$P_1 = \frac{1}{T_s} \int_0^{T_s} p_1(t) dt = \frac{1}{T_s} \int_0^{T_s} v_{ac,1}(t) i_L(t) dt \quad (1.6)$$

In [19], three types of modulations are proposed for a DAB converter, depending on the amount of power flowing through it. At low power, a triangular modulation is used and at intermediate power, a trapezoidal modulation is used. Triangular and trapezoidal modulations use the internal and external phase shifts as control parameters in order to provide the AC current in the transformer a triangular or trapezoidal shape, respectively. This will allow the decrease of the system's losses by reducing the circulating currents and the switching losses. At high power, the internal phase shifts of both ports are made equal to zero and the external phase shift between those ports is the only used control parameter. For each modulation technique, the AC voltages and current waveforms are imposed, decreasing the voltage sequences possibilities and therefore reducing the number of considered working modes. Then, an analytical model is developed and the average power flow expression is established for each modulation technique.

In [21], a time-domain modelling of a DAB converter is proposed, where the internal phase shift of one of the ports is made equal to zero. Therefore, the only control parameters that are used in this modulation technique are the internal phase shift of the other port and the external phase shift between the two ports. Additionally, the power flow of the studied DAB converter is considered unidirectional in this paper. This facilitates the time-domain modelling of the DAB converter by reducing the number of its working modes. Only two working modes are considered in this study and are shown in Figure 1.6. The main drawback of this technique is the loss of a control degree of freedom by setting an internal phase shift to zero.

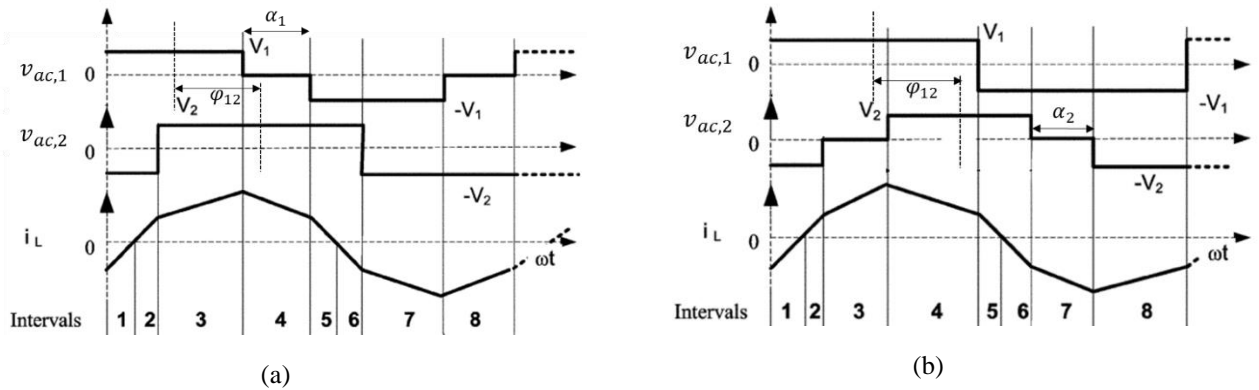


Figure 1.6: Ideal voltages and current waveforms of the DAB converter using the modulation proposed in [21]: (a) $\alpha_2 = 0$, (b) $\alpha_1 = 0$.

Nevertheless, a time-domain-based model of a MAB converter consisting of more than two ports is very complex to achieve. In fact, the number of working modes increases dramatically

when the number of ports increases. This is due to the increase in the number of control parameters and the superposition of more AC voltages at the transformer windings. For example, a Triple-Active Bridge (TAB) converter, which is a MAB converter with three ports, has 720 working modes [22], [23]. Therefore, generalizing the time-based modelling and modulation techniques proposed for a DAB converter to a MAB converter consisting of n ports is complicated. For this reason, a frequency-domain-based study would be a better solution.

In a frequency-domain model, the AC signals of the MAB converter are represented by their Fourier series expressions, which is a more generic expression that is independent from the working mode. The Fourier series expansion of a function $f(t)$, having a period of $T_s = 1/f_s = 2\pi/\omega_s$, is written as follows:

$$f(t) = a_0 + \sum_{k=1}^{\infty} a_k \cos(k\omega_s t) + b_k \sin(k\omega_s t) \quad (1.7)$$

where:

$$a_0 = \frac{1}{T_s} \int_0^{T_s} f(t) dt$$

$$a_k = \frac{2}{T_s} \int_0^{T_s} f(t) \cos(k\omega_s t) dt$$

$$b_k = \frac{2}{T_s} \int_0^{T_s} f(t) \sin(k\omega_s t) dt$$

k is the harmonic order. The 0th harmonic a_0 represents the mean value of $f(t)$, and is also called the DC component of this signal.

1.3.1. First Harmonic Approximation

In literature, many works have modelled a MAB converter in the frequency domain by only considering the first harmonic ($k = 1$, also called the fundamental) of each AC signal at the transformer windings. In other words, each AC voltage $v_{ac,i}$ and current i_{ij} is approximated by a sine wave that corresponds to its first Fourier series harmonic $\tilde{v}_{ac,i}$ and \tilde{i}_{ij} , respectively. This simplifies the AC signals' expressions and therefore facilitates the modelling of the MAB converter and reduces the calculation complexity and burden [9], [17], [24], [25], [26].

From Figure 1.3 and expression (1.7) with $k = 1$, we can deduce the first harmonic expressions of the AC voltages of the reference port #1 and a port #i. In an ideal scenario, these voltages are purely AC, which means that their DC components are considered zero. Voltage $v_{ac,1}$, as represented in Figure 1.3, is an odd function ($v_{ac,1}(-t) = -v_{ac,1}(t)$). Consequently, its a_k components are equal to zero for $k = [1, \infty[$. Therefore, the first harmonic representations of the AC voltages referred to port #1 can be written as:

$$\tilde{v}_{ac,1}(t) = \frac{4V_1}{\pi} \cos\left(\frac{\alpha_1}{2}\right) \sin(\omega_s t)$$

$$\tilde{v}_{ac,i}'(t) = \frac{4V_i}{n_{1i}\pi} \cos\left(\frac{\alpha_i}{2}\right) \sin(\omega_s t - \varphi_{1i}) \quad (1.8)$$

With $n_{1i} = \frac{n_i}{n_1}$.

Alternatively, these first harmonic voltage approximations can be written in the complex form as follows:

$$\overline{v_{ac,1}} = \frac{4V_1}{\pi\sqrt{2}} \cos\left(\frac{\alpha_1}{2}\right) \quad (1.9)$$

$$\overline{v_{ac,i}'} = \frac{4V_i}{n_{1i}\pi\sqrt{2}} \cos\left(\frac{\alpha_i}{2}\right) e^{-j\varphi_{1i}} = \frac{4V_i}{n_{1i}\pi\sqrt{2}} \cos\left(\frac{\alpha_i}{2}\right) (\cos(\varphi_{1i}) - j\sin(\varphi_{1i}))$$

From expression (1.9) and the delta equivalent circuit of Figure 1.2(b), the current i_{1i} flowing from port #1 to port #i through the link inductance L_{1i} can be expressed in the complex form as follows:

$$\begin{aligned} \overline{i_{1i}} &= \frac{\overline{v_{ac,1}} - \overline{v_{ac,i}'}}{L_{1i}\omega_s j} \\ &= \frac{4}{\sqrt{2}\pi L_{1i}\omega_s} \left\{ \left[\frac{V_1}{n_{1i}} \cos\left(\frac{\alpha_1}{2}\right) \cos(\varphi_{1i}) - V_1 \cos\left(\frac{\alpha_1}{2}\right) \right] \cdot j + \frac{V_i}{n_{1i}} \cos\left(\frac{\alpha_i}{2}\right) \sin(\varphi_{1i}) \right\} \end{aligned} \quad (1.10)$$

The apparent power flowing from port #1 to port #i can be deduced from expressions (1.9) and (1.10) as follows:

$$\begin{aligned} S_{1i} &= \overline{v_{ac,1}} \times \overline{i_{1i}}^* \\ &= \frac{8}{\pi^2} \frac{V_1}{L_{1i}\omega_s} \cos\left(\frac{\alpha_1}{2}\right) \left\{ \left[V_1 \cos\left(\frac{\alpha_1}{2}\right) - \frac{V_i}{n_{1i}} \cos\left(\frac{\alpha_i}{2}\right) \cos(\varphi_{1i}) \right] \cdot j \right. \\ &\quad \left. + \frac{V_i}{n_{1i}} \cos\left(\frac{\alpha_i}{2}\right) \sin(\varphi_{1i}) \right\} \end{aligned} \quad (1.11)$$

$\overline{i_{1i}}^*$ is the complex conjugate of $\overline{i_{1i}}$.

Knowing that $S_{1i} = Q_{1i} \cdot j + P_{1i}$, where Q_{1i} is the reactive power and P_{1i} is the active power flowing from port #1 to port #i, we can deduce the following first harmonic approximation expressions:

$$Q_{1i} = \frac{8}{\pi^2} \frac{V_1}{L_{1i}\omega_s} \cos\left(\frac{\alpha_1}{2}\right) \left(V_1 \cos\left(\frac{\alpha_1}{2}\right) - \frac{V_i}{n_{1i}} \cos\left(\frac{\alpha_i}{2}\right) \cos(\varphi_{1i}) \right) \quad (1.12)$$

$$P_{1i} = \frac{8}{\pi^2} \frac{V_1 V_i}{n_{1i} L_{1i} \omega_s} \cos\left(\frac{\alpha_1}{2}\right) \cos\left(\frac{\alpha_i}{2}\right) \sin(\varphi_{1i}) \quad (1.13)$$

The generalization of expressions (1.12) and (1.13) gives the following expressions for the active and reactive powers flowing from a port #i to a port #j of a MAB converter, if the first harmonic approximation of the AC signals is applied:

$$Q_{ij} = \frac{8}{\pi^2} \frac{V_i}{L_{ij}\omega_s} \cos\left(\frac{\alpha_i}{2}\right) \left(V_i \cos\left(\frac{\alpha_i}{2}\right) - \frac{V_j}{n_{ij}} \cos\left(\frac{\alpha_j}{2}\right) \cos(\varphi_{ij}) \right) \quad (1.14)$$

$$P_{ij} = \frac{8}{\pi^2} \frac{V_i V_j}{n_{ij} L_{ij} \omega_s} \cos\left(\frac{\alpha_i}{2}\right) \cos\left(\frac{\alpha_j}{2}\right) \sin(\varphi_{ij}) \quad (1.15)$$

As a result, the total active power received by a port #i will be:

$$P_i = \sum_{j \neq i}^n P_{ji} = \sum_{j \neq i}^n \frac{8}{\pi^2} \frac{V_j V_i}{n_{ji} L_{ij} \omega_s} \cos\left(\frac{\alpha_j}{2}\right) \cos\left(\frac{\alpha_i}{2}\right) \sin(\varphi_j - \varphi_i) \quad (1.16)$$

As we can notice from (1.16), the maximum power that can be transferred between two ports is inversely proportional to the size of their link inductance. If large inductances are employed, instantaneous active power transfer can often become close to its maximum value and a greater amount of reactive power will flow between the ports, thus increasing the total system losses. On the other hand, small inductances will lead to sharper current changes and a limited range of soft switching [9], [25]. For that reason, a compromise should be done.

In [9], the non-linear increase of the flowing currents due to the increase of the reactive power was studied in a MAB converter in function of the amount of active power flowing in the system. The results are shown in Figure 1.7. As we can notice, the non-linear behaviour of the current becomes clear when the system is operating at more than 60% of its maximum transferrable power value. Therefore, in order to solve this problem, the sizing of the MAB converter is achieved considering that the nominal power that will flow in it will be equal to 60% of its maximum transferred power.

This hardware oversizing method limits the maximum attained external phase shift values (maximum external phase shift of $\arcsin(0,6) = 37^\circ$ between two ports when internal phase shifts are equal to zero). Consequently, we can consider that $\sin\varphi_{ij} \approx \varphi_{ij}$ on all the operation range (maximum error of 7.3% when internal phase shifts are zero [9]), hence linearizing expression (1.16). The linearization of this expression simplifies the control of the system and further reduces the calculation burden.

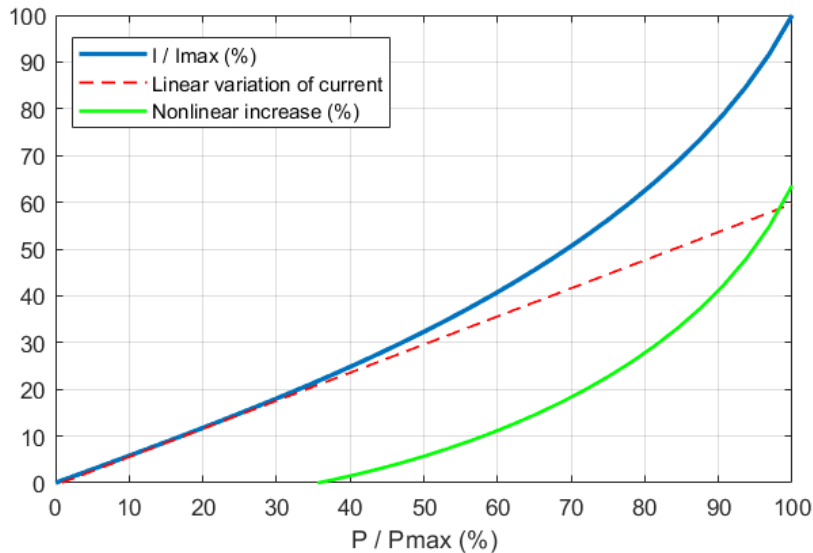


Figure 1.7: Non-linear increase of current in an active bridge of a MAB converter as the power transfer gets closer to its maximum value [9].

When only the external phase shifts are used to control the system, the first harmonic approximation of the AC signals accurately reflects the system's behaviour, enabling the calculation of the external phase shifts required to achieve a specific set of desired power values.

However, when both internal and external phase shifts are used, the first harmonic approximation fails to represent the system correctly. In other words, the first harmonic approximation brings simplicity to the MAB converter's model but lacks precision in certain cases.

For the sake of simplicity, the control of a MAB converter using only its external phase shifts will be called "External Phase Shift modulation" (EPS modulation) from now on in this manuscript. Similarly, the control of a MAB converter using all of its internal and external phase shifts will be called "Multiple Phase Shift modulation" (MPS modulation).

1.3.2. Generalized Harmonic Approximation (GHA)

In order to increase the frequency-domain model precision of the MAB converter, more harmonics should be considered in the Fourier series expansion of the AC signals. In [22], the GHA model of a TAB converter was developed. A GHA model represents each AC signal as an infinite summation of its harmonics in the frequency domain. In this thesis, the generic GHA model of a MAB converter with n ports is elaborated, as described in this section.

Using the GHA, the expression of the AC voltage $v_{ac,i}'$ of a port # i referred to the reference port #1 can be written as follows, using Figure 1.3 and expression (1.7) for $k = 1, 3, \dots, \infty$:

$$v_{ac,i}'(t) = \frac{4V_i}{n_{1i} \cdot \pi} \sum_{\substack{k=1 \\ k \text{ odd}}}^{\infty} \frac{1}{k} \cos\left(k \frac{\alpha_i}{2}\right) \sin(k \cdot (w_s t - \varphi_{1i})) \quad (1.17)$$

$w_s = 2\pi f_s$ where f_s is the switching frequency.

The current flowing from port # i to port # j of the MAB converter referred to the reference port #1 can be deduced from the delta model of Figure 1.2(b) and expression (1.17) as follows:

$$\begin{aligned} i_{ij}(t) &= \frac{1}{L_{ij}} \int_0^t (v_{ac,i}'(t) - v_{ac,j}'(t)) dt \\ &= \frac{4}{\pi w_s L_{ij}} \sum_{\substack{k=1 \\ k \text{ odd}}}^{\infty} \left[-\frac{V_i}{n_{1i} k^2} \cos\left(k \frac{\alpha_i}{2}\right) \cos(k \cdot (w_s t - \varphi_{1i})) \right. \\ &\quad \left. + \frac{V_j}{n_{1j} k^2} \cos\left(k \frac{\alpha_j}{2}\right) \cos(k \cdot (w_s t - \varphi_{1j})) \right] \end{aligned} \quad (1.18)$$

Consequently, we can get the expression of the total current sourced by a port # i into the other ports, referred to its own side of the transformer, as follows:

$$i_{L,i}(t) = \sum_{\substack{j=1 \\ j \neq i}}^n \frac{i_{ij}(t)}{n_{1i}} \quad (1.19)$$

$$= \frac{4}{\pi \omega_s n_{1i}} \sum_{\substack{k=1 \\ k \text{ odd}}}^{\infty} \left[-\frac{V_i}{n_{1i} k^2} \left(\sum_{j=1, j \neq i}^n \frac{1}{L_{ij}} \right) \cos\left(k \frac{\alpha_i}{2}\right) \cos(k(\omega_s t - \varphi_{1i})) \right. \\ \left. + \sum_{j=1, j \neq i}^n \frac{V_j}{n_{1j} k^2} \frac{1}{L_{ij}} \cos\left(k \frac{\alpha_j}{2}\right) \cos(k(\omega_s t - \varphi_{1j})) \right]$$

n is the total number of ports of the considered MAB converter.

The average active power flowing from port # i to port # j during a switching period T_s can be deduced as follows:

$$P_{ij} = \frac{1}{T_s} \int_0^{T_s} p_{ij}(t) dt = \frac{1}{T_s} \int_0^{T_s} v_{ac,i}'(t) \times i_{ij}(t) dt \\ = \frac{4}{\pi^3 f_s} \sum_{\substack{k=1 \\ k \text{ odd}}}^{\infty} \frac{1}{k^3} \frac{V_i V_j}{n_{1i} n_{1j}} \frac{1}{L_{ij}} \cos\left(k \frac{\alpha_i}{2}\right) \cos\left(k \frac{\alpha_j}{2}\right) \sin\left(k(\varphi_{1j} - \varphi_{1i})\right) \quad (1.20)$$

The total active power received by a port # i is therefore expressed by:

$$P_i = \sum_{\substack{j=1 \\ j \neq i}}^n P_{ji} = \frac{4}{\pi^3 f_s} \sum_{\substack{k=1 \\ k \text{ odd}}}^{\infty} \left[\sum_{j=1, j \neq i}^n \frac{1}{k^3} \frac{V_i V_j}{n_{1i} n_{1j}} \frac{1}{L_{ij}} \cos\left(k \frac{\alpha_i}{2}\right) \cos\left(k \frac{\alpha_j}{2}\right) \sin\left(k(\varphi_{1i} - \varphi_{1j})\right) \right] \quad (1.21)$$

Considering that $\sin \varphi_{ij} \approx \varphi_{ij}$ (as explained earlier), expression (1.21) becomes:

$$P_i = \sum_{\substack{j=1 \\ j \neq i}}^n P_{ji} = \frac{4}{\pi^3 f_s} \sum_{\substack{k=1 \\ k \text{ odd}}}^{\infty} \left[\sum_{j=1, j \neq i}^n \frac{1}{k^3} \frac{V_i V_j}{n_{1i} n_{1j}} \frac{1}{L_{ij}} \cos\left(k \frac{\alpha_i}{2}\right) \cos\left(k \frac{\alpha_j}{2}\right) \cdot (k(\varphi_{1i} - \varphi_{1j})) \right] \quad (1.22)$$

The GHA model offers more precision than the first approximation model, and this precision is directly proportional to the highest order k of the considered harmonics. However, increasing the precision of the model does not come without cost. In fact, when harmonics are added, the system's model becomes more complex and the computational burden it requires in order to be implemented can become enormous. Therefore, a compromise between precision and complexity should be done in order to decide where to truncate the series.

1.3.3. Cross Coupling Between the Ports of a MAB Converter

In the previous section, a generic frequency-domain steady state model was developed for a MAB converter with n ports using the GHA technique. From this model, the expression of the active power received by each port was elaborated in function of the $(2n - 1)$ control parameters of this system, which are the internal and external phase shifts of the n ports (with $\varphi_1 = 0$ because port #1 is the reference port). Therefore, in order to get a set of desired power values at the different ports of the MAB converter, a set of control parameter values should be calculated from this model and applied to the ports of the system.

However, as we can notice from expression (1.21), the power received by each port depends on all the internal and external phase shifts of the MAB converter. This means that the MAB structure is highly coupled and a change in one of the control variables will affect all the ports of the system. The cross coupling between the ports also means that controlling one port cannot be done independently. Therefore, the control system of a MAB converter should be perceived as a multivariable system with Multiple-Inputs and Multiple-Outputs (MIMO), which adds complexity to its implementation. One potential solution to this problem is the implementation of a multivariable control strategy, or alternatively, the addition of a decoupling strategy to the control of this structure and the implementation of multiple single-variable controllers.

To better visualize the cross coupling issue between the ports of a MAB converter with n ports, expression (1.22) can be written in a matrix form in function of the external phase shifts (considering the internal phase shifts constant in this section for linearization purposes) as follows:

$$\begin{bmatrix} P_1 \\ P_2 \\ \dots \\ P_n \end{bmatrix} = \begin{bmatrix} G_{11} & G_{12} & \dots & G_{1n} \\ G_{21} & G_{22} & \dots & G_{2n} \\ \dots & \dots & \dots & \dots \\ G_{n1} & G_{n2} & \dots & G_{nn} \end{bmatrix} \cdot \begin{bmatrix} \varphi_1 \\ \varphi_{12} \\ \dots \\ \varphi_{1n} \end{bmatrix} \quad (1.23)$$

with:

$$G_{ii} = \frac{4}{\pi^3 f_s} \times \sum_{\substack{k=1 \\ k \text{ odd}}}^{\infty} \sum_{\substack{j=1 \\ j \neq i}}^n \frac{1}{k^2} \frac{V_i' V_j'}{L_{ij}} \cos\left(k \frac{\alpha_i}{2}\right) \cos\left(k \frac{\alpha_j}{2}\right)$$

$$G_{ij} = G_{ji} = -\frac{4}{\pi^3 f_s} \times \sum_{\substack{k=1 \\ k \text{ odd}}}^{\infty} \frac{1}{k^2} \frac{V_i' V_j'}{L_{ij}} \cos\left(k \frac{\alpha_i}{2}\right) \cos\left(k \frac{\alpha_j}{2}\right) \quad \forall i \neq j$$

In a multiport converter, the algebraic sum of all input and output powers of the system is equal to zero according to the law of power conservation (neglecting the system's losses). Therefore, for a MAB converter with n ports, we can write:

$$\sum_{i=1}^n P_i = 0 \quad (1.24)$$

Consequently, when controlling a MAB converter with n ports, only $(n - 1)$ desired power values can be selected. The power of the remaining uncontrolled port will be naturally determined from expression (1.24). In this manuscript, the uncontrolled port will be the reference port #1 for simplicity reasons.

In addition to that, and as explained previously, the external phase shift φ_1 of the reference port #1 is considered zero. Therefore, the first row and column of matrix (1.23) can be removed, and this matrix becomes:

$$\begin{bmatrix} P_2 \\ P_3 \\ \dots \\ P_n \end{bmatrix} = \begin{bmatrix} G_{22} & G_{23} & \dots & G_{2n} \\ G_{32} & G_{33} & \dots & G_{3n} \\ \dots & \dots & \dots & \dots \\ G_{n2} & G_{n3} & \dots & G_{nn} \end{bmatrix} \cdot \begin{bmatrix} \varphi_{12} \\ \varphi_{13} \\ \dots \\ \varphi_{1n} \end{bmatrix} = G \cdot \begin{bmatrix} \varphi_{12} \\ \varphi_{13} \\ \dots \\ \varphi_{1n} \end{bmatrix} \quad (1.25)$$

The non-diagonal elements of this matrix ($G_{ij} \forall i \neq j$) represent the cross coupling and inner interaction between the ports of the MAB converter, whereas the diagonal elements (G_{ii}) represent the direct effect of the control parameters on the power values [23]. Generally, as we can notice from the matrix elements' expressions in (1.23), the absolute values of the diagonal elements are greater than the non-diagonal ones. Additionally, they have opposite signs. Consequently, we deduce that diagonal elements have a greater and direct effect on the control outputs of the system and that non-diagonal elements act like a perturbation.

The ratio between the non-diagonal and the diagonal elements' values is called the cross-coupling degree. When the values of the non-diagonal elements are decreased or/and when the values of the diagonal elements are increased, the cross-coupling degree is reduced and the MAB converter will act more like a decoupled structure. If matrix G is a diagonal matrix, then the MAB converter is perfectly decoupled. It is interesting to note that when ports are added to the system, the values of the diagonal elements become greater and the cross-coupling degree approaches zero (Figure 1.8) [23].

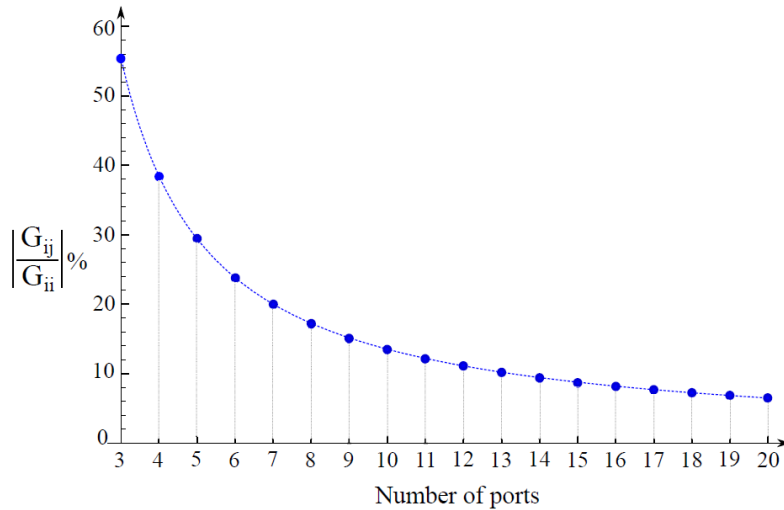


Figure 1.8: The cross-coupling degree in function of the MAB's number of ports [23].

Decoupling a MAB converter is transforming its control from a MIMO system to a Single-Input Single-Output (SISO) system. This will enhance the reliability of this control and improve the dynamic performance of the MAB converter. In literature, many decoupling strategies are proposed for MAB converters. Reference [23] is an interesting and exhaustive survey that explains in details the cross-coupling problem of MAB converters and describes the existent decoupling solutions. In the remaining part of this section, a brief description and evaluation of some of these solutions is done.

Two main types of decoupling strategies exist: Hardware decoupling and Software decoupling.

a) Hardware decoupling

The idea of hardware decoupling is to make a small change in the topology of the system in a way to decouple the ports without adding a complex decoupling layer to the control system. While sharing a single multi-winding transformer among different ports is the main advantage of the MAB converter topology, it causes natural interaction between these ports. Therefore,

the changes made by a hardware decoupling strategy will usually be at the transformer level of the system.

- i. *Using separate two-winding transformers:* A hardware solution that is proposed in literature is to replace the multi-winding transformer by multiple classic two-winding transformers [27], [28]. This technique decouples the MAB converter by transforming it into several independent DAB converters (depending on the connection of the transformers). Additionally, this method presents several advantages such as the simplicity to design and manufacture a conventional two-winding transformer compared to a multi-winding one, better heat dissipation and improved galvanic isolation between the ports. However, the main drawback of using separate transformers is the power density decrease and the potential overall efficiency reduction it causes.
- ii. *Omitting a series inductance:* Another hardware decoupling solution would be to make the value of the series inductance L_i of one of the ports equal to zero or negligible compared to the series inductances of the other ports [18]. This port will therefore be called the “Master” port, while all other ports will be the “Slave” ports. This is usually achieved by adding external series inductances to the slave ports. Considering that port #1 is chosen to be the master port, its series inductance L_1 (Figure 1.2(a)) will therefore be considered equal to zero. Consequently, from expression (1.1), the link inductances of the delta-equivalent circuit of the MAB converter become:

$$\begin{cases} NA & \text{if } i = j \\ L_{ij} = L_j' & \text{if } i = 1, j \neq i \\ L_{ij} = L_i' & \text{if } j = 1, i \neq j \\ L_{ij} = \infty & \text{if } i \neq 1, j \neq 1, i \neq j \end{cases} \quad (1.26)$$

This means that only the link inductances that connect the master port to slave ports have finite values. Therefore, power is only directly exchanged between the master port and the slave ports. Slave ports do not directly exchange power together, which means that the MAB converter acts like several independent DAB converters. When expression (1.26) is used to calculate the link inductances in expression (1.25), the gain matrix G becomes a diagonal matrix, which validates this decoupling method.

This hardware decoupling method is simple to achieve and it can increase the converter’s efficiency due to the omitted inductance. Scalability of the system is another key advantage of this strategy since adding ports would be an easy task. Nevertheless, the symmetry of the MAB converter is lost and its reliability is decreased because losing the master port would stop the system from being decoupled and can therefore lead to instability issues and the need to implement a backup software decoupling strategy.

b) *Software decoupling*

This type of decoupling does not modify the topology of the MAB converter. The control system is used in this case to decouple the ports.

- i. *Inverse matrix decoupling:* This method is known as the conventional decoupling method in literature and is also called feedforward decoupling method in some references. It is a classical decoupling solution used in MIMO systems for decades

(Boksenbom and Hood decoupling method, 1949) [29]. The idea behind this technique is to multiply the gain matrix “ G ” of expression (1.25) by its inverse matrix. That way, we get a diagonal gain matrix with a cross-coupling degree of zero ($G \cdot G^{-1} = I$, where I is the identity matrix) (Figure 1.9). This inverse matrix will act like a pre-compensator to the system, and can therefore represent a set of pre-calculated, feedforwarded values of the control parameters (control inputs) corresponding to a set of desired power values (control outputs) [14], [25]:

$$\begin{bmatrix} \varphi_{12} \\ \varphi_{13} \\ \dots \\ \varphi_{1n} \end{bmatrix} = G^{-1} \begin{bmatrix} P_2 \\ P_3 \\ \dots \\ P_n \end{bmatrix} \quad (1.27)$$

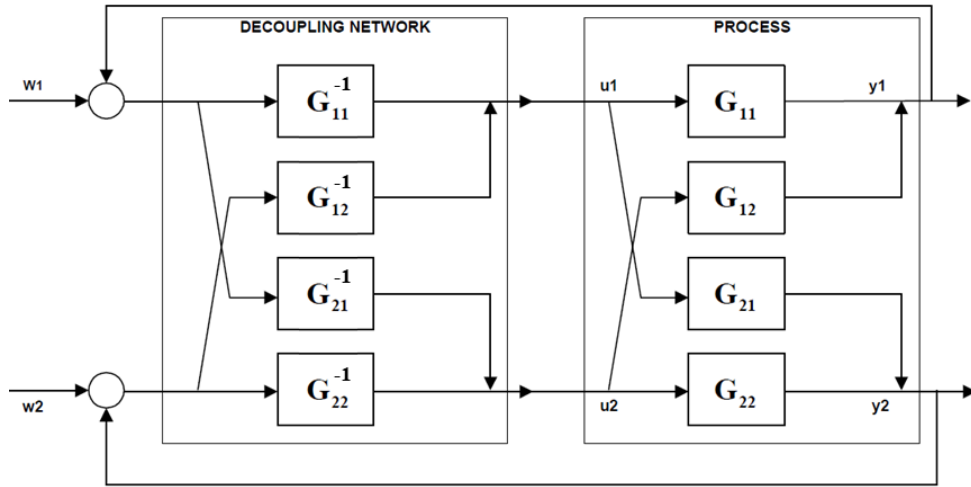


Figure 1.9: Inverse matrix decoupling method for a MIMO system with two inputs (w_1 and w_2) and two outputs (y_1 and y_2) [29].

This method can simply be implemented into the control of the MAB converter. It also has the advantage of boosting its time response because feedforwarding the control parameters to the system will rapidly lead it very close to its desired operating point.

- ii. *Time-sharing control:* In this method, only two ports of the MAB converter are activated at once at each time instant, one port acting like an input port and the other one like an output port, while the remaining ports are deactivated [30]. In other words, the MAB converter behaves like a DAB converter at each moment. Figure 1.10 illustrates the principles of this control strategy applied on a QAB converter (MAB converter with 4 ports). In the application proposed in [30], port #1 is an input port while ports #2, #3 and #4 are output ports. At each moment, the input port sends power to only one output port. A time period T_m is set as the time-sharing period, such that $T_m \gg T_s$ where T_s is the switching period. The time-sharing period is divided into n parts, n being the number of ports, which is 4 for a QAB converter. D_i is the time-sharing ratio. Consequently, port #1 delivers power to port #2 during D_2 , to port #3 during D_3 and to port #4 during D_4 such that $D_1 + D_2 + D_3 \leq 1$. The phase shifts are fixed and the only control parameters that are used in this strategy are the time-sharing ratios D_i in order to get the desired power values.

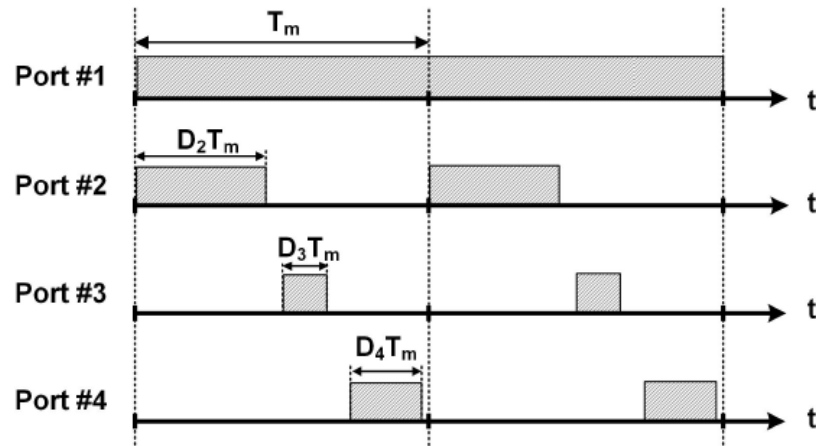


Figure 1.10 : Time-sharing control of a QAB converter (a grey area indicates an activated port).

This method decouples the power flow of a MAB converter and makes its control very easy. Additionally, it allows the implementation of optimized control strategies that are developed for DAB converters, since the system acts like one at each instant. However, time-sharing ratios should be controlled carefully in order to avoid operation overlapping. Additionally, the maximum power rating is limited and larger filtering capacitors at the DC-links are needed for the voltage ripples caused by the discontinuous operation, especially when the number of ports increases. Consequently, the efficiency of this method decreases at heavy loads.

- iii. *Linear Active Disturbance Rejection:* In [11], a linear extended state observer (LESO) is designed for each port of a MAB converter to observe and detect the coupling disturbances, along with any other type of disturbances. Decentralized linear active disturbance rejection controllers (ADRC) are then used to actively compensate these disturbances, making this method a dynamic, model independent, robust, decentralized and scalable decoupling method.

In summary, many decoupling techniques exist in literature, each one having advantages and drawbacks. The optimal method that should be employed depends on the application, i.e. the number of ports of the MAB converter, the voltage and power ratings of its ports, the switching frequency, the potential intermittent nature of some of its ports' inputs, etc... In this manuscript, the inverse matrix decoupling method has been selected as it can be easily implemented and it reduces the time response of the MAB converter. Furthermore, it allows for a generic MAB converter architecture, which is independent of the operation of the ports' connected loads or sources.

1.4. Dynamic Modelling of a MAB Converter

The dynamic model of the MAB converter is needed in order to study its behaviour when getting from an operating point to another and when perturbations occur on its ports. More importantly, a dynamic model allows the design of the controllers of the system that will help it settle at a certain operating point and reject external perturbations while keeping the system stable. In a MAB converter that is decoupled using one of the decoupling techniques proposed

in the previous section, each port can be controlled independently. Therefore, one controller per port should be designed, based on the dynamic model of the MAB converter.

In literature, many works have achieved the dynamic modelling of a DAB converter. In [31], the conventional average modelling method is used for a DAB converter that is controlled as a Buck or a Boost, for Electrical Vehicles' (EV) applications. This modelling method approximates each signal to its average value. Therefore, the AC signals are considered equal to zero in this method, thus decreasing its accuracy. A Simplified model is used in [32] for a DAB converter connected to a voltage source on one port and a variable resistive load on the other port. This work used the expression of the RMS AC current transferred between the ports in order to simplify the modelling of the DAB converter. Then the linearization of the model is achieved by defining an auxiliary parameter instead of using the conventional small-signal model that only linearizes the system around an operating point. In [33], an extended model of a DAB converter was achieved by dividing its state variables between slow (DC) and fast (AC) variables and then eliminating the fast ones to reduce the order of the system and to simplify the model. The generalized average model of a DAB converter was developed in many works [34], [35], [36], [37], and this model is the most accurate one as it takes into consideration the AC signals of the DAB converter. In [38], the generalized average model of a TAB converter with one port connected to an ideal voltage source and two ports connected to ideal current sources is developed.

In general, the control of a MAB converter aims to provide the desired active power at each port. More specifically, some ports will require voltage control (e.g. ports connected to a resistive DC load...) while other ports will require current control (e.g. ports connected to a battery system or the grid...). In this section, the TAB converter shown in Figure 1.11 is considered and its dynamic modelling is achieved. This TAB converter consists of: an uncontrolled reference port #1, the power of which will be determined from expression (1.24); port #2, which is connected to a voltage source (e.g. a battery) through an LC filter; port #3 which is connected to a resistive load. Therefore, the two types of ports are represented in this considered TAB converter, where port #2 requires the control of its DC current i_2 and port #3 requires the control of its output DC voltage V_3 .

In literature, the internal phase shifts are often considered zero when modelling a MAB converter, for simplification purposes. However, in this section, a generic model is built taking into consideration both the internal and the external phase shifts of the MAB converter.

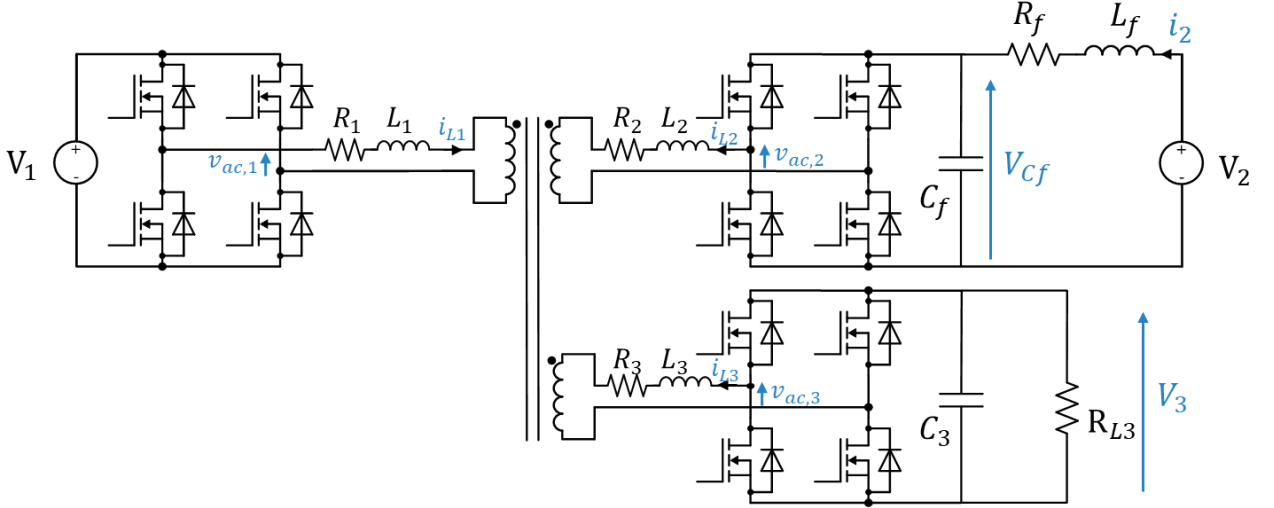


Figure 1.11: TAB converter topology considered for the dynamic modelling.

1.4.1. Generalized Average Model of a TAB Converter

Figure 1.12 shows the star-delta equivalent circuits of the TAB converter presented in Figure 1.11 referred to port #1.

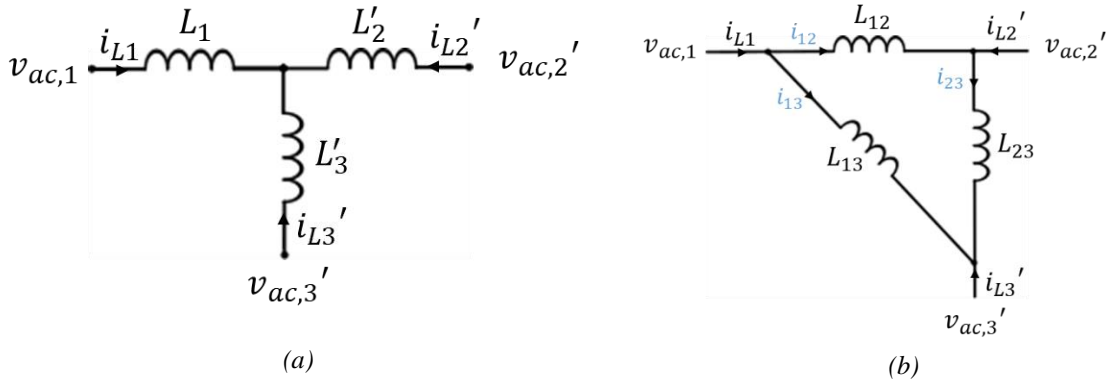


Figure 1.12: Equivalent models of the considered TAB converter: (a) Star equivalent model; (b) Delta equivalent model.

In Figure 1.12, the AC voltages have the following expressions:

$$\begin{aligned}
 v_{ac,1} &= S_1 V_1 \\
 v_{ac,2'} &= \frac{n_1}{n_2} S_2 V_{Cf} \\
 v_{ac,3'} &= \frac{n_1}{n_3} S_3 V_3
 \end{aligned} \tag{1.28}$$

S_1 , S_2 and S_3 are the switching functions of ports #1, #2 and #3 respectively. These switching functions are plotted in Figure 1.13, with $i = 2, 3$.

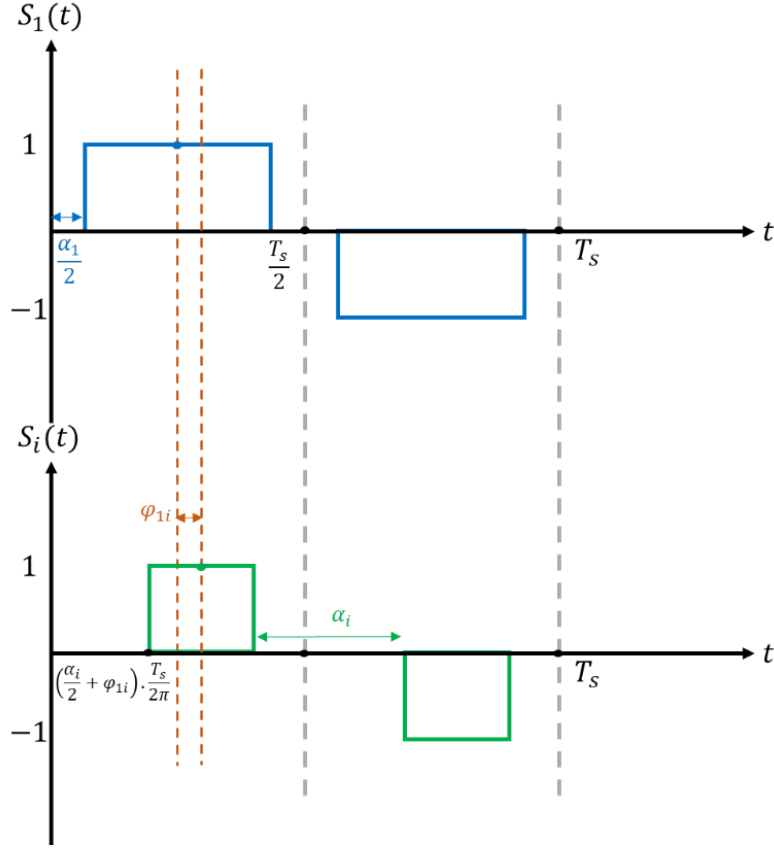


Figure 1.13: Switching functions of the TAB converter's ports if an EPS modulation is applied.

The state space representation of this considered TAB converter can be written as:

- $L_f \frac{di_2}{dt} = V_2 - V_{C_f} - R_f i_2$
- $C_f \frac{dV_{C_f}}{dt} = i_2 + S_2 i_{12} \frac{n_1}{n_2} - S_2 i_{23} \frac{n_1}{n_2}$
- $C_3 \frac{dV_3}{dt} = -\frac{V_3}{R_{L3}} + S_3 i_{13} \frac{n_1}{n_3} + S_3 i_{23} \frac{n_1}{n_3}$
- $L_{12} \frac{di_{12}}{dt} = V_1 S_1 - \frac{n_1}{n_2} S_2 V_{C_f} - R_{12} i_{12}$
- $L_{13} \frac{di_{13}}{dt} = V_1 S_1 - \frac{n_1}{n_3} S_3 V_3 - R_{13} i_{13}$
- $L_{23} \frac{di_{23}}{dt} = \frac{n_1}{n_2} S_2 V_{C_f} - \frac{n_1}{n_3} S_3 V_3 - R_{23} i_{23}$ (1.29)

In this representation, the magnetizing transformer current, the transients of the switches and the voltage drops across the parallel diodes of the switches are neglected.

The conventional average modelling usually used for power electronic converters takes into consideration the average values of their state variables in order to transform this discontinuous-time model into a continuous one. This averaging method cannot be implemented for a MAB converter as it results in zero transformer currents (since transformer signals are considered as

purely AC variables). The generalized average model uses more Fourier series terms of the system variables, hence its ability to capture the transformer harmonics and to represent the behaviour of the MAB converter more correctly [35]. Therefore, the generalized average model of this system is developed in order to study it as a continuous-time model while representing its AC signals with more precision than the classical average model. In this section, DC signals will be represented by their average values (0th Fourier series coefficient) and AC signals will be represented by their fundamentals (1st Fourier series real and imaginary coefficients) for simplicity.

The Fourier series development of a variable x (expressed in equation (1.7)) is written as follows in the complex form [35]:

$$x(t) = \sum_{k=-\infty}^{+\infty} \langle x \rangle_k(t) \cdot e^{jw_s kt} \quad (1.30)$$

$$\text{With: } \langle x \rangle_k(t) = \frac{1}{T_s} \int_0^{T_s} x(t) \cdot e^{-jw_s kt} dt = \frac{1}{T_s} \int_0^{T_s} x(t) \cdot (\cos(w_s kt) - j \cdot \sin(w_s kt)) dt$$

Where $\langle x \rangle_k(t)$ is the k^{th} coefficient of the Fourier series and it is a complex number denoted as:

$$\langle x \rangle_k(t) = \langle x \rangle_{kR} + j \langle x \rangle_{kI}$$

R and I refer to the real and imaginary parts of the complex number, respectively.

Coefficients $\langle x \rangle_k(t)$ and $\langle x \rangle_{-k}(t)$ satisfy:

$Real\{\langle x \rangle_k(t)\} = Real\{\langle x \rangle_{-k}(t)\}$ and $Im\{\langle x \rangle_k(t)\} = -Im\{\langle x \rangle_{-k}(t)\}$, where $Real\{\}$ and $Im\{\}$ denote the real and imaginary parts of the complex coefficients respectively. The derivative of the k^{th} coefficient of the Fourier series of a variable x is:

$$\frac{d}{dt} \langle x \rangle_k(t) = \left\langle \frac{d}{dt} x \right\rangle_k(t) - jkw_s \langle x \rangle_k(t) \quad (1.31)$$

In addition to that, the k^{th} coefficient of the product of two variables is:

$$\langle xy \rangle_k = \sum_{i=-\infty}^{+\infty} \langle x \rangle_{k-i} \langle y \rangle_i \quad (1.32)$$

Therefore, from equation (1.32) and considering that the 1st and the -1st coefficients are complex conjugates, the 0th coefficient of the product of two variables x and y is [35]:

$$\langle xy \rangle_0 = \langle x \rangle_0 \langle y \rangle_0 + 2(\langle x \rangle_{1R} \langle y \rangle_{1R} + \langle x \rangle_{1I} \langle y \rangle_{1I}) \quad (1.33)$$

and the 1st coefficient of the product of two variables x and y is:

$$\begin{aligned} \langle xy \rangle_{1R} &= \langle x \rangle_0 \langle y \rangle_{1R} + \langle x \rangle_{1R} \langle y \rangle_0 \\ \langle xy \rangle_{1I} &= \langle x \rangle_0 \langle y \rangle_{1I} + \langle x \rangle_{1I} \langle y \rangle_0 \end{aligned} \quad (1.34)$$

Fourier coefficients of the switching functions are given by the following expressions, using equation (1.30) and Figure 1.13:

$$\begin{aligned}
\langle S_i \rangle_0 &= 0 \quad \forall i = 1, 2, 3 \\
\langle S_i \rangle_{1R} &= -\frac{2}{\pi} \cos\left(\frac{\alpha_i}{2}\right) \sin(\varphi_{1i}) \quad \forall i = 1, 2, 3 \\
\langle S_i \rangle_{1I} &= -\frac{2}{\pi} \cos\left(\frac{\alpha_i}{2}\right) \cos(\varphi_{1i}) \quad \forall i = 1, 2, 3
\end{aligned} \tag{1.35}$$

By applying equations (1.30) to (1.35) to system (1.29), the large signal model of the system is derived as:

- $\frac{d\langle i_2 \rangle_0}{dt} = \frac{V_2}{L_f} - \frac{\langle V_{C_f} \rangle_0}{L_f} - \frac{R_f}{L_f} \langle i_2 \rangle_0$
- $\frac{d\langle V_{C_f} \rangle_0}{dt} = \frac{\langle i_2 \rangle_0}{C_f} + \frac{2}{C_f} \frac{n_1}{n_2} \cdot \langle S_2 \rangle_{1R} \langle i_{12} \rangle_{1R} + \frac{2}{C_f} \frac{n_1}{n_2} \langle S_2 \rangle_{1I} \langle i_{12} \rangle_{1I} - \frac{2}{C_f} \frac{n_1}{n_2} \langle S_2 \rangle_{1R} \langle i_{23} \rangle_{1R} - \frac{2}{C_f} \frac{n_1}{n_2} \langle S_2 \rangle_{1I} \langle i_{23} \rangle_{1I}$
- $\frac{d\langle V_3 \rangle_0}{dt} = -\frac{\langle V_3 \rangle_0}{C_3 R_{L3}} + \frac{2}{C_3} \frac{n_1}{n_3} \langle S_3 \rangle_{1R} \langle i_{13} \rangle_{1R} + \frac{2}{C_3} \frac{n_1}{n_3} \langle S_3 \rangle_{1I} \langle i_{13} \rangle_{1I} + \frac{2}{C_3} \frac{n_1}{n_3} \langle S_3 \rangle_{1R} \langle i_{23} \rangle_{1R} + \frac{2}{C_3} \frac{n_1}{n_3} \langle S_3 \rangle_{1I} \langle i_{23} \rangle_{1I}$
- $\frac{d\langle i_{12} \rangle_{1R}}{dt} = \frac{V_1}{L_{12}} \langle S_1 \rangle_{1R} - \frac{1}{L_{12}} \frac{n_1}{n_2} \langle S_2 \rangle_{1R} \langle V_{C_f} \rangle_0 - \frac{R_{12}}{L_{12}} \langle i_{12} \rangle_{1R} + w_s \langle i_{12} \rangle_{1I}$
- $\frac{d\langle i_{12} \rangle_{1I}}{dt} = \frac{V_1}{L_{12}} \langle S_1 \rangle_{1I} - \frac{1}{L_{12}} \frac{n_1}{n_2} \langle S_2 \rangle_{1I} \langle V_{C_f} \rangle_0 - \frac{R_{12}}{L_{12}} \langle i_{12} \rangle_{1I} - w_s \langle i_{12} \rangle_{1R}$
- $\frac{d\langle i_{13} \rangle_{1R}}{dt} = \frac{V_1}{L_{13}} \langle S_1 \rangle_{1R} - \frac{1}{L_{13}} \frac{n_1}{n_3} \langle S_3 \rangle_{1R} \langle V_3 \rangle_0 - \frac{R_{13}}{L_{13}} \langle i_{13} \rangle_{1R} + w_s \langle i_{13} \rangle_{1I}$
- $\frac{d\langle i_{13} \rangle_{1I}}{dt} = \frac{V_1}{L_{13}} \langle S_1 \rangle_{1I} - \frac{1}{L_{13}} \frac{n_1}{n_3} \langle S_3 \rangle_{1I} \langle V_3 \rangle_0 - \frac{R_{13}}{L_{13}} \langle i_{13} \rangle_{1I} - w_s \langle i_{13} \rangle_{1R}$
- $\frac{d\langle i_{23} \rangle_{1R}}{dt} = \frac{1}{L_{23}} \frac{n_1}{n_2} \langle S_2 \rangle_{1R} \langle V_{C_f} \rangle_0 - \frac{1}{L_{23}} \frac{n_1}{n_3} \langle S_3 \rangle_{1R} \langle V_3 \rangle_0 - \frac{R_{23}}{L_{23}} \langle i_{23} \rangle_{1R} + w_s \langle i_{23} \rangle_{1I}$
- $\frac{d\langle i_{23} \rangle_{1I}}{dt} = \frac{1}{L_{23}} \frac{n_1}{n_2} \langle S_2 \rangle_{1I} \langle V_{C_f} \rangle_0 - \frac{1}{L_{23}} \frac{n_1}{n_3} \langle S_3 \rangle_{1I} \langle V_3 \rangle_0 - \frac{R_{23}}{L_{23}} \langle i_{23} \rangle_{1I} - w_s \langle i_{23} \rangle_{1R}$ (1.36)

The control input parameters of this system are the internal and the external phase shifts of the ports ($\alpha_1, \alpha_2, \alpha_3, \varphi_2$ and φ_3). These parameters appear in the expressions of the switching functions, as written in equation (1.35). The control output parameters are $\langle i_2 \rangle_0$ and $\langle V_3 \rangle_0$. Therefore, the obtained equations are non-linear. A linearization should be done around an operating point to be able to use classical linear controllers, such as PID (Proportional-Integral-

Derivative) controllers. The linear small signal model of the system is obtained by introducing small perturbations to the system's variables at an operating point and using the Taylor series expansion, such that:

$$\langle x \rangle = \langle x_{eq} \rangle + \widehat{\langle x \rangle}$$

Where variables with the symbol “ ^ ” represent the small signals (perturbations around the operating point) and $\langle x_{eq} \rangle$ represents the value of $\langle x \rangle$ at the operating point, also called equilibrium point.

The perturbations of the voltage sources around their average values can be neglected in this study ($\widehat{V}_1 = \widehat{V}_2 = 0$). This is mainly due to their slow variation compared to the fast control dynamics of the system. The obtained linearized mathematical model is a 9th order system which can be represented as following:

- $$\frac{d\widehat{\langle l_2 \rangle}_0}{dt} = -\frac{\widehat{\langle V_{C_f} \rangle}_0}{L_f} - \frac{R_f}{L_f} \widehat{\langle l_2 \rangle}_0$$
- $$\begin{aligned} \frac{d\widehat{\langle V_{C_f} \rangle}_0}{dt} = & \frac{\widehat{\langle l_2 \rangle}_0}{C_f} - \frac{4}{C_f \pi n_2} \cos\left(\frac{\alpha_{2,eq}}{2}\right) \cdot \sin(\varphi_{12,eq}) \widehat{\langle l_{12} \rangle}_{1R} - \\ & \frac{4}{\pi C_f n_2} \cos\left(\frac{\alpha_{2,eq}}{2}\right) \cos(\varphi_{12,eq}) \widehat{\langle l_{12} \rangle}_{1I} + \frac{4}{\pi C_f n_2} \cos\left(\frac{\alpha_{2,eq}}{2}\right) \sin(\varphi_{12,eq}) \widehat{\langle l_{23} \rangle}_{1R} + \\ & \frac{4}{\pi C_f n_2} \cos\left(\frac{\alpha_{2,eq}}{2}\right) \cos(\varphi_{12,eq}) \widehat{\langle l_{23} \rangle}_{1I} + \frac{4}{C_f \pi n_2} \cos\left(\frac{\alpha_{2,eq}}{2}\right) \left[-\cos(\varphi_{12,eq}) I_{12,1R} + \right. \\ & \left. \sin(\varphi_{12,eq}) I_{12,1I} + \cos(\varphi_{12,eq}) I_{23,1R} - \sin(\varphi_{12,eq}) I_{23,1I} \right] \cdot \widehat{\varphi}_{12} + \\ & \frac{2}{\pi C_f n_2} \cdot \left[\sin\left(\frac{\alpha_{2,eq}}{2}\right) \cdot \sin(\varphi_{12,eq}) I_{12,1R} + \sin\left(\frac{\alpha_{2,eq}}{2}\right) \cos(\varphi_{12,eq}) I_{12,1I} - \right. \\ & \left. \sin\left(\frac{\alpha_{2,eq}}{2}\right) \sin(\varphi_{12,eq}) I_{23,1R} - \sin\left(\frac{\alpha_{2,eq}}{2}\right) \cos(\varphi_{12,eq}) I_{23,1I} \right] \cdot \widehat{\alpha}_2 \end{aligned}$$
- $$\begin{aligned} \frac{d\widehat{\langle V_3 \rangle}_0}{dt} = & -\frac{\widehat{\langle V_3 \rangle}_0}{C_3 \cdot R_{L3}} - \frac{4}{\pi C_3 n_3} \cos\left(\frac{\alpha_{3,eq}}{2}\right) \sin(\varphi_{13,eq}) \widehat{\langle l_{13} \rangle}_{1R} - \\ & \frac{4}{\pi C_3 n_3} \cos\left(\frac{\alpha_{3,eq}}{2}\right) \cos(\varphi_{13,eq}) \widehat{\langle l_{13} \rangle}_{1I} - \frac{4}{\pi C_3 n_3} \cos\left(\frac{\alpha_{3,eq}}{2}\right) \sin(\varphi_{13,eq}) \widehat{\langle l_{23} \rangle}_{1R} - \\ & \frac{4}{\pi C_3 n_3} \cos\left(\frac{\alpha_{3,eq}}{2}\right) \cos(\varphi_{13,eq}) \widehat{\langle l_{23} \rangle}_{1I} - \frac{4}{\pi C_3 n_3} \cos\left(\frac{\alpha_{3,eq}}{2}\right) \left[\cos(\varphi_{13,eq}) I_{13,1R} - \right. \\ & \left. \sin(\varphi_{13,eq}) I_{13,1I} + \cos(\varphi_{13,eq}) I_{23,1R} - \sin(\varphi_{13,eq}) I_{23,1I} \right] \cdot \widehat{\varphi}_{13} + \\ & \frac{2}{\pi C_3 n_3} \cdot \left[\sin\left(\frac{\alpha_{3,eq}}{2}\right) \sin(\varphi_{13,eq}) I_{13,1R} + \sin\left(\frac{\alpha_{3,eq}}{2}\right) \cos(\varphi_{13,eq}) I_{13,1I} + \right. \\ & \left. \sin\left(\frac{\alpha_{3,eq}}{2}\right) \sin(\varphi_{13,eq}) I_{23,1R} + \sin\left(\frac{\alpha_{3,eq}}{2}\right) \cos(\varphi_{13,eq}) I_{23,1I} \right] \cdot \widehat{\alpha}_3 \end{aligned}$$
- $$\begin{aligned} \frac{d\widehat{\langle l_{12} \rangle}_{1R}}{dt} = & \frac{2}{\pi L_{12} n_2} \cos\left(\frac{\alpha_{2,eq}}{2}\right) \sin(\varphi_{12,eq}) \widehat{\langle V_{C_f} \rangle}_0 - \frac{R_{12}}{L_{12}} \widehat{\langle l_{12} \rangle}_{1R} + w_s \widehat{\langle l_{12} \rangle}_{1I} + \\ & \frac{2}{\pi L_{12} n_2} V_{C_f,eq} \cos\left(\frac{\alpha_{2,eq}}{2}\right) \cos(\varphi_{12,eq}) \cdot \widehat{\varphi}_{12} - \\ & \frac{1}{\pi L_{12} n_2} V_{C_f,eq} \sin\left(\frac{\alpha_{2,eq}}{2}\right) \sin(\varphi_{12,eq}) \cdot \widehat{\alpha}_2 \end{aligned}$$
- $$\begin{aligned} \frac{d\widehat{\langle l_{12} \rangle}_{1I}}{dt} = & \frac{1}{\pi} \cdot \frac{V_1}{L_{12}} \sin\left(\frac{\alpha_{1,eq}}{2}\right) \cdot \widehat{\alpha}_1 + \frac{2}{\pi L_{12} n_2} \cos\left(\frac{\alpha_{2,eq}}{2}\right) \cos(\varphi_{12,eq}) \widehat{\langle V_{C_f} \rangle}_0 - \\ & \frac{R_{12}}{L_{12}} \widehat{\langle l_{12} \rangle}_{1I} - w_s \widehat{\langle l_{12} \rangle}_{1R} - \frac{2}{\pi L_{12} n_2} V_{C_f,eq} \cos\left(\frac{\alpha_{2,eq}}{2}\right) \sin(\varphi_{12,eq}) \cdot \widehat{\varphi}_{12} - \\ & \frac{1}{\pi L_{12} n_2} V_{C_f,eq} \sin\left(\frac{\alpha_{2,eq}}{2}\right) \cos(\varphi_{12,eq}) \cdot \widehat{\alpha}_2 \end{aligned}$$

$$\begin{aligned}
& \bullet \frac{d\langle \widehat{l}_{13} \rangle_{1R}}{dt} = \frac{2}{\pi L_{13}} \frac{n_1}{n_3} \cos\left(\frac{\alpha_{3,eq}}{2}\right) \sin(\varphi_{13,eq}) \langle \widehat{V}_3 \rangle_0 - \frac{R_{13}}{L_{13}} \langle \widehat{l}_{13} \rangle_{1R} + w_s \langle \widehat{l}_{13} \rangle_{1I} + \\
& \frac{2}{\pi L_{13}} \frac{n_1}{n_3} V_{3,eq} \cos\left(\frac{\alpha_{3,eq}}{2}\right) \cos(\varphi_{13,eq}) \cdot \widehat{\varphi}_{13} - \frac{1}{\pi L_{13}} \frac{n_1}{n_3} V_{3,eq} \sin\left(\frac{\alpha_{3,eq}}{2}\right) \sin(\varphi_{13,eq}) \cdot \widehat{\alpha}_3 \\
& \bullet \frac{d\langle \widehat{l}_{13} \rangle_{1I}}{dt} = \frac{1}{\pi L_{13}} V_1 \sin\left(\frac{\alpha_{1,eq}}{2}\right) \cdot \widehat{\alpha}_1 + \frac{2}{\pi L_{13}} \frac{n_1}{n_3} \cos\left(\frac{\alpha_{3,eq}}{2}\right) \cos(\varphi_{13,eq}) \langle \widehat{V}_3 \rangle_0 - \\
& \frac{R_{13}}{L_{13}} \langle \widehat{l}_{13} \rangle_{1I} - w_s \langle \widehat{l}_{13} \rangle_{1R} - \frac{2}{\pi L_{13}} \frac{n_1}{n_3} V_{3,eq} \cos\left(\frac{\alpha_{3,eq}}{2}\right) \sin(\varphi_{13,eq}) \cdot \widehat{\varphi}_{13} - \\
& \frac{1}{\pi L_{13}} \frac{n_1}{n_3} V_{3,eq} \sin\left(\frac{\alpha_{3,eq}}{2}\right) \cos(\varphi_{13,eq}) \cdot \widehat{\alpha}_3 \\
& \bullet \frac{d\langle \widehat{l}_{23} \rangle_{1R}}{dt} = -\frac{2}{\pi L_{23}} \frac{n_1}{n_2} \cos\left(\frac{\alpha_{2,eq}}{2}\right) \sin(\varphi_{12,eq}) \langle \widehat{V}_{C_f} \rangle_0 + \\
& \frac{2}{\pi L_{23}} \frac{n_1}{n_3} \cos\left(\frac{\alpha_{3,eq}}{2}\right) \sin(\varphi_{13,eq}) \cdot \langle \widehat{V}_3 \rangle_0 - \frac{R_{23}}{L_{23}} \langle \widehat{l}_{23} \rangle_{1R} + w_s \langle \widehat{l}_{23} \rangle_{1I} - \\
& \frac{2}{\pi L_{23}} \frac{n_1}{n_2} V_{C_f,eq} \cos\left(\frac{\alpha_{2,eq}}{2}\right) \cos(\varphi_{12,eq}) \cdot \widehat{\varphi}_{12} + \\
& \frac{1}{\pi L_{23}} \frac{n_1}{n_2} V_{C_f,eq} \sin\left(\frac{\alpha_{2,eq}}{2}\right) \sin(\varphi_{12,eq}) \cdot \widehat{\alpha}_2 + \\
& \frac{2}{\pi L_{23}} \frac{n_1}{n_3} V_{3,eq} \cos\left(\frac{\alpha_{3,eq}}{2}\right) \cos(\varphi_{13,eq}) \cdot \widehat{\varphi}_{13} - \frac{1}{\pi L_{23}} \frac{n_1}{n_3} V_{3,eq} \sin\left(\frac{\alpha_{3,eq}}{2}\right) \sin(\varphi_{13,eq}) \cdot \widehat{\alpha}_3 \\
& \bullet \frac{d\langle \widehat{l}_{23} \rangle_{1I}}{dt} = -\frac{2}{\pi L_{23}} \frac{n_1}{n_2} \cos\left(\frac{\alpha_{2,eq}}{2}\right) \cos(\varphi_{12,eq}) \langle \widehat{V}_{C_f} \rangle_0 + \\
& \frac{2}{\pi L_{23}} \frac{n_1}{n_3} \cos\left(\frac{\alpha_{3,eq}}{2}\right) \cos(\varphi_{13,eq}) \langle \widehat{V}_3 \rangle_0 - \frac{R_{23}}{L_{23}} \langle \widehat{l}_{23} \rangle_{1I} - w_s \langle \widehat{l}_{23} \rangle_{1R} + \\
& \frac{2}{\pi L_{23}} \frac{n_1}{n_2} V_{C_f,eq} \cos\left(\frac{\alpha_{2,eq}}{2}\right) \sin(\varphi_{12,eq}) \cdot \widehat{\varphi}_{12} + \\
& \frac{1}{\pi L_{23}} \frac{n_1}{n_2} V_{C_f,eq} \sin\left(\frac{\alpha_{2,eq}}{2}\right) \cos(\varphi_{12,eq}) \cdot \widehat{\alpha}_2 - \\
& \frac{2}{\pi L_{23}} \frac{n_1}{n_3} V_{3,eq} \cos\left(\frac{\alpha_{3,eq}}{2}\right) \sin(\varphi_{13,eq}) \cdot \widehat{\varphi}_{13} - \frac{1}{\pi L_{23}} \frac{n_1}{n_3} V_{3,eq} \sin\left(\frac{\alpha_{3,eq}}{2}\right) \cos(\varphi_{13,eq}) \cdot \widehat{\alpha}_3
\end{aligned} \tag{1.37}$$

This linearized system (1.37) can be written in the following matrix representation:

$$\dot{\widehat{X}} = A\widehat{X} + B\widehat{U}$$

where $\widehat{X} = [\langle \widehat{l}_2 \rangle_0 \ \langle \widehat{V}_{C_f} \rangle_0 \ \langle \widehat{V}_3 \rangle_0 \ \langle \widehat{l}_{12} \rangle_{1R} \ \langle \widehat{l}_{12} \rangle_{1I} \ \langle \widehat{l}_{13} \rangle_{1R} \ \langle \widehat{l}_{13} \rangle_{1I} \ \langle \widehat{l}_{23} \rangle_{1R} \ \langle \widehat{l}_{23} \rangle_{1I}]^T$ and $\widehat{U} = [\widehat{\alpha}_1 \ \widehat{\alpha}_2 \ \widehat{\alpha}_3 \ \widehat{\varphi}_{12} \ \widehat{\varphi}_{13}]^T$.

Finally, the control system's transfer functions can be calculated using the Laplace transform of the obtained linearized model ($\dot{\widehat{X}} = \widehat{X}.s$) and have an order of 9. The system's controllers are then designed using these transfer functions. Controllers are employed to reject the system's perturbations and to cancel the steady state error on the control outputs once the desired operating point is reached. This steady state error is caused by the approximations that were made while developing the mathematical model, such as the truncation of the Fourier series at a certain finite harmonic order and the uncertainties of the system's parameters, such as the values of the inductances.

1.4.2. Simulation Results and Validation of the Dynamic Model

For the TAB converter presented and modelled in the previous section, we consider that the external phase shift of each port is used as its control input parameter to control its power value. Therefore, two transfer functions are needed for the design of the system's controllers: the

transfer function linking the DC current i_2 of port #2 to the external phase shift φ_{12} and the transfer function linking the DC output voltage V_3 of port #3 to the external phase shift φ_{13} .

$$G_{i_2}(s) = \frac{I_2(s)}{\varphi_{12}(s)} \Bigg|_{\substack{\hat{\varphi}_{13}=0 \\ \hat{\alpha}_1=0; \hat{\alpha}_2=0 \\ \hat{\alpha}_3=0}} \quad (1.38)$$

$$G_{V_3}(s) = \frac{V_3(s)}{\varphi_{13}(s)} \Bigg|_{\substack{\hat{\varphi}_{12}=0 \\ \hat{\alpha}_1=0; \hat{\alpha}_2=0 \\ \hat{\alpha}_3=0}} \quad (1.39)$$

External phase shifts are chosen to be the inputs for these transfer functions (the linear controller's outputs) because changing the internal phase shift values will change the AC voltages' shapes and duty cycles, which can increase the circulating currents and the losses on some operating point. This will be explained in more details in the next chapter of this manuscript. Since the internal phase shifts' dynamics will be much slower than those of the external phase shifts in this case, their variations will be neglected ($\hat{\alpha}_i = 0 \forall i = 1,2,3$).

Based on these transfer functions, PID controllers are designed for each one of the two control loops. Due to the high order of the transfer functions, the design of the controllers was achieved using Matlab's "Control System Designer" tool in this section. The controllers' parameters are therefore calculated from these transfer functions by choosing the desired response characteristics, such as the time response, the stability margins, the overshoot percentage ... The block diagrams of these two control loops are displayed in Figure 1.14. In future works, a method for reducing the order of the transfer functions should be developed to facilitate real-time controller design without relying on an offline tool.

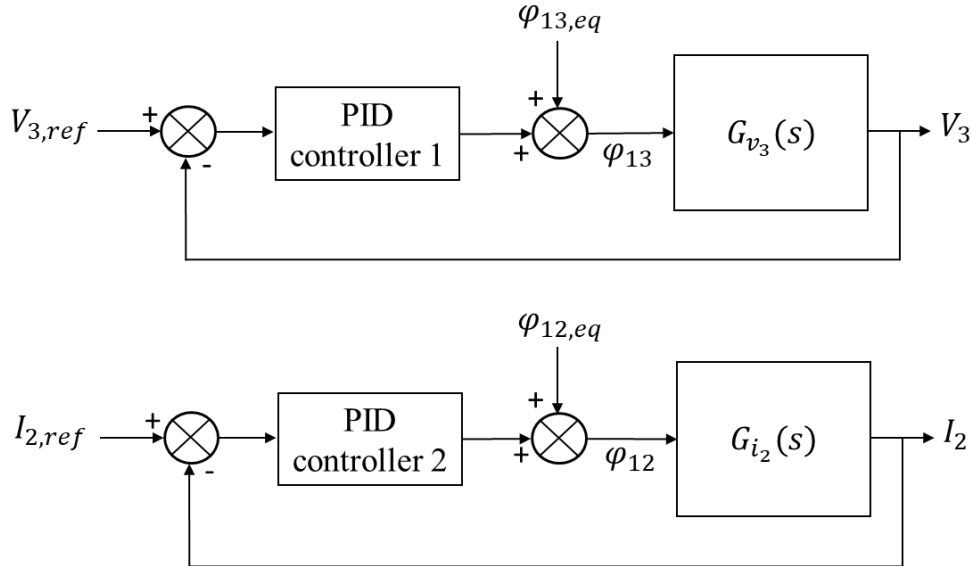
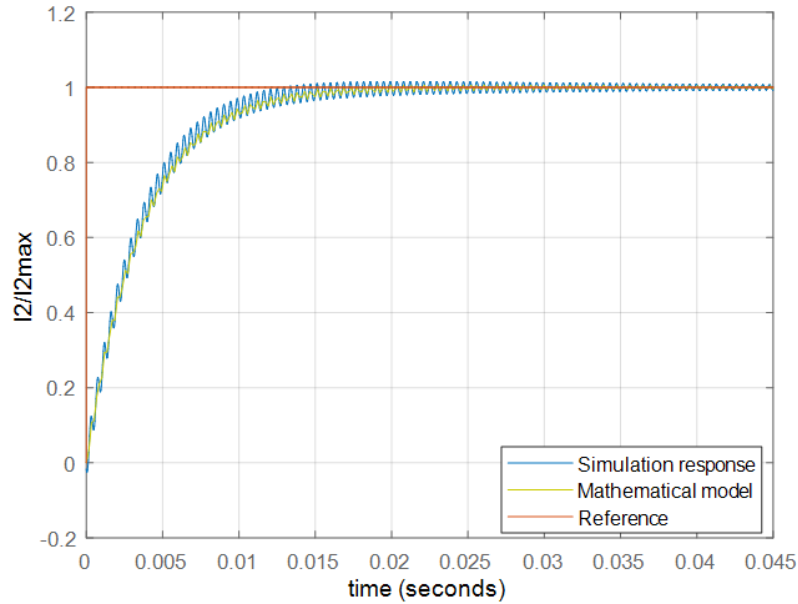


Figure 1.14: Control loops of the proposed TAB converter for the control of the DC current of port #2 and the DC voltage of port #3.

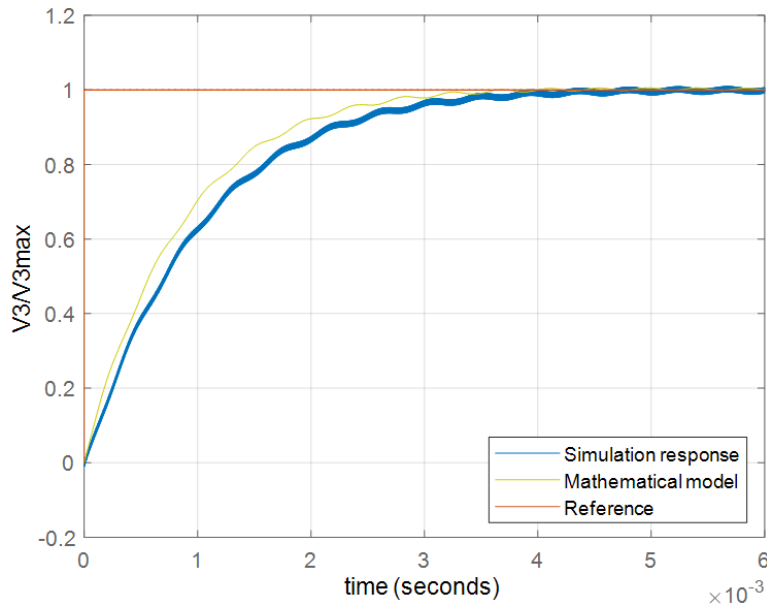
In order to evaluate the validity and precision of the generalized average model developed in the previous section, this mathematical model was compared to a simulated model of the proposed TAB converter consisting of all the components shown in Figure 1.11, using the Matlab/Simulink simulation tool. The parameters of the simulated TAB converter are given in Table 1.1. EPS modulation was applied for this validation. In Figure 1.15 the closed-loop step

responses of transfer functions $G_{i_2}(s)$ and $G_{V_3}(s)$ are plotted from both the mathematical model and the simulated model, for the same designed PID controllers.

To prevent any interaction or perturbations between the two closed loops, the time response to attain 95% of the desired reference of the voltage control loop of port #3 ($t_{3r,95\%} = 2.5 \text{ ms}$) has been selected to be four times faster than that of the current control loop of port #2 ($t_{2r,95\%} = 10 \text{ ms}$). The gain margins of the voltage and current control loops are respectively equal to 10 dB and 2 dB , with phase margins equal to 90° in both loops.



(a)



(b)

Figure 1.15: Closed loop response comparison of the mathematical model and the simulated model of the proposed TAB converter: (a) DC current i_2 of port #2; (b) Output DC voltage V_3 of port #3.

The low frequency oscillations that can be observed at both responses of Figure 1.15 correspond to the resonance frequency of the LC filter at port #2. These oscillations are present at the DC

voltage response of port #3 due to the coupling between the ports. This type of oscillations and their effects on the MAB converter will be discussed in more details in the next section.

We can notice that the response characteristics of both the mathematical model and the simulated model are quite similar, with a slight disparity due to the generalized average model's uncertainties and approximations, especially that only the first harmonic of each AC signal was considered. In order to enhance the accuracy of the suggested model, a higher harmonic order can be considered. However, this will increase the complexity of the model. Nonetheless, the suggested model presents a reasonable trade-off between accuracy and complexity.

The dynamic model developed in this section can be generalized to a MAB converter with n ports. However, the addition of more ports results in an increase in the system's order and complexity. Order reduction techniques exist for this type of systems, but these will also reduce the precision of the model [39].

1.5. Interaction of a MAB Converter with an Externally Connected LC filter

The MAB converter inherently introduces a high level of harmonics into its output and input DC currents, as shown in Figure 1.16. This can be an issue, especially for applications with strict requirements on current ripples, such as those involving battery charging and discharging [40]. To improve the quality of the current, current filters, such as LC filters, are necessary to suppress these harmonics. An LC circuit can also be the result of connecting long wires to the ports of the MAB converter.

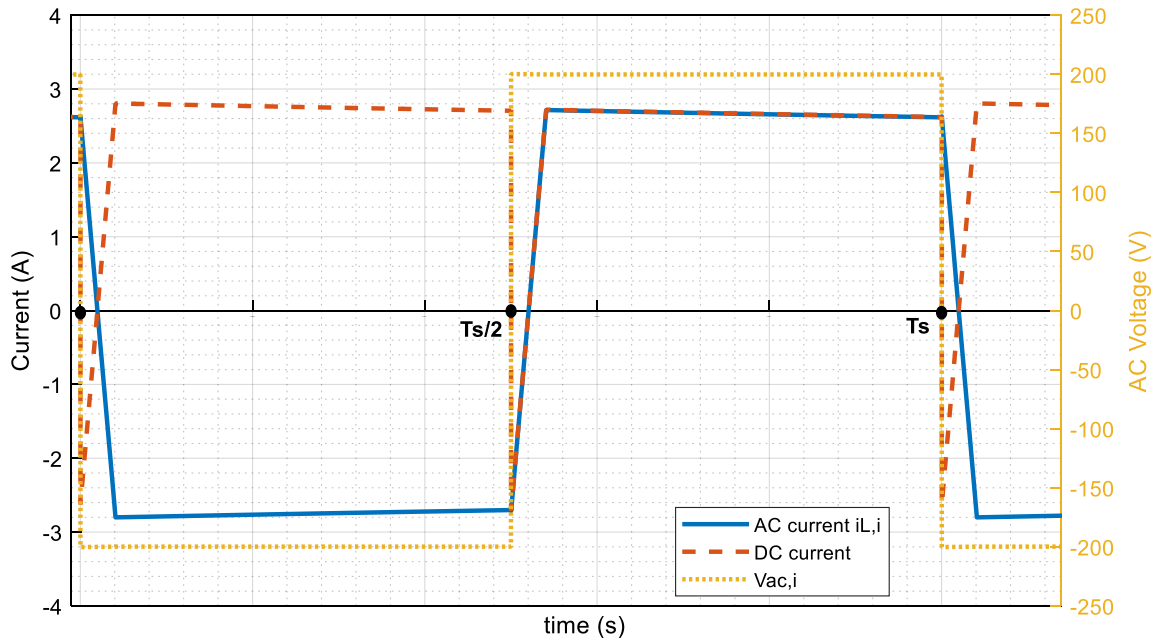


Figure 1.16: Waveforms of the AC and DC currents at a port of a MAB converter.

This section examines the impact of connecting an LC filter to one of the ports of a MAB converter and proposes an active solution to eliminate these effects and to maintain system stability.

Although a MAB converter is always stable individually [41], its cascaded connection with an LC filter can lead to system instability issues. This is due to their impedance interactions [42]. In fact, this connection can result in oscillations at the DC-link voltage between the LC filter and the MAB converter. Additionally, as explained previously in this chapter, the ports of a MAB converter are strongly coupled. Therefore, these oscillations will not only affect the port connected to the LC filter, but they will also travel through the transformer and cause oscillations on all the ports of the system.

In the previous section, a TAB converter with an LC filter connected to its port #2 was modelled and the active power exchange between its ports was controlled. However, as we can notice from the closed-loop control responses shown in Figure 1.15, the DC current of port #2 oscillates at a low frequency corresponding to the resonance frequency of the LC filter connected to its port. These oscillations also appear at the DC voltage of port #3 due to the coupling between the MAB's ports. Oscillations appear on all the converter's ports whenever a change occurs in the system, such as a perturbation or an operating point change. The oscillations are naturally damped after a while.

The Bode plot of the transfer function $G_{i_2}(s)$ of expression (1.38) is displayed in Figure 1.17. The parameters of the considered TAB converter are given in Table 1.1.

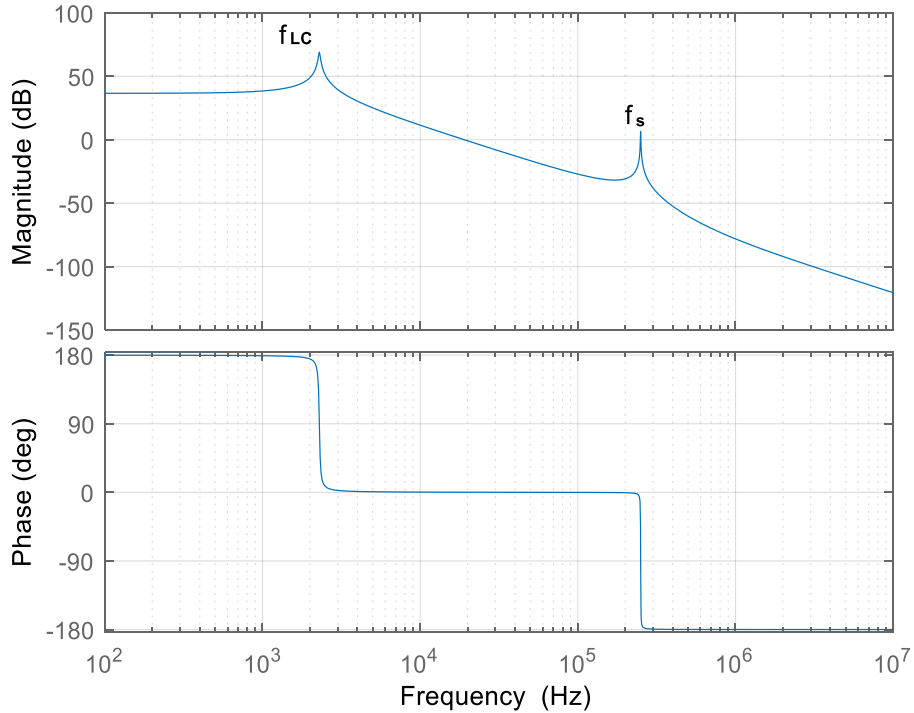


Figure 1.17: Bode plot of transfer function $G_{i_2}(s) = I_2(s)/\varphi_2(s)$.

The resonance frequency of the LC filter is calculated as follows:

$$f_{LC} = \frac{1}{2\pi\sqrt{L_f C_f}} \approx 2300\text{Hz} \quad (1.40)$$

It can be observed from Figure 1.17 that the first resonance in the Bode plot corresponds to the resonance frequency of port #2's LC filter. This frequency falls within the bandwidth of this

TAB converter's dynamics, which explains the significant impact of the LC filter on the closed loop responses.

Table 1.1: Parameter values of the considered TAB converter in Chapter 1 Section 4.

Parameter	Parameter value
Total number of ports n	3
V_1	200 V
V_2	330 V
$V_{3,nom}$	300 V
R_{L3}	15 Ω
C_3	100 μF
$P_{nom,1} = P_{nom,2} = P_{nom,3}$	6 kW
L_{12}	11 μH
L_{13}	11 μH
L_{23}	3 μH
L_f	260 μH
C_f	20 μF
R_f	80 m Ω
f_s	250 kHz

Numerous literary works have addressed the interaction issue between a DAB converter and externally connected LC filters. Several oscillation-damping methods have been proposed and they can be classified into two types: passive and active damping methods. Passive damping involves adding passive elements to the circuit, such as RC and RL circuits. However, this approach increases the system's volume, weight, and energy losses, thereby reducing overall efficiency. Another passive method involves decreasing the value of the filter's capacitance C_f , which increases the filter's resonance frequency f_{LC} . If this parasitic frequency becomes high enough, it could move away from the DAB converter's bandwidth, thus reducing its influence on the closed-loop control responses [43]. However, it is important to maintain a minimum capacitance value to buffer energy from the DAB's switching process.

Active damping can be achieved by adding a control loop to compensate for the oscillations and stabilize the system without additional passive components that increase energy losses, volume, and weight. Several papers proposed active damping methods based on the shaping of the output impedance of the LC filter in order to prevent any interactions with the dynamics of any connected load converter, which is the MAB converter in our case. The Middlebrook stability criterion for cascaded systems was used in this case [42], [44], [45]. According to this criterion, for a cascaded system to be stable, the phase difference between the input impedance of the load converter and the output impedance of the LC filter should be less than 180° when their magnitudes are equal. In [46], this active damping strategy was adapted to an LC filter connected to a DAB converter. Therefore, the Middlebrook stability criterion for this application can be expressed as following:

$$|\varphi(Z_{out,LC}) - \varphi(Z_{in,DAB}^{CL})| < 180^\circ \text{ when } |Z_{out,LC}| = |Z_{in,DAB}^{CL}|$$

$Z_{in,DAB}^{CL}$ is the closed loop input impedance of the DAB converter and $Z_{out,LC}$ is the output impedance of the LC filter. Figure 1.18 illustrates the active damping method proposed in [46].

In this figure, u_o and i_2 are the output DC voltage and DC current of the secondary port of the DAB converter, respectively. u_{in} is the input DC voltage of the primary port, which is connected to the LC filter and therefore undergoes oscillation. Two cascaded closed-loops are implemented in order to control the active power exchange between the two ports by controlling the secondary port's DC voltage and DC current. A third active damping control loop is then added to the input DC voltage of the primary port in order to stabilize it. This control loop functions as a virtual impedance that is added between the LC filter and the DAB converter. It reshapes the input impedance of the DAB converter and ensures that the Middlebrook stability criterion is satisfied.

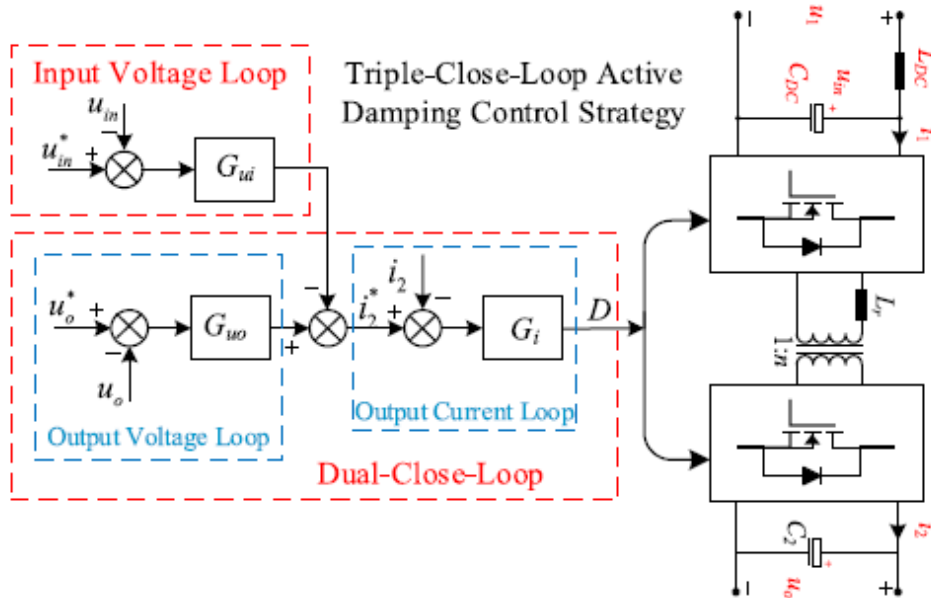


Figure 1.18: Active damping method proposed in [46] based on the shaping of the LC filter's output impedance.

A more straightforward solution to solve this oscillation issue is to include a control loop that aims to eliminate the oscillations of the DC-link voltage in question by injecting damping components to the control of the system. In [47], an application where a DC voltage source is connected to the grid through a three-phase inverter and an LC filter is considered (Figure 1.19). In this application, voltage oscillations occur at the filter capacitors due to their interaction with the inductances of the grid lines. This paper proposes a method to actively damp these parasitic oscillations by isolating them from the fundamental AC grid current and cancelling them through the control of the three-phase inverter using a Proportional controller, as shown in Figure 1.20.

A similar approach is proposed in [48] in a metro traction drive system where a Band Pass Filter (BPF) is implemented to isolate the parasitic oscillations caused by an LC filter and cancel them using a Proportional controller.

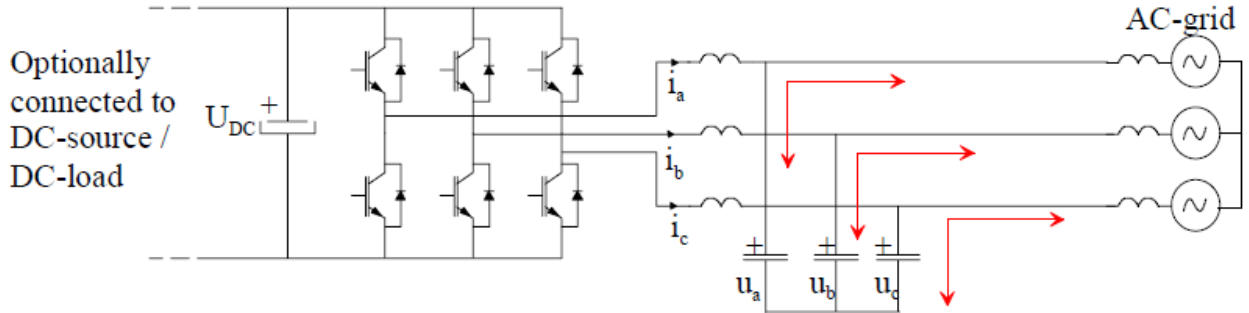


Figure 1.19: Power circuit of grid-connected voltage source with LC-filter considered in [47]. The red arrows illustrate the parasitic oscillations addressed in this paper between the filter's capacitors and the grid's inductances.

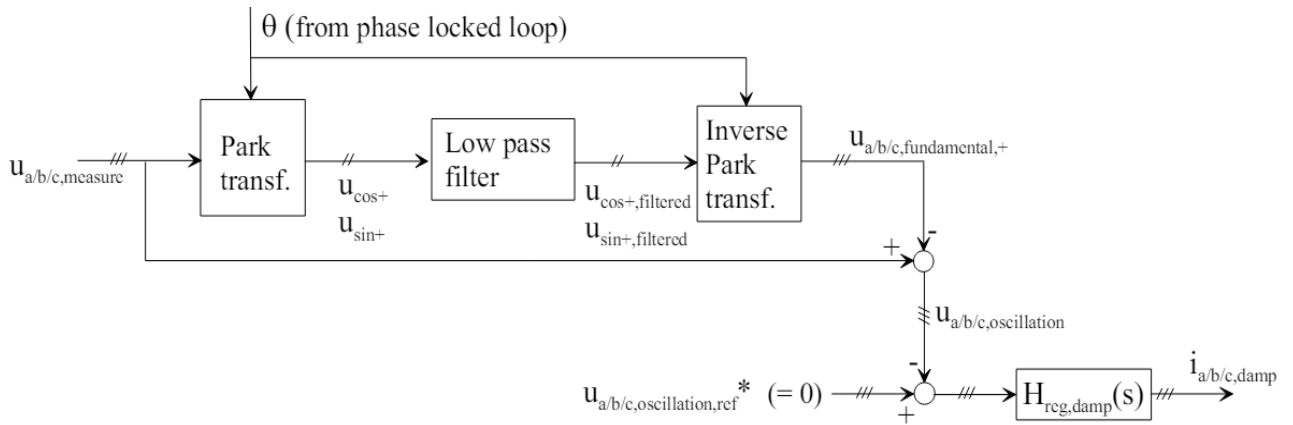


Figure 1.20: Active damping block diagram proposed in [47].

In this section, an active damping method inspired by the work presented in [47] and [48] is developed for a MAB converter having one or more ports connected to an LC filter. The block diagram of this active damping method is shown in Figure 1.21 for a MAB converter with a port # i connected to an LC filter. The active damping control loop is added to the DC current control loop of the port connected to the LC filter in order to continuously eliminate any oscillations that may occur on its DC-link voltage $V_{cf,i}$ due to a change in the system. First, a BPF is used to extract the DC-link voltage oscillations at the desired frequency. Filtering out the low frequency part of the DC voltage is essential to avoid affecting the power flow control of the MAB converter. Filtering out the high-frequency component of the DC voltage is optional. This will eliminate voltage ripples at the switching frequency, allowing for complete isolation of the oscillations at the resonance frequency of the LC filter that require cancellation. These oscillations are then cancelled by comparing them to a zero reference and using the resulting error as an input to a negative gain Proportional controller. By doing this, the error is inverted, multiplied by a gain and fed back into the system via the external phase shift of the corresponding port.

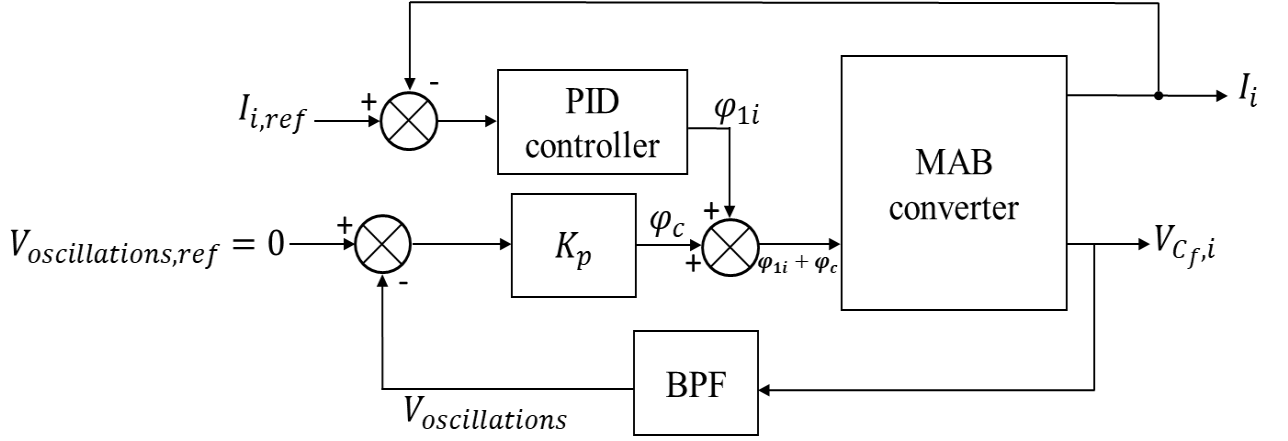


Figure 1.21: Block diagram of the proposed active damping method for a MAB converter with a port #i connected to an LC filter.

In Figure 1.21, K_p represents the gain of the proportional controller, and φ_c is the damping component injected into the external phase shift of the port connected to the LC filter to cancel the oscillations.

The transfer function of the second order BPF is the following:

$$G_{BPF}(s) = G_{LPF}(s) \times G_{HPF}(s) = \frac{\omega_L}{s + \omega_L} \times \frac{s}{s + \omega_H} \quad (1.41)$$

Where $\omega_L = 2\pi \times f_{LPF}$ and f_{LPF} is the cut-off frequency of the low pass filter (LPF).

$\omega_H = 2\pi \times f_{HPF}$ and f_{HPF} is the cut-off frequency of the high pass filter (HPF).

The selected values of these cut-off frequencies are discussed in the next section.

1.5.1. Simulation Results of the Proposed Active Damping Method

In this section, the proposed active damping method is applied to the TAB converter that was presented and modelled in Section 1.4. The parameter values of this TAB converter are given in Table 1.1. The LC filter connected to port #2 has a resonance frequency of 2.3 kHz (Equation (1.40)). The cut-off frequencies of the BPF used in the active damping control are selected with a decade of difference with respect to the LC resonance frequency. Selecting a broad filter bandwidth will guarantee the effective functioning of the active damping strategy, which will remain uninfluenced by potential fluctuations in inductance and capacitance values that could eventually alter the resonance frequency. Therefore, for the considered TAB converter, the following BPF cut-off frequencies are selected:

$$f_{LPF} = 23kHz$$

$$f_{HPF} = 230Hz$$

Additionally, the closed-loop response frequency of port #2's current controller ($f_{2r,95\%} = \frac{1}{10ms} = 100Hz$) is not included in the bandwidth of the BPF. This will prevent any interactions between the two control loops.

The Bode plot of the selected BPF is illustrated in Figure 1.22. As it can be noticed, the resonance frequency of the LC filter falls within the bandwidth of the used BPF.

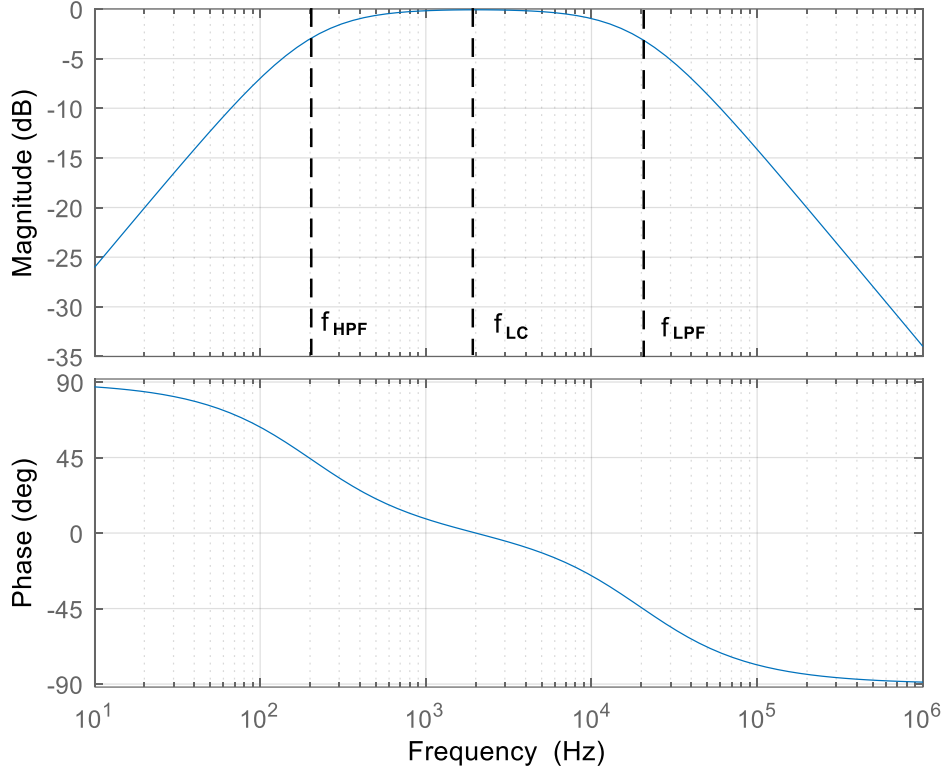


Figure 1.22: Bode plot of the designed BPF for the active damping control.

The output of the BPF will be the oscillations of port #2's DC voltage bus at the resonance frequency f_{LC} . These oscillations are then compared to a zero reference, as explained before, and the resulting error is used as an input to a proportional controller. The design of this controller is achieved by using the proposed TAB converter's generalized average model developed in Section 1.4.

The Laplace transform of the linearized model presented in (1.37) leads to the open-loop transfer function linking the DC-link voltage V_{C_f} of port #2 to the external phase shift φ_{12} of this same port:

$$G_{V_{C_f}}(s) = \left. \frac{V_{C_f}(s)}{\varphi_{12}(s)} \right|_{\substack{\hat{\varphi}_{13}=0 \\ \hat{\alpha}_1=0; \hat{\alpha}_2=0 \\ \hat{\alpha}_3=0; \hat{\alpha}_4=0}}$$

Transfer function $G_{V_{C_f}}(s)$ has an order of 9. The root locus of the open-loop transfer function $G_{V_{C_f}}(s) \times G_{BPF}(s)$ is displayed in Figure 1.23. It is observed that the maximum allowable proportional controller gain is $K_{p,max} = -0.63$. In fact, applying a negative proportional gain with an absolute value greater than $|K_{p,max}|$ would result in two unstable poles (poles with positive real parts) in the closed-loop transfer function, leading to system instability. To avoid this, it is crucial to keep the proportional gain within the specified limit.

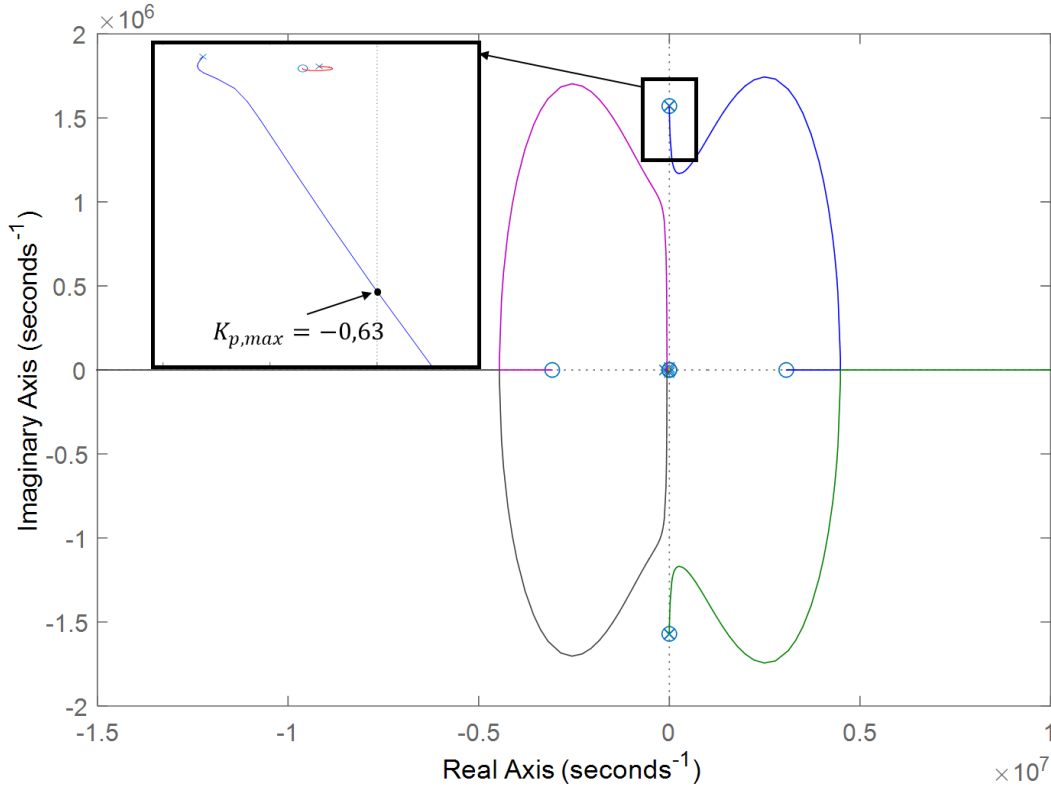
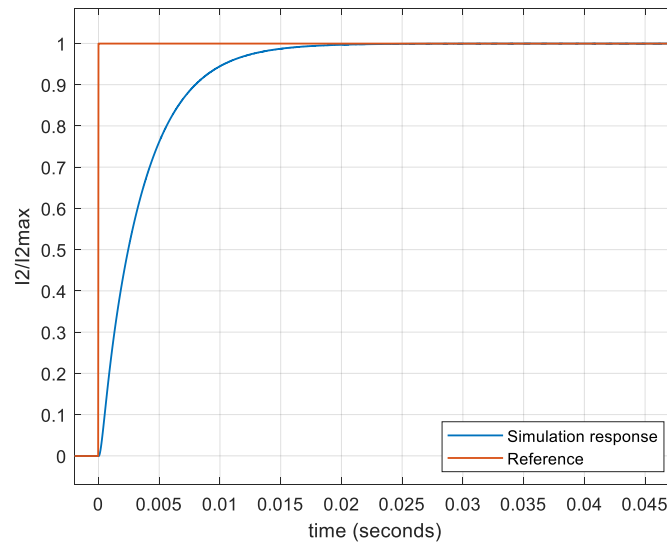


Figure 1.23: Root locus of open-loop transfer function $G_{V_{C_f}}(s) \times G_{BPF}(s)$.

For the TAB converter presented in Section 1.4, a proportional gain of $K_p = -0.063$ is selected using the ‘Control System Designer’ tool of Matlab, corresponding to a time response of 1.5 ms.

Figure 1.24 shows the closed-loop responses of the DC current control of port #2 and the DC voltage control of port #3 when the active damping control loop is activated. By comparing these responses to those in Figure 1.15, where no active damping was applied, we can see that the low frequency oscillations caused by the resonance of the LC filter were successfully cancelled.



(a)

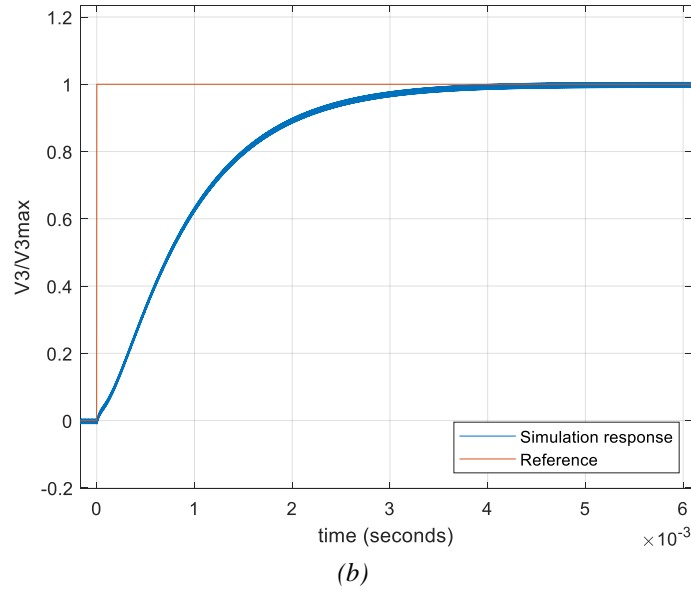


Figure 1.24: Application of the proposed active damping method and its effects on the active power control of the system: (a) DC current i_2 of port #2; (b) Output DC voltage V_3 of port #3.

The active damping method proposed in this section can be extrapolated and adapted to a MAB converter with any number of ports.

1.6. Conclusion

MAB converters are multi-port converters with inherent galvanic isolation. This is achieved by connecting their ports through a high-frequency multi-winding transformer. Nevertheless, connecting these ports through a common part of the system can cause a cross-coupling issue, which makes it challenging to manage the power flow between them. Therefore, it is essential to employ a decoupling technique.

This chapter presents the selected MAB converter topology featured throughout the manuscript and its corresponding mathematical model.

Mathematical models are highly useful because they facilitate the study of the behaviour of a system and the design of its controllers. Both the steady-state model and the dynamic model of the MAB converter are elaborated in this chapter. The former represents the system at a specific operating point while the latter represents it between two different operating points. The steady-state model of the MAB converter was elaborated using the Generalized Harmonic Approximation method. Its dynamic behaviour was represented by the Generalized Average Model, considering up to the first harmonic of each signal.

The interaction between a MAB converter and an LC filter externally connected to one of its ports has been also investigated in this chapter. Additionally, an active solution is proposed in this thesis, aiming to damp the oscillations caused by the LC filter, without the addition of any passive components.

In the following chapter, the process of calculating conduction and switching losses will be outlined and an optimized control strategy is proposed to minimize these losses, resulting in increased efficiency of a MAB converter on its entire operating range.

CHAPTER 2: LOSS CALCULATION AND EFFICIENCY OPTIMIZATION OF A MAB CONVERTER

2.1. Introduction

In the previous chapter, the MAB converter's dynamic and steady state modelling was achieved. Mathematical models are commonly used in preliminary converter studies due to their ease of implementation and manipulation, in order to precisely capture and reproduce the system's behaviour. They are also useful for the control of the systems they represent. From the steady-state model of a system, the control input parameters can be calculated in order to drive the system to a specific steady-state operating point and to obtain the desired control output values. From the dynamic model, closed-loop controllers can be designed to control and monitor the dynamics of the system when the operating point changes or when disturbances occur.

The primary goal of controlling a MAB converter is to be able to provide each port with its required power value. However, an optimized control strategy will also seek to maximize the efficiency of the converter by minimizing its losses. Different types of losses exist in a MAB converter, such as conduction losses, switching losses and magnetic core losses. This chapter details a technique for computing the switching and conduction losses based on the steady-state model developed in Chapter 1. Additionally, an optimized control strategy is proposed for the MAB converter, aiming to minimize the total system losses by decreasing the peak and RMS currents in the transformer windings and increasing the number of soft switching events.

2.2. Power Flow Control of a MAB Converter

The control of a MAB converter can be divided into three control levels, as shown in Figure 2.1. The primary, or high-level controller, calculates the necessary power value that should be delivered to or drawn from each port. Therefore, the high-level controller produces power references for the lower control level using real-time data on, for example, solar irradiance for PV panels, wind speed for wind turbines, battery system charge status, electrical load demand... [9], [13]. A predetermined strategy utilizes this information to determine how the power must flow in the MAB converter. This control level will not be further studied in this thesis and power references will be considered given by the user. The second or mid-level of control ensures the realization of the scenario produced by the first level of control by delivering the necessary power to each port. At this stage, the modulation technique to be employed is determined based on the references generated by the high-level controller and other system parameters. The control inputs' values (internal and external phase shift values) necessary to sustain optimal and stable operation of the MAB converter are computed. The main focus of this chapter will be on this level of control. Then, the third or low-level controller generates the PWM commands for the switches of the ports, relying on the control inputs calculated by the mid-level controller. Ultimately, these PWM commands are transmitted to the drivers of the switches.

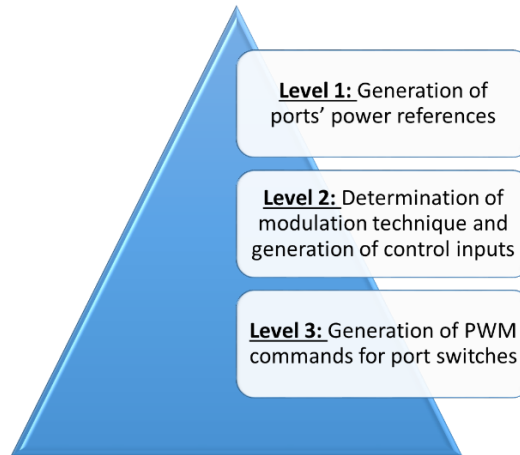


Figure 2.1: Hierarchical representation of the three levels of control of a MAB converter.

In Chapter 1, it was stated that an n -port MAB converter comprises $(2n - 1)$ control input parameters and $(n - 1)$ control outputs. The control inputs consist of the internal and external phase shifts of the ports, where port #1 is considered the reference port and has an external phase shift of zero. The control outputs represent the active power values of the controlled ports, with the power of the reference port #1 being determined by the law of power conservation, as previously explained. This means that the control system of a MAB converter corresponds to a system of $(n - 1)$ equations with $(2n - 1)$ unknowns, which are the control inputs. Consequently, there is an infinity of possible solutions for this system, each resulting in a different combination of the control inputs generating the same active power values at the ports. However, certain combinations may result in higher losses, whilst others bring the system closer to optimal operation.

External Phase Shift (EPS) modulation is a commonly employed technique in literature to control a MAB converter. It involves fixing a duty cycle of 50% on the AC voltages of all ports by equating all internal phase shifts to zero. Subsequently, only the external phase shifts between ports are utilized as control inputs. That way, the external phase shift of each port will determine the power drawn from or received by it. In fact, by setting all internal phase shifts of the MAB converter to zero, the number of control inputs decreases from $(2n - 1)$ to $(n - 1)$. Consequently, the control system becomes equivalent to a system of $(n - 1)$ equations with $(n - 1)$ unknowns, having only one unique solution. Nevertheless, this solution is not necessarily the optimal one.

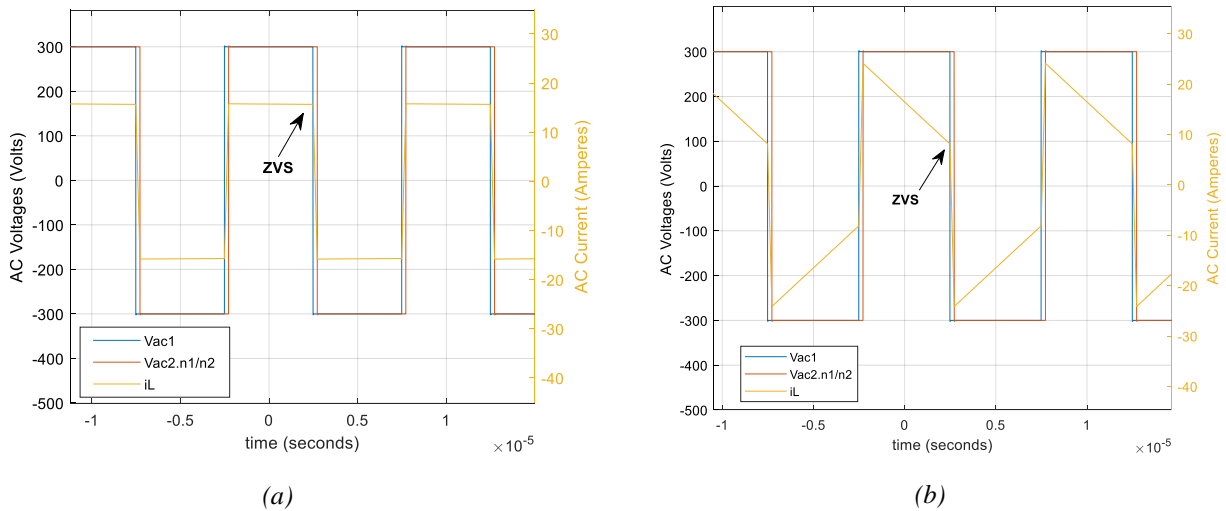
In [30], a Newton-Raphson solver is implemented to find the corresponding external phase shifts for a given set of desired port powers, based on an analytical expression linking these two sets of parameters. In [24], [25], an EPS modulation technique is also proposed, using both a feedforward and feedback loop simultaneously to drive the system to a specific operating point. The feedforward predicts the external phase shift values corresponding to a desired operating point. Additionally, it decouples the control system, as discussed in the previous chapter. This feedforward is based on the first harmonic approximation model of the system that was explained in Chapter 1. The feedback loop consists of PI controllers that correct the prediction errors at each port separately.

When operating at nominal power, the EPS modulation is an effective and straightforward approach to control the active power flow in a MAB converter. However, EPS modulation can

lead to elevated losses at certain operating points, especially when low power is flowing through the system or when voltage mismatches occur. These losses arise mainly due to the limited soft switching range and the elevation of RMS and peak currents brought on by this modulation technique at these operating points. A voltage mismatch is defined as a situation in which the ratio of the DC voltages of two ports differs from their corresponding transformer windings' ratio. This is caused by the disturbance of the DC voltages of these ports.

In a real scenario, the ports of a MAB converter are connected to different non-ideal electrical sources, loads or ESS, leading to changes in their DC voltages. For example, a port of a MAB converter that is directly connected to a photovoltaic panel can function as an MPPT (Maximum Power Point Tracker). Therefore, it may continuously adjust the DC output voltage of the photovoltaic panel to extract the maximum amount of power from it. Similarly, the output voltage of a battery changes continuously according to its state of charge (SoC), temperature, state of health (SoH) and technology. Any variations in the DC voltage can impact the MAB converter's performance. Therefore, it is important to take into account the voltage variations at each port. This thesis will consider a maximum range of $\pm 20\%$ for each port's DC voltage variation.

Figure 2.2 displays the AC current waveform of a DAB converter at both nominal power and low power, with and without the occurrence of a voltage mismatch, when EPS modulation is applied. As we can notice, a voltage mismatch increases peak and RMS current, and may result in the loss of Zero Voltage Switching (ZVS), which is more likely to happen when low power flows through the system. The criteria for ZVS will be explained in the upcoming sections of this chapter. For the purpose of analysing the waveforms presented in Figure 2.2 and verifying the occurrence of ZVS, it can be stated at this level that ZVS occurs when the AC current i_L (yellow curve) at port #1 of this DAB converter is positive at the moment when the AC voltage $v_{ac,1}$ (blue curve) of this port transitions from its positive to its negative state.



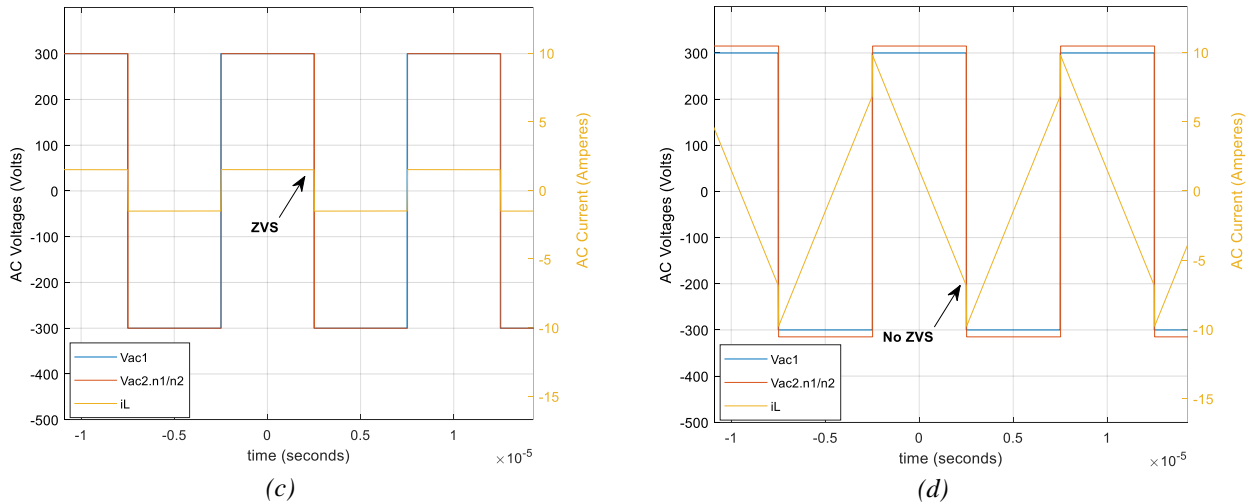


Figure 2.2: AC waveforms of a DAB converter when EPS modulation is applied: (a) at nominal power with no voltage mismatch; (b) at nominal power with +5% DC voltage at port 2; (c) at 10% of nominal power with no voltage mismatch; (d) at 10% of nominal power with +5% DC voltage at port 2.

To avoid the limitations of EPS modulation and optimize the MAB converter's efficiency throughout the entire operational range, it is necessary to introduce supplementary control parameters.

In [49], the switching frequency of the MAB converter is used as the additional control parameter, along with the external phase shifts, to decrease the total system losses. Increasing the switching frequency results in increased losses in passive components whilst decreasing it leads to the loss of the soft switching (ZVS), thereby increasing switching losses. Consequently, a frequency sweep algorithm is utilized to determine the optimum switching frequency that will give the best efficiency. The purpose of this approach, as shown in Figure 2.3, is minimising switching losses by ensuring soft switching while also minimising losses in passive components. However, the variable switching frequency could lead to electromagnetic compatibility (EMC) problems and complex passive component sizing.

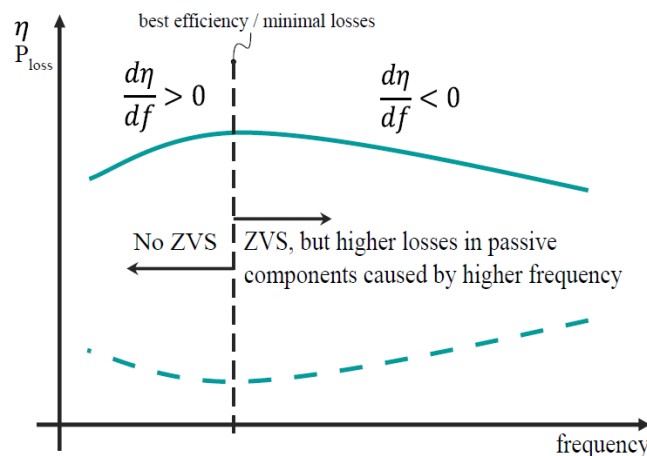


Figure 2.3: Losses and efficiency in function of the switching frequency in a MAB converter [49].

In [26], a Perturb and Observe (P&O) algorithm is employed in order to track the minimum RMS current point of the MAB converter by changing its internal phase shifts. The external phase shifts are adjusted using PI controllers in order to keep the desired active power values

at the ports. This simple control method leads to decreased conduction losses, does not require a lot of computational effort, is easily scalable and does not necessitate any mathematical model or former knowledge of the system's parameters. However, it does not take into consideration other types of losses such as switching losses. Additionally, the P&O algorithm can easily set the system into a local minimum of losses.

In [50], a mathematical model based on the generalized harmonic approximation (GHA) technique presented in the previous chapter is developed for a TAB converter, considering both its internal and external phase shifts. Then, an objective function is formulated to represent the total system losses including conduction losses, switching losses, transformer losses, and DC link capacitor losses. An optimization problem is therefore established, aiming to minimize this objective function while maintaining the desired active power flow constraints. Solving this problem generates optimal control variables at any operating point. Although this MPS modulation technique absolutely leads to a system with maximum efficiency, it comes at a cost. Actually, the computational effort required to solve this complex, five variable optimization problem is enormous and therefore cannot be performed in real time. Lookup tables are utilized to store the pre-calculated control variables at certain chosen operating points. However, in this case, control inputs at operating points that are not present in the lookup tables would either be equal to the optimal control inputs of the closest operating point stored in the lookup tables or calculated by applying multi-dimensional interpolation. Both methods would lead to suboptimal system behaviour at these points.

A similar drawback is also observed in the research presented in [51]. Therein, an optimization problem is formulated for a TAB converter aiming to minimize the conduction losses while considering the power flows and the ZVS conditions as constraints.

As we can notice, the works in [26] and [50] represent two extreme solutions to the same problem. The former chose simplicity and little computational effort but risks settling the system to a suboptimal solution. The latter went all the way in, developing an all-inclusive, five-variable optimization problem that leads the system to a global optimum at the considered operating points. However, computational complexity is not considered. The purpose of this chapter is to propose a solution that lies between these two extremes. Therefore, an efficiency-optimization control method is developed, aiming to decrease the conduction and switching losses of a MAB converter with a tolerable amount of computational effort and without the risk of operating in a local minimum. The GHA model that was developed in the previous chapter is used for that purpose. This model represents the system accurately enough to be able to predict its losses for several combinations of its control variables at the same operating point. The developed algorithm finally chooses the optimal combination resulting minimum conduction and switching losses.

2.3. Calculation of the Conduction Losses

The primary type of loss targeted in this chapter for optimal control of an n -port MAB converter are the conduction losses. These losses mainly take place in the copper wires, inductance and transformer windings as well as the conducting switches. Conduction losses in a port are directly proportional to the square value of the RMS AC current flowing in its corresponding winding. Therefore, they escalate quickly with the increase of power flow.

The conduction losses of a port # i in a MAB converter can be calculated from the following expression:

$$P_{cond,i} = (R_i + 2R_{ds_on})I_{i,rms}^2 \quad (2.1)$$

R_i is the sum of the series resistances of the copper connections, such as wires and PCB (Printed Circuit Board) tracks, the transformer winding and the series inductance of port # i . At a certain operating temperature, the resistance value R_i can be calculated analytically using the following expression, neglecting the skin effect caused by the high switching frequency:

$$R_i = \rho \frac{l}{S}$$

Where ρ is the resistivity of the conducting material, which is usually copper, l is the length of the wire and S is the wire cross section. A more precise value of R_i can also be determined via an impedance analyser after the development of the prototype.

R_{ds_on} is the resistance of a turned on switch, knowing that at each time instant, a maximum of two switches are turned on at once in each port. The resistance value R_{ds_on} can be obtained from the datasheet of the selected switch, considering a certain operating temperature range.

$I_{i,rms}$ is the RMS value of the AC current flowing through the transformer winding of port # i at the steady state of the considered operating point. From expression (1.19) of the GHA model developed in Chapter 1, the value of $I_{i,rms}^2$ can be calculated as follows:

$$\begin{aligned} I_{i,rms}^2 &= \frac{1}{T_s} \int_0^{T_s} i_{L,i}^2(t) dt \\ &= \frac{4T_s}{n_{1i}^2 \cdot \pi^4} \left[\frac{V_i^2}{n_{1i}^2} \left(\sum_{j \neq i}^n \frac{1}{L_{ij}} \right)^2 \cdot A(i, i) + \sum_{j \neq i}^n \left[\frac{V_j^2}{n_{1j}^2 L_{ij}^2} \cdot A(j, j) \right] \right. \\ &\quad \left. - 2 \left(\sum_{l \neq i}^n \frac{1}{L_{il}} \right) \sum_{j \neq i}^n \left[\frac{V_i V_j}{n_{1i} n_{1j} L_{ij}} \cdot A(i, j) \right] + 2 \sum_{\substack{j=1, l=1 \\ j \neq i, l \neq i \\ j \neq l}}^n \left[\frac{V_j V_l}{n_{1j} n_{1l} L_{ij} L_{il}} \cdot A(j, l) \right] \right] \end{aligned} \quad (2.2)$$

Where:

$$A(i, j) = \frac{T_s}{2} \sum_{\substack{k=1 \\ k \text{ odd}}}^{\infty} \frac{1}{k^4} \cos\left(k \frac{\alpha_i}{2}\right) \cos\left(k \frac{\alpha_j}{2}\right) \cos\left(k(\varphi_i - \varphi_j)\right)$$

2.4. Soft Switching Evaluation and Calculation of Switching Losses

The MAB converter is recognized for having a naturally broad soft switching range [9]. Nevertheless, the possibility of operating with hard switching escalates when operating at low power or when the DC links' voltages undergo disturbances. The loss of soft switching can significantly increase switching losses, depending on the operating point and the selected system's switches [9]. In this section, the ZVS criteria for each port will be defined at first. After that, the expression of the switching losses will be developed accordingly.

2.4.1. Elaboration of the ZVS Criteria

In an ideal case, a switch is turned on at zero voltage (ZVS) if its drain current is negative during its switching instant (Figure 2.4). This negative current will circulate through its anti-parallel body diode, turning it on, hence the voltage drop at the switch. In other words, under an ideal scenario, the ZVS operation of a switch only depends on the direction of the current flowing through it. Nevertheless, this condition is not sufficient to ensure the ZVS operation in a practical converter. In fact, the parasitic capacitance C_{oss} between the drain and the source of the switch imposes a minimum amount of energy to be flowing through the port's inductance for a minimum amount of time during the switching instant in order to be fully charged or discharged. A minimum amount of energy means that a minimum amount of current should be flowing through each port during its switching instants. This energy value can be calculated using the Thevenin equivalent circuit of a port #i shown in Figure 2.5, and will be elaborated in this section [22].

Consequently, in order to achieve a ZVS, three conditions must be met at every switching instant of a port. Two of these conditions relate to the AC current flowing through the port during the switching point under consideration. The current must flow in the correct direction and be equal to or greater than the minimum current required to charge and discharge the parasitic output capacitances of the switching switches. The third condition involves having a sufficient dead time to allow the energy exchange between the inductance of the port and the parasitic capacitances of the switches to be completed in order to fully charge/discharge these capacitances.

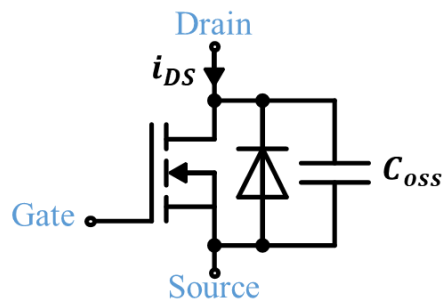


Figure 2.4: Switch symbol showing the drain-source capacitance and drain current.

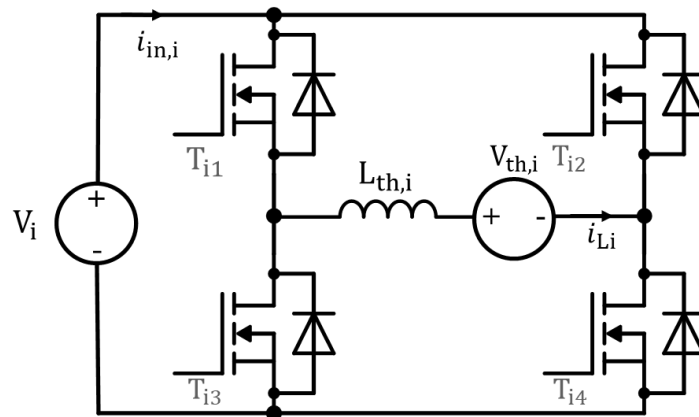


Figure 2.5: Generic port-equivalent circuit of a MAB converter.

The voltage source $V_{th,i}$ and the inductance $L_{th,i}$ of Figure 2.5 replace the remaining ports of the MAB converter and are calculated from:

$$L_{th,i} = \frac{1}{\sum_{\substack{j=1 \\ j \neq i}}^n \frac{1}{L_{ij}}} \quad (2.3)$$

$$V_{th,i}(t) = \sum_{j=1, j \neq i}^n v_{ac,j}(t) \times \frac{L_{th,i}}{L_{ij}} \quad (2.4)$$

For each port, there are four switching instants in a switching period T_s . These instants are shown in Figure 2.6 for a port #i and are denoted by: τ_{i1} , τ_{i2} , τ_{i1}' and τ_{i2}' . Since the current in each port is half-cycle symmetric, only two switching time instants should be studied for each port: τ_{i1} and τ_{i2} . In each one of these instants, one switch is turned on and another switch is turned off. The switch that is being turned on is the switch where the ZVS conditions are examined. A soft switching (ZVS) will lead to nearly zero switching losses.

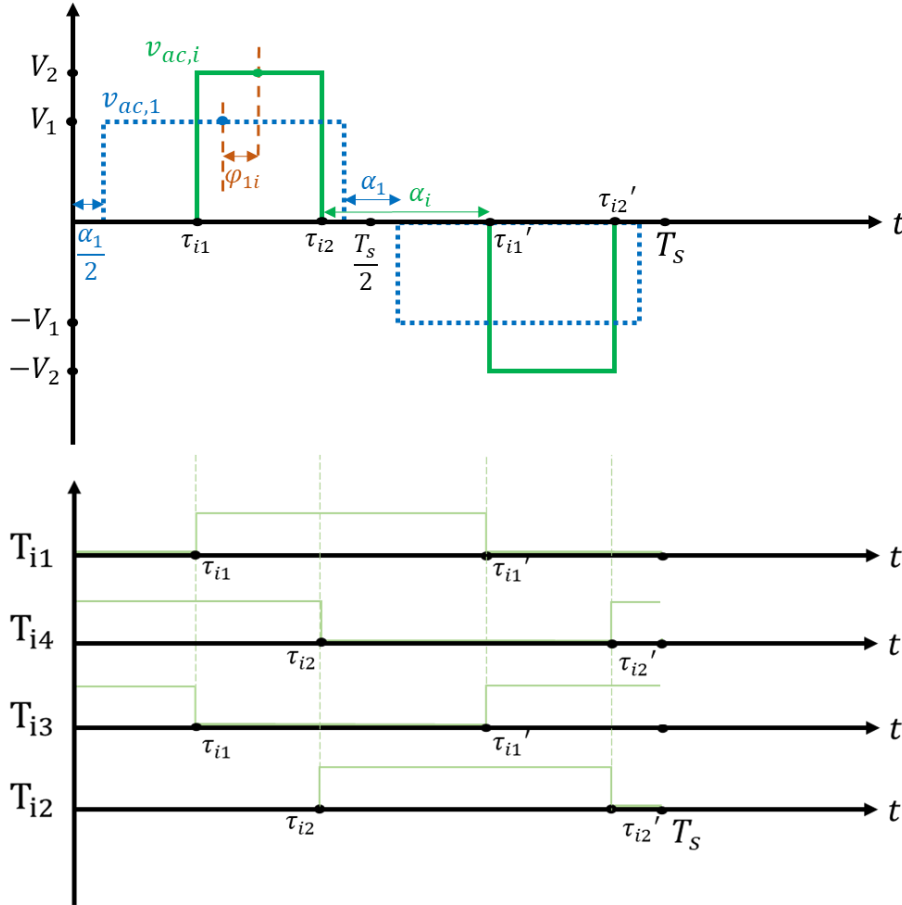


Figure 2.6: Representation of the switching instants of a port #i.

From Figure 2.6, the studied switching time instants of a port #i can be expressed in function of its phase shifts as follows:

$$\tau_{i1} = \left(\varphi_{1i} + \frac{\alpha_i}{2} \right) \frac{T_s}{2\pi} \quad (2.5)$$

$$\tau_{i2} = \frac{T_s}{2} + \left(\varphi_{1i} - \frac{\alpha_i}{2} \right) \frac{T_s}{2\pi} \quad (2.6)$$

If a port # i is operating in full-wave mode, i.e. if its internal phase shift is null ($\alpha_i = 0$), it would only have two symmetrical switching instants ($\tau_{i2} = \frac{T_s}{2} + \tau_{i1}$), one of which should be studied (only τ_{i1} would be studied in this case).

In the following, two cases will be studied. The first case is for a port with a three-level AC voltage ($\alpha_i > 0$), where two switching instants should be studied. The second case is for a port with a two-level AC voltage ($\alpha_i = 0$), where the examination of only one switching instant is sufficient.

a) *Case 1: port # i with $\alpha_i > 0$*

i. *Switching instant τ_{i1}*

At time instant τ_{i1} , the AC voltage of port # i switches from 0V to $+V_i$. For this to happen, there are two options: either switches T_{i1} and T_{i2} were ON before τ_{i1} , so switch T_{i2} is turned off and T_{i4} is turned on during τ_{i1} , or T_{i3} and T_{i4} were ON before τ_{i1} , so switch T_{i3} is turned off and T_{i1} is turned on during τ_{i1} . Both options lead to the same ZVS conditions. The second scenario will be examined in this section.

Figure 2.7 shows the equivalent circuit of a port # i during the dead time of switching instant τ_{i1} in this case. Switch T_{i3} is being turned off and T_{i1} is being turned on. For the anti-parallel diode of T_{i1} to be turned on during τ_{i1} , the AC current $i_{L,i}(t)$ should be negative. The second current condition is derived from the minimum energy that should be circulating through port # i for the parasitic capacitances of the switches to be charged/discharged. We can write from Figure 2.7:

$$i_{L,i}(\tau_{i1}) = -2C_{oss} \frac{dv_x}{dt} \quad (2.7)$$

$$i_{in,i}(\tau_{i1}) = \frac{i_{L,i}}{2} = -C_{oss} \frac{dv_x}{dt} \quad (2.8)$$

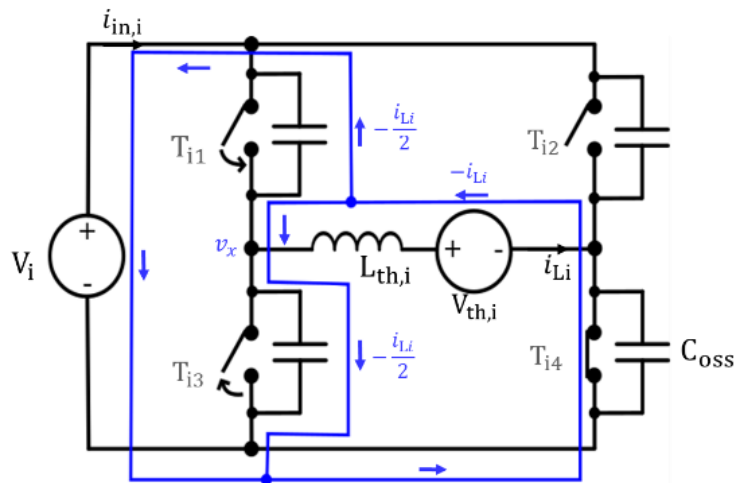


Figure 2.7: Current circulation at port # i during switching instant τ_{i1} when $\alpha_i > 0$.

The energy exchanged between the inductance and the parasitic capacitances can be calculated as follows [22], [50]:

$$\begin{aligned}
 E_{absorbed} &= \int_{\tau_{i1}^-}^{\tau_{i1}^+} [V_{th,i}(\tau_{i1}) \cdot i_{L,i}(\tau_{i1}) - V_i \cdot i_{in,i}(\tau_{i1})] dt \\
 &= \int_{\tau_{i1}^-}^{\tau_{i1}^+} \left[V_{th,i}(\tau_{i1}) \cdot \left(-2C_{oss} \frac{dv_x}{dt} \right) - V_i \cdot \left(-C_{oss} \frac{dv_x}{dt} \right) \right] dt \\
 &= \int_0^{V_i} [-2C_{oss}V_{th,i}(\tau_{i1}) + C_{oss}V_i] dv_x \\
 &= -2C_{oss}V_{th,i}(\tau_{i1})V_i + C_{oss}V_i^2
 \end{aligned} \tag{2.9}$$

Where τ_{i1}^- and τ_{i1}^+ are the time instants right before and right after the switching instant τ_{i1} , respectively.

From equation (2.9), the minimum current value required for a soft turn on of switch T_{i1} during τ_{i1} can be written as:

$$\frac{1}{2}L_{th,i}i_{L,i}^2(\tau_{i1}) \geq -2C_{oss}V_{th,i}(\tau_{i1})V_i + C_{oss}V_i^2 \tag{2.10}$$

Therefore, the second current condition at τ_{i1} would be:

$$|i_{L,i}(\tau_{i1})| \geq \sqrt{2 \frac{C_{oss}V_i^2}{L_{th,i}} - 4 \frac{C_{oss}V_{th,i}(\tau_{i1})V_i}{L_{th,i}}} \tag{2.11}$$

If $V_{th,i}(\tau_{i1}) > \frac{V_i}{2}$, the second ZVS condition is always achieved in this case. The instantaneous current value $i_{L,i}(\tau_{i1})$ is calculated from expression (1.19) of the GHA model developed in Chapter 1.

If the first two conditions concerning the direction and the minimum value of the AC current are fulfilled, the third condition should be examined next to ensure the achievement of a ZVS. As previously mentioned, the third ZVS condition involves the minimum dead time that should be used to allow the energy exchange between the inductance $L_{th,i}$ and the parasitic capacitances to fully charge/discharge these capacitances. The satisfaction of the second examined condition means that sufficient energy is stored in the port's inductance at the switching instant for the completion of this charge/discharge. However, if the dead time does not last long enough, the required energy will not have the time to be transferred to the C_{oss} of the switching switches, preventing the occurrence of a ZVS.

The dynamics of the resonant LC circuit of Figure 2.7 can be represented by the following expression:

$$L_{th,i} \frac{di_{L,i}}{dt}(t) = v_x(t) - V_{th,i}(t) \tag{2.12}$$

Considering that the voltage $V_{th,i}(t)$ does not vary during the switching instant τ_{i1} and stays equal to its value $V_{th,i}(\tau_{i1})$ calculated from equation (2.4), we can write:

$$L_{th,i} \frac{d^2i_{L,i}}{dt^2}(t) = \frac{dv_x}{dt}(t) = -\frac{i_{L,i}(t)}{2C_{oss}} \tag{2.13}$$

By rearranging equation (2.13), we can write the following differential equation:

$$\frac{d^2 i_{L,i}}{dt^2}(t) + \frac{1}{2L_{th,i}C_{oss}} i_{L,i}(t) = 0 \quad (2.14)$$

The solution to this homogeneous second order differential equation can be written as follows:

$$i_{L,i}(t) = A_{i1} \cos(w_r t) + B_{i1} \sin(w_r t) \quad (2.15)$$

Where A_{i1} and B_{i1} are real constants and $w_r = \frac{1}{\sqrt{2L_{th,i}C_{oss}}} = 2\pi f_r$ with f_r the resonance frequency of this LC circuit.

From the initial conditions of equations (2.12) and (2.15) at the beginning of the switching instant $t = 0$, we can calculate the values of the constants A_{i1} and B_{i1} as following:

- $i_{L,i}(0) = i_{L,i}(\tau_{i1}) = A_{i1}$
- $v_x(0) = 0 = L_{th,i} \frac{di_{L,i}}{dt}(0) + V_{th,i}(0) = L_{th,i} B_{i1} w_r + V_{th,i}(\tau_{i1})$

Therefore, we can write:

$$A_{i1} = i_{L,i}(\tau_{i1}) < 0 \quad (2.16)$$

$$B_{i1} = -\frac{V_{th,i}(\tau_{i1})}{L_{th,i} w_r} \quad (2.17)$$

The minimum required dead time, denoted as $t_{di1,min}$ in this case, corresponds to the time instant where the voltage $v_x(t_{di1,min})$ reaches the value V_i . This indicates that switch T_{i3} 's parasitic capacitance is fully charged, while switch T_{i1} 's parasitic capacitance is fully discharged, resulting in ZVS. Consequently, $t_{di1,min}$ can be calculated as following:

$$\begin{aligned} v_x(t_{di1,min}) &= V_i \\ &= V_{th,i}(t_{di1,min}) \\ &\quad + L_{th,i}(-A_{i1} w_r \sin(w_r \cdot t_{di1,min}) + B_{i1} w_r \cos(w_r t_{di1,min})) \end{aligned}$$

So,

$$\cos(w_r t_{di1,min}) - \frac{A_{i1}}{B_{i1}} \sin(w_r t_{di1,min}) = \frac{V_i - V_{th,i}(\tau_{i1})}{B_{i1} L_{th,i} w_r} \quad (2.18)$$

Considering a constant θ such that $\tan \theta = \frac{\sin \theta}{\cos \theta} = \frac{A_{i1}}{B_{i1}}$, equation (2.18) becomes:

$$\cos(\theta) \cos(w_r t_{di1,min}) - \sin(\theta) \sin(w_r \cdot t_{di1,min}) = \frac{(V_i - V_{th,i}(\tau_{i1}))}{B_{i1} L_{th,i} w_r} \cos(\theta)$$

Therefore,

$$\cos(w_r t_{di1,min} + \theta) = \frac{(V_i - V_{th,i}(\tau_{i1}))}{B_{i1} L_{th,i} w_r} \cos(\theta)$$

Finally, the minimum required dead time for the achievement of ZVS at a port #i at switching instant τ_{i1} and for an AC current value $i_{L,i}(\tau_{i1})$ can be expressed as following:

$$t_{di1,min} = \frac{1}{\omega_r} \left(\arccos \left(-\frac{(V_i - V_{th,i}(\tau_{i1}))}{V_{th,i}(\tau_{i1})} \cos \left(\arctan \frac{A_{i1}}{B_{i1}} \right) \right) - \arctan \frac{A_{i1}}{B_{i1}} \right) \quad (2.19)$$

Figure 2.8 shows the waveforms of the AC current $i_{L,i}$ and the voltage v_x of Figure 2.7. In this figure, the AC current $i_{L,i}(\tau_{i1})$ is considered equal to its minimum required value calculated in expression (2.11). As a result, this current becomes zero at $t = t_{di1,min}$ when v_x reaches its final desired value V_i because the energy stored in the inductance is exactly equal to the energy required to fully charge and discharge of the parasitic capacitances in this case. This is an extreme case where the dead time should end at a specific point in order to have ZVS. Otherwise, if $i_{L,i}(\tau_{i1})$ was greater than its minimum required value, it would remain negative at time instant $t_{di1,min}$ and v_x will remain at V_i for a longer period due to the presence of the diodes, allowing the switches more time to switch with ZVS.

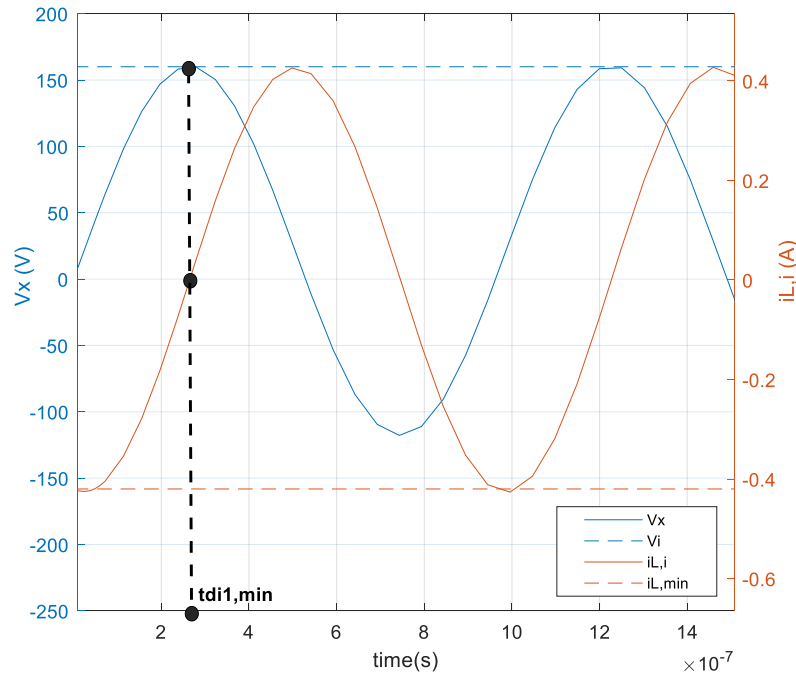


Figure 2.8: Port current $i_{L,i}$ and voltage v_x waveforms during the dead time of switching instant τ_{i1} when $\alpha_i > 0$, considering that $i_{L,i}$ is equal to its minimum required value for a ZVS at the beginning of τ_{i1} .

It is important to select a dead time for port #i at the switching instant τ_{i1} that is not significantly greater than its minimum required value $t_{di1,min}$. This is because the energy between the inductance $L_{th,i}$ and the parasitic capacitances of the switches will continue to oscillate back and forth between these components, as shown in Figure 2.8. Therefore, the capacitance of switch T_{i1} could be charged again and the capacitance of switch T_{i3} could be discharged again, preventing the occurrence of ZVS.

The parameters used for the simulation results of Figure 2.8 are given in Table 2.1.

Table 2.1: Considered parameter values of the equivalent port.

Parameter symbol	Parameter value
$L_{th,i}$	$50 \mu H$
C_{oss}	235 pF
f_s	40 kHz
$V_{th,i}$	21 V
V_i	160 V

ii. Switching instant τ_{i2}

At time instant τ_{i2} , the AC voltage of port #i switches from $+V_i$ to $0V$. Switches T_{i1} and T_{i4} were ON before τ_{i2} , so switch T_{i4} is turned off and T_{i2} is turned on during τ_{i2} .

Figure 2.9 shows the equivalent circuit of port #i during the switching instant τ_{i2} . Switch T_{i4} is being turned off and T_{i2} is being turned on. For the anti-parallel diode of T_{i2} to be turned on during τ_{i2} in this case, the AC current $i_{L,i}(t)$ should be positive.

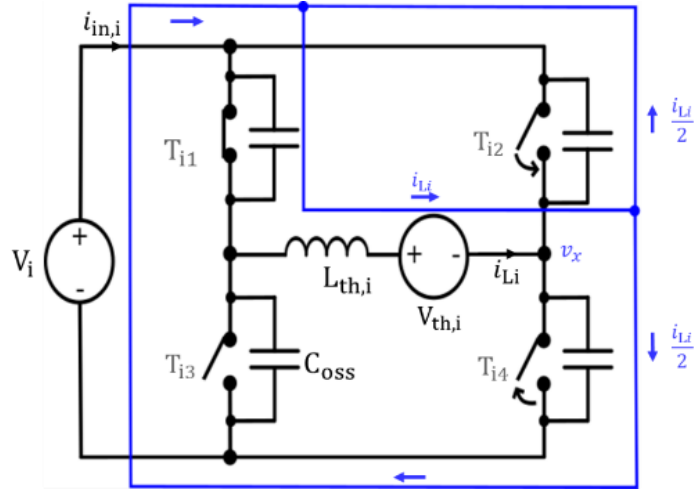


Figure 2.9: Current circulation at port #i during switching instant τ_{i2} when $\alpha_i > 0$.

We can write from Figure 2.9:

$$i_{L,i}(\tau_{i2}) = 2C_{oss} \frac{dv_x}{dt} \quad (2.20)$$

$$i_{in,i}(\tau_{i2}) = \frac{i_{L,i}}{2} = C_{oss} \frac{dv_x}{dt} \quad (2.21)$$

The energy exchanged between the inductance and the parasitic capacitances can be calculated as follows:

$$\begin{aligned} E_{absorbed} &= \int_{\tau_{i2}^-}^{\tau_{i2}^+} [V_{th,i}(\tau_{i2}) \cdot i_{L,i}(\tau_{i2}) - V_i \cdot i_{in,i}(\tau_{i2})] dt \\ &= \int_{\tau_{i2}^-}^{\tau_{i2}^+} \left[V_{th,i}(\tau_{i2}) \cdot \left(2C_{oss} \frac{dv_x}{dt} \right) - V_i \left(C_{oss} \frac{dv_x}{dt} \right) \right] dt \\ &= \int_0^{V_i} [2C_{oss}V_{th,i}(\tau_{i2}) - C_{oss}V_i] dv_x \\ &= 2C_{oss}V_{th,i}(\tau_{i2})V_i - C_{oss}V_i^2 \end{aligned} \quad (2.22)$$

The minimum current value required for a soft turn on of switch T_{i2} during τ_{i2} is:

$$\frac{1}{2}L_{th,i}i_{L,i}^2(\tau_{i2}) \geq 2C_{oss}V_{th,i}(\tau_{i2})V_i - C_{oss}V_i^2$$

Therefore, the second current condition at τ_{i2} would be:

$$|i_{L,i}(\tau_{i2})| \geq \sqrt{-2\frac{C_{oss}V_i^2}{L_{th,i}} + 4\frac{C_{oss}V_{th,i}(\tau_{i2})V_i}{L_{th,i}}} \quad (2.23)$$

If $V_{th,i}(\tau_{i2}) < \frac{V_i}{2}$, the second ZVS condition is always achieved in this case.

If the first two conditions concerning the direction and the minimum value of the AC current are fulfilled, the third condition involving the minimum required dead time should be examined next to ensure the achievement of a ZVS. The dynamics of the resonant LC circuit of Figure 2.9 can be represented by the following expression:

$$L_{th,i}\frac{di_{L,i}}{dt}(t) = V_i - v_x(t) - V_{th,i}(t) \quad (2.24)$$

Considering that the voltage $V_{th,i}(t)$ does not vary during the switching instant τ_{i2} and stays equal to its value $V_{th,i}(\tau_{i2})$ calculated from equation (2.4), we can write:

$$L_{th,i}\frac{d^2i_{L,i}}{dt^2}(t) = -\frac{dv_x}{dt}(t) = -\frac{i_{L,i}(t)}{2C_{oss}} \quad (2.25)$$

By rearranging equation (2.25), we can write the following differential equation:

$$\frac{d^2i_{L,i}}{dt^2}(t) + \frac{1}{2L_{th,i}C_{oss}} \cdot i_{L,i}(t) = 0 \quad (2.26)$$

The solution to this homogeneous second order differential equation can be written as follows:

$$i_{L,i}(t) = A_{i2} \cdot \cos(w_r t) + B_{i2} \cdot \sin(w_r t) \quad (2.27)$$

Where A_{i2} and B_{i2} are real constants and $w_r = \frac{1}{\sqrt{2L_{th,i}C_{oss}}} = 2\pi f_r$ with f_r the resonance frequency of this LC circuit.

From the initial conditions of equations (2.24) and (2.27) at the beginning of the switching instant $t = 0$, we can calculate the values of the constants A_{i2} and B_{i2} as following:

- $i_{L,i}(0) = i_{L,i}(\tau_{i2}) = A_{i2}$
- $v_x(0) = 0 = L_{th,i}\frac{di_{L,i}}{dt}(0) - V_i + V_{th,i}(0) = L_{th,i}B_{i2}w_r - V_i + V_{th,i}(\tau_{i2})$

Therefore, we can write:

$$A_{i2} = i_{L,i}(\tau_{i2}) > 0 \quad (2.28)$$

$$B_{i2} = \frac{V_i - V_{th,i}(\tau_{i2})}{L_{th,i}w_r} \quad (2.29)$$

The minimum required dead time, denoted as $t_{di2,min}$ in this case, corresponds to the time instant where the voltage $v_x(t_{di2,min})$ reaches the value V_i . This indicates that switch T_{i4} 's parasitic capacitance is fully charged, while switch T_{i2} 's parasitic capacitance is fully discharged, resulting in ZVS. Consequently, $t_{di2,min}$ can be calculated as following:

$$\begin{aligned} v_x(t_{di2,min}) &= V_i \\ &= V_i - V_{th,i}(t_{di2,min}) \\ &\quad - L_{th,i}(-A_{i2} \omega_r \sin(\omega_r t_{di2,min}) + B_{i2} \omega_r \cos(\omega_r t_{di2,min})) \end{aligned}$$

So,

$$t_{di2,min} = \frac{1}{\omega_r} \left(\arccos \left(-\frac{V_{th,i}(\tau_{i2})}{(V_i - V_{th,i}(\tau_{i2}))} \cos \left(\arctan \frac{A_{i2}}{B_{i2}} \right) \right) - \arctan \frac{A_{i2}}{B_{i2}} \right) \quad (2.30)$$

It is important to select a dead time for port #i at switching instant τ_{i2} that is not significantly greater than its minimum required value $t_{di2,min}$ to avoid energy oscillation between $L_{th,i}$ and the parasitic capacitances of the switches, which may prevent the occurrence of ZVS.

By symmetry, the satisfaction of the soft switching conditions at switching instants τ_{i1} and τ_{i2} means that soft switching will also occur at τ_{i1}' and τ_{i2}' respectively. In this case, all four switches of the studied port will turn on with ZVS.

b) Case 2: port #i with $\alpha_i = 0$

As explained before, the study of only one switching instant τ_{i1} is sufficient for a port operating with a full-wave AC voltage. If the switching conditions at τ_{i1} are satisfied, all four switches of this port will turn on with ZVS. Otherwise, hard switching will occur on all four switches.

At time instant τ_{i1} , the AC voltage of port #i switches from $-V_i$ to $+V_i$. Switches T_{i2} and T_{i3} are turned off at τ_{i1} , while switches T_{i1} and T_{i4} are turned on.

Figure 2.10 shows the equivalent circuit of port #i during the switching instant τ_{i1} in this case. For the anti-parallel diodes of T_{i1} and T_{i4} to be turned on during τ_{i1} , the AC current $i_{L,i}(t)$ should be negative. The parasitic capacitances C_{oss} of all switches are being charged/discharged during this dead time. We can write from Figure 2.10:

$$i_{L,i}(\tau_{i1}) = -2C_{oss} \frac{dv_{x1}}{dt} \quad (2.31)$$

$$i_{in,i}(\tau_{i1}) = 0 \quad (2.32)$$

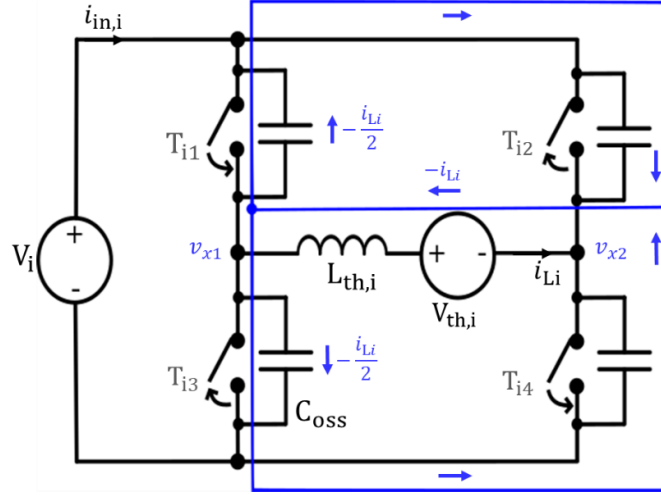


Figure 2.10: Current circulation at port # i during the dead time of the switching instant τ_{i1} when $\alpha_i = 0$.

The energy exchanged between the inductance and the parasitic capacitances can be calculated as follows:

$$\begin{aligned}
 E_{absorbed} &= \int_{\tau_{i1}^-}^{\tau_{i1}^+} [V_{th,i}(\tau_{i1}) \cdot i_{L,i}(\tau_{i1}) - V_i \cdot i_{in,i}(\tau_{i1})] dt \\
 &= \int_{\tau_{i1}^-}^{\tau_{i1}^+} \left[V_{th,i}(\tau_{i1}) \cdot \left(-2C_{oss} \frac{dv_{x1}}{dt} \right) - 0 \right] dt \\
 &= \int_0^{V_i} [-2C_{oss} V_{th,i}(\tau_{i1})] dv_{x1} = -2C_{oss} V_{th,i}(\tau_{i1}) V_i
 \end{aligned} \tag{2.33}$$

The minimum current value required during τ_{i1} can be written as:

$$\frac{1}{2} L_{th,i} i_{L,i}^2(\tau_{i1}) \geq -2C_{oss} V_{th,i}(\tau_{i1}) V_i$$

Therefore, the second current condition at τ_{i1} would be:

$$|i_{L,i}(\tau_{i1})| \geq 2 \sqrt{-\frac{C_{oss} V_{th,i}(\tau_{i1}) V_i}{L_{th,i}}} \tag{2.34}$$

If $V_{th,i}(\tau_{i1}) > 0$, the second ZVS condition is always achieved in this case.

If the first two conditions concerning the direction and the minimum value of the AC current are fulfilled, the third condition involving the minimum required dead time should be examined next to ensure the achievement of a ZVS. The dynamics of the resonant LC circuit of Figure 2.10 can be represented by the following expression:

$$L_{th,i} \frac{di_{L,i}}{dt}(t) = v_{x1}(t) - v_{x2}(t) - V_{th,i}(t) \tag{2.35}$$

Considering that the voltage $V_{th,i}(t)$ does not vary during the switching instant τ_{i1} and stays equal to its value $V_{th,i}(\tau_{i1})$ calculated from equation (2.4), we can write:

$$L_{th,i} \frac{d^2 i_{L,i}}{dt^2}(t) = \frac{dv_{x1}}{dt}(t) - \frac{dv_{x2}}{dt}(t) = -\frac{i_{L,i}(t)}{C_{oss}} \quad (2.36)$$

By rearranging equation (2.36), we can write the following differential equation:

$$\frac{d^2 i_{L,i}}{dt^2}(t) + \frac{1}{L_{th,i} C_{oss}} \cdot i_{L,i}(t) = 0 \quad (2.37)$$

The solution to this homogeneous second order differential equation can be written as follows:

$$i_{L,i}(t) = A_{i1} \cdot \cos(w_r t) + B_{i1} \cdot \sin(w_r t) \quad (2.38)$$

Where A_{i1} and B_{i1} are real constants and $w_r = \frac{1}{\sqrt{L_{th,i} C_{oss}}} = 2\pi f_r$ with f_r the resonance frequency of this LC circuit.

From the initial conditions of equations (2.35) and (2.38) at the beginning of the switching instant $t = 0$, we can calculate the values of the constants A_{i1} and B_{i1} as following:

- $i_{L,i}(0) = i_{L,i}(\tau_{i1}) = A_{i1}$
- $v_{x1}(0) = 0$
- $v_{x2}(0) = V_i$

Therefore, we can write:

$$A_{i1} = i_{L,i}(\tau_{i1}) < 0 \quad (2.39)$$

$$B_{i1} = \frac{-V_i - V_{th,i}(\tau_{i1})}{L_{th,i} w_r} \quad (2.40)$$

The minimum required dead time, denoted as $t_{di1,min}$ in this case, corresponds to the time instant where the voltage $v_{x1}(t_{di1,min})$ reaches the value V_i and $v_{x2}(t_{di1,min})$ reaches zero. This indicates that the parasitic capacitances of switches T_{i2} and T_{i3} are fully charged, while the parasitic capacitances of switches T_{i1} and T_{i4} are fully discharged, resulting in ZVS. Consequently, $t_{di1,min}$ can be calculated as following:

$$\begin{aligned} v_{x1}(t_{di1,min}) - v_{x2}(t_{di1,min}) &= V_i \\ &= V_{th,i}(t_{di1,min}) \\ &\quad + L_{th,i}(-A_{i1} \cdot w_r \cdot \sin(w_r t_{di1,min}) + B_{i1} w_r \cos(w_r t_{di1,min})) \end{aligned}$$

So,

$$t_{di1,min} = \frac{1}{w_r} \left(\arccos \left(\frac{(V_i - V_{th,i}(\tau_{i1}))}{(-V_i - V_{th,i}(\tau_{i1}))} \cos \left(\arctan \frac{A_{i1}}{B_{i1}} \right) \right) - \arctan \frac{A_{i1}}{B_{i1}} \right) \quad (2.41)$$

Table 2.2 summarizes the ZVS conditions of a port #i for all the cases elaborated in this section.

The value of the switches' parasitic capacitors increases with an increasing drain-to-source voltage. In this thesis, the value of the C_{oss} is considered constant for simplicity. In future studies, the variation of this parameter's value can be taken into consideration in order to enhance the precision of the loss model.

Table 2.2: ZVS conditions of a port #i.

Internal phase shift value	Current direction condition	Minimum current value	Minimum dead time value
$\alpha_i > 0$	$i_{L,i}(\tau_{i1}) < 0$	$ i_{L,i}(\tau_{i1}) \geq \sqrt{2 \frac{C_{oss} V_i^2}{L_{th,i}} - 4 \frac{C_{oss} V_{th,i}(\tau_{i1}) V_i}{L_{th,i}}}$	$t_{di1,min} = \frac{1}{w_r} \left(\arccos \left(-\frac{(V_i - V_{th,i}(\tau_{i1}))}{V_{th,i}(\tau_{i1})} \cos \left(\arctan \frac{A_{i1}}{B_{i1}} \right) \right) - \arctan \frac{A_{i1}}{B_{i1}} \right)$
	$i_{L,i}(\tau_{i2}) > 0$	$ i_{L,i}(\tau_{i2}) \geq \sqrt{-2 \frac{C_{oss} V_i^2}{L_{th,i}} + 4 \frac{C_{oss} V_{th,i}(\tau_{i2}) V_i}{L_{th,i}}}$	$t_{di2,min} = \frac{1}{w_r} \left(\arccos \left(-\frac{V_{th,i}(\tau_{i2})}{(V_i - V_{th,i}(\tau_{i2}))} \cos \left(\arctan \frac{A_{i2}}{B_{i2}} \right) \right) - \arctan \frac{A_{i2}}{B_{i2}} \right)$
$\alpha_i = 0$	$i_{L,i}(\tau_{i1}) < 0$	$ i_{L,i}(\tau_{i1}) \geq 2 \sqrt{-\frac{C_{oss} V_{th,i}(\tau_{i1}) V_i}{L_{th,i}}}$	$t_{di1,min} = \frac{1}{w_r} \left(\arccos \left(\frac{(V_i - V_{th,i}(\tau_{i1}))}{(-V_i - V_{th,i}(\tau_{i1}))} \cos \left(\arctan \frac{A_{i1}}{B_{i1}} \right) \right) - \arctan \frac{A_{i1}}{B_{i1}} \right)$

In summary, ZVS occurs when the three conditions on the AC current and the dead time are simultaneously satisfied. Conversely, hard switching arises if the current direction criterion is not fulfilled as the voltage of the switch being turned on will not drop, and its parasitic capacitance will remain fully charged during the switching instant. Therefore, its energy will not be used to charge the C_{oss} of the switch being turned off during the same switching instant. Consequently, after the switching instant, the discharge will take place in $R_{DS,on}$, causing additional losses in the system. Moreover, the voltage source will charge the C_{oss} of the turning off switch, further contributing to the losses.

If the current direction condition holds, but either the current value or the dead time value falls below their minimum required value for soft switching, "an incomplete ZVS" will occur.

If a switch at a port #i undergoes an incomplete ZVS when it is switched on, its parasitic capacitance C_{oss} will not be fully discharged and a voltage ΔV will remain in it at the end of the switching instant. Likewise, its complementary switch's C_{oss} will not charge to completion during its turning off, and its final remaining voltage will be $(V_i - \Delta V)$ instead of V_i . Consequently, the remaining charge will be drawn from the source, resulting in additional system losses [52].

Considering the scenario where the direction condition and the minimum value condition of the AC current $i_{L,i}$ are both satisfied, but the selected dead time t_{di} is smaller than its minimum required value $t_{di,min}$, the parasitic capacitances of the switches will not have enough time to charge or discharge completely. In this case, the remaining voltage ΔV can be calculated as follows:

a) Case 1: port #i with $\alpha_i > 0$

i. Switching instant τ_{i1}

At the end of the dead time t_{di1} , where $0 < t_{di1} < t_{di1,min}$ in this case, we can write:

$$v_x(t_{di1}) = V_i - \Delta V \quad (2.42)$$

From equations (2.12) and (2.42), we deduce the following:

$$\begin{aligned} v_x(t_{di1}) - V_{th,i}(t_{di1}) &= V_i - \Delta V - V_{th,i}(\tau_{i1}) \\ &= L_{th,i}(-A_{i1} w_r \sin(w_r t_{di1}) + B_{i1} w_r \cos(w_r t_{di1})) \end{aligned}$$

Therefore,

$$\Delta V = V_i - V_{th,i}(\tau_{i1}) - L_{th,i}(-A_{i1} w_r \sin(w_r t_{di1}) + B_{i1} w_r \cos(w_r t_{di1})) \quad (2.43)$$

ii. *Switching instant τ_{i2}*

At the end of the dead time t_{di2} , where $0 < t_{di2} < t_{di2,min}$ in this case, we can write:

$$v_x(t_{di2}) = V_i - \Delta V \quad (2.44)$$

From equations (2.24) and (2.44), we deduce the following:

$$\begin{aligned} V_i - v_x(t_{di2}) - V_{th,i}(t_{di2}) &= \Delta V - V_{th,i}(\tau_{i2}) \\ &= L_{th,i}(-A_{i2} w_r \sin(w_r t_{di2}) + B_{i2} w_r \cos(w_r t_{di2})) \end{aligned}$$

Therefore,

$$\Delta V = V_{th,i}(\tau_{i2}) + L_{th,i}(-A_{i2} w_r \sin(w_r t_{di2}) + B_{i2} w_r \cos(w_r t_{di2})) \quad (2.45)$$

b) *Case 2: port #i with $\alpha_i = 0$*

i. *Switching instant τ_{i1}*

At the end of the dead time t_{di1} , where $0 < t_{di1} < t_{di1,min}$ in this case, we can write:

$$v_{x1}(t_{di1}) = V_i - \Delta V \quad (2.46)$$

$$v_{x2}(t_{di1}) = \Delta V \quad (2.47)$$

From equations (2.35), (2.46) and (2.47), we deduce the following:

$$\begin{aligned} v_{x1}(t_{di1}) - v_{x2}(t_{di1}) - V_{th,i}(t_{di1}) &= V_i - 2 \cdot \Delta V - V_{th,i}(\tau_{i1}) \\ &= L_{th,i}(-A_{i1} w_r \sin(w_r t_{di1}) + B_{i1} w_r \cos(w_r t_{di1})) \end{aligned}$$

Therefore,

$$\begin{aligned} \Delta V &= \frac{1}{2} \cdot [V_i - V_{th,i}(t_{di1}) \\ &\quad - L_{th,i}(-A_{i1} w_r \sin(w_r t_{di1}) + B_{i1} w_r \cos(w_r t_{di1}))] \end{aligned} \quad (2.48)$$

The other scenario to consider is where only the current direction condition is satisfied. In this case, the energy stored in the port's inductance is not sufficient to completely discharge or charge the parasitic capacitances of the switches. However, since the current is in the right direction, a partial charge/discharge will take place in these capacitances and, as explained before, an incomplete ZVS will occur. In this case, the remaining voltage ΔV in the capacitances can be calculated as follows:

a) *Case 1: port #i with $\alpha_i > 0$*

i. *Switching instant τ_{i1}*

To minimize losses in this scenario, it is best to end the dead time at the instant when all the energy stored in the inductance is used to partially charge and discharge the parasitic capacitances. This means that the voltage ΔV would be equal to its minimum possible value in this scenario, and v_x will be closest to V_i . In other words, the dead time t_{di1} should be set to the time instant t_{0i1} where the current $i_{L,i}$ reaches zero, as shown in Figure 2.11.

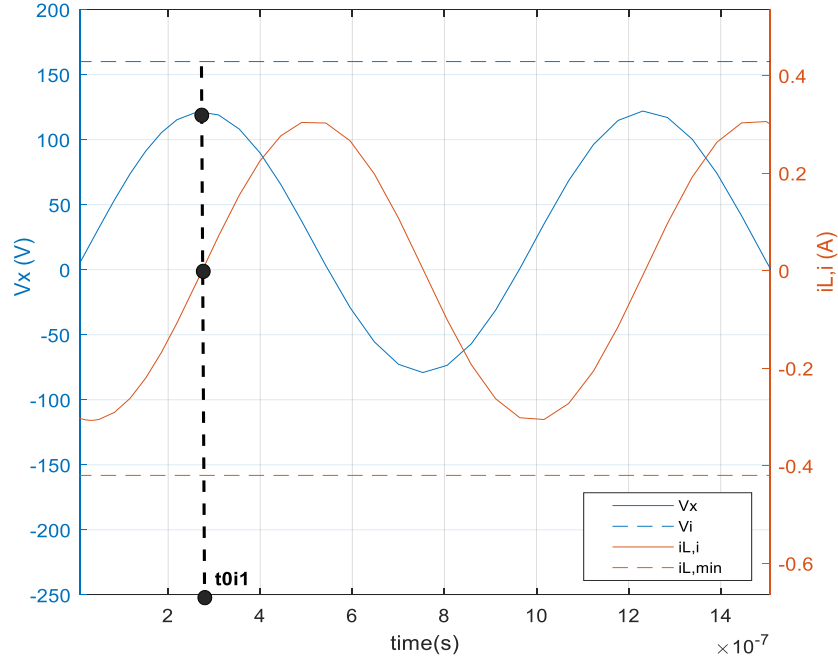


Figure 2.11: Port current $i_{L,i}$ and voltage v_x waveforms during the dead time of switching instant τ_{i1} when $\alpha_i > 0$, considering that $i_{L,i}$ is smaller than its minimum required value for a ZVS at the beginning of τ_{i1} .

Therefore, we can write:

$$i_{L,i}(t_{0i1}) = 0 \quad (2.49)$$

$$t_{di1} = t_{0i1} \quad (2.50)$$

From (2.15) and (2.49), we can deduce the value of t_{0i1} as following:

$$t_{0i1} = \frac{1}{w_r} \left[\arctan\left(-\frac{A_{i1}}{B_{i1}}\right) + \pi \right] \quad (2.51)$$

Therefore, if the equality (2.50) is satisfied, ΔV will have the following expression:

$$\Delta V = V_i - V_{th,i}(\tau_{i1}) - L_{th,i}(-A_{i1} w_r \sin(w_r t_{0i1}) + B_{i1} w_r \cos(w_r t_{0i1})) \quad (2.52)$$

However, if the selected dead time t_{di1} is smaller than t_{0i1} ($0 \leq t_{di1} < t_{0i1}$), voltage ΔV will have a larger value, resulting in more losses and it is calculated using expression (2.43).

Otherwise, if the selected dead time t_{di1} is greater than t_{0i1} , the current $i_{L,i}$ may become positive, which may lead to hard switching where $\Delta V = V_i$.

ii. *Switching instant τ_{i2}*

In this case, the dead time t_{di2} should be set to the time instant t_{0i2} where the current $i_{L,i}$ reaches zero in order to minimize the value of ΔV as much as possible. Therefore, we can write:

$$i_{L,i}(t_{0i2}) = 0 \quad (2.53)$$

$$t_{di2} = t_{0i2} \quad (2.54)$$

From (2.27) and (2.53), we can deduce the value of t_{0i2} as following:

$$t_{0i2} = \frac{1}{w_r} \left[\arctan\left(-\frac{A_{i2}}{B_{i2}}\right) + \pi \right] \quad (2.55)$$

Therefore, if the equality (2.54) is satisfied, ΔV will have the following expression:

$$\Delta V = V_{th,i}(\tau_{i2}) + L_{th,i}(-A_{i2} w_r \sin(w_r t_{0i2}) + B_{i2} w_r \cos(w_r t_{0i2})) \quad (2.56)$$

However, if the selected dead time t_{di2} is smaller than t_{0i2} ($0 \leq t_{di2} < t_{0i2}$), voltage ΔV is calculated using expression (2.45).

Otherwise, if the selected dead time t_{di2} is greater than t_{0i2} , the current $i_{L,i}$ may become negative, which may lead to hard switching where $\Delta V = V_i$.

b) *Case 2: port #i with $\alpha_i = 0$*

i. *Switching instant τ_{i1}*

In this case, the dead time t_{di1} should be set to the time instant t_{0i1} where the current $i_{L,i}$ reaches zero in order to minimize the value of ΔV as much as possible.

Therefore, we can write:

$$i_{L,i}(t_{0i1}) = 0 \quad (2.57)$$

$$t_{di1} = t_{0i1} \quad (2.58)$$

From (2.38) and (2.57), we can deduce the value of t_{0i1} as following:

$$t_{0i1} = \frac{1}{w_r} \left[\arctan\left(-\frac{A_{i1}}{B_{i1}}\right) + \pi \right] \quad (2.59)$$

Therefore, if the equality (2.58) is satisfied, ΔV will have the following expression:

$$\Delta V = \frac{1}{2} \left[V_i - V_{th,i}(t_{di1}) - L_{th,i}(-A_{i1} w_r \sin(w_r t_{0i1}) + B_{i1} w_r \cos(w_r t_{0i1})) \right] \quad (2.60)$$

However, if the selected dead time t_{di1} is smaller than t_{0i1} ($0 \leq t_{di1} < t_{0i1}$), voltage ΔV is using expression (2.48).

Otherwise, if the selected dead time t_{di1} is greater than t_{0i1} , the current $i_{L,i}$ may become positive, which may lead to hard switching where $\Delta V = V_i$.

At the end of a switching instant, the final voltage value of the C_{oss} of the switch that is being turned on can be expressed as follows:

$$V_{C_{oss},final}(t) = \begin{cases} 0 & \text{if ZVS occurs} \\ V_i & \text{if hard switching occurs} \\ \Delta V & \text{if incomplete ZVS occurs} \end{cases} \quad (2.61)$$

From this section, it can be concluded that one way to ensure ZVS and reduce the switching losses of the MAB converter is to continuously adjust the selected dead time at each operating point and at the different switching instants of the different ports. Although this technique would enhance the MAB's performance from different points of view (efficiency, EMC...), it is practically challenging to apply. This thesis considers a fixed dead time at all operating points. Future research could investigate the theory presented in this section and develop a control algorithm that continuously adjusts the dead time values to maximize the number of soft switching events at any operating point in a MAB converter.

2.4.2. Calculation of the Switching Losses

The switching cycle of a switch is shown in Figure 2.12. When a switch is turned on, its drain-to-source current i_{DS} starts increasing from zero until it reaches its final value I_D . Then, the

drain-to-source voltage starts dropping from its open state value V_D to zero. During this interval of time t_{ON} , switching losses take place. Then, when the switch is ON and it is conducting power, conduction losses occur. After that, when the switch is turned off, its drain-to-source voltage starts increasing from zero until it reaches its final value V_D . Then, the drain-to-source current starts dropping from I_D to zero. During this interval of time t_{OFF} , switching losses also take place. ZVS occurs if $V_D = 0$ and ZCS (Zero Current Switching) occurs if $I_D = 0$ during the switching event.

The areas of the power curve shown in Figure 2.12 represent the energy dissipated during turn on (E_{ON}) and turn off (E_{OFF}). The switching losses during the turn on and turn off of one switch would therefore be [53]:

$$P_{ON} = E_{ON} \times f_s = \frac{V_D I_D}{2} \times t_{ON} \times f_s \quad (2.62)$$

$$P_{OFF} = E_{OFF} \times f_s = \frac{V_D I_D}{2} \times t_{OFF} \times f_s \quad (2.63)$$

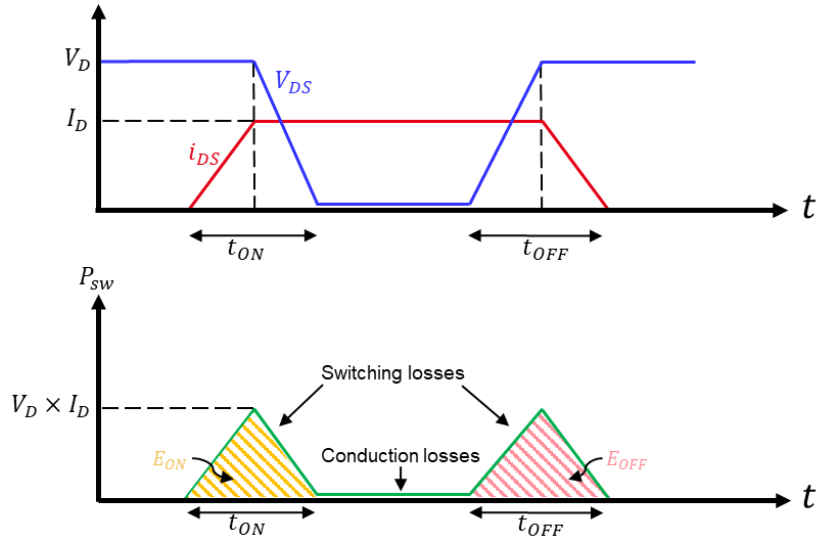


Figure 2.12: Switching cycle and associated losses of a switch.

For a port #i, we consider a function ZVS_{ik} to evaluate the fulfilment of the ZVS requirements at a switching instant τ_{ik} as outlined in Table 2.2, such that:

$$ZVS_{ik} = \begin{cases} 1 & \text{if all three conditions at } \tau_{ik} \text{ are satisfied} \\ 0 & \text{otherwise} \end{cases} \quad (2.64)$$

A switch turned on with ZVS is considered to have zero turn on switching losses ($P_{ON} = 0$).

Additionally, the power loss caused by the charge/discharge of the parasitic capacitance of a switch at the end of its switching instant is calculated as follows, using expression (2.61):

$$P_{C_{oss}}(t) = \frac{1}{2} C_{oss} V^2 c_{oss,final}(t) \cdot f_s \quad (2.65)$$

When $\alpha_i > 0$, one switch is turned on and another switch is turned off at each switching instant (τ_{i1} and τ_{i2}). Therefore, during a switching period T_s , the switching losses of a port #i are calculated as follows in this case, using expressions (2.62) to (2.65):

$$\begin{aligned}
 P_{sw,i} &= 2. [P_{ON}(\tau_{i1}) + P_{OFF}(\tau_{i1}) + P_{ON}(\tau_{i2}) + P_{OFF}(\tau_{i2})] + 2P_{C_{oss}}(\tau_{i1}) \\
 &\quad + 2P_{C_{oss}}(\tau_{i2}) \\
 &= V_D(\tau_{i1})I_D(\tau_{i1})f_s[t_{ON}(1 - ZVS_{i1}) + t_{OFF}] \\
 &\quad + V_D(\tau_{i2})I_D(\tau_{i2})f_s[t_{ON}(1 - ZVS_{i2}) + t_{OFF}] + 2P_{C_{oss}}(\tau_{i1}) \\
 &\quad + 2P_{C_{oss}}(\tau_{i2})
 \end{aligned} \tag{2.66}$$

Where:

$$\begin{aligned}
 V_D(\tau_{ik}) &= V_i \\
 I_D(\tau_{ik}) &= |i_{L,i}(\tau_{ik})|
 \end{aligned}$$

When $\alpha_i = 0$, the switching losses of port #i are calculated as follows:

$$\begin{aligned}
 P_{sw,i} &= 2. [2P_{ON}(\tau_{i1}) + 2P_{OFF}(\tau_{i1})] + 4P_{C_{oss}}(\tau_{i1}) \\
 &= 2V_D(\tau_{i1})I_D(\tau_{i1})f_s[t_{ON}(1 - ZVS_{i1}) + t_{OFF}] + 4P_{C_{oss}}(\tau_{i1})
 \end{aligned} \tag{2.67}$$

2.5. Efficiency Optimization

2.5.1. Minimization of the Exchanged Reactive Power

From the first harmonic approximation steady state model of a MAB converter that was developed in Chapter 1 Section 1.3.1, the reactive power flowing out of a port #i and towards a port #j is given by expression (1.14), which is:

$$Q_{ij} = \frac{8}{\pi^2} \frac{V_i}{L_{ij}\omega_s} \cos\left(\frac{\alpha_i}{2}\right) \left(V_i \cos\left(\frac{\alpha_i}{2}\right) - \frac{V_j}{n_{ij}} \cos\left(\frac{\alpha_j}{2}\right) \cos(\varphi_{ij}) \right) \tag{2.68}$$

Consequently, the expression of the reactive power flowing out of port #j and towards port #i can be deduced as the following (Figure 2.13):

$$Q_{ji} = \frac{8}{\pi^2} \frac{V_j}{L_{ij}\omega_s} \cos\left(\frac{\alpha_j}{2}\right) \left(V_j \cos\left(\frac{\alpha_j}{2}\right) - \frac{V_i}{n_{ji}} \cos\left(\frac{\alpha_i}{2}\right) \cos(\varphi_{ij}) \right) \tag{2.69}$$

Generally, the first harmonic component of each AC signal in the transformer is dominant. This is because the amplitude of each harmonic is inversely proportional to its order k . Therefore, for the sake of simplicity, only fundamental components are considered for the minimization of the exchanged reactive power.

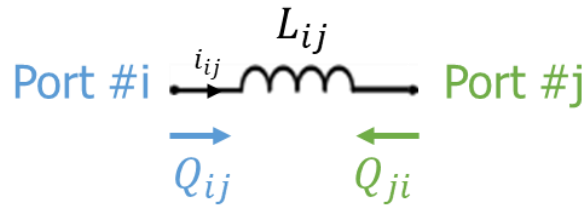


Figure 2.13: Reactive power flow between port #i and port #j, as considered in expressions (2.68) and (2.69).

The magnetizing inductance is neglected in this study since its value is significantly greater than the series inductance value. The series inductances at the transformer level of the MAB converter are the main reactive power consumers [9]. Therefore, from Figure 2.13, we can write:

$$Q_{ij} + Q_{ji} = L_{ij}\omega_s i_{ij}^2 \quad (2.70)$$

From equations (2.68) and (2.69) of the first harmonic approximation model, the reactive power exchange between port #i and port #j can be expressed as follows [9]:

$$Q_{ij} - Q_{ji} = \frac{8}{\pi^2 L_{ij} \omega_s} \left[\left(\frac{V_i}{n_{1i}} \right)^2 \cos^2 \left(\frac{\alpha_i}{2} \right) - \left(\frac{V_j}{n_{1j}} \right)^2 \cos^2 \left(\frac{\alpha_j}{2} \right) \right] \quad (2.71)$$

If the reactive powers Q_{ij} and Q_{ji} of these two ports are equal, both ports will supply the same amount of reactive power to the link inductance and no power exchange will occur between them. Otherwise, one of the ports will provide more power than the other and the port that provides less may even absorb some reactive power.

When reactive power is exchanged between ports, the circulating currents increase and so do the losses of the system. Therefore, minimizing the reactive power exchange between ports will increase the system's efficiency at some operating points, especially at light loads. This is due to the fact that the reactive power's ratio from the total apparent power is higher when the active power is low.

From equation (2.71), we can deduce that eliminating the reactive power exchange between ports can be done by achieving the following equality:

$$\frac{V_i}{n_{1i}} \cos \left(\frac{\alpha_i}{2} \right) = \frac{V_j}{n_{1j}} \cos \left(\frac{\alpha_j}{2} \right) \quad (2.72)$$

Completing this equality also means that the RMS values of the AC voltages' first harmonics of ports #i and #j are made equal. This could be interesting when voltage mismatches occur, as it compensates for the DC links' voltage variations and it could help re-establish the soft switching that can be lost due to these mismatches.

A reference port is chosen for the internal phase shift values. Consequently, the internal phase shifts of all the other ports can be calculated based on the reference port's chosen internal phase shift value, using (2.72), as follows:

$$\alpha_i = 2 \arccos \left(\frac{V_r'}{V_i'} \cos \left(\frac{\alpha_r}{2} \right) \right) \quad (2.73)$$

Where port #r is the chosen reference port for the internal phase shift values and port #i is any other port of the MAB converter. The internal phase shift values cannot be negative or greater than π (rad) ($0 \leq \alpha_i < \pi$ rad $\forall i \in [1, n]$). For simplicity, port #r can be the same reference port chosen for the external phase shifts ($\varphi_r = 0$). As mentioned previously, port #1 is the chosen reference port.

By using this method to minimize the reactive power exchange, the number of control degrees of freedom of the MAB will be reduced from $(2n - 1)$ to (n) , n being the total number of ports. The remaining control parameters will be the $(n - 1)$ external phase shifts of the non-reference ports and the internal phase shift of the reference port. This will simplify solving the optimization problem aiming to minimize the total losses of the MAB converter. In this proposed Multiple Phase Shift (MPS) modulation technique, the external phase shifts φ_i will be used for the active power flow control and the internal phase shift α_1 of the reference port is used for the loss minimization.

2.5.2. Minimization of Total System Losses

In this thesis, the total system losses of the MAB converter are considered equal to the sum of the conduction losses and the switching losses of all its ports. As a first approximation, other losses such as iron losses in the transformer and the series inductances are neglected. Therefore, from expressions (2.1), (2.66) and (2.67), we can write:

$$P_{total\ losses} = \sum_{i=1}^n P_{cond,i} + \sum_{i=1}^n P_{sw,i} \quad (2.74)$$

n is the total number of ports.

In order to choose the optimal value of the reference internal phase shift α_1 using the proposed MPS modulation technique at a certain operating point, a mathematical sweep of this parameter between 0 and $\pi(rad)$ is completed using the GHA model developed in Chapter 1. For each value of α_1 in this sweep, the internal phase shifts α_i of the remaining ports are calculated using (2.73) and their external phase shifts φ_i are calculated using (1.22), where P_i is equal to the desired power at a port # i . The total number of switches operating at ZVS and total system losses are then calculated using the loss model developed in the previous sections of this chapter, along with expression (2.74).

An example of the percentage accuracy of the GHA model in calculating the RMS AC currents as a function of the harmonic order k for a MAB converter is shown in Figure 2.14. The value of k is a positive odd integer. It can be seen that the consideration of harmonics 1 to 7 is sufficient to obtain an accurate prediction of the RMS current without adding unnecessary computational burden to the control of the system. Therefore, in this thesis, a harmonic order of $k = 7$ is considered for the calculation of the conduction losses.

The instantaneous values of the AC currents are required to calculate the ZVS criteria and the switching losses developed in Section 2.4. Therefore, in contrast to the RMS current value, more accuracy is required, so a higher order of harmonics is taken into account. A harmonic order of $k = 101$ is considered in this thesis for an accurate evaluation of the ZVS criteria and calculation of the switching losses.

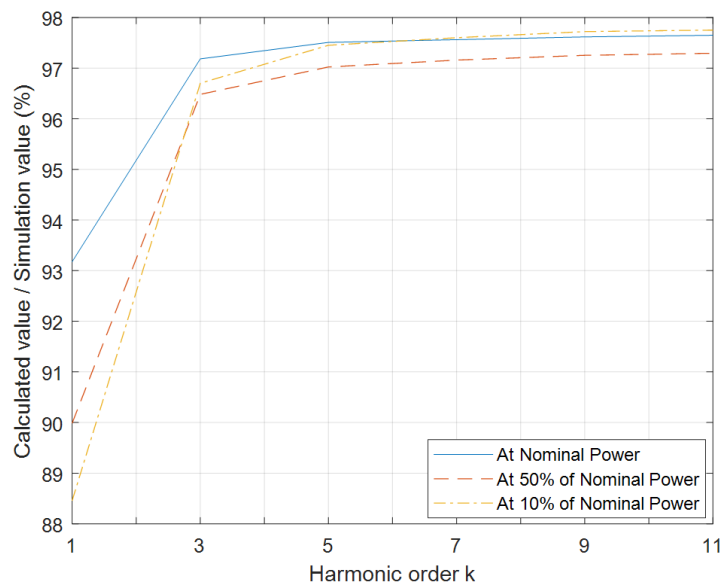


Figure 2.14: Accuracy percentage of the calculated total RMS current in a QAB converter using the developed GHA model and the proposed MPS modulation for $\alpha_1 = 1.5$ in function of the considered order of harmonics.

Figure 2.15, Figure 2.16 and Figure 2.17 display the results of the mathematical sweep of α_1 when applying the proposed MPS modulation technique on a four-port $4 \times 500W$ MAB converter, also known as a QAB converter. The parameters of this QAB converter are shown in Table 2.3. A maximum distortion of $\pm 20\%$ is considered at the DC voltage source of each port ($V_1 + 10\%$, $V_2 - 10\%$, $V_3 + 20\%$, $V_4 - 20\%$).

In Figure 2.15, the considered QAB converter is operating at 60% of its nominal power ($4 \times 300W$). The converter has 16 switches in total, with 4 switches at each port. When using EPS modulation under the same operating conditions, the total system losses would be $17W$ and the total number of switches with ZVS would be 8. When using the proposed modulation technique, the worst-case scenario (shown in Figure 2.15 at $\alpha_1 = 0$) exhibits better performance, with a total loss of $13W$ and the same number of switches with ZVS. At $\alpha_1 = 1.4$, ZVS is achieved on all 16 of the system's switches and the losses are reduced to $9W$, almost dividing them by two compared to EPS modulation. At $\alpha_1 = 1.8$, the total losses are further reduced to $7.85W$, but ZVS is lost again on several switches, leading to a total of 12 switches with ZVS. The selection of the optimal operating point for the QAB converter should be based on the priorities of the application. If the priority is to achieve ZVS on all switches while reducing the total losses as much as possible, then $\alpha_1 = 1.4$ should be applied. On the other hand, if the priority is to maximize the overall efficiency of the QAB converter, then $\alpha_1 = 1.8$ should be applied. Figure 2.15.c displays the distribution of the total losses between conduction and switching losses. Figure 2.15.d illustrates the RMS current values at each port as a function of α_1 .

Figure 2.16 and Figure 2.17 display the percentage of the total losses of the considered QAB converter and the total number of switches with ZVS when the proposed MPS modulation is applied compared to the conventional EPS modulation at various power levels. The presence of local minima in the total loss curves is caused by the saturation of certain internal phase shifts of the non-reference ports at zero. Theoretically, these values cannot be negative or greater than π in radians. Practically, the internal phase shifts will never reach their maximum limit of π since it results in a zero AC voltage at the corresponding port. Therefore, when an internal phase shift saturates, its minimum limit of zero is the one in question. Additionally, the existence of local minima demonstrates that a Perturb and Observe algorithm cannot achieve optimal operation that minimizes total system losses, as it will terminate the sweep at the first local minimum it encounters.

In Figure 2.15, Figure 2.16 and Figure 2.17, the sweep automatically stops when at least one of the calculated external phase shifts reaches its maximum allowed value of 37° for all ports. This maximum external phase shift value is a result of the hardware oversizing that was explained in Chapter 1, Section 1.3.1. Additionally, setting this limit to the external phase shifts will maintain the validity of the $\sin\varphi_{ij} \approx \varphi_{ij}$ approximation and reduce the computational burden by linearizing the GHA model.

Figure 2.16 shows that using the proposed MPS modulation reduces total system losses compared to the classical EPS modulation, particularly at low loads. Furthermore, for each operating point, there exists one value of α_1 where these losses reach a global minimum. The values of the control parameters at this point are considered optimal if the system's control objective is to reduce the total system losses as much as possible, regardless of the number of switches with ZVS in this case.

When the proposed MPS modulation is applied, the decrease in the total losses becomes more important as the operating point power decreases. For instance, in the case presented in Figure 2.16, when the QAB converter operates at 10% of its nominal power, the total system losses are decreased by 90% at the global minimum point, compared to when EPS modulation is applied. On the other hand, when the QAB is operating at 60% of its nominal power, the total system losses are reduced by approximately 53% at the global minimum point.

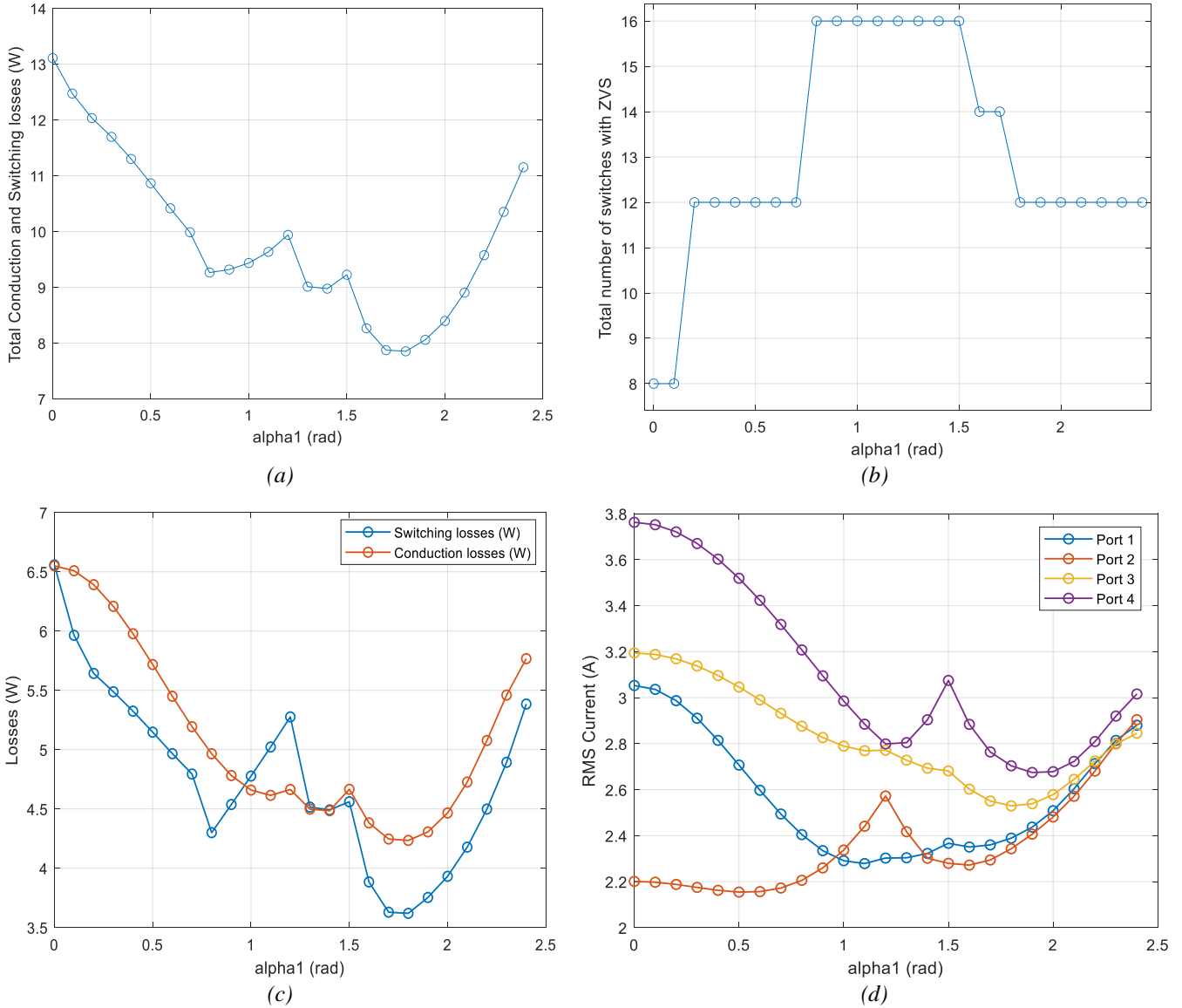


Figure 2.15: a) Total losses; b) total number of switches operating at ZVS; c) separated total conduction and total switching losses; d) Ports' RMS currents: as a function of the reference internal phase shift α_1 in a QAB converter using the proposed MPS modulation technique at 60% of nominal power and with a maximum of $\pm 20\%$ distortion on the DC voltage sources.

Furthermore, as demonstrated in Figure 2.17, the proposed MPS modulation also enables ZVS restoration at certain switches of the MAB converter. For the example depicted in Figure 2.17, the total number of switches with ZVS is doubled for specific values of α_1 ($1 \leq \alpha_1 \leq 1.4$ for all power values) in comparison to when EPS modulation is employed. As explained before, the equality established in equation (2.72) compensates for the voltage mismatches in the DC sources. These mismatches are the primary cause of soft switching loss, particularly at light

loads. In fact, the voltage mismatches cause a change in the AC current's sign before the switching instant, as illustrated in Figure 2.2, preventing the satisfaction of the ZVS criteria related to the current direction.

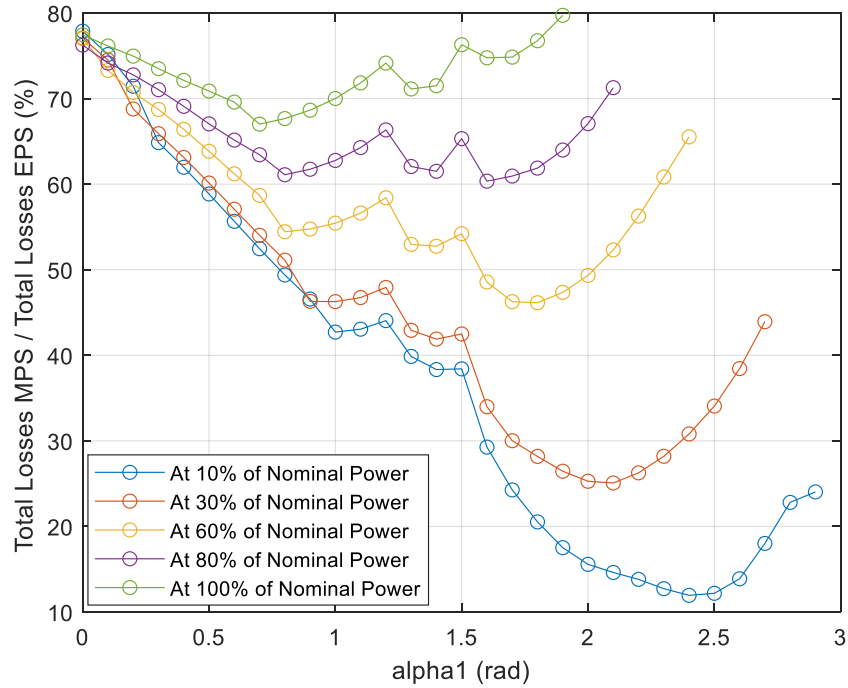


Figure 2.16: Total loss percentage of the proposed MPS modulation as a function of the reference internal phase shift α_1 compared to the conventional EPS modulation applied in a QAB converter at different power levels and with $\pm 20\%$ distortion on the DC voltage sources.

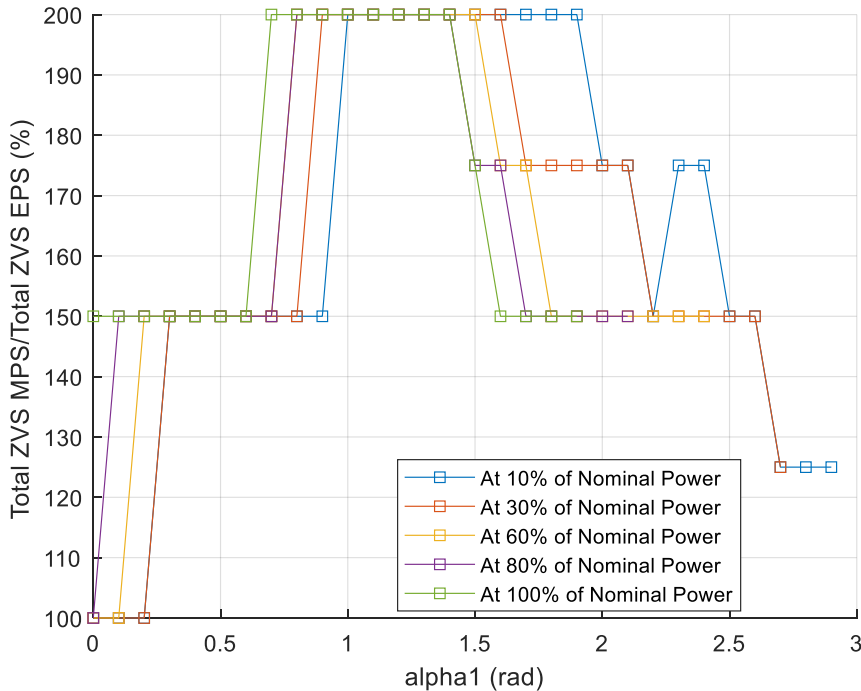


Figure 2.17: Total number of ZVS switches percentage of the proposed MPS modulation as a function of the reference internal phase shift α_1 compared to the conventional EPS modulation applied in a QAB converter at different power levels and with $\pm 20\%$ distortion on the DC voltage sources.

As the value of α_1 continues to increase, the total RMS currents flowing through the transformer may decrease, and so do the total losses. However, this may also result in the loss of ZVS again at some switches due to incomplete soft switching. In other words, as the RMS currents in the transformer decrease significantly, the circulating energy at some switching instants will not be sufficient to charge/discharge the parasitic capacitors of the switching switches, hence the incomplete ZVS.

Therefore, the optimal solution depends on the application and the user's preferences. If keeping the ZVS at all the MAB converter's switches is required, even if it leads to suboptimal efficiency, then the value of α_1 leading to the maximum number of switches operating at ZVS with minimum losses should be chosen. Otherwise, if the main optimization objective is to minimize the total system losses, even if it leads to losing the ZVS at some switches, then the value of α_1 corresponding to the global minimum of the loss curve should be retained.

We should note that the curves resulting from this sweep vary according to the parameters of the considered MAB converter (e.g. DC voltage values, power ratings, switching frequency, inductance values, DC voltage perturbations, components' parameters and sizing...). In some cases, applying the proposed MPS modulation could lead to more losses than applying the classical EPS modulation, especially when the MAB converter is operating close to its nominal power. In fact, reducing the RMS voltages of some ports by increasing their internal phase shifts is not always the best solution for reducing the system losses. At some operating points, even if the reactive power exchanged is reduced by applying this method, the total losses will increase. By applying the proposed MPS modulation around nominal power in some cases, the decrease of the RMS values of the ports' AC voltages may be compensated by an increase in the RMS values of the AC currents in order to provide the required average active powers to the ports. Therefore, in this case, the reduction in reactive power and its associated losses is counterbalanced by higher current values, thus increasing the final total amount of losses in the system. This is shown in Figure 2.18 for a QAB converter having different parameters than the one considered in the example of Figure 2.15 to Figure 2.17. The parameters of the two studied QAB converters are shown in Table 2.3. Consequently, using EPS modulation would be a better solution in this case. However, at light loads, where the amount of active power flowing through the system is low, a higher percentage of losses are usually caused by reactive power. Therefore, it would be interesting to reduce it and apply the proposed MPS modulation technique.

In Figure 2.18, the total RMS current in the transformer is calculated using the following expression:

$$I_{rms} = \sqrt{\sum_{i=1}^n I_{rms,i}^2} \quad (2.75)$$

Where $I_{rms,i}$ is the RMS current flowing in the transformer winding of port #i expressed in equation (2.2).

Another sweep example of α_1 is shown in Figure 2.19 where the proposed MPS modulation is applied to the QAB converter considered in Figure 2.18. As we can notice from Table 2.3, this QAB converter has different voltages and inductance values at each port and operates at higher power and much higher frequency. Therefore, its ZVS criteria are different and so are the resulting loss curves when MPS modulation is applied.

As it can be noticed, the proposed control method is only effective at low powers in this example. When close to nominal power, EPS modulation should be used as it results in fewer losses. Furthermore, in this case, the external phase shift values may become excessively large, leading to saturation and preventing the port active powers from converging to their desired values.

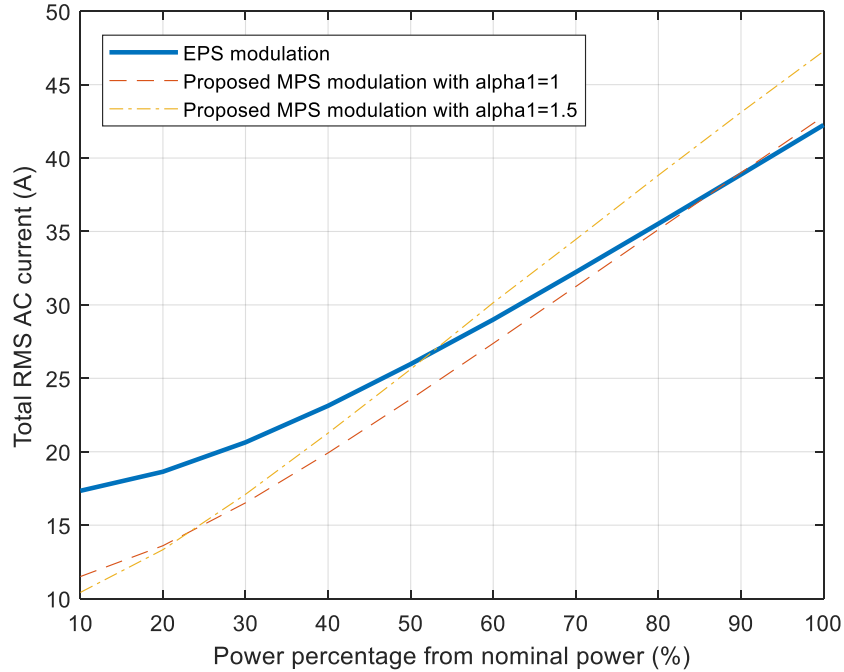


Figure 2.18: Total RMS current in the transformer windings of a MAB converter in function of the total power percentage from nominal power flowing through the system using the conventional EPS modulation and the proposed MPS modulation for two different values of the reference internal phase shift α_1 . A perturbation of $\pm 20\%$ is considered at the DC voltage source of each port.

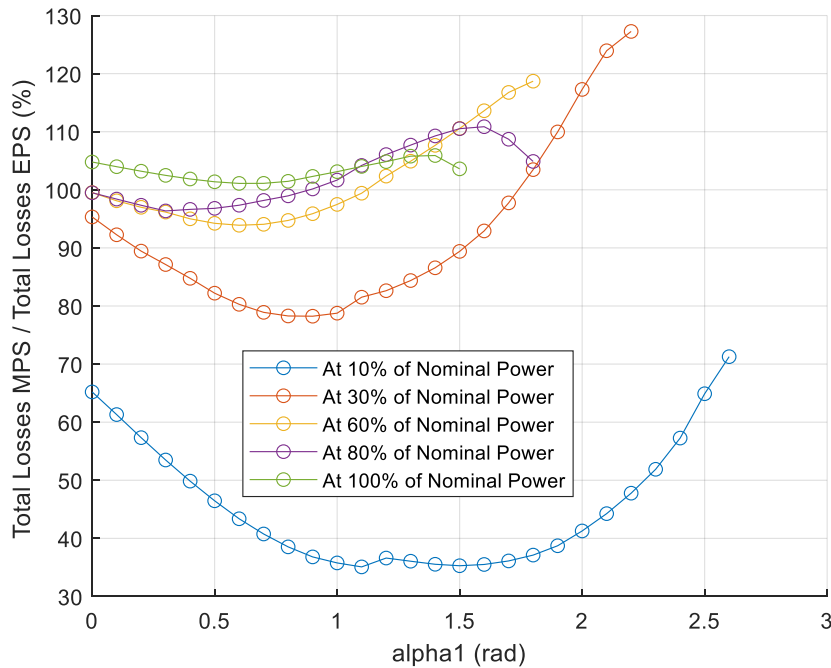


Figure 2.19: Total loss percentage of the proposed MPS modulation as a function of the reference internal phase shift α_1 compared to the conventional EPS modulation applied in a different QAB converter at different power levels and with $\pm 20\%$ distortion on the DC voltage sources.

Figure 2.18 and Figure 2.19 show that separating the operating points suitable for the proposed MPS modulation from those suitable for the EPS modulation can be challenging due to the dependence on the parameters of the considered MAB converter.

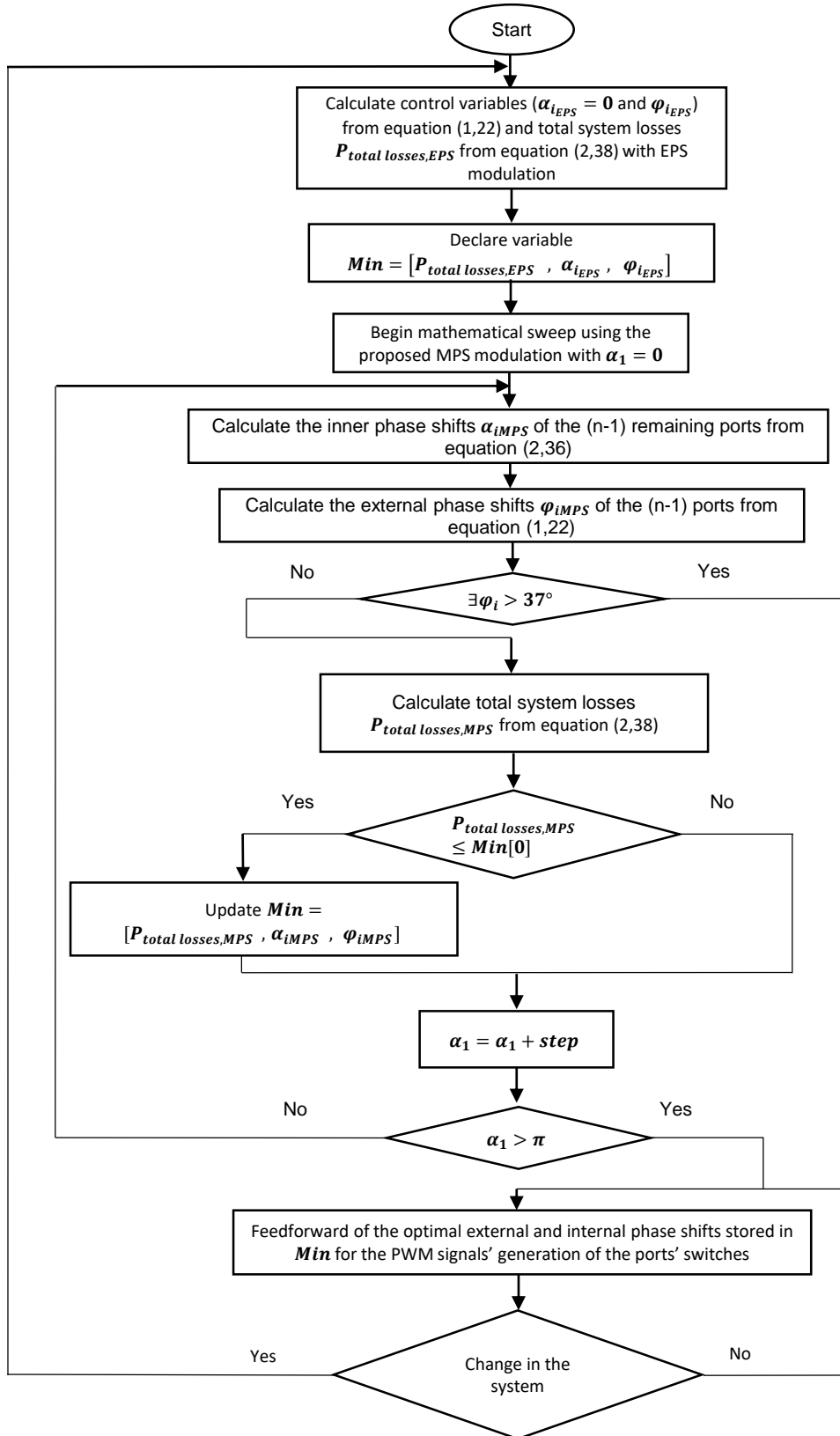
Table 2.3: Parameter values of the two considered QAB converters.

Parameter symbol	Parameter value for Figure 2.15, Figure 2.16 and Figure 2.17	Parameter value for Figure 2.18 and Figure 2.19
V_1	200 V	330 V
V_2	200 V	200 V
V_3	200 V	300 V
V_4	200 V	48 V
f_s	40 kHz	250 kHz
L_{12}	0.15 mH	31 μ H
L_{13}	0.15 mH	8 μ H
L_{14}	0.15 mH	94 μ H
L_{23}	0.15 mH	31 μ H
L_{24}	0.15 mH	94 μ H
L_{34}	0.15 mH	94 μ H
P_{nom}	500 W	6 kW

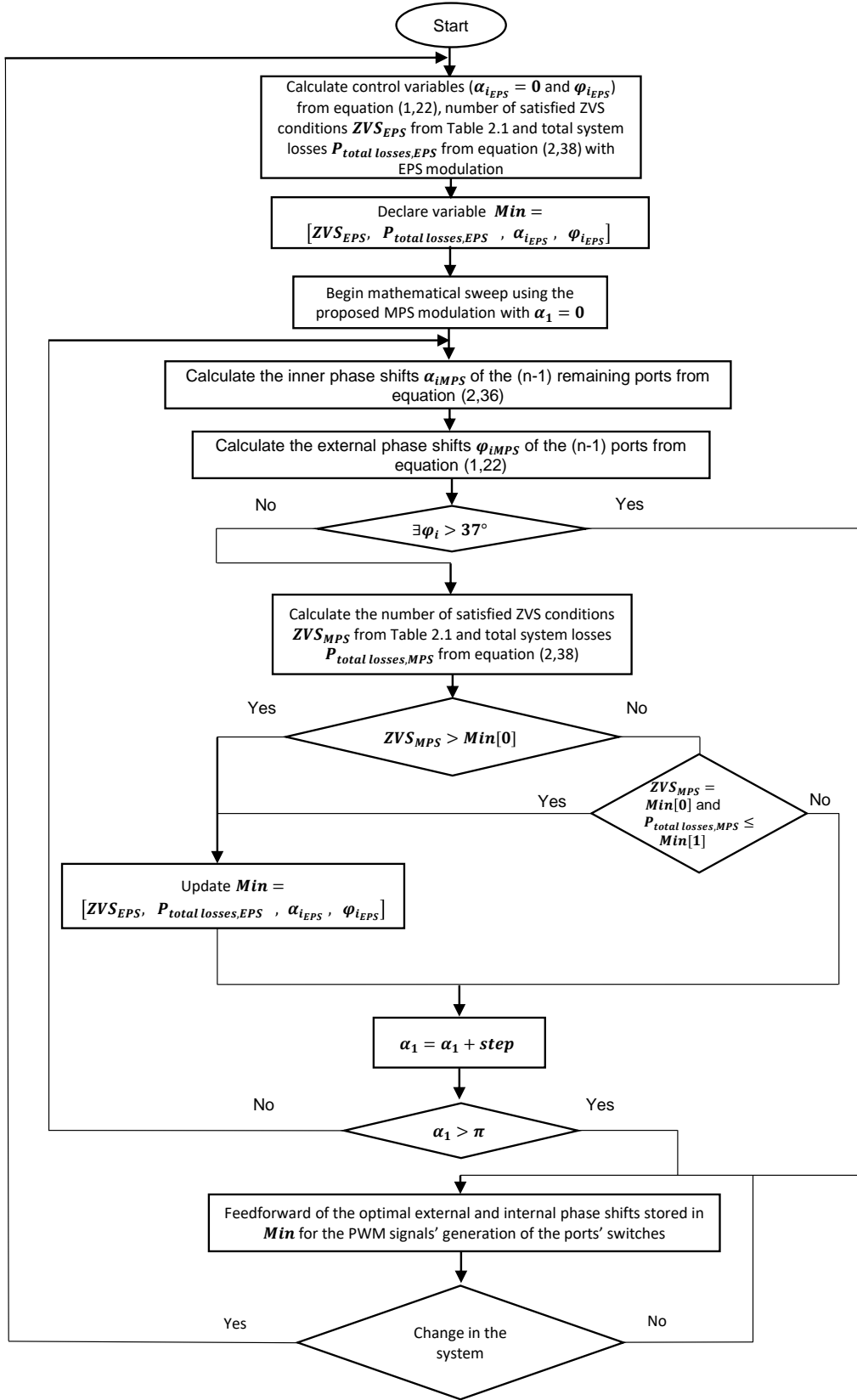
To address this issue, a solution would be to perform a mathematical sweep of α_1 for the considered QAB converter each time the operating point changes. This sweep enables the real-time prediction of the optimal control parameter values, given a change in the desired power value or the DC voltage on one or more ports. For this reason, an optimization algorithm is proposed in this thesis for the calculation of the optimal control parameters at each operating point change. Figure 2.20 shows the flow chart of this algorithm for the two cases mentioned previously: case (a) where the objective is minimizing the total system losses even if it leads to hard switching at certain switches; and case (b) where the objective is maximizing the total number of switches with ZVS while decreasing the total system losses, even if it leads to suboptimal system efficiency.

In both cases, the algorithm starts by calculating the external phase shifts that should be applied to the considered MAB converter if the EPS modulation is used at the given operating point. Then, the total system losses are calculated and stored for this modulation technique in case (a), and both the total losses and the total number of satisfied ZVS conditions are calculated and stored in case (b). After that, the algorithm performs the mathematical sweep of α_1 while applying the proposed MPS modulation technique. The results of the EPS modulation are then compared to those of the MPS modulation. Finally, the global optimal point is determined, along with its corresponding control parameter values, which are then fed forward to the PWM generation unit (Control Level 3). Adding a feedforward will also decouple the dynamic control of the different ports, as explained in Chapter 1, Section 1.3.3 (inverse matrix decoupling).

This optimization algorithm is executed once each time a relatively significant change occurs in at least one of the power references or voltage sources of the system.



(a)



(b)

Figure 2.20: Flow chart of the proposed optimization algorithm where the main objective is: (a) minimizing the total system losses at any cost; (b) maximizing the number of satisfied ZVS conditions while decreasing the system losses.

The optimization precision of the algorithm is determined by the sweep step of α_1 . Choosing a small value for this step brings the system closer to optimal behavior, increasing its precision. However, a smaller step also means that more values of α_1 must be evaluated during the sweep. This leads to more iterations, resulting in an increased calculation burden and longer total execution time of the algorithm. In this thesis, a step value of 0.1 is used as it provides a suitable balance between precision and execution time.

The GHA model's approximations and the considered harmonic order may cause a steady-state error in the ports' active power values if only an open-loop control (a feedforward) is used to control the MAB converter. Therefore, a feedback loop using a PI controller is added to the control of each port in order to correct the feed forward value of its external phase shift and cancel the steady state error of its active power value. These feedback loops will also control the dynamics of the system when the operating point changes or when disturbances occur. The complete block diagram of the MAB converter's proposed control system is given in Figure 2.21. The PI controllers' parameters are calculated using the first harmonic approximation of the developed dynamic model for simplicity reasons. Their calculation will be detailed in the next chapter.

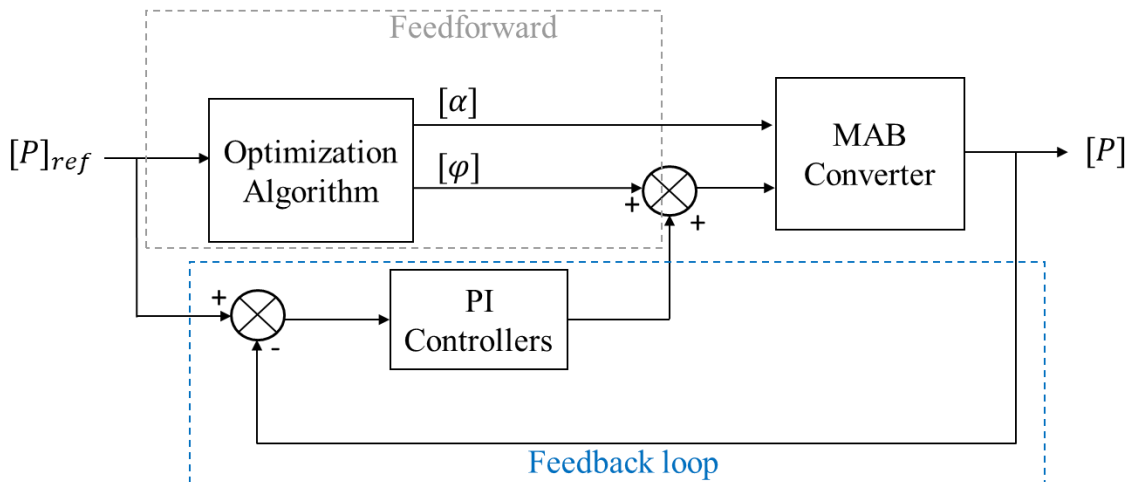


Figure 2.21: Block diagram of the proposed control system of a MAB converter.

2.6. Conclusion

The classical way to control the power transfer between a MAB converter's ports is by fixing a duty cycle to its AC voltages and varying the phase shifts between them. This method is called EPS modulation, and it is only efficient for certain operating points, especially at nominal power. In this chapter, a Multiple-Phase Shift (MPS) modulation technique is proposed, aiming to improve the efficiency of a MAB converter with n ports across its entire operating range. This technique uses the internal and external phase shifts of all the ports to reduce the amount of reactive power exchanged between them. The GHA model developed in the previous chapter for a generic MAB converter is used to predict the losses with different combinations of the control variables. An optimization algorithm is then employed to select the optimal combination, resulting in minimized system losses. This chapter details the calculation of conduction and switching losses of the MAB converter, which are the only types of losses considered in the optimization. In future works, other types of losses, such as iron losses in the transformer and inductances, could be added to this study to further improve its accuracy.

CHAPTER 3: EXPERIMENTAL RESULTS AND VALIDATION

3.1. Introduction

Chapters 1 and 2 of this thesis presented the theoretical study of a selected topology of an n -port MAB converter. Chapter 1 introduced the selected MAB topology and described the development of its mathematical model. Chapter 2 provided a detailed calculation of the conduction and switching losses for this topology and proposed a new control strategy to minimize these losses based on the mathematical model developed in Chapter 1.

To validate this theoretical part of the thesis, a MAB prototype consisting of four ports was built. The sizing method of this prototype is described in the first part of this chapter. After that, the experimental validation of the optimization algorithm proposed in Chapter 2 is presented.

The remaining part of this chapter discusses the potential presence of DC current bias in the converter's transformer, which may eventually lead to its saturation, causing overcurrent flow and temperature rise. This chapter provides a summary of the existing literature on this issue and proposes an active solution to address it through control. Additionally, experimental validation is presented.

3.2. QAB Converter Prototype Sizing

The chosen number of ports for the built MAB prototype is four, making it a Quadruple Active Bridge (QAB) converter. The selected nominal power level for this prototype is $500W$, allowing the QAB converter to transfer this power value to or from each port without exceeding the 37 -degree limit of the external phase shifts when EPS modulation is used.

For the sake of simplicity, a symmetrical QAB prototype was constructed, with all ports having identical nominal DC voltage values and power ratings. The nominal DC port voltage for all four ports is set at $200V$, with a maximum potential deviation of $\pm 20\%$ at each voltage. The switching frequency selected for this prototype is $40kHz$. The aim of this initial prototype is solely to validate the control strategies developed in this thesis for a MAB converter. In future works, another prototype, with higher power ratings and switching frequency, can be built to show the relevance of this work when employed in an industrial application.

To construct the four H-bridges of the QAB prototype, four standard Printed Circuit Boards (PCBs) that were available in the laboratory were used. These PCBs use $650V$ GaN switches with an integrated driver to perform the high-frequency DC-AC conversion between the DC voltage source and the transformer. As stated earlier, the only purpose of this prototype is to validate the control strategy proposed in this thesis. Therefore, the optimization of the hardware's components and volume is not a priority in this work.

The remaining components' sizing of this prototype is detailed in the subsequent parts of this section.

3.2.1. Series Inductances

The value of the transformer's series inductances determines the maximum power that can be transferred on each port. As explained in Chapter 1, the nominal converter power should be equal to 60% of its maximum possible power in order to limit the non-linear increase of the circulating reactive power. Therefore, the maximum possible transferrable power of this QAB prototype can be calculated as follows:

$$P_{max} = \frac{P_{nom}}{0.6} \quad (3.1)$$

Therefore, for a nominal power P_{nom} of 500W, the maximum power P_{max} would be 834W. The values of the link inductances are determined using the maximum power value P_{max} and the first harmonic approximation expression of the active power (1.15) from Chapter 1, considering that EPS modulation is employed ($\alpha_i = \alpha_j = 0$). If maximum power P_{max} flows between a port #i and a port #j of the QAB converter with EPS modulation, the external phase shift φ_{ij} between these ports would be equal to its maximum possible value, which is $\frac{\pi}{2}$ in radians. Therefore, expression (1.15) becomes:

$$P_{ij} = P_{max} = \frac{8}{\pi^2} \frac{V_i V_j}{n_{ij} L_{ij} \omega_s} \quad (3.2)$$

Consequently, the link inductances are calculated from expression (3.2) as following:

$$L_{ij} = \frac{8}{\pi^2} \frac{V_i V_j}{n_{ij} P_{max} \omega_s} \quad (3.3)$$

Where $\omega_s = 2\pi f_s$.

From expression (3.3) and the parameter values selected in the previous section, the link inductance L_{ij} between any two ports of the QAB prototype should be equal to 0.15mH. The series inductance at each port is then calculated from the delta-to-star equivalent circuit transformation as follows:

$$L_i = \frac{L_{ij}}{4} = 37\mu H$$

The leakage inductance value of each winding of the designed transformer should be less than or equal to this calculated value of L_i . If the leakage inductance of a winding is less than this value, an external inductance should be connected in series with that winding so that the sum of the leakage inductance and the external inductance equals 37 μH .

3.2.2. Multi-winding Transformer Design

A four-winding transformer was built to connect the four ports of the QAB prototype. From the Figure of Merit (FoM) shown in Figure 3.1, we deduce that the 3C90 ferrite material may be selected for the transformer's core since the chosen switching frequency of 40kHz falls within the operating frequency range of this material.

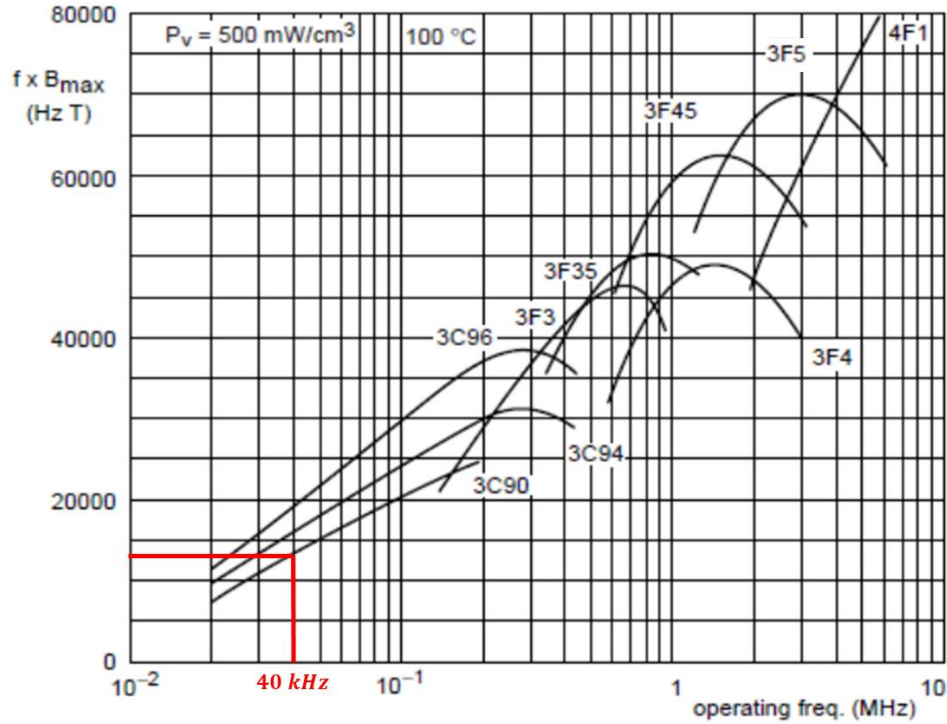


Figure 3.1: Ferrite material operating frequency ranges [54].

The dimensions of the transformer's magnetic core are illustrated in Figure 3.2. The winding area is denoted as W_a , whereas the effective area of the ferrite core is denoted as A_e . The effective area can be expressed as following:

$$A_e = \frac{\phi_{max}}{B_{max}} \quad (3.4)$$

Where ϕ_{max} is the maximum magnetic flux and B_{max} the maximum magnetic flux density reached in the transformer's magnetic core.

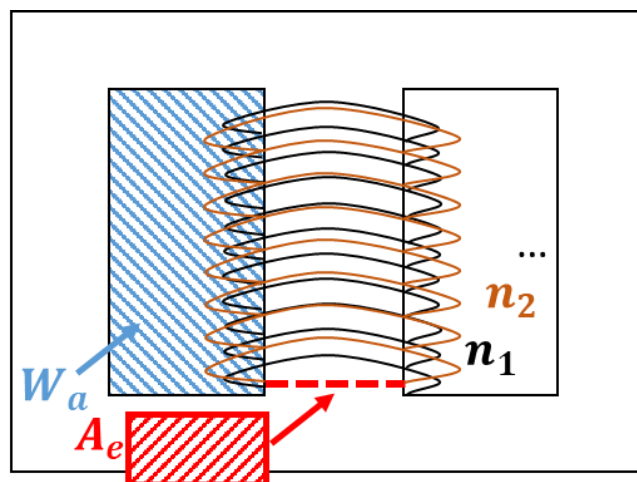


Figure 3.2: Magnetic core of the transformer.

Faraday's law of electromagnetic induction states that the magnetic flux variation can be expressed as follows [55]:

$$v_{ac,i} = n_i \frac{d\phi}{dt} \quad (3.5)$$

n_i is the number of winding turns at a port #i.

Figure 3.3 illustrates the magnetic flux variation in the transformer's core during a switching period. From Figure 3.3 and expression (3.5), we can deduce the following:

$$V_i = n_i \frac{\Delta\phi}{\Delta t} = n_i \frac{2\phi_{max}}{D_i T_s} \quad (3.6)$$

Where $T_s = \frac{1}{f_s}$ is the switching period and D_i is the duty cycle ratio of $v_{ac,i}$.

Therefore, by replacing ϕ_{max} by its expression from (3.6), equation (3.4) becomes:

$$A_e = \frac{V_i \cdot D_i}{2f_s n_i B_{max}} \quad (3.7)$$

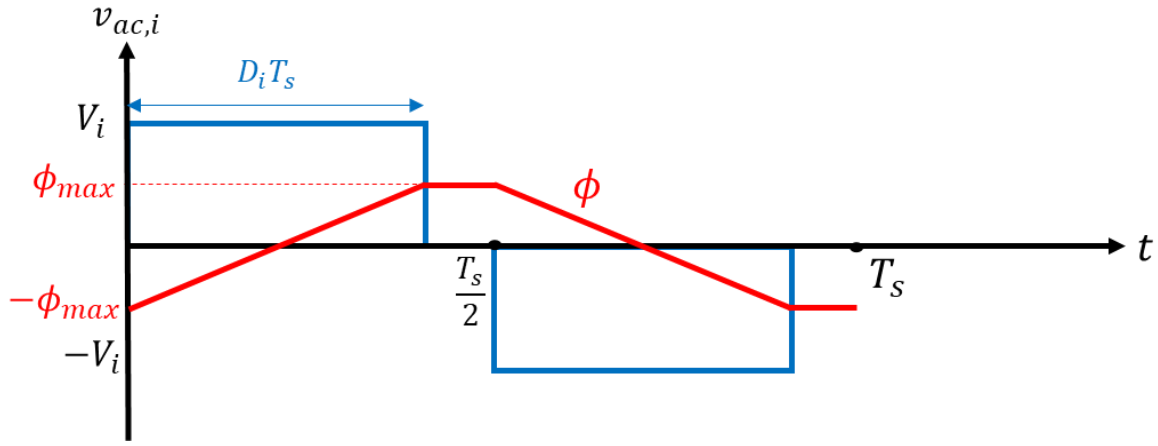


Figure 3.3: Magnetic flux variation in the magnetic core of the transformer during a switching period.

During the design of the transformer, it is important to consider the scenario where ϕ_{max} reaches its maximum possible value. Consequently, in this section, the AC voltage $v_{ac,i}$ is considered a two-level voltage with a duty cycle D_i equal to its maximum value of 0.5.

The winding area of the transformer's core should be able to contain the four windings of the four ports and can be expressed as following:

$$W_a = \sum_{i=1}^4 \frac{K_{W,i} n_i I_{RMS,i}}{J_i} \quad (3.8)$$

Where $K_{W,i}$ is the window space factor of winding #i, $I_{RMS,i}$ is the RMS current at winding #i and J_i is the current density of winding #i.

From equations (3.7) and (3.8), the product of the winding area and the effective area of the four-winding transformer can be deduced as following:

$$W_a \times A_e = \left(\frac{K_{W,1}}{J_1} + \frac{K_{W,2}}{J_2} + \frac{K_{W,3}}{J_3} + \frac{K_{W,4}}{J_4} \right) \cdot \frac{V_i I_{RMS,i}}{4f_s B_{max}} \quad (3.9)$$

From equation (3.9), we deduce that the transformer's size is directly proportional to the converter's power rating and inversely proportional to the switching frequency.

The considered parameter values to get the required area product of the QAB prototype's transformer are given in Table 3.1. The obtained value is $W_a \times A_e = 25\,000\text{ mm}^4$.

Table 3.1: Parameter values for the prototype's transformer design.

Parameter symbol	Parameter value
$K_{W,1} = K_{W,2} = K_{W,3} = K_{W,4}$	2
$J_1 = J_2 = J_3 = J_4$	5 A/mm^2
$V_i I_{RMS,i} = P_i$	500 W
B_{max}	0.2 T

The section of the wire that should be used to create the transformer windings is calculated as follows:

$$S_{Cu} = \frac{I_{RMS,i}}{J_i} = \frac{2.5}{5} = 0.5\text{ mm}^2 \quad (3.10)$$

Therefore, the diameter of the used wire should be $D_{Cu} = 0.8\text{ mm}$.

To evaluate the skin effect on the copper windings caused by the high-frequency alternating current, the skin depth is calculated as follows (Figure 3.4):

$$\delta = \sqrt{\frac{2\rho_{Cu}}{2\pi f_s \mu_{Cu}}} = 0.35\text{ mm} \quad (3.11)$$

Where $\rho_{Cu} = 2 \times 10^{-8}\Omega m$ is the resistivity of copper at 60°C and $\mu_{Cu} = 1.256629 \times 10^{-6}\text{ H/m}$ is the copper permeability.

Therefore, if a single-core copper wire with a diameter of 0.8 mm were used, the current would not be able to circulate on 12.5% of its diameter because of the skin effect. Therefore, Litz wires were used to create the four windings of the prototype transformer.

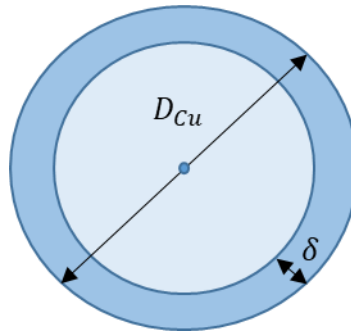


Figure 3.4: Copper wire diameter and skin depth representation.

The area product obtained by using two ETD54 cores would be $2 \times 88\,500\text{ mm}^4 = 177\,000\text{ mm}^4$. This value is greater than the minimum required area product ($25\,000\text{ mm}^4$) calculated in this section from expression (3.9) and Table 3.1. Therefore, it can potentially be used to build the four-winding transformer of the QAB prototype. Oversizing the magnetic core was necessary in our case in order to ensure a sufficient winding area that is able to contain the

four windings. The next step for choosing the magnetic core is to calculate the number of turns required for each winding and then verify that the available winding area of this core is able to contain all the ports' windings.

The effective area of this selected core is $A_e = 280 \text{ mm}^2$. All four windings should have the same number of turns since the voltage ratio between the ports is one. Therefore, from expression (3.7), for a voltage value of $V_i = 200V$, the turn number of each port's winding is calculated as follows:

$$n_1 = n_2 = n_3 = n_4 = 22 \text{ turns} \quad (3.12)$$

Each winding could consist of a single row of 22 turns. The four windings are then stacked on top of each other, with a layer of Kapton tape in between to ensure proper insulation.

The coil former dimensions of the selected ETD54 magnetic core are shown in Figure 3.5. To check if the available winding area is sufficient to contain the four windings of the ports, the following conditions should be verified:

$$\text{length} = 22 \text{ turns/row} \times 0.8 \text{ mm} = 17.6 \text{ mm} \leq 36.8 \text{ mm}$$

$$\text{height} = 1 \text{ row/winding} \times 4 \text{ windings} \times 0.8 \text{ mm} = 3.2 \text{ mm} \leq \frac{(39.5 - 19.8)}{2} = 9.85 \text{ mm}$$

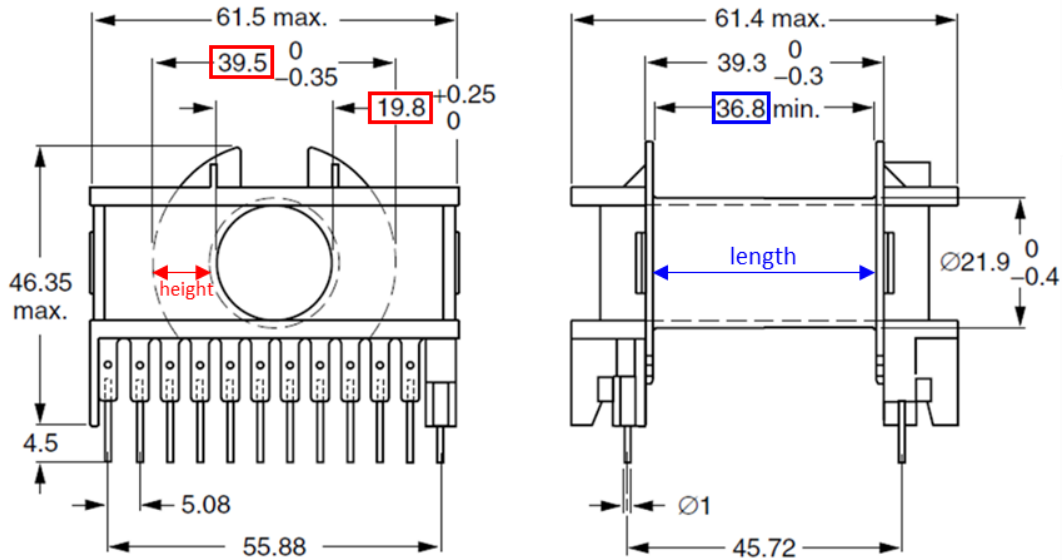


Figure 3.5: Dimensions of the coil former of the selected ETD54 magnetic core.

Since the winding area satisfies the length and height conditions and can accommodate the four windings of the QAB converter, two ETD54 magnetic cores were used to build the QAB prototype's transformer shown in Figure 3.6.

The transformer's characteristics were measured using an impedance analyser, resulting in the following values:

- The leakage inductance at each winding of the built transformer is approximately $3\mu H$. Therefore, in order to get a total series inductance of $37\mu H$ at each port, as calculated previously, an external inductance of $33\mu H$ (SER2918H-333KL) is connected in series with each transformer winding.

- The measured total DC series resistance at each port is $R_i = 50m\Omega$, this value being the sum of the DC series resistances of the transformer windings and the added series inductors.
- The total measured magnetizing inductance of the transformer is $3mH$. This measured value is sufficiently greater than the leakage inductances' values, so it can be neglected.

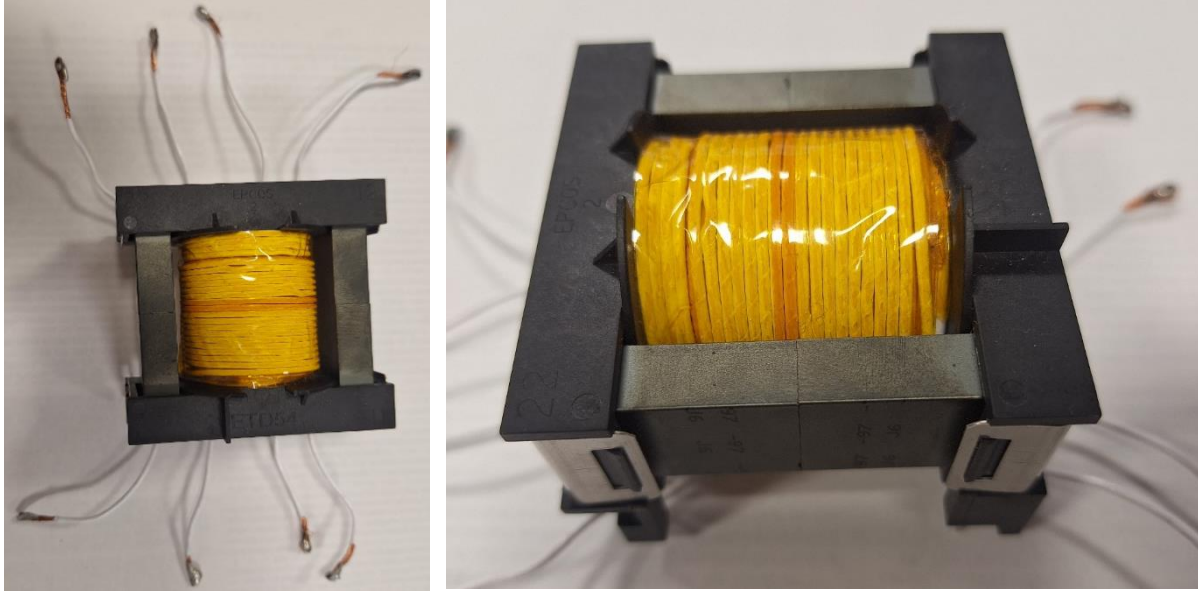


Figure 3.6: Transformer built for the 500W QAB prototype.

The parameter values of the built QAB converter prototype are summarized in Table 3.2. The complete QAB prototype is illustrated in Figure 3.7. A control interface PCB (Figure 3.8) was designed to generate the PWM command signals of the ports' switches using an STM32H743 microcontroller board. The selected microcontroller's core runs at a frequency of $240MHz$, is equipped with three ADCs (Analog-to-Digital Converters) with up to 36 channels and a 10-channel high resolution timer that was used to generate the phase-shifted PWM command signals of the switches. Two PWM command signals are sent through coaxial cables to each port and an electronic circuit implemented in the port's PCB generates their complementary signals. The measured DC voltage and current values at each port are sent through F/UTP (Foil Shielded Cable / Unshielded Twisted Pair) Ethernet cables (RJ45) to the ADC channels of the microcontroller in order to achieve the closed-loop control.

Table 3.2: Summary of the QAB prototype's parameter values.

Parameter	Parameter value
Total number of ports n	4
$V_1 = V_2 = V_3 = V_4$	200 V
$n_1:n_2:n_3:n_4$	1
$P_{nom,1} = P_{nom,2} = P_{nom,3} = P_{nom,4}$	500 W
$L_1 = L_2 = L_3 = L_4$	37 μH
$R_1 = R_2 = R_3 = R_4$	50 $m\Omega$
f_s	40 kHz
Transformer magnetic core	2 x ETD54 (3C90)
Winding wires	Litz wires

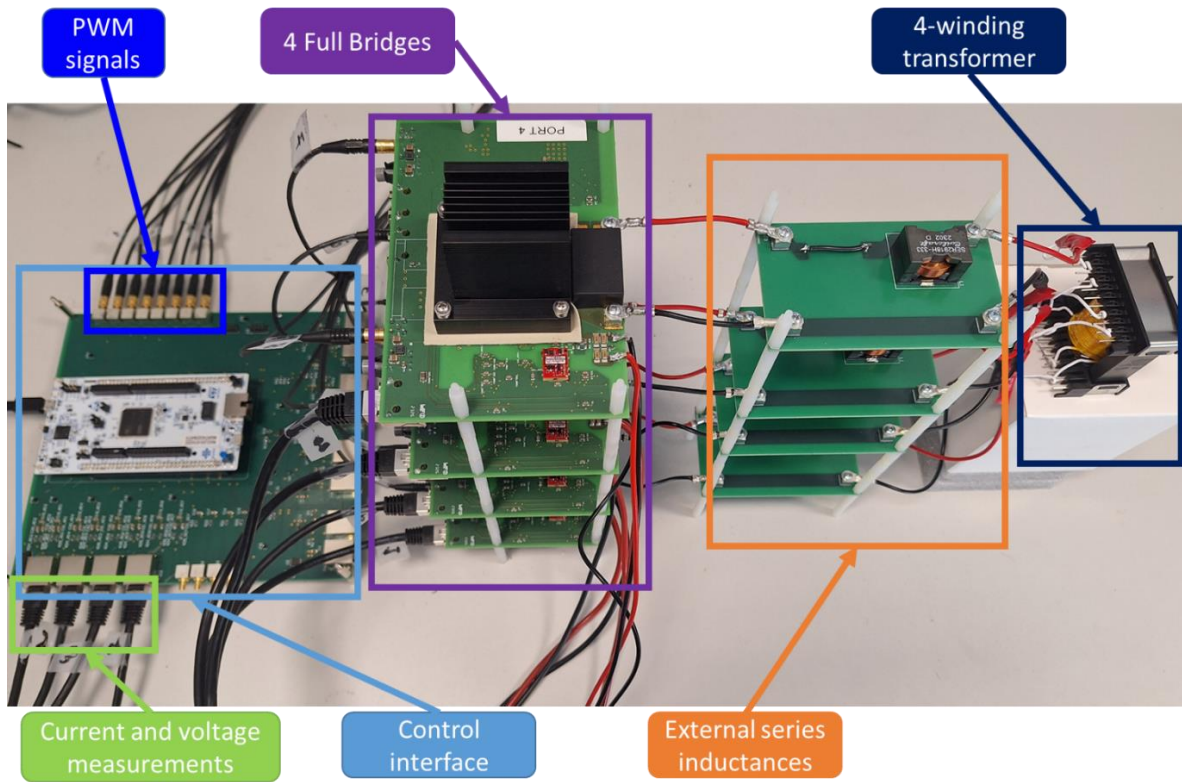


Figure 3.7: Built QAB prototype.

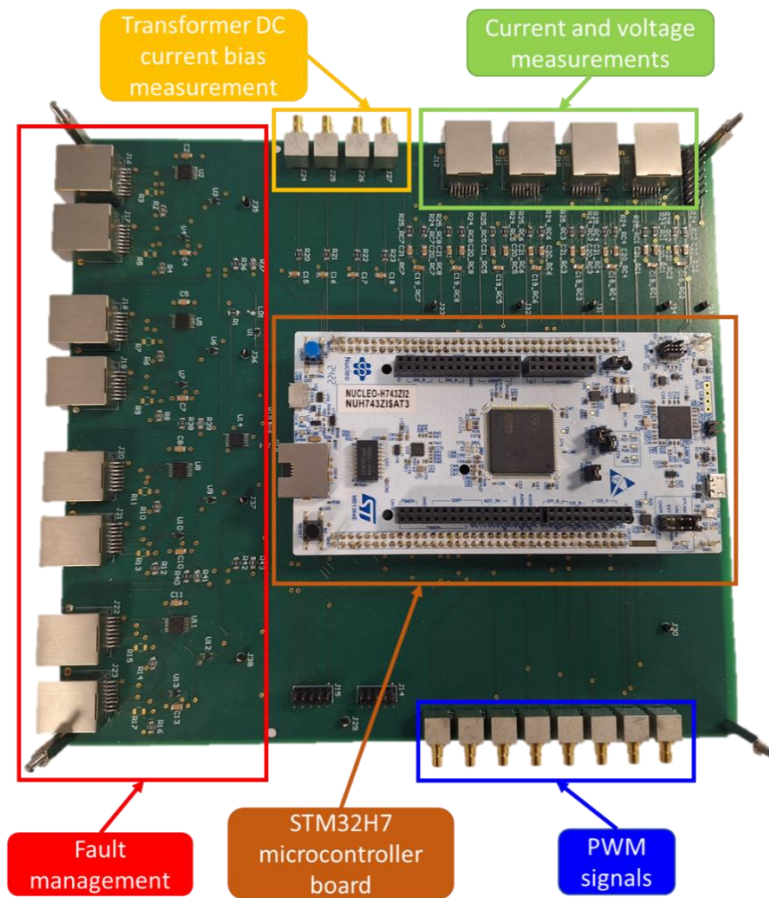


Figure 3.8: Control interface PCB.

3.3. Optimization Algorithm Implementation and Results

The optimization algorithm presented in Chapter 2 was implemented on the STM32H743 microcontroller board shown in Figure 3.7. In this thesis, the algorithm aiming for the minimization of total system losses illustrated in Figure 2.20.a was selected and tested experimentally. The complete control algorithm implemented in the microcontroller is displayed in the block diagram of Figure 3.9.

The optimization algorithm's execution time using the selected microcontroller and sweep parameters is 80 *ms*. The length of this execution time depends on various factors, including the order of harmonics considered in the mathematical sweep of the reference internal phase shift, the sweep step, and the selected microcontroller's core.

This algorithm is run in real-time at each relatively significant change in operating point and calculates the optimum open-loop values of the QAB control parameters, i.e. the external and internal phase shifts. These values are fed forward to generate the corresponding PWM command signals, which are sent to the prototype's drivers to bring the system as close as possible to the desired operating point. This is particularly relevant for applications where the ports' parameters (DC voltages and power references) do not have high dynamics in normal operation, such as batteries, PV panels and the grid connected through an intermediate AC/DC stage to the MAB converter. As this thesis targets such applications, the execution time of 80 *ms* was deemed acceptable. EPS modulation is applied to control the QAB prototype during the 80 *ms* execution of the optimization algorithm.

The real-time execution of the optimization algorithm prevents any memory-allocation based challenges (lookup tables), while simultaneously maintaining an accurate record of the real-time variations in DC voltage values and power references of the ports.

Sensors implemented in the Active-Bridge PCBs measure the DC voltage and DC current of each port. These values are then passed through differential RC filters and multiplied in the microcontroller to calculate the measured average power value of the corresponding port. After that, as shown in Figure 2.21 of Chapter 2, these measured power values are compared to their desired references, and the resulting errors are used as input to PI controllers. The controllers aim to cancel the steady-state error of the active power values by adjusting the ports' external phase shifts. Three separate closed-loops are therefore implemented in the microcontroller to regulate the power values of the three non-reference ports of the QAB prototype using the aforementioned PI controllers. As previously explained, the active power of the reference port will be determined by the power conservation law.

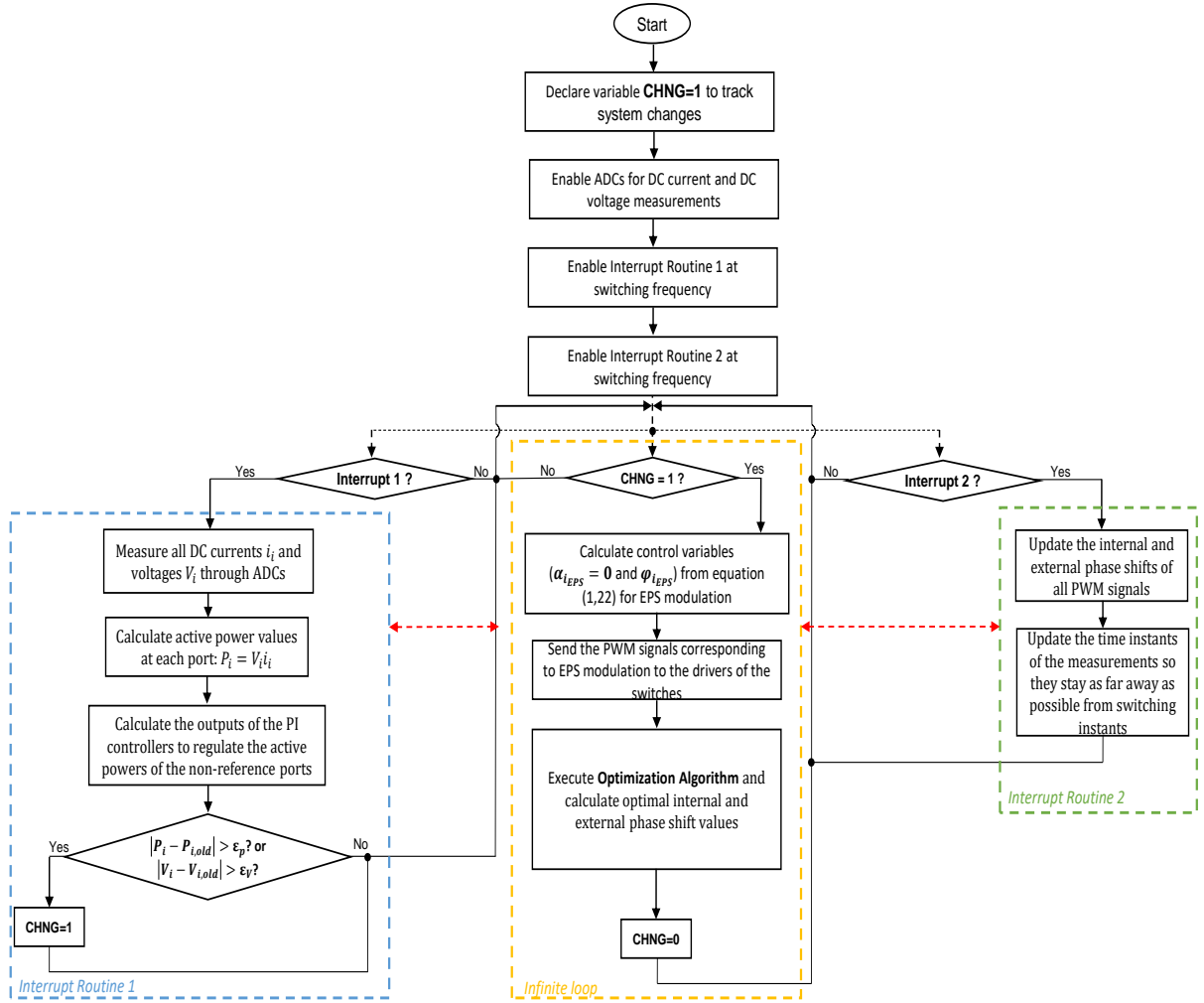


Figure 3.9: Block diagram representing the control algorithm implemented in the microcontroller.

Figure 3.10 compares the AC currents' waveforms of the ports predicted by the GHA model developed in Chapter 1 with the waveforms obtained experimentally from the QAB prototype. The considered operating point's parameters are given in Table 3.3. This comparison aims to validate the mathematical model and, therefore, the reliability of the optimization algorithm. The internal and external phase shifts applied in the results shown in Figure 3.10 were obtained from the optimization algorithm implemented in the microcontroller. As we can notice, the experimentally-obtained waveforms are quite similar to those predicted by the developed mathematical model. The slight mismatch is a result of the approximations made during the development of the GHA model, the truncation of the Fourier series at a finite harmonic order, and the uncertainties of the system's component values, such as the inductances. Nevertheless, this level of accuracy was accepted in this thesis as it provides a good compromise between precision and computational burden. This validates the developed GHA model and demonstrates its ability to predict the instantaneous and RMS current values required for calculating the conduction and switching losses of the system, as detailed in Chapter 2.

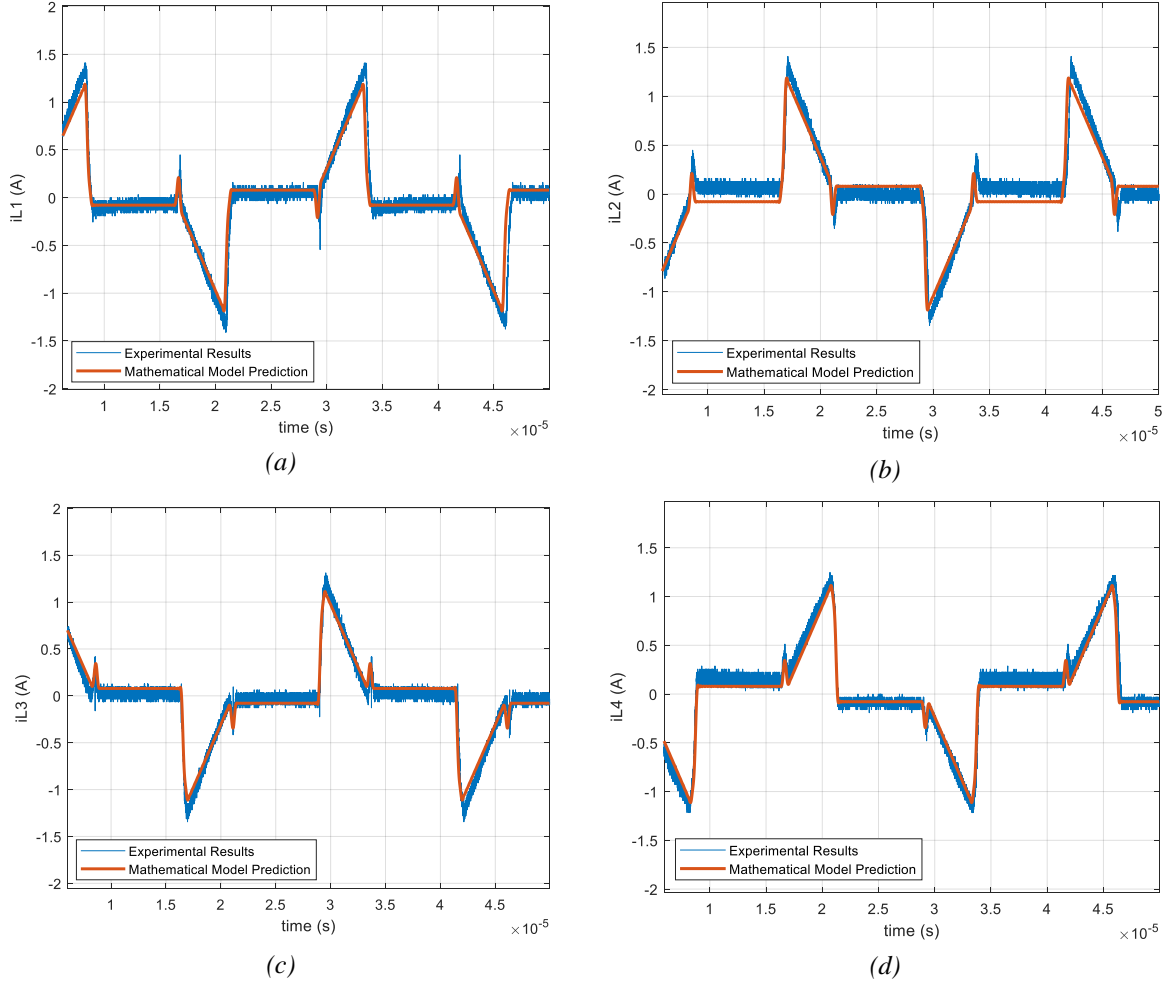


Figure 3.10: Comparison of the AC current waveforms obtained experimentally to the waveforms predicted by the GHA model developed in Chapter 1: (a) port #1; (b) port #2; (c) port #3; port #4.

Table 3.3: Parameter values of considered operating point.

Parameter	Parameter value
$V_1 = V_2$	190 V
$V_3 = V_4$	170 V
$P_1 = P_3$	-40 W
$P_2 = P_4$	40 W

Figure 3.11 displays the AC current and voltage waveforms at the different ports of the QAB converter prototype at the operating point given in Table 3.3. The QAB converter operates at low power at the selected operating point, specifically at 8% of its nominal power value. In Figure 3.11(a), the conventional EPS modulation technique is applied. In Figure 3.11(b), the proposed control strategy is employed, using the control parameters corresponding to the global minimum point of total system losses generated by the implemented optimization algorithm. A DC voltage perturbation of 5% was applied to ports #1 and #2, leading to the value of 190V instead of 200V. A 15% perturbation was applied to ports #3 and #4.

From Figure 3.11, we deduce that the average RMS current flowing through each port at the chosen operating point is $I_{rms,i} = 1.1 A$ when EPS modulation is applied, and is reduced to $I_{rms,i} = 462.5 mA$ by using the proposed control strategy. In other words, the RMS current is

reduced by approximately 58% when the proposed MPS modulation is employed on this studied operating point, leading to less conduction losses. Additionally, it can be noticed that the ZVS is restored at ports #3 and #4, and the turning off of the switches occurs at nearly zero current when the MPS modulation is applied in this case, thus reducing the switching losses. Peak AC currents are also significantly reduced, which leads to less iron losses in the transformer and the inductors of the QAB converter.

The proposed optimization control strategy was tested at various power levels for the same voltage values provided in Table 3.3. Figure 3.12 shows a comparison of the AC current and voltage waveforms of the ports at 130W (26% of nominal power) when EPS modulation and the proposed MPS modulation were applied. Similarly, Figure 3.13 provides a comparison at a power level of 380W (76% of nominal power). It can be observed that the proposed control strategy naturally applies a triangular AC current modulation to the converter at low power levels and a trapezoidal current modulation at higher power levels.

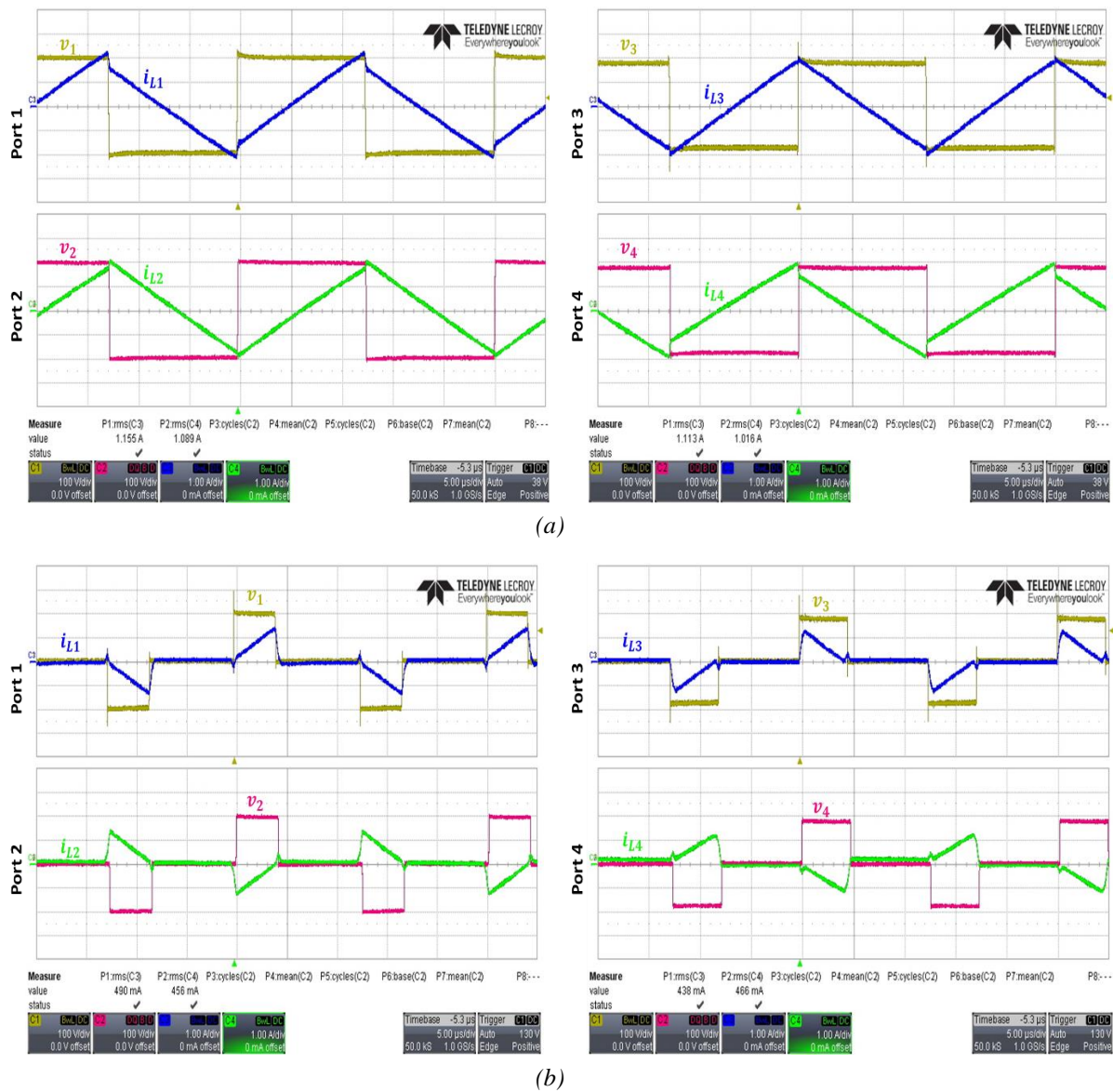
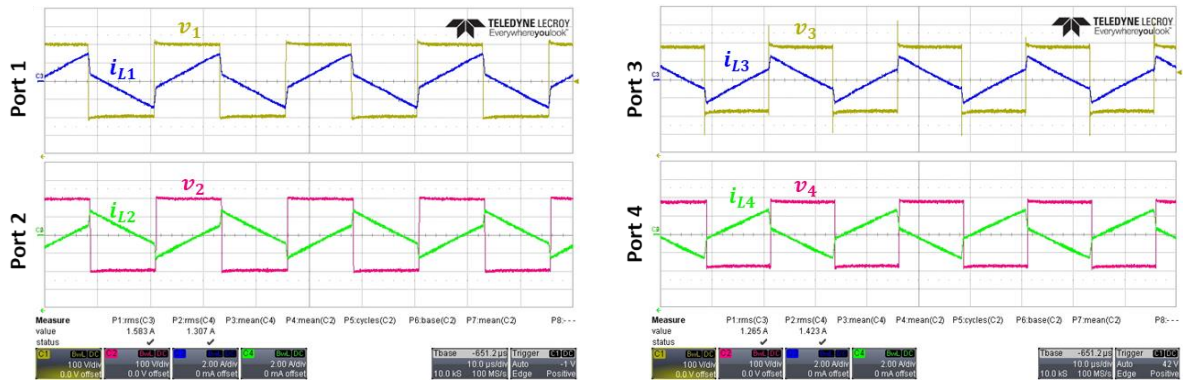
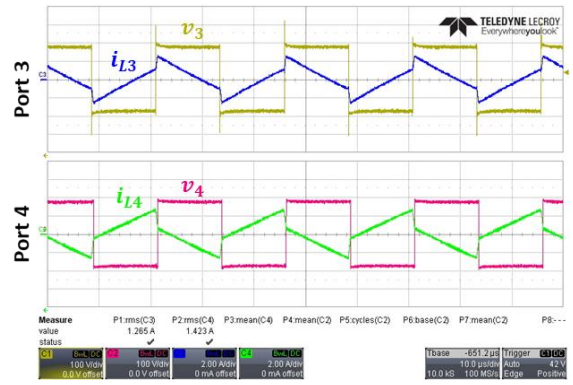


Figure 3.11: Experimental results showing the AC current and voltage waveforms of each port at 40W (8% of P_{nom}) when: (a) EPS modulation is applied; (b) the proposed MPS modulation is applied.

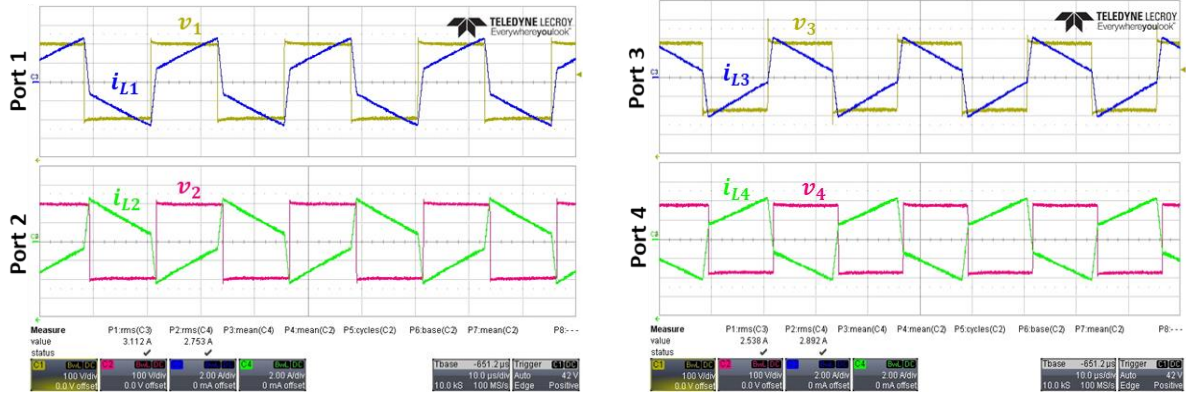


(a)

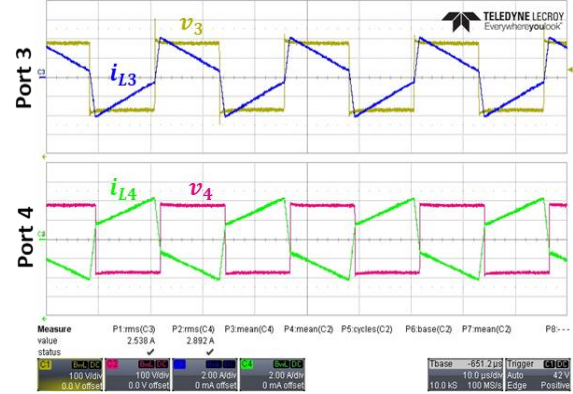


(b)

Figure 3.12: Experimental results showing the AC current and voltage waveforms of each port at 130W (26% of P_{nom}) when: (a) EPS modulation is applied; (b) the proposed MPS modulation is applied.



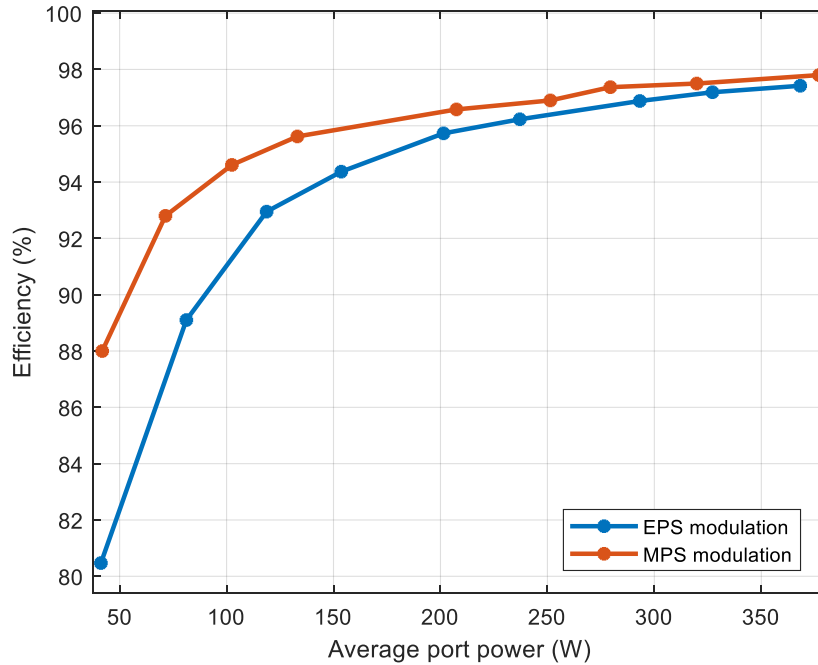
(a)



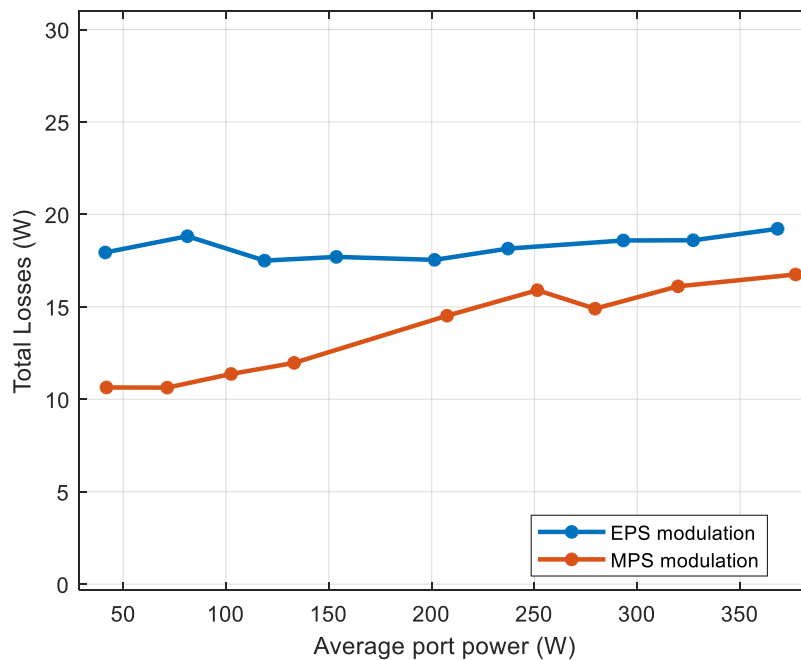
(b)

Figure 3.13: Experimental results showing the AC current and voltage waveforms of each port at 380W (76% of P_{nom}) when: (a) EPS modulation is applied; (b) the proposed MPS modulation is applied.

We can deduce that the proposed control strategy significantly reduces conduction and switching losses compared to the classical EPS modulation, resulting in an increase in the total efficiency of the QAB converter on its entire operating range. This can also be deduced from the experimental efficiency curve shown in Figure 3.14. This gain is particularly noticeable at operating points where low power circulates through the QAB converter and when perturbations occur at the ports' DC voltages, as stated in Chapter 2.



(a)



(b)

Figure 3.14: Experimentally measured efficiency and total losses of the QAB prototype in function of the average port power when using the classical EPS modulation compared to using the proposed MPS modulation.

Figure 3.15 illustrates the QAB prototype's efficiency curve obtained using the developed mathematical model. The considered DC voltage values are those applied to the QAB prototype for the results of Figure 3.14 and are given in Table 3.3. As it was stated in Chapter 2, the developed mathematical model only considers the conduction and switching losses of the system. However, Figure 3.15 shows that this approximation is optimistic, particularly at low power, where even a small additional loss would significantly impact the converter's overall efficiency. Nevertheless, despite the difference between the calculated and actual power losses of the system, the proposed control strategy is still able to achieve its primary objective, which is improving the overall efficiency of the QAB converter across its entire operating range.

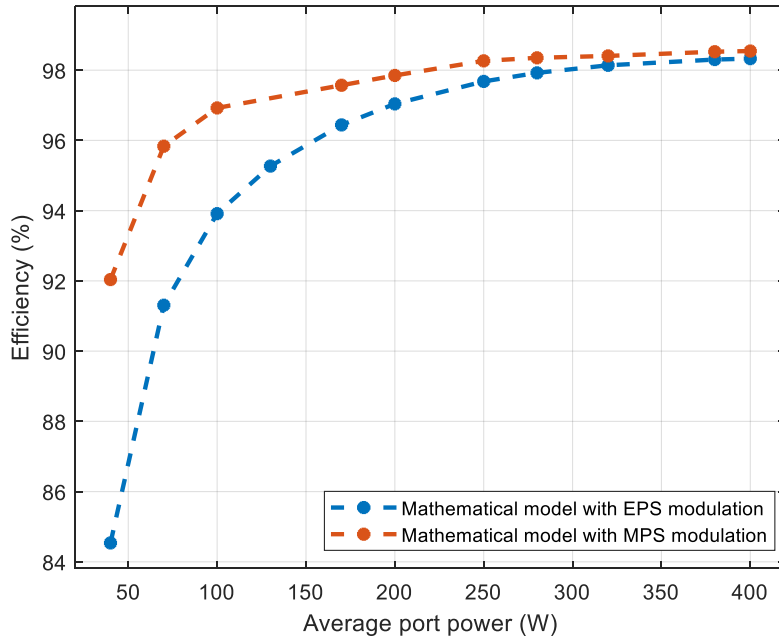


Figure 3.15: Calculated efficiency of the QAB prototype in function of the average port power using the developed mathematical model that only considers the conduction and switching losses of the system.

To gain a better understanding of the mismatch between the calculated and actual total losses of the QAB prototype, the iron losses of the four-winding prototype transformer were measured. The measurements were taken at full supply voltage on the primary winding, while the three remaining windings were left open circuit. A value of $4.23W$ was obtained and was added to the efficiency curve of Figure 3.15 acquired using the developed mathematical model. The results of this addition are displayed in Figure 3.16. By comparing Figure 3.16 to Figure 3.14, we can notice that adding the iron losses to the mathematical model significantly reduces the mismatch between the predicted and the actual total system losses. In future works, if more precision is required in the calculation of the total QAB converter losses, the transformer's iron losses should be taken into consideration in the mathematical model, using the Improved General Steinmetz equation for example.

The inaccuracies in the parameter values, the mathematical model, and the measurement equipment, as well as the unconsidered loss sources can also cause a mismatch between the mathematical predictions and the experimental results. More specifically, at low power operating points, the magnetic core losses of the series inductances and the transformer's magnetizing current losses would greatly affect the system's efficiency. At higher power values, the mismatch may be attributed to an underestimation of the conduction losses due to skin effect and proximity effects in the transformer windings and the series inductances.

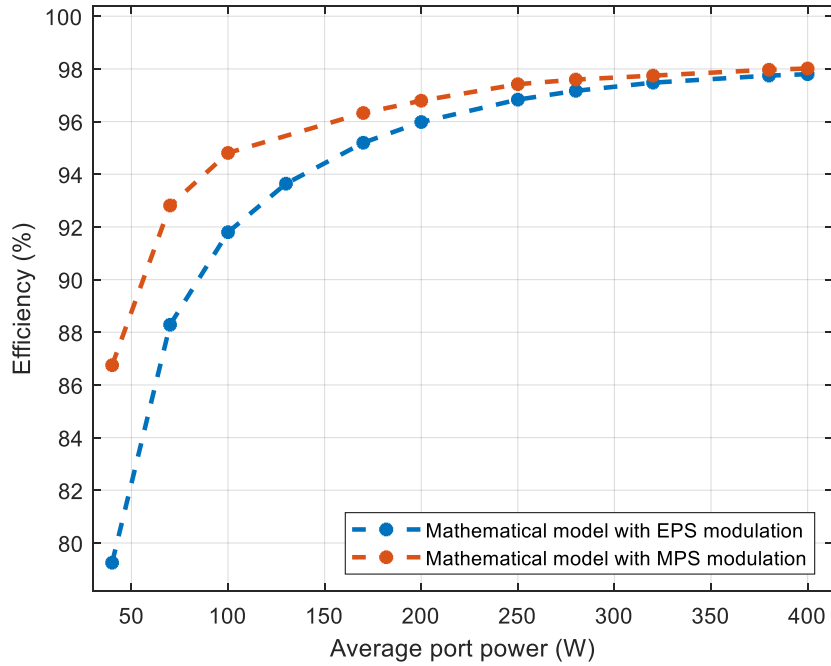
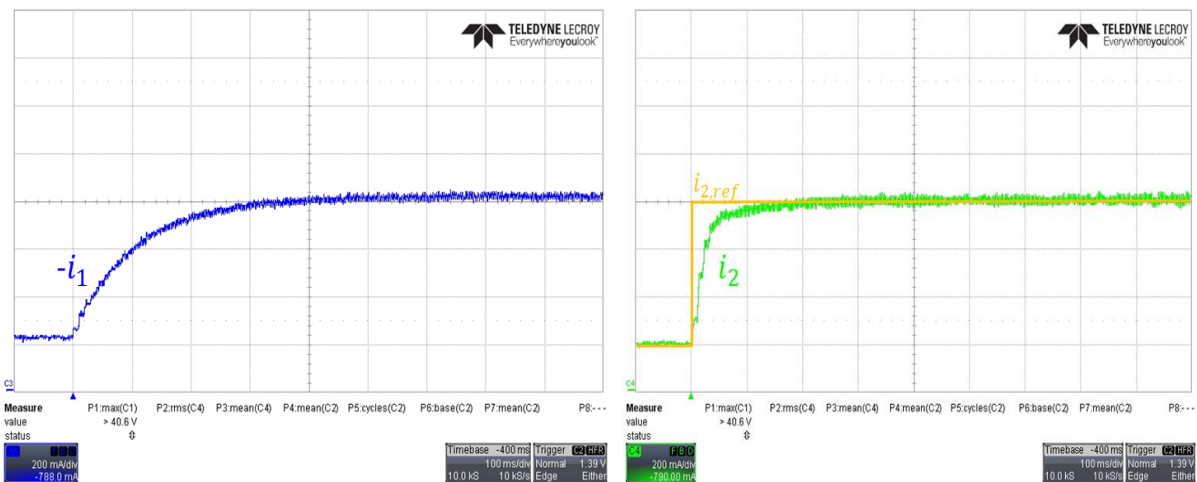


Figure 3.16: Efficiency curve of the QAB prototype obtained by adding the measured iron losses of the transformer to the conduction and switching losses calculated from the developed mathematical model.

Figure 3.17 shows the closed-loop responses of the DC currents at each port in response to a power reference change. The DC current at port #1 is determined by the power conservation law and does not follow any reference. The active powers at ports #2, #3 and #4 are controlled by PI controllers, as it was explained earlier, in order to correct the steady-state error of the mathematical model used by the developed optimization algorithm and to compensate for any perturbations. For the responses shown in Figure 3.17, the QAB converter is operated using EPS modulation. The optimization algorithm was deactivated in this part in order to study and validate the functioning of the feedback loops of the control system individually.

As explained in Chapter 1 Section 5, the DC currents of a MAB converter are rich in high frequency harmonics. Therefore, Figure 3.17 displays the filtered signals of the ports' DC currents in order to only visualize their DC components, i.e. their average values.



(a)

(b)

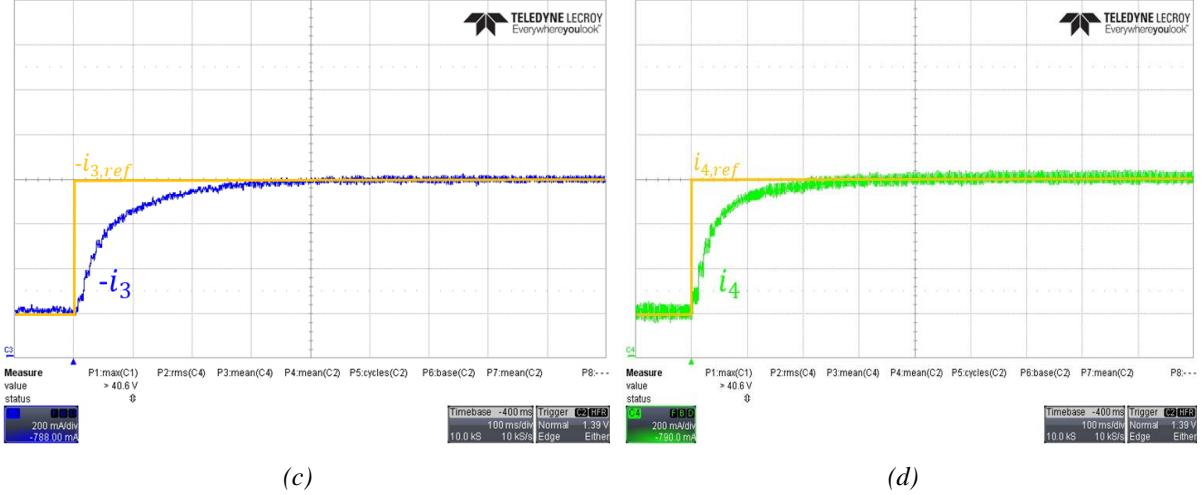


Figure 3.17: Closed-loop responses of DC currents at different ports after the occurrence of an active power reference change: (a) uncontrolled reference port #1; (b) port #2; (c) port #3; (d) port #4.

The PI controller of each closed-loop is designed using the first harmonic approximation model developed in Chapter 1. From the linearization of equation (1.16) ($\sin \varphi \approx \varphi$), the following relation between the active power and the external phase shift of a port # i can be written:

$$G_{P_i} = \frac{P_i}{\varphi_i} \Big|_{\substack{\varphi_j=0 \\ \forall j \neq i}} = \sum_{j \neq i}^n -\frac{8}{\pi^2} \frac{V_j V_i}{n_{ji} L_{ij} \omega_s} \cos\left(\frac{\alpha_j}{2}\right) \cos\left(\frac{\alpha_i}{2}\right) = \gamma_i = \text{constant} \quad (3.13)$$

The closed-loop transfer function when using an Integral controller can be written as follows:

$$CLTF_{P_i} = \frac{\gamma_i K_{i,i}}{s + \gamma_i K_{i,i}} = \frac{1}{\frac{1}{\gamma_i K_{i,i}} s + 1} = \frac{1}{\tau_i s + 1} \quad (3.14)$$

Where $K_{i,i}$ is the integral gain of the controller and $\tau_i = \frac{1}{\gamma_i K_{i,i}}$ is the time constant of the first-order closed-loop transfer function. The value of $K_{i,i}$ can be calculated by selecting a desired time response $t_{ir,95\%} = 3 \cdot \tau_i$ to the closed-loop control of the active power at a port # i as following:

$$K_{i,i} = \frac{3}{\gamma_i t_{ir,95\%}} \quad (3.15)$$

In Figure 3.17, the selected time responses for ports #2, #3 and #4 are 100ms, 200ms and 150ms respectively. As we can notice, these selected time responses were obtained experimentally, thus validating the proposed closed-loop control strategy.

3.4. DC Bias in Transformer Windings and Magnetic Core Saturation

The implementation of a high frequency transformer in a MAB converter provides galvanic isolation to this system, which is one of its most appreciated features. However, it brings the possibility of DC bias, which can eventually lead to transformer saturation and over-current flow [56], [57]. This can generate a decrease in the system's efficiency and an increase in its temperature, potentially causing converter damage and failure. For this reason, addressing this problem is crucial in MAB converters.

DC bias occurs when DC current flows through the transformer's windings, adding a DC offset to its magnetic flux density. The saturation of a transformer's core takes place when the magnetic flux density circulating in it surpasses its maximum allowed value B_{max} . This limit depends on the core's material. The DC magnetic flux density $B_{DC,i}$ depends on different parameters, such as the core's material and physical dimensions, as well as the number of turns of the transformer. The relationship between the DC magnetic flux density $B_{DC,i}$ at a winding #i and a constant current $I_{DC,i}$ flowing through this winding is given as following [9], [58]:

$$B_{DC,i} = \frac{\mu n_i I_{DC,i}}{l} \quad (3.16)$$

Where μ is the magnetic permeability of the core's material, l is the length of the magnetic path, and n_i is the number of turns at port #i's side of the transformer.

In a MAB converter, DC bias at a certain port is caused by the imbalance between the positive part and the negative part of its AC voltage. In other words, the positive part and the negative part of the AC voltage at any port should always be equal in order to avoid the creation of any DC current that will circulate through the transformer. Otherwise, the created DC current will generate a DC magnetic flux density in the transformer's core (from equation (3.16)), potentially leading to its saturation. This concept is displayed in Figure 3.18.

There are two types of DC bias: transient DC bias and steady-state DC bias. Transient DC bias is caused by changes in the converter's operating point or parameters, such as its phase shifts or the DC voltage values at its ports. Steady-state DC bias is mainly caused by the non-ideal behaviour of some components, such as unmatched switching times, delays in gate driving signals, and inconsistent parameters between switching devices due to factors such as device manufacturing or differences in heat dissipation [56].

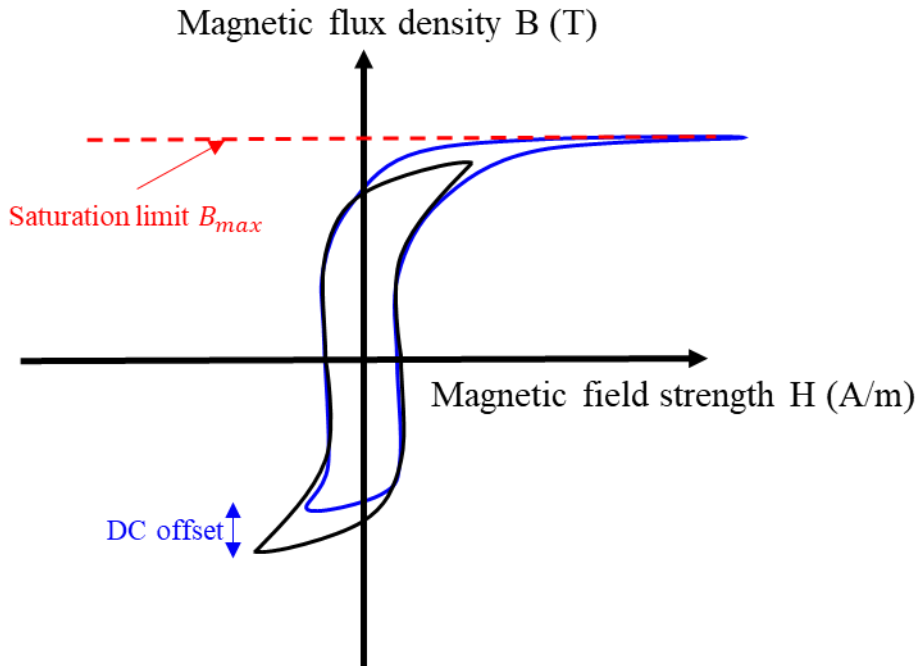


Figure 3.18: Effect of the DC bias on the hysteresis loop of the transformer's core.

Various flux-balancing methods have been developed in the literature to eliminate the DC bias in the HF transformer. These methods can be either passive or active solutions [9], [56]. One

passive solution involves connecting a capacitor in series with the transformer windings of the MAB converter, as shown in Figure 3.19. In fact, connecting a capacitor in series with the transformer's windings eliminates DC bias by blocking the DC currents and not allowing them to flow into the transformer. However, adding capacitors to the converter's topology increases the system's power losses and volume/weight. Additionally, these series-connected capacitors will undergo significant currents, which may result in accelerated deterioration.

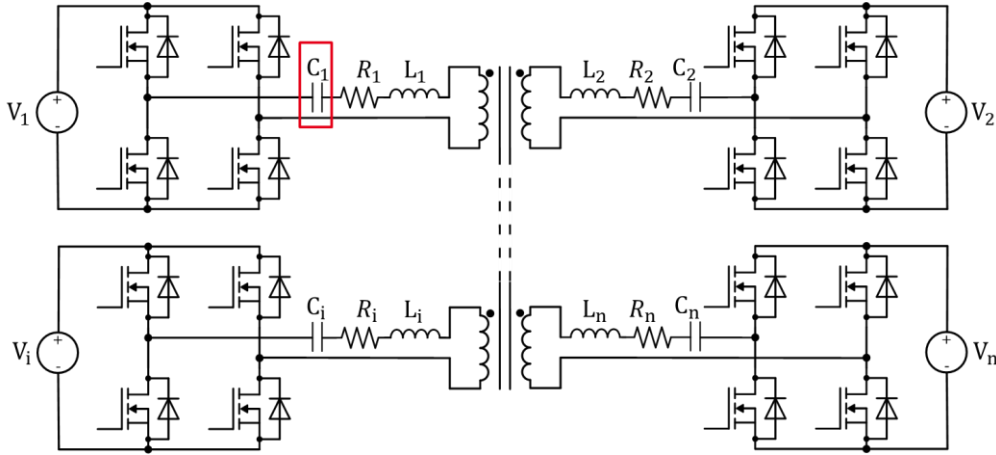


Figure 3.19: Resonant MAB converter topology.

Another passive solution is inserting an air gap into the magnetic core of the transformer. This increases the maximum amount of DC current that the transformer can tolerate without saturating. In fact, in equation (3.16), the magnetic permeability μ and the length of the magnetic path l change by adding a gap, thus increasing the maximum reachable DC current value $I_{DC,i}$ that causes the magnetic core to saturate. This effect can also be explained by comparing the hysteresis loops of the ferrite core before and after adding the air gap, as shown in Figure 3.20. However, this method only aims to increase the DC bias tolerance of the magnetic core, making it more difficult to saturate. It does not eliminate the DC flux component that increases the system's losses and temperature. Furthermore, introducing air gaps into the transformer's magnetic core reduces its magnetizing inductance, thus increasing their total resulting losses [9].

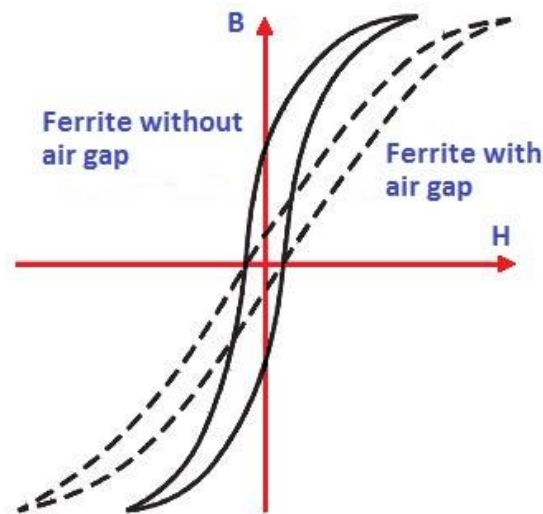


Figure 3.20: Comparison of hysteresis loops of a ferrite core with and without an air gap [59].

In [60], a passive method for cancelling only the transient DC bias caused by the phase shift change in a DAB converter is presented. In this method, the external phase shift change is applied in two steps whenever an operating point change occurs,: the first 50% of the new external phase shift is applied in the positive half cycle, and the remaining 50% is applied in the negative half cycle, as shown in Figure 3.21(b). In other words, an intermediate phase shift φ_{int} is applied to the voltage waveforms between the old and the new phase shifts, and its value is calculated as follows:

$$\varphi_{int} = \frac{\varphi_{old} + \varphi_{new}}{2} = \varphi_{old} + \frac{|\varphi_{new} - \varphi_{old}|}{2} = \varphi_{old} + \frac{|\Delta\varphi|}{2}$$

In this way, the voltage waveforms are balanced, resulting in balanced transformer current.

If an MPS modulation is used to control the MAB converter, this proposed method can also be achieved by also applying the new external phase shift value in two steps, as explained before. The new values of the internal phase shifts would be the same during both the positive and negative half cycles after the operating point change.

This method can be easily scaled up to apply on a MAB converter with more than two ports. Furthermore, this method does not require any information about the currents and voltages of the transformer windings, eliminating the need for sensors and reducing complexity and cost.

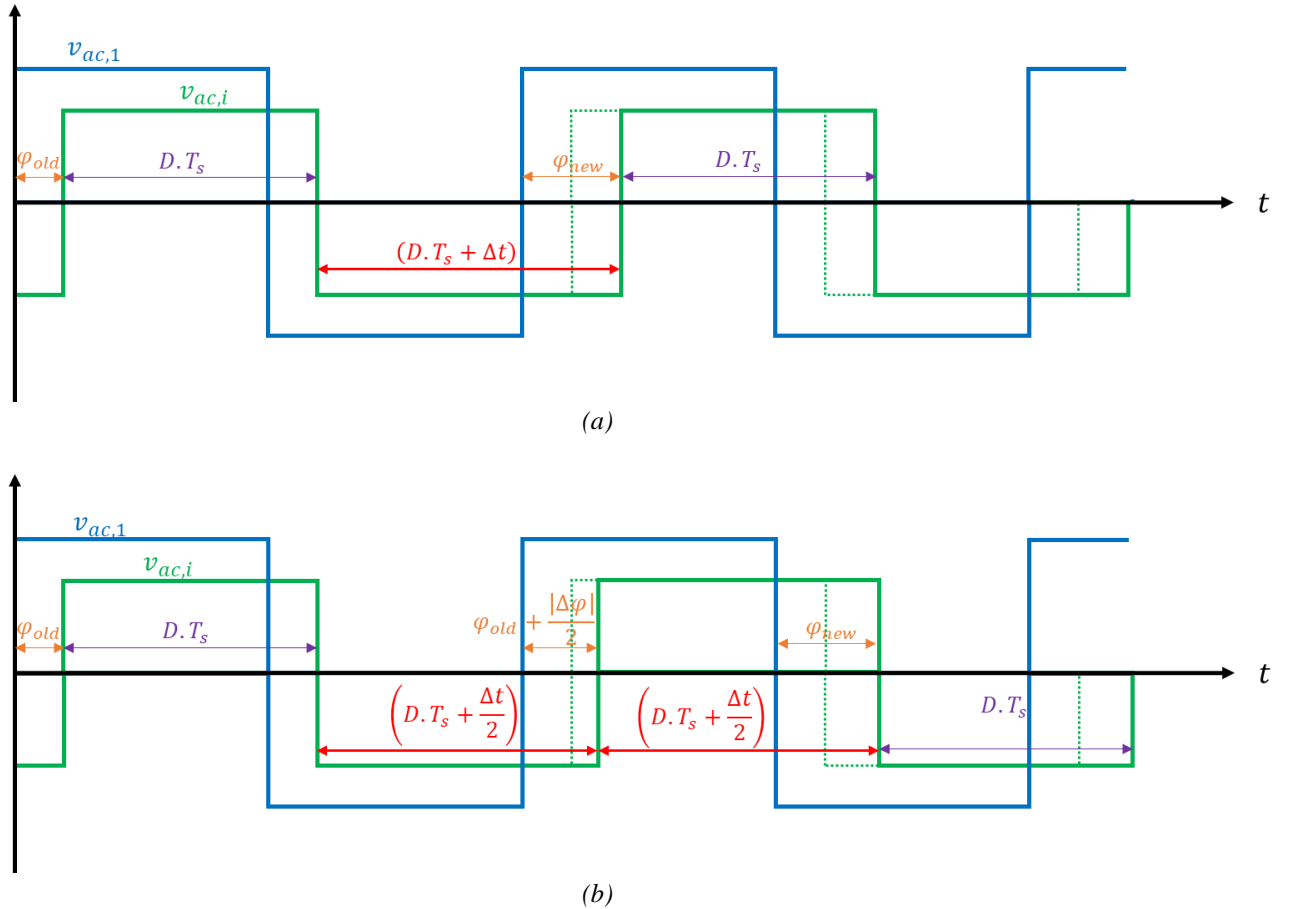


Figure 3.21: Waveforms of the AC voltages of a DAB converter with EPS modulation when an external phase shift change occurs: (a) without DC current bias elimination (unbalanced waveforms) b) with two-step phase shift method for transient DC bias elimination (balanced waveforms).

In [56], a prediction method of the maximum steady-state DC bias is developed considering the inconsistency between the switching devices of a DAB converter, such as their unmatched turn on/off times or their different characteristics. This way, if the maximum DC bias tolerated by the transformer is known, the range of permitted inconsistency of the switching devices can be obtained. This would help in the selection of the semiconductor devices and the sizing of the transformer. However, this method does not cancel the circulating DC current, and only aims to avoid the saturation of the transformer's core. Additionally, oversizing the transformer may be necessary to increase its DC bias tolerance. Furthermore, predicting the non-ideal behaviour of semiconductor devices with precision is difficult, as the characteristics of each switch may change differently over time. Therefore, closed-loop cancellation of this bias based on measurements would be more effective [9].

Active solutions usually require dynamic measurement of the magnetic flux. This is not an easy task as special sensors or additional components are required to detect the magnetic flux variations [9], [56]. In [58], a closed-loop flux balancing control method is proposed for a DAB converter using a magnetic ear to continuously measure the DC flux component. As shown in Figure 3.22, the flux measurement in this work is achieved by adding an auxiliary core with a winding W_s to the main transformer's core. The auxiliary core and the main core share a part of the magnetic path, which is represented by the reluctance R_m . When the main core gets closer to saturation, its permeability μ decreases, thus increasing the value of R_m and finally decreasing the value of the measured inductance L_s of the auxiliary winding W_s . Therefore, a measured drop in the value of inductance L_s directly indicates that the main core is approaching saturation. The absolute value of the DC flux component is obtained from the measured value of L_s , using a pre-built lookup table. The polarity of the DC flux component is determined by comparing the measured magnetic flux density when the AC voltage of the main transformer winding switches from positive to negative with when it switches from negative to positive. A PI controller is then used to cancel the measured DC flux in the transformer's core by varying the internal phase shift of the primary port of the DAB converter.

This active flux balancing method necessitates the use of various additional components such as the auxiliary magnetic core and winding along with an auxiliary electronic circuit required to measure the value of the inductance L_s . This will affect the DAB's efficiency and will add to its volume. Additionally, when the DC flux is directly measured from the transformer's core, it is impossible to determine which port is the source of the DC bias. Therefore, generalizing this method to a MAB converter with n ports would mean that one port would always be required to compensate for the DC bias caused by all the other ports. This compensation is therefore done by injecting a DC bias in the opposite direction to the one already circulating in the magnetic core. This will result in a decrease in the global efficiency of the MAB converter.

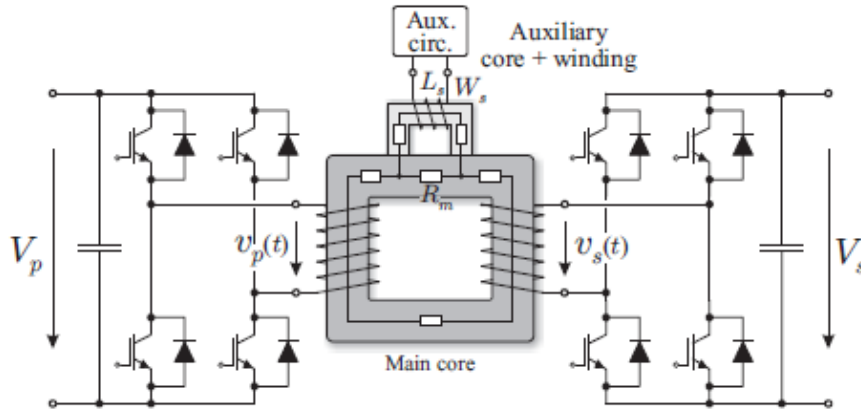


Figure 3.22: Flux density measurement using a magnetic ear [58].

Instead of measuring the DC component of the flux, the DC component of the transformer's AC current can also be measured. Nevertheless, measuring the DC offset in the transformer current that has high harmonic content is not an easy task. This is mainly due to the very small value of the DC current component compared to the AC components' values. Actually, a normal current sensor, which is chosen based on the nominal AC current value, would not be able to detect the DC component, since its value will be less than the sensor's error value.

In the G2ELab, an innovative method to measure the DC current component was developed and is shown in Figure 3.23 [9]. It consists of creating a copy of the AC component of the transformer current alone by using a Current Transformer (CT) with a turn ratio equal to one, and a short-circuited secondary winding. A Hall current sensor is then used in a way that the main transformer current and the copy of its AC component flow in it in opposite directions in it. Consequently, the AC components will cancel each other and the sensor will only measure the DC current component of the main transformer current. In other words, the magnetic fields of the AC current components flowing in opposite directions cancel each other in the Hall Sensor, leaving only the magnetic field of the DC current. As a result, the sensor provides the value of the DC current component. Additionally, since the cancellation of the AC components is expected, the Hall sensor is sized according to the DC component's magnitude, making it more accurate. An active cancellation loop is then implemented in order to eliminate the measured DC component. It consists of a feedback loop that aims to re-equalize the transformer voltages' positive and negative parts through the use of a PI controller. This technique is applied to each port of the converter individually, allowing it to cancel out both the transient and steady-state DC bias it generates.

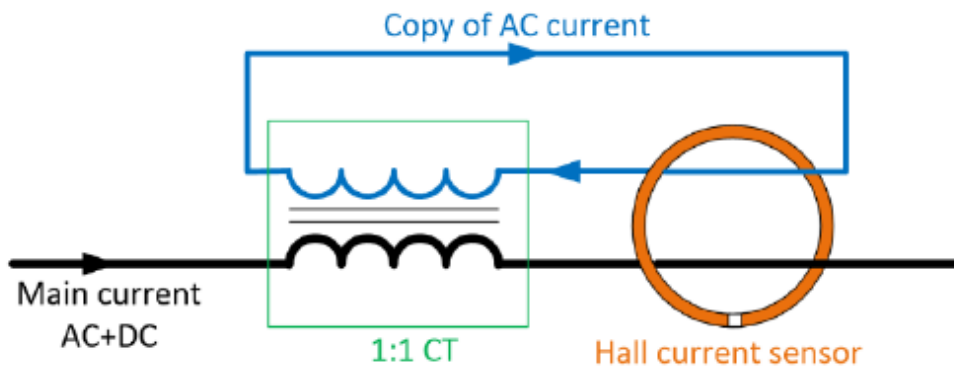


Figure 3.23: DC component measuring of the MAB's transformer current [9].

This DC bias cancellation method was employed in the prototype of this thesis due to its effectiveness and ease of implementation. A mathematical model is developed in this section in order to properly represent and predict the system's behaviour. This model is also used to design the closed-loop PI controllers that aim to cancel the DC bias at each port. Figure 3.24 shows the built circuit for the DC current component measurement at each port. In future works, a smaller version of this circuit could be designed in order to optimize the volume of the final prototype.

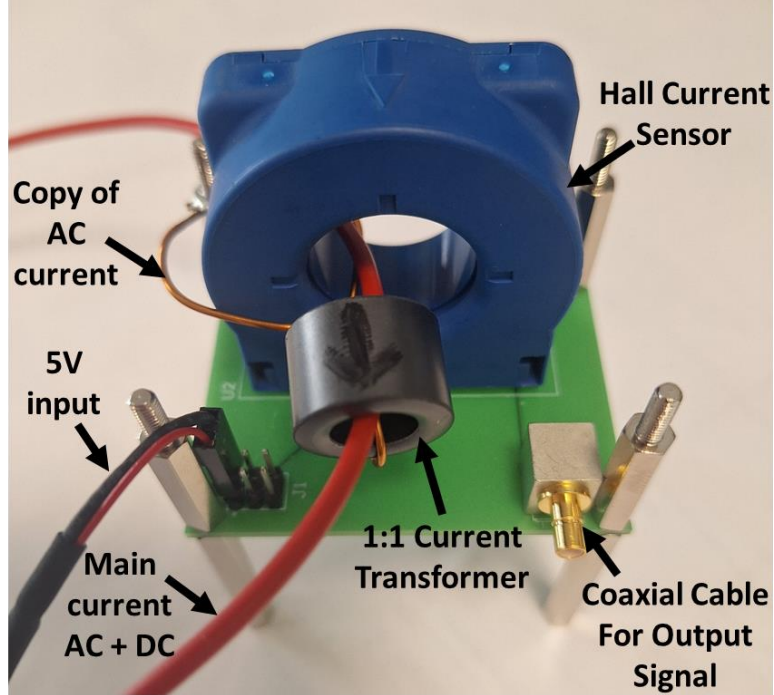


Figure 3.24: Developed circuit for the DC current component measurement.

Figure 3.25 displays the steady-state AC voltage waveform of a port # i , illustrating the duty cycles $D_{i,p}$ and $D_{i,n}$ of its positive and negative half cycles respectively, along with the corresponding command waveforms of the port's switches. These duty cycles can be expressed as following:

$$D_{i,p} \cdot T_s = \frac{\beta_{i1}}{2} \cdot T_s - \alpha_i \cdot \frac{T_s}{2\pi} + \frac{\beta_{i2}}{2} \cdot T_s \quad (3.17)$$

$$D_{i,n} \cdot T_s = \frac{(1 - \beta_{i1})}{2} \cdot T_s - \alpha_i \cdot \frac{T_s}{2\pi} + \frac{(1 - \beta_{i2})}{2} \cdot T_s \quad (3.18)$$

Where β_{i1} and β_{i2} are the command duty cycles of switches T_{i1} and T_{i4} respectively, as shown in Figure 3.25. T_s is the switching period.

In an ideal scenario, duty cycles $D_{i,p}$ and $D_{i,n}$ would have equal values and no DC bias would circulate in the corresponding transformer winding. This means that the command duty cycles β_{i1} and β_{i2} are both equal to 50%. However, in a practical converter, the unmatched switching instants and the inconsistent characteristics of the switches may lead to a mismatch in the values of β_{i1} and β_{i2} , creating a DC component in the AC voltage $v_{ac,i}$. This will cause the generation of a DC current in the transformer winding that can eventually lead to the saturation of its magnetic core.

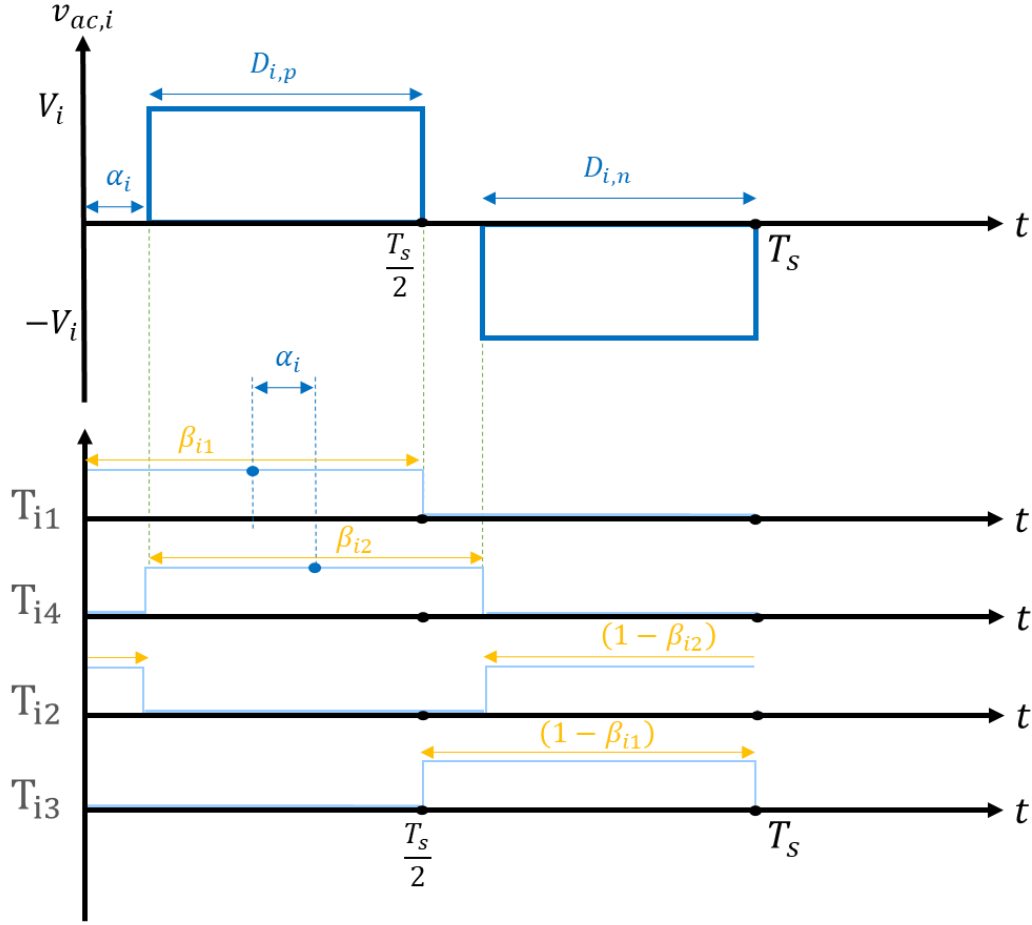


Figure 3.25: Duty cycles representation of the positive and negative half-cycles of the AC voltage of a port #i with their corresponding switch commands' waveforms.

The created DC component of the voltage $v_{ac,i}$ is denoted as $\langle v_{ac,i} \rangle_0$ and can be expressed as follows:

$$\langle v_{ac,i} \rangle_0 = \frac{1}{T_s} \cdot \int_0^{T_s} v_{ac,i}(t) \cdot dt = V_i \cdot [D_{ip} - D_{in}] = V_i \cdot \Delta D_i \quad (3.19)$$

The dynamic expression of the DC components at the transformer winding between port #i and a port #j can be written as following, using the delta equivalent circuit displayed in Chapter 1:

$$L_{ij} \cdot \frac{d\langle i_{ij} \rangle_0}{dt} = \langle v_{ac,i} \rangle_0 - \langle v_{ac,j} \rangle_0 - R_{ij} \cdot \langle i_{ij} \rangle_0 \quad (3.20)$$

DC bias cannot be transmitted from port #j to port #i through the transformer windings. Therefore, we can write:

$$\langle v_{ac,j} \rangle_0 = 0 \quad \forall j \neq i \quad (3.21)$$

Therefore, expression (3.20) becomes:

$$L_{ij} \cdot \frac{d\langle i_{ij} \rangle_0}{dt} = \frac{V_i}{n_{1i}} \cdot \Delta D_i - R_{ij} \cdot \langle i_{ij} \rangle_0 \quad (3.22)$$

Equation (3.22) is linear. Applying the Laplace transform on this equation, we can write:

$$L_{ij} \cdot s \cdot I_{ij,DC}(s) = \frac{V_i}{n_{1i}} \cdot \Delta D_i(s) - R_{ij} \cdot I_{ij,DC}(s) \quad (3.23)$$

The frequency-domain transfer function linking the delta-equivalent circuit's DC current component $I_{ij,DC}(s)$ between port #i and port #j to the duty cycle difference $\Delta D_i(s) = (D_{i,p} - D_{i,n})$ at port #i can be expressed as following:

$$\frac{I_{ij,DC}(s)}{\Delta D_i(s)} = \frac{\frac{V_i}{n_{1i} \cdot L_{ij}}}{\left(s + \frac{R_{ij}}{L_{ij}}\right)} \quad (3.24)$$

From expression (3.24), the transfer function linking the star-equivalent circuit's DC current component $I_{i,DC}(s)$ at port #i to the duty cycle difference $\Delta D_i(s) = (D_{i,p} - D_{i,n})$ at this port can be deduced as follows:

$$G_{i,DC}(s) = \frac{I_{i,DC}(s)}{\Delta D_i(s)} = \sum_{\substack{j=1 \\ j \neq i}}^n \frac{I_{ij,DC}(s)}{\Delta D_i(s)} \quad (3.25)$$

Using the developed current sensor shown in Figure 3.24, the DC component $I_{i,DC}(s)$ of the current flowing through the transformer winding of port #i is measured. Then, a PI controller is employed to cancel the measured DC bias and generate the required value of ΔD_i . The PI controller parameters are calculated using transfer function $G_{i,DC}(s)$ of equation (3.25).

From expressions (3.17) and (3.18), we can write the following:

$$\Delta D_i = D_{ip} - D_{in} = \beta_{i1} + \beta_{i2} - 1 \quad (3.26)$$

The DC current component $I_{i,DC}(s)$ at port #i can be cancelled by fixing a value of 0.5 to the command duty cycle β_{i2} and only manipulating the value of β_{i1} to get the required value of ΔD_i that cancels $I_{i,DC}(s)$.

The block diagram of this DC bias cancellation technique developed in this thesis is displayed in Figure 3.26.

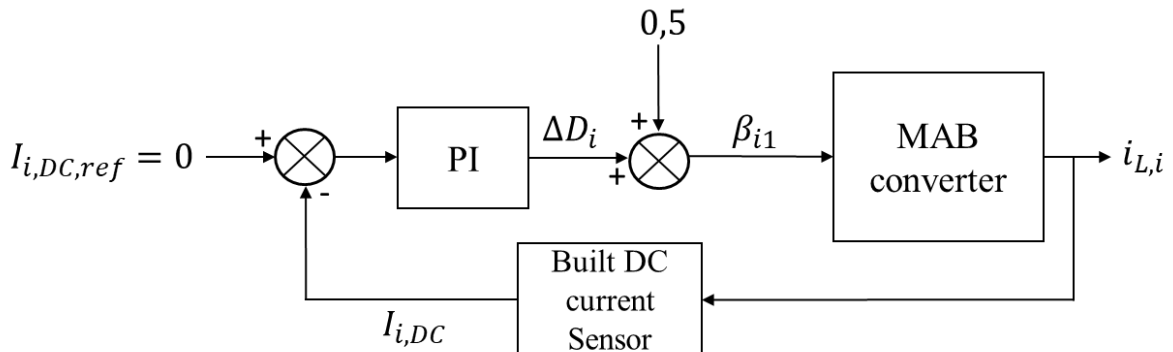


Figure 3.26: Block diagram of the developed DC current component cancellation technique at a port #i.

For the built QAB prototype, the expression of transfer function $G_{i,DC}(s)$ of all the ports is the same due to the symmetry between ports. It is a first order transfer function expressed as follows:

$$G_{i,DC}(s) = \frac{3 \cdot \frac{V_i}{n_{ij}L_{ij}}}{s + \frac{R_{ij}}{L_{ij}}} \quad (3.27)$$

The PI controller illustrated in Figure 3.26 has the following expression:

$$C_{DC}(s) = \frac{K_p(T_i s + 1)}{T_i s} \quad (3.28)$$

We choose $T_i = \frac{L_{ij}}{R_{ij}}$. Therefore, the closed loop transfer function of this control loop would be:

$$CLTF_{DC} = \frac{C_{DC}(s)G_{i,DC}(s)}{1 + C_{DC}(s)G_{i,DC}(s)} = \frac{3 \cdot \frac{V_i}{n_{ij}L_{ij}}}{\frac{1}{K_p}s + 3 \cdot \frac{V_i}{n_{ij}L_{ij}}} = \frac{1}{\tau_{DC} \cdot s + 1}$$

With $\tau_{DC} = \frac{1}{K_p} \frac{n_{ij}L_{ij}}{3V_i}$ the time constant of the closed loop system.

Considering that the time response value of this closed-loop transfer function to cancel 95% of the DC bias at a port #i is $t_{r,95\%} = 3 \cdot \tau_{DC}$, the gain K_p is chosen for a desired value of $t_{r,95\%}$, such that:

$$K_p = \frac{n_{ij}L_{ij}}{V_i \cdot t_{r,95\%}} \quad (3.29)$$

The proposed closed-loop DC bias cancellation method was applied to the QAB prototype, and the experimental results obtained at port #4 are displayed in Figure 3.27. The time response chosen to obtain the parameter values of the PI controllers was $t_{r,95\%} = 10 \text{ ms}$. Figure 3.27 shows that the obtained time response is quite close to the selected one, thus validating the

theoretical study presented in this section. The main cause of the mismatch is the difference between the theoretical and actual parameter values of V_i , L_{ij} , and R_{ij} .

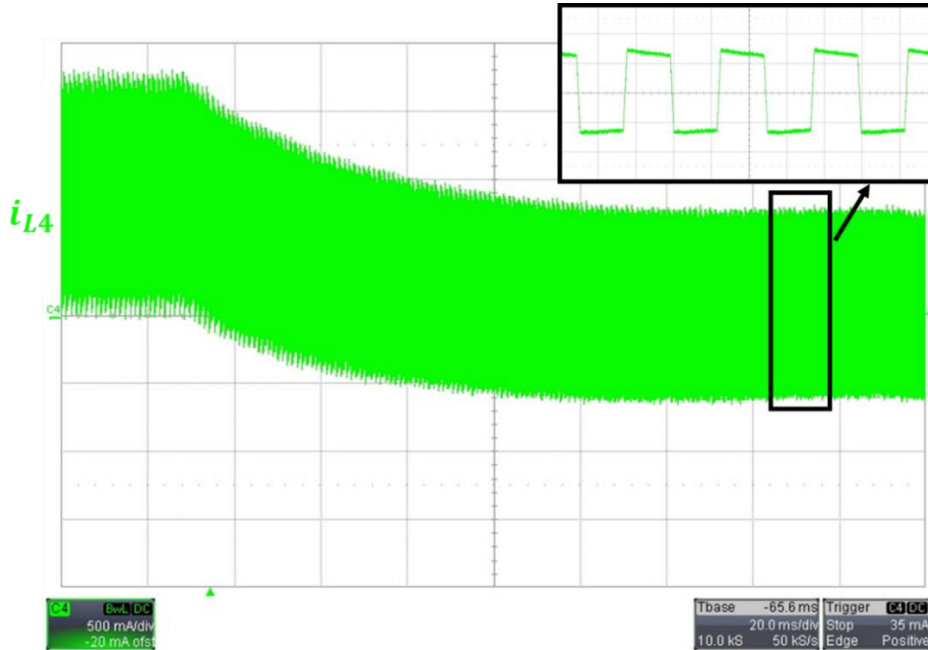


Figure 3.27: Closed-loop response of the proposed DC bias cancellation control method on port #4.

3.5. Conclusion

The first chapter of this manuscript detailed the mathematical modelling of an n -port MAB converter with DC voltage ports. The second chapter proposed an optimization control strategy for this selected topology of MAB converter, with the aim of minimizing its conduction and switching losses.

The primary objective of the third chapter is to experimentally validate the theory presented in the first two chapters. A $4 \times 500W$ QAB converter prototype was built for this purpose. The sizing of this prototype is detailed in the first part of this chapter. Then, the optimization algorithm developed in this thesis was implemented in a microcontroller and tested on the built prototype. Experimental results are provided in this chapter, validating the developed mathematical model and proving that the proposed optimization control strategy improves the overall efficiency of the QAB converter on its entire operating range. As predicted in Chapter 2, the increase in efficiency is more significant at lower power levels.

Furthermore, the issue of the potential presence of DC bias in the transformer is addressed and an active solution to suppress this bias is proposed and validated experimentally in this chapter.

In the final chapter, a new topology of a hybrid-fed MAB converter is proposed, studied and modelled. Unlike the classical voltage-fed MAB converter selected in the first three chapters, this hybrid-fed MAB converter consists of both voltage-fed and current-fed ports. The current-fed port is useful for several applications, such as those involving PV panels. Chapter 4 also presents a control strategy for this proposed hybrid-fed MAB topology.

CHAPTER 4: MODELLING AND CONTROL OF A HYBRID-FED MAB CONVERTER

4.1. Introduction

Multi-Active Bridge (MAB) converters, as described in literature, are typically based on voltage converters. This implies that all their ports are either supplied by a voltage source or connected to loads that behave like a voltage source (e.g. a parallel capacitor). However, in certain situations, a current-fed input port may be desirable due to load characteristics or operational constraints. A port is current-fed if it is connected to a current source. For instance, a photovoltaic (PV) panel or a battery connected to the MAB converter through a series inductance can be considered a current source. A hybrid-fed MAB structure mixes both current-fed and voltage-fed ports.

Current-fed DAB converters have been presented in several papers in literature [61], [62], [63], [64]. Similarly, some previous works have introduced different topologies of multiport converters with one or more current-fed ports [65], [66], [67]. In [65], a three-port converter topology is proposed, where a solar PV panel, a battery and a DC load are connected together, as shown in Figure 4.1. The topology used in this paper is a current-fed Dual-Active Bridge topology, where the battery and PV panel share the same transformer winding. As a result, there is no galvanic isolation between these two ports. This paper proposes a small-signal mathematical model and a control strategy to regulate the battery current and the DC link voltage at the load side.

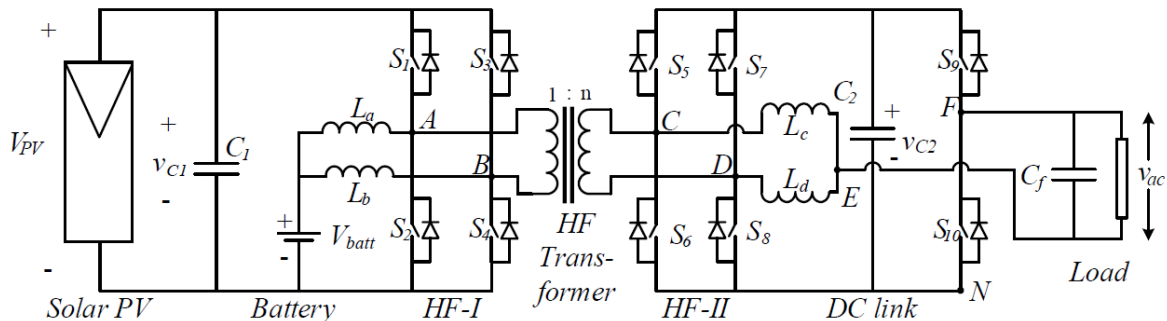


Figure 4.1: Proposed current-fed DAB converter topology in [65].

In [66], a Triple-Active Bridge (TAB) topology is proposed combining two input DC current sources in a magnetic form, by connecting them to a resistive load through a coupled multi-winding transformer (Figure 4.2). The operation principle is explained, and a control strategy for the power flow regulation is achieved. However, this topology consists of three unidirectional ports, which only allow power to flow from the sources to the load. It would be more interesting to have bidirectional ports in renewable energy applications for connecting a battery system or the grid for example.

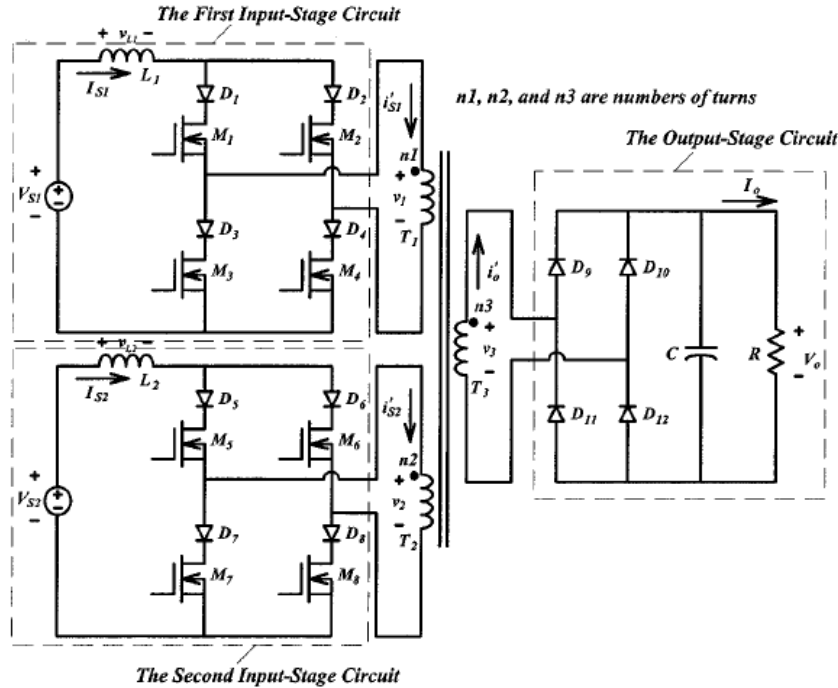


Figure 4.2: Proposed current-fed TAB topology in [66].

In this chapter, a new hybrid-fed, fully coupled Triple-Active Bridge (TAB) converter topology is studied, modelled and controlled. The topology has two voltage-fed ports and one current-fed port, with the current-fed port and one of the voltage-fed ports being unidirectional, while the second voltage-fed port is bidirectional. The coupling between the ports is due to the presence of inductances at the transformer windings of all the ports. This will make this study generic and all-inclusive. Therefore, any simplification of the system, such as the absence of an inductance at one of the ports for decoupling purposes (as proposed in reference [68], presented in the Appendix), will be a particular case of the study presented in this chapter. Thus, the proposed control strategy is more robust as it will remain valid even if one of the voltage-fed ports is lost.

The addition of a current-fed port offers several advantages over classical voltage-fed converters. These include inherent soft switching on the full operation range, even at light loads and when voltage mismatches occur, and the absence of an input capacitor on the current port, which can decrease the system's efficiency and generate resonances as shown in Chapter 1 Section 5. However, the current-fed port does introduce complexity to the system's control. In fact, using a current inverter at one of the ports of a MAB converter imposes control conditions on all the system's ports. Non-compliance with any of these conditions can cause various problems, ranging from hard switching on some ports to brutal over-voltages on the current port.

The main purpose of this chapter is to investigate the feasibility of developing a closed-loop control strategy for the proposed fully-coupled hybrid-fed MAB converter topology. This must take into account the strict control restrictions imposed by the current-fed port, which limit the operational area of this converter.

Firstly, this chapter details the operating principles and control limits of the proposed topology. Following this, a generalized average model is developed to calculate the control parameters and guide the system towards a desired operating point. A controller is then used to eliminate the steady state error of the generalized average model, which is caused by certain simplifying assumptions that are made. A reduced-order model is also elaborated to simplify the study of the system's dynamic behaviour and the design of its controllers. This will allow a real-time calculation of these controllers when the operating point or the control characteristics change. Finally, based on these developed mathematical models, a control strategy is proposed in order to regulate the power flows of this system, while taking into consideration its control restrictions and imposing response characteristics such as time responses. Simulation results using Matlab/Simulink are presented to validate the proposed strategy.

4.2. The Proposed Converter

4.2.1. Topology of the Hybrid-Fed TAB Converter

A current inverter is a type of DC-AC converter that uses a current source on the DC side [69]. Figure 4.3 shows the proposed topology of a coupled TAB converter having a current inverter connected to a temporary current source at port #1 and classical H-Bridges at ports #2 and #3. Port #1 represents a unidirectional current source, such as a PV module. Port #2 is a bidirectional voltage-fed port that can be connected to a battery system or the grid for example. Port #3 is a unidirectional voltage-fed port that is connected to a DC load.

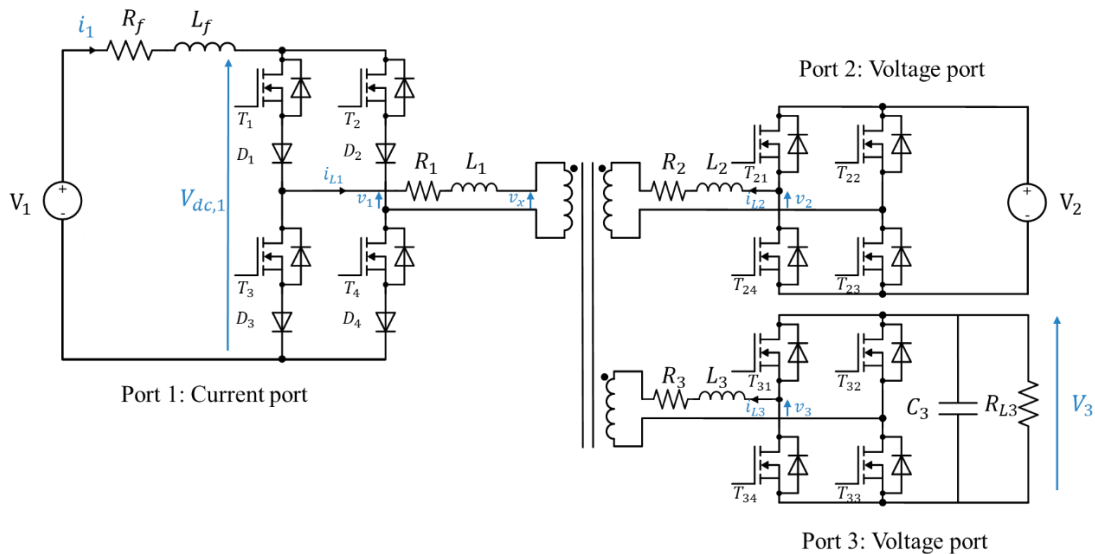


Figure 4.3: Coupled hybrid-fed TAB converter topology.

The ports of this TAB converter are coupled because of the presence of an inductance at each port. This inductance can either be the leakage inductance of the transformer alone or in series with an externally connected one. Consequently, this converter behaves as a multi-variable system with multiple inputs and outputs (MIMO), as explained in Chapter 1. In other words, changing one control input parameter would affect all the converter's ports.

Controlling the power flows of this converter can be done by regulating port #1's input current i_1 and port #3's output voltage V_3 . As this is a coupled multiport converter, the algebraic sum of all input and output powers of the system should be approximately equal to zero (or equal to

the system's losses), in accordance with the law of power conservation. Therefore, the power that will be flowing from port #2 into the transformer will be imposed by the following expression (neglecting the losses and the power stored in the magnetic core of the transformer):

$$P_2 = -P_1 - P_3,$$

where P_1 and P_3 are the powers flowing from ports #1 and #3 respectively.

The waveforms of this TAB's AC signals circulating in the transformer windings are shown in Figure 4.4, all along with the command signals of switches T_1 , T_{21} and T_{31} . The command signal of switch T_4 is similar to that of T_1 . The command signals of T_2 and T_3 are similar and can be obtained by shifting the command signal of switch T_1 by 180° . Similarly, the command signals of switches T_{23} and T_{33} of the voltage ports are similar to those of T_{21} and T_{31} respectively. The command signals of T_{22} and T_{24} are similar, as are those of T_{32} and T_{34} . These can be obtained by shifting the command signals of switches T_{21} and T_{31} by 180° , respectively.

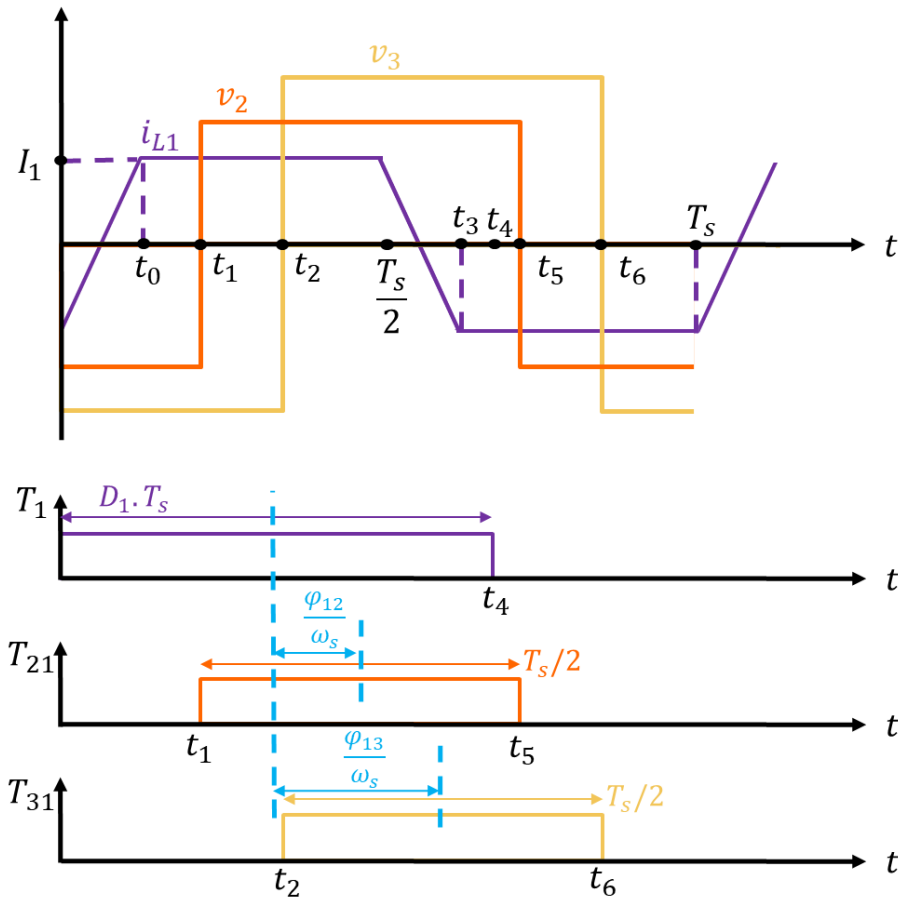


Figure 4.4: AC waveforms of the hybrid-fed TAB converter.

The trapezoidal current i_{L1} shown in Figure 4.4 is, as presented in Figure 4.3, the current circulating in the transformer winding at port #1. v_2 and v_3 are the AC voltages on the transformer side of ports #2 and #3 respectively. D_1 is the duty cycle of the command of port #1's switches ($0.5 < D_1 < 1$). φ_{12} and φ_{13} are the phase shifts (in radians) of the command signals of switches T_{21} and T_{31} with respect to T_1 , respectively. The command duty cycles of the voltage ports' switches are fixed to $D_2 = D_3 = 50\%$ on all the operation range, so v_2 and v_3 are 2-level voltages as shown in Figure 4.4. T_s is the switching period (f_s is the switching frequency).

Figure 4.5 shows the star-delta equivalent circuits of the transformer windings referred to port #1, with $v_2' = \frac{n_1}{n_2} \cdot S_2 \cdot V_2$ and $v_3' = \frac{n_1}{n_3} \cdot S_3 \cdot V_3$. S_2 and S_3 are the switching functions of ports #2 and #3 respectively. n_i is the number of turns of the transformer winding of port #i. In these equivalent circuits, the current-fed port #1 is replaced by an equivalent voltage source. The expression of v_1 , the AC voltage on the transformer side of port #1, will be developed in the next section. The voltage at the star point v_x can be obtained by the following expression:

$$v_x = L_a \cdot v_1 + L_b \cdot v_2' + L_c \cdot v_3' \quad (4.1)$$

where:

$$L_a = \frac{\frac{1}{\frac{1}{L_2'} + \frac{1}{L_3'}}}{L_1 + \frac{1}{\frac{1}{L_2'} + \frac{1}{L_3'}}}; \quad L_b = \frac{\frac{1}{\frac{1}{L_1} + \frac{1}{L_3'}}}{L_2' + \frac{1}{\frac{1}{L_1} + \frac{1}{L_3'}}}; \quad L_c = \frac{\frac{1}{\frac{1}{L_1} + \frac{1}{L_2'}}}{L_3' + \frac{1}{\frac{1}{L_1} + \frac{1}{L_2'}}$$

With $L'_k = \left(\frac{n_1}{n_k}\right)^2 L_k$.

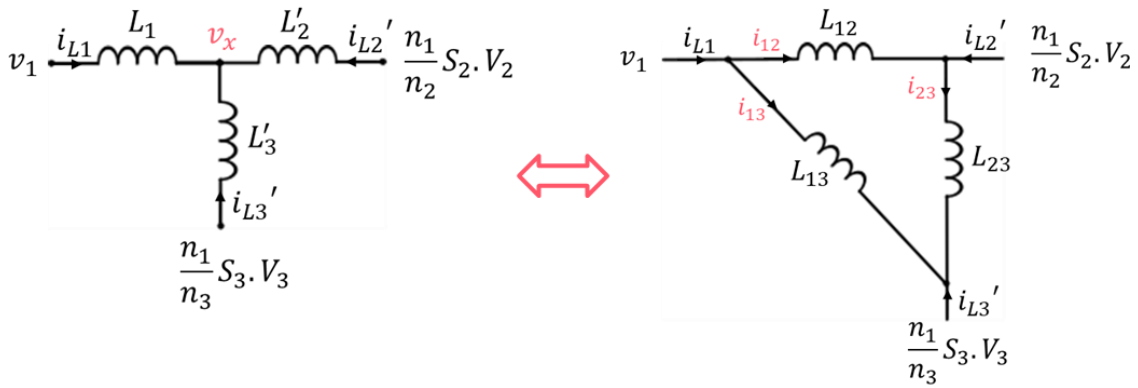


Figure 4.5: Star-delta transformation of the transformer windings referred to port #1.

The link inductances of the delta equivalent circuit can be calculated by using equation (1.1), which is:

$$L_{ij} = \begin{cases} NA, & \forall i = j \\ L'_i + L'_j + L'_i L'_j \left(\sum_{k \neq i, j}^n \frac{1}{L'_k} \right), & \forall i \neq j \end{cases}$$

4.2.2. Working Principle

At each operating point, the operation cycle of this TAB converter is divided into several time intervals (Figure 4.4), allowing both power transfer and current sign change at port #1. It is also important to note that the operation principle of port #1 differs from that of ports #2 and #3 because the switches of port #1 are composed of a transistor and a series-connected diode. Consequently, bidirectional voltage and unidirectional current flow are allowed at this port. The integration of the series-connected diodes will facilitate the automatic blocking of current in the switches, which will be employed during the current sign change phases.

a) $0 \leq t \leq t_0$: (*Current sign change interval*)

At $t = 0$, switches T_1 and T_4 are turned on. T_2 and T_3 were already ON before $t = 0$ from the previous cycle and the value of port #1's AC current i_{L1} was equal to $-I_1$. In this time interval, all the switches of current port #1 are ON, meaning that $v_1 = 0$ (Figure 4.6.a). Therefore, we can deduce from expression (4.1) that $v_x = L_b \cdot v_2' + L_c \cdot v_3'$. At the voltage ports, switches T_{22} , T_{24} , T_{32} and T_{34} should be ON, so that $v_2' = -V_2 \cdot \frac{n_1}{n_2}$, $v_3' = -V_3 \cdot \frac{n_1}{n_3}$ and $v_x < 0$. This will allow the transformer current i_{L1} of port #1 to increase from $-I_1$ to I_1 in this interval. i_{L1} is represented by the following expression (neglecting the series resistance R_1 of the leakage inductance at port #1):

$$i_{L1}(t) = -\frac{v_x}{L_1}t - I_1 = \frac{L_b \cdot V_2 \cdot \frac{n_1}{n_2} + L_c \cdot V_3 \cdot \frac{n_1}{n_3}}{L_1}t - I_1 \quad (4.2)$$

where I_1 is the value of the input current i_1 of the current port at the chosen operating point. This current is maintained constant at each operating point by the input inductance L_f , which's value is a lot bigger than the value of the leakage inductance L_1 .

As i_{L1} gets closer to I_1 , the current starts passing more through diodes D_1 and D_4 and less through D_2 and D_3 . At $t = t_0$, diodes D_2 and D_3 are naturally turned off (Figure 4.6.b).

b) $t_0 \leq t \leq \frac{T_s}{2}$: (*Power transfer interval*)

In this time interval, the input current I_1 passes through T_1 , T_4 , D_1 and D_4 and $i_{L1} = I_1$. Switches T_2 and T_3 can be turned off between t_0 and t_1 at zero current (ZCS). The switching of the voltage ports is then achieved in order to allow the transformer current i_{L1} to switch in the next time interval. At $t = t_1$, voltage port #2's H-Bridge is switched and $v_2' = V_2 \cdot \frac{n_1}{n_2}$ (Figure 4.6.c). At $t = t_2$, voltage port #3's H-Bridge is switched and $v_3' = V_3 \cdot \frac{n_1}{n_3}$ (Figure 4.6.d). This model neglects the series resistance R_1 , leading to the following expression of the AC voltage at port #1:

$$v_1 = v_x = \frac{L_b \cdot v_2' + L_c \cdot v_3'}{(1 - L_a)} > 0 \quad (4.3)$$

c) $\frac{T_s}{2} \leq t \leq t_3$: (*Current sign change interval*)

At $t = \frac{T_s}{2}$, T_2 and T_3 are turned on at zero current. Therefore, all the current inverter's switches are ON again and the voltage $v_1 = 0$ (Figure 4.6.e). The star point voltage will be $v_x = L_b \cdot v_2' + L_c \cdot v_3' > 0$, with $v_2' = V_2 \cdot \frac{n_1}{n_2}$ and $v_3' = V_3 \cdot \frac{n_1}{n_3}$. The transformer current at port #1 decreases from I_1 to $-I_1$ and it is represented by the following expression:

$$i_{L1}(t) = \frac{-v_x}{L_1} \left(t - \frac{T_s}{2} \right) + I_1 = -\frac{\left(L_b \cdot V_2 \cdot \frac{n_1}{n_2} + L_c \cdot V_3 \cdot \frac{n_1}{n_3} \right)}{L_1} \left(t - \frac{T_s}{2} \right) + I_1 \quad (4.4)$$

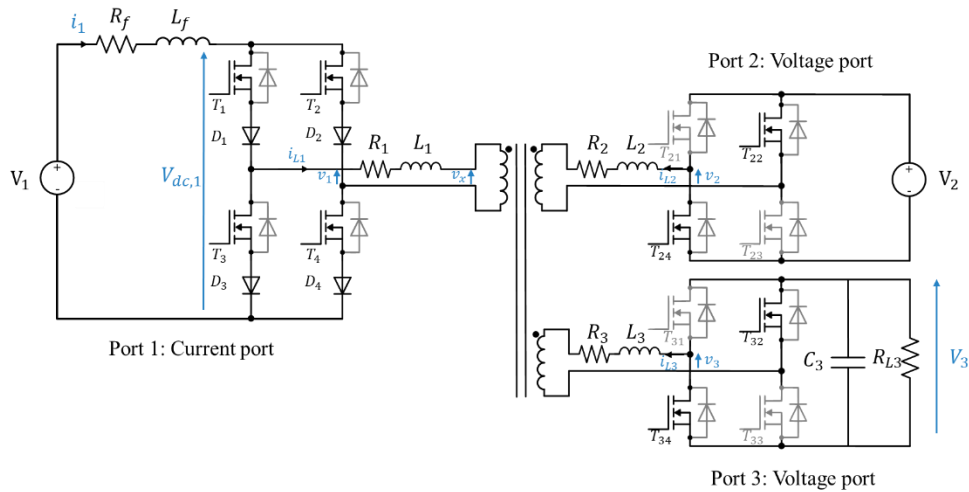
At $t = t_3$, diodes D_1 and D_4 are naturally blocked.

d) $t_3 \leq t \leq T_s$: (Power transfer interval)

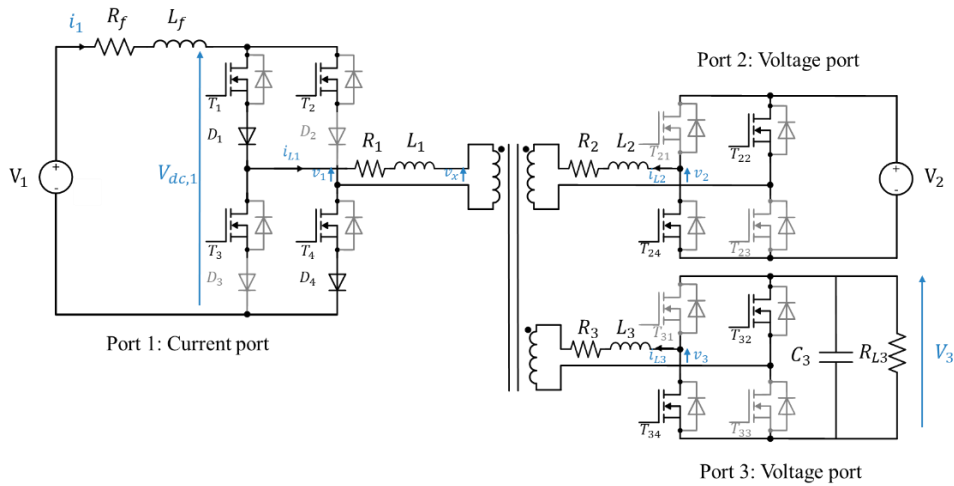
The input current passes entirely through T_2 , T_3 , D_2 and D_3 in this time interval and $i_{L1} = -I_1$. At $t = t_4$, T_1 and T_4 are turned off at zero current. At $t = t_5$ and $t = t_6$, voltage ports #2 and #3 are switched respectively and $v_2' = -V_2 \cdot \frac{n_1}{n_2}$, $v_3' = -V_3 \cdot \frac{n_1}{n_3}$. The AC voltage at port #1 will be:

$$v_1 = v_x = \frac{L_b \cdot v_2' + L_c \cdot v_3'}{(1 - L_a)} < 0 \quad (4.5)$$

This cycle is then repeated for each switching period T_s .



(a)



(b)

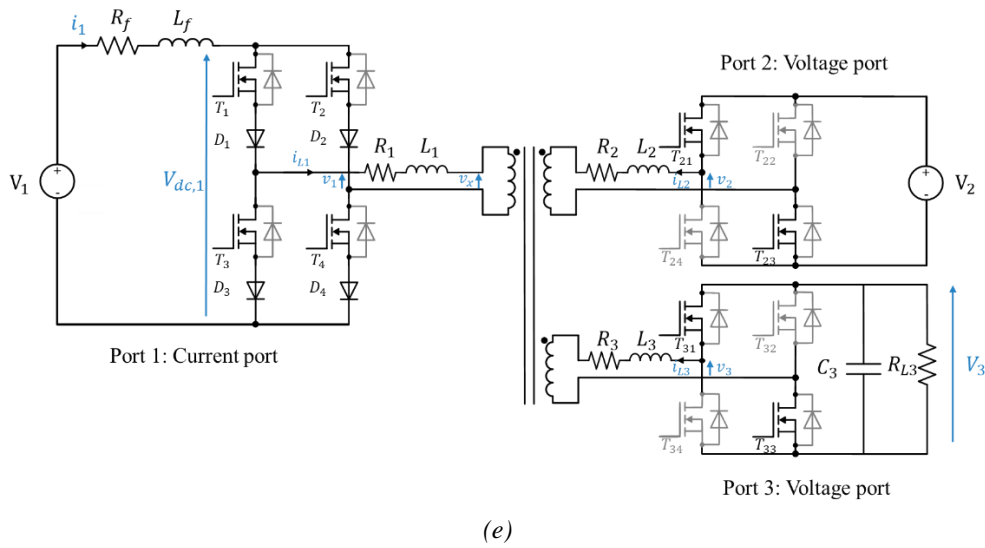
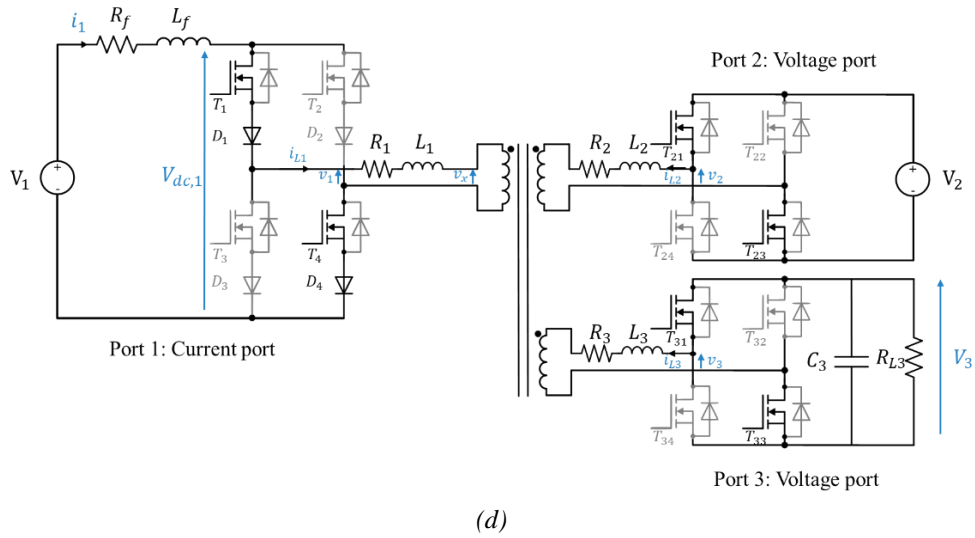
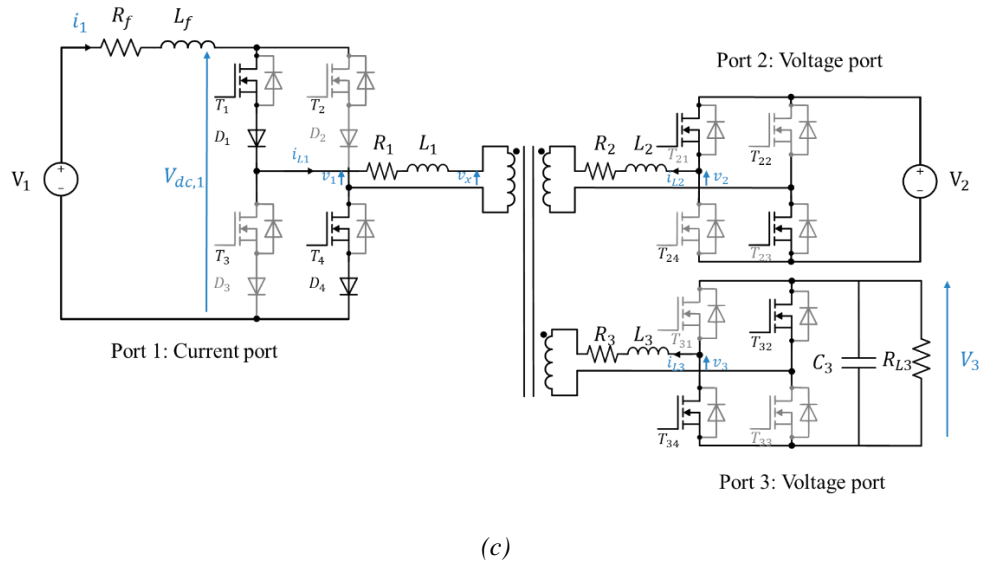


Figure 4.6: Equivalent circuits of the converter at: (a) $0 < t < t_0$; (b) $t_0 < t < t_1$; (c) $t_1 < t < t_2$; (d) $t_2 < t < \frac{T_S}{2}$; (e) $\frac{T_S}{2} < t < t_3$ (switches in grey are OFF).

4.2.3. Operating Conditions

In order to be able to transfer power between ports, achieve a soft switching on the whole operation range for all the active bridges and prevent over-voltages at port #1, three main conditions must be met. These will be detailed in this section for the second half of a switching period. The conditions that should be met during the first half of the switching period can be easily obtained due to the operational symmetry.

- a) To avoid over-voltages and achieve soft switching at port #1, it is necessary to ensure that the current inverter's switches are not turned off until the transformer current i_{L1} has completely reversed and their series diodes have blocked. Otherwise, these switches would block an important current in the link inductance, resulting in abrupt over-voltages at port #1. This condition can be written as follows:

$$t_4 \geq t_3 \rightarrow D_1 T_s \geq \frac{T_s}{2} + t_0$$

With $t_0 = \frac{2L_1 I_1}{(L_b \cdot V_2 \cdot \frac{n_1}{n_2} + L_c \cdot V_3 \cdot \frac{n_1}{n_3})}$ from equation (4.2).

Therefore,

$$D_1 \geq \frac{2L_1 I_1}{(L_b \cdot V_2 \cdot \frac{n_1}{n_2} + L_c \cdot V_3 \cdot \frac{n_1}{n_3}) \cdot T_s} + \frac{1}{2} \quad (4.6)$$

- b) The voltage ports' AC voltages v_2' and v_3' should be reversed after the current i_{L1} 's full reversal and the blocking of both the diodes and their series switches at port #1. If v_2 and/or v_3 are reversed before that, the current i_{L1} may not be able to reverse, so no power can be exchanged between the ports. Additionally, if they are reversed between the blocking of the diodes and their series switches, the diodes can be turned on again, causing over-voltages at port #1. This condition also ensures a soft switching (ZVS) at the voltage ports and it can be written as the two following expressions:

$$t_5 \geq t_4 \rightarrow \frac{D_1 T_s}{2} + \varphi_{12} \frac{T_s}{2\pi} + \frac{T_s}{4} \geq D_1 T_s$$

$$t_6 \geq t_4 \rightarrow \frac{D_1 T_s}{2} + \varphi_{13} \frac{T_s}{2\pi} + \frac{T_s}{4} \geq D_1 T_s$$

Therefore,

$$\varphi_{12} \geq \pi \cdot \left(D_1 - \frac{1}{2} \right) \quad (4.7)$$

$$\varphi_{13} \geq \pi \cdot \left(D_1 - \frac{1}{2} \right) \quad (4.8)$$

We can deduce from equations (4.2) and (4.4) that the slope of current i_{L1} during its reversal is proportional to $-v_x = -(L_b \cdot v_2' + L_c \cdot v_3')$. Therefore, the reversal of this current is guaranteed if both AC voltages of ports #2 and #3 have the same sign (both negative for a positive slope or both positive for a negative slope). Additionally, current i_{L1} 's slope will be maximized this way. Consequently, conditions (4.7) and (4.8) should always be respected simultaneously.

As we can notice, conditions (4.6) to (4.8) depend on the operating point of the converter, with the values of $I_1, V_3, D_1, \varphi_{12}$ and φ_{13} varying according to the desired power flows.

Additionally, the value of port #1's duty cycle D_1 constrains the phase shift values of ports #2 and #3. For these reasons, the control of this topology is considered complex.

4.3. Full-Order Generalized Average Model of the Hybrid-Fed TAB Converter

The state space equations of the studied system are:

$$\begin{aligned}
\bullet \quad L_f \frac{di_1}{dt} &= V_1 - V_{dc,1} - R_f \cdot i_1 \\
\bullet \quad C_3 \frac{dV_3}{dt} &= -\frac{V_3}{R_{L3}} + S_3 \cdot i_{13} \cdot \frac{n_1}{n_3} + S_3 \cdot i_{23} \cdot \frac{n_1}{n_3} \\
\bullet \quad L_{12} \frac{di_{12}}{dt} &= v_1 - \frac{n_1}{n_2} S_2 \cdot V_2 - R_{12} \cdot i_{12} \\
\bullet \quad L_{13} \frac{di_{13}}{dt} &= v_1 - \frac{n_1}{n_3} S_3 \cdot V_3 - R_{13} \cdot i_{13} \\
\bullet \quad L_{23} \frac{di_{23}}{dt} &= \frac{n_1}{n_2} S_2 \cdot V_2 - \frac{n_1}{n_3} S_3 \cdot V_3 - R_{23} \cdot i_{23}
\end{aligned} \tag{4.9}$$

with:

$$V_{dc,1} = \begin{cases} v_1 & \text{for } 0 \leq t \leq \frac{T_s}{2} \\ -v_1 & \text{for } \frac{T_s}{2} \leq t \leq T_s \end{cases};$$

$$S_2(t) = \begin{cases} 1 & \text{for } t_1 \leq t < t_5 \\ -1 & \text{for } 0 \leq t < t_1 \text{ and } t_5 \leq t < T_s \end{cases};$$

$$S_3(t) = \begin{cases} 1 & \text{for } t_2 \leq t < t_6 \\ -1 & \text{for } 0 \leq t < t_2 \text{ and } t_6 \leq t < T_s \end{cases}$$

As explained in Chapter 1, the conventional average modelling typically used for power electronic converters is not suitable for a MAB converter due to its inadequate representation of AC variables. Therefore, a generalized average model of this system is developed in order to study it as a continuous-time model. For simplicity, DC signals will be represented by their average values (0th Fourier series coefficient) and AC signals will be represented by their fundamentals (1st Fourier series coefficient).

As it was stated in Chapter 1, The k^{th} coefficient of the Fourier series of a variable x is a complex number and it is denoted as:

$$\langle x \rangle_k(t) = \langle x \rangle_{kR} + j \langle x \rangle_{kI}$$

R and I refer to the real and imaginary parts of the complex number, respectively. The large signal model of the system is derived from equations (4.9) as:

$$\begin{aligned}
\frac{d\langle i_1 \rangle_0}{dt} &= \frac{V_1}{L_f} - \frac{\langle V_{dc,1} \rangle_0}{L_f} - \frac{R_f}{L_f} \cdot \langle i_1 \rangle_0 \\
\frac{d\langle V_3 \rangle_0}{dt} &= -\frac{\langle V_3 \rangle_0}{C_3 R_{L3}} + \frac{2}{C_3} \cdot \frac{n_1}{n_3} \cdot \langle S_3 \rangle_{1R} \cdot \langle i_{13} \rangle_{1R} + \frac{2}{C_3} \cdot \frac{n_1}{n_3} \cdot \langle S_3 \rangle_{1I} \cdot \langle i_{13} \rangle_{1I} + \frac{2}{C_3} \cdot \frac{n_1}{n_3} \cdot \langle S_3 \rangle_{1R} \cdot \langle i_{23} \rangle_{1R} \\
&\quad + \frac{2}{C_3} \cdot \frac{n_1}{n_3} \cdot \langle S_3 \rangle_{1I} \cdot \langle i_{23} \rangle_{1I}
\end{aligned}$$

$$\begin{aligned}
\frac{d\langle i_{12} \rangle_{1R}}{dt} &= -\frac{R_{12}}{L_{12}} \cdot \langle i_{12} \rangle_{1R} + \omega_s \cdot \langle i_{12} \rangle_{1I} + \frac{\langle v_1 \rangle_{1R}}{L_{12}} - \frac{n_1 \langle S_2 \rangle_{1R}}{n_2 L_{12}} \cdot V_2 \\
\frac{d\langle i_{12} \rangle_{1I}}{dt} &= -\omega_s \cdot \langle i_{12} \rangle_{1R} - \frac{R_{12}}{L_{12}} \cdot \langle i_{12} \rangle_{1I} + \frac{\langle v_1 \rangle_{1I}}{L_{12}} - \frac{n_1 \langle S_2 \rangle_{1I}}{n_2 L_{12}} \cdot V_2 \\
\frac{d\langle i_{13} \rangle_{1R}}{dt} &= -\frac{R_{13}}{L_{13}} \cdot \langle i_{13} \rangle_{1R} + \omega_s \cdot \langle i_{13} \rangle_{1I} + \frac{\langle v_1 \rangle_{1R}}{L_{13}} - \frac{n_1 \langle S_3 \rangle_{1R}}{n_3 L_{13}} \cdot \langle V_3 \rangle_0 \\
\frac{d\langle i_{13} \rangle_{1I}}{dt} &= -\omega_s \cdot \langle i_{13} \rangle_{1R} - \frac{R_{13}}{L_{13}} \cdot \langle i_{13} \rangle_{1I} + \frac{\langle v_1 \rangle_{1I}}{L_{13}} - \frac{n_1 \langle S_3 \rangle_{1I}}{n_3 L_{13}} \cdot \langle V_3 \rangle_0 \\
\frac{d\langle i_{23} \rangle_{1R}}{dt} &= -\frac{R_{23}}{L_{23}} \cdot \langle i_{23} \rangle_{1R} + \omega_s \cdot \langle i_{23} \rangle_{1I} + \frac{n_1 \langle S_2 \rangle_{1R}}{n_2 L_{23}} \cdot V_2 - \frac{n_1 \langle S_3 \rangle_{1R}}{n_3 L_{23}} \cdot \langle V_3 \rangle_0 \\
\frac{d\langle i_{23} \rangle_{1I}}{dt} &= -\omega_s \cdot \langle i_{23} \rangle_{1R} - \frac{R_{23}}{L_{23}} \cdot \langle i_{23} \rangle_{1I} + \frac{n_1 \langle S_2 \rangle_{1I}}{n_2 L_{23}} \cdot V_2 - \frac{n_1 \langle S_3 \rangle_{1I}}{n_3 L_{23}} \cdot \langle V_3 \rangle_0
\end{aligned} \tag{4.10}$$

Where:

$$\langle S_2 \rangle_0 = \langle S_3 \rangle_0 = 0$$

$$\langle S_2 \rangle_{1R} = \frac{2}{\pi} \cos(D_1\pi + \varphi_{12})$$

$$\langle S_2 \rangle_{1I} = -\frac{2}{\pi} \sin(D_1\pi + \varphi_{12})$$

$$\langle S_3 \rangle_{1R} = \frac{2}{\pi} \cos(D_1\pi + \varphi_{13})$$

$$\langle S_3 \rangle_{1I} = -\frac{2}{\pi} \sin(D_1\pi + \varphi_{13})$$

$$\begin{aligned}
\langle v_1 \rangle_{1R} &= \frac{1}{\pi} \cdot \left(\frac{2L_b}{(1-L_a)} \cdot \frac{n_1}{n_2} \cdot V_2 \cdot \cos(D_1\pi + \varphi_{12}) + \frac{2L_c}{(1-L_a)} \cdot \frac{n_1}{n_3} \cdot \langle V_3 \rangle_0 \cdot \cos(D_1\pi + \varphi_{13}) \right. \\
&\quad \left. + \left(L_b \cdot V_2 \cdot \frac{n_1}{n_2} + L_c \cdot \langle V_3 \rangle_0 \cdot \frac{n_1}{n_3} \right) \cdot \frac{\sin(\omega_s t_0)}{(1-L_a)} \right)
\end{aligned}$$

$$\begin{aligned}
\langle v_1 \rangle_{1I} &= \frac{1}{\pi} \cdot \left(\frac{-2L_b}{(1-L_a)} \cdot \frac{n_1}{n_2} \cdot V_2 \cdot \sin(D_1\pi + \varphi_{12}) - \frac{2L_c}{(1-L_a)} \cdot \frac{n_1}{n_3} \cdot \langle V_3 \rangle_0 \cdot \sin(D_1\pi + \varphi_{13}) \right. \\
&\quad \left. + \left(L_b \cdot V_2 \cdot \frac{n_1}{n_2} + L_c \cdot \langle V_3 \rangle_0 \cdot \frac{n_1}{n_3} \right) \cdot \frac{\cos(\omega_s t_0)}{(1-L_a)} \right. \\
&\quad \left. - \left(L_b \cdot V_2 \cdot \frac{n_1}{n_2} + L_c \cdot \langle V_3 \rangle_0 \cdot \frac{n_1}{n_3} \right) \cdot \frac{1}{(1-L_a)} \right)
\end{aligned}$$

$$\begin{aligned}
\langle V_{dc,1} \rangle_0 &= -2 \cdot \left(L_b \cdot V_2 \cdot \frac{n_1}{n_2} + L_c \cdot \langle V_3 \rangle_0 \cdot \frac{n_1}{n_3} \right) \cdot \frac{D_1}{(1-L_a)} \\
&\quad + 2 \cdot \left(L_b \cdot V_2 \cdot \frac{n_1}{n_2} + L_c \cdot \langle V_3 \rangle_0 \cdot \frac{n_1}{n_3} \right) \cdot \frac{1}{(1-L_a)} - \frac{2L_b}{(1-L_a)} \cdot \frac{n_1}{n_2} \cdot V_2 \cdot \frac{\varphi_{12}}{\pi} \\
&\quad - \frac{2L_c}{(1-L_a)} \cdot \frac{n_1}{n_3} \cdot \langle V_3 \rangle_0 \cdot \frac{\varphi_{13}}{\pi} + \frac{4L_1}{(1-L_a) \cdot T_s} \cdot \langle i_1 \rangle_0
\end{aligned}$$

The large signal model (4.10) can be represented by:

$$\dot{X} = A.X + B.U,$$

where $X = [\langle i_1 \rangle_0 \langle V_3 \rangle_0 \langle i_{12} \rangle_{1R} \langle i_{12} \rangle_{1I} \langle i_{13} \rangle_{1R} \langle i_{13} \rangle_{1I} \langle i_{23} \rangle_{1R} \langle i_{23} \rangle_{1I}]^T$ and $U = [V_1 V_2]^T$.

The system's control input parameters consist of the duty cycle D_1 as well as the phase shifts φ_{12} and φ_{13} . Meanwhile, the control output parameters are $\langle i_1 \rangle_0$ and $\langle V_3 \rangle_0$. Therefore, the obtained averaged equations linking the output and the input parameters are non-linear. To use classical linear controllers, it is necessary to linearize the equations around an operating point. The system's linear small signal model is derived by introducing minor perturbations to its variables at an operating point and using the Taylor series expansion, such that:

$$\langle x \rangle = x_{eq} + \widehat{x}$$

Where variables with the symbol “ $\widehat{}$ ” represent the small signals (perturbations around the operating point) and x_{eq} represents the value of $\langle x \rangle$ at the operating point, also called equilibrium point.

In this study, we can neglect the perturbations of the voltage sources around their average values ($\widehat{V}_1 = \widehat{V}_2 = 0$). This is because their variation (e.g. voltage of a PV panel, a battery system or the grid) is very slow compared to the fast control dynamics. The resulting linearized mathematical model has an order of 8.

4.4. Reduced-Order Model of the Hybrid-Fed TAB Converter

The reduced-order model is a simplified version of a system that is easier to study and simulate. It also simplifies the design of the system controllers [39], allowing for real-time recalculation of the controllers when the operating point changes. However, a drawback of this order reduction is the decreased precision of the mathematical model.

Reduced-order averaged modelling involves splitting the system's dynamics in the frequency domain into two parts: the low-frequency dynamics (slow variables) and the high-frequency dynamics (fast variables) [39]. The study of the system's behaviour then only considers the dominant dynamics.

For the hybrid-fed TAB converter, the DC variables can be considered as slow variables and the AC variables as fast variables. In this case, the slow variables represent the input/output parameters of the system, whereas the fast variables represent the internal functioning of the converter. Since the control of this TAB converter aims to regulate the slow input/output parameters, the dominant low-frequency dynamics are preserved and the fast dynamics are ignored in the reduced-order model. The two subsystems can therefore be represented as follows:

- The slow-dynamics subsystem which will be indexed by “s”
- The fast-dynamics subsystem which will be indexed by “f”

The state vector X of the full-order system (4.10) will then be split into two parts:

$$X = [X_s X_f]^T$$

Where: $X_s = [\langle i_1 \rangle_0 \quad \langle V_3 \rangle_0]^T$ and
 $X_f = [\langle i_{12} \rangle_{1R} \quad \langle i_{12} \rangle_{1I} \quad \langle i_{13} \rangle_{1R} \quad \langle i_{13} \rangle_{1I} \quad \langle i_{23} \rangle_{1R} \quad \langle i_{23} \rangle_{1I}]^T$.

Therefore, system (4.10) becomes:

$$\dot{X} = A \cdot X + B \cdot U \rightarrow \begin{cases} \dot{X}_s = A_{ss} \cdot X_s + A_{sf} \cdot X_f + B_s \cdot U \\ \dot{X}_f = A_{fs} \cdot X_s + A_{ff} \cdot X_f + B_f \cdot U \end{cases}$$

Matrices A_{ss} , A_{sf} , A_{fs} , A_{ff} , B_s and B_f are obtained through a proper rearrangement of matrices A and B . To obtain the reduced-order model, we start by solving the fast dynamics subsystem at a chosen operating (equilibrium) point ($\dot{X}_{f,eq} = 0$), by considering the slow variables constant and equal to their average values ($X_s = X_{s,eq}$, so $\langle i_1 \rangle_0 = I_{1,eq}$ and $\langle V_3 \rangle_0 = V_{3,eq}$). The average response $X_{f,eq}$ of the fast subsystem is obtained from this step. After that, in the slow subsystem, the fast variables will be replaced by their average response ($X_f = X_{f,eq}$) calculated in the previous step. Then, the slow subsystem is linearized around the chosen operating point while ignoring the dynamics of the fast variables. This will give us the linearized reduced-order model of the converter, which is:

$$\begin{aligned} \frac{d\langle \hat{i}_1 \rangle_0}{dt} &= \left(-\frac{R_f}{L_f} - \frac{4L_1}{L_f \cdot (1 - L_a) \cdot T_s} \right) \cdot \langle \hat{i}_1 \rangle_0 \\ &+ \frac{2L_c}{L_f \cdot (1 - L_a)} \cdot \frac{n_1}{n_3} \left(D_{1,eq} - 1 + \frac{\varphi_{13,eq}}{\pi} \right) \cdot \langle \hat{V}_3 \rangle_0 \\ &+ \left(\frac{2L_b}{L_f \cdot (1 - L_a)} \cdot \frac{n_1}{n_2} \cdot V_2 + \frac{2L_c}{L_f \cdot (1 - L_a)} \cdot \frac{n_1}{n_3} \cdot V_{3,eq} \right) \cdot \hat{D}_1 \\ &+ \frac{2L_b}{L_f \cdot (1 - L_a)} \cdot \frac{n_1}{n_2} \cdot V_2 \cdot \frac{\hat{\varphi}_{12}}{\pi} + \frac{2L_c}{L_f \cdot (1 - L_a)} \cdot \frac{n_1}{n_3} \cdot V_{3,eq} \cdot \frac{\hat{\varphi}_{13}}{\pi} \\ \frac{d\langle \hat{V}_3 \rangle_0}{dt} &= -\frac{\langle \hat{V}_3 \rangle_0}{C_3 R_{L3}} \\ &- \frac{4}{C_3} \cdot \frac{n_1}{n_3} \cdot [I_{13,R,eq} \cdot \sin(D_{1,eq} \cdot \pi + \varphi_{13,eq}) \\ &+ I_{13,I,eq} \cdot \cos(D_{1,eq} \cdot \pi + \varphi_{13,eq}) + I_{23,R,eq} \cdot \sin(D_{1,eq} \cdot \pi + \varphi_{13,eq}) \\ &+ I_{23,I,eq} \cdot \cos(D_{1,eq} \cdot \pi + \varphi_{13,eq})] \cdot \hat{D}_1 \\ &- \frac{4}{\pi C_3} \cdot \frac{n_1}{n_3} \cdot [I_{13,R,eq} \cdot \sin(D_{1,eq} \cdot \pi + \varphi_{13,eq}) \\ &+ I_{13,I,eq} \cdot \cos(D_{1,eq} \cdot \pi + \varphi_{13,eq}) + I_{23,R,eq} \cdot \sin(D_{1,eq} \cdot \pi + \varphi_{13,eq}) \\ &+ I_{23,I,eq} \cdot \cos(D_{1,eq} \cdot \pi + \varphi_{13,eq})] \cdot \hat{\varphi}_{13} \end{aligned} \quad (4.11)$$

As it can be noticed, the order of the system's mathematical model has been reduced from 8 to 2 by using the reduced-order modelling method. This simplifies the study of the dynamical behaviour and control design of the TAB converter.

The Laplace transform of the obtained linearized reduced-order model (4.11) will lead to the following reduced transfer functions linking the input current I_1 of port #1 to the duty cycle D_1 on the one hand and the output DC voltage V_3 of port #3 to the phase shift φ_{13} on the other hand:

$$G_{i1_r}(s) = \frac{I_1(s)}{D_1(s)} \Big|_{\substack{\hat{\varphi}_2=0 \\ \hat{\varphi}_3=0}} = \frac{a \cdot s + b}{(s + c)(s + d)} \quad (4.12)$$

$$G_{v3_r}(s) = \frac{V_3(s)}{\varphi_3(s)} \Big|_{\substack{\hat{\varphi}_2=0 \\ \hat{D}_1=0}} = \frac{e}{(s + d)} \quad (4.13)$$

With:

$$a = \frac{2L_b}{L_f \cdot (1 - L_a)} \cdot \frac{n_1}{n_2} \cdot V_2 + \frac{2L_c}{L_f \cdot (1 - L_a)} \cdot \frac{n_1}{n_3} \cdot V_{3,eq}$$

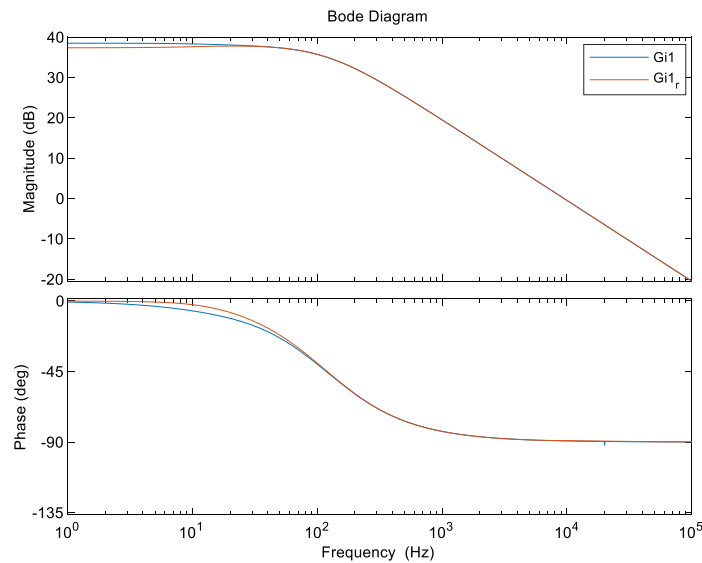
$$b = \frac{a}{C_3 R_{L3}} - \frac{8}{C_3} \cdot \frac{L_c}{L_f \cdot (1 - L_a)} \cdot \left(\frac{n_1}{n_3}\right)^2 \cdot \left(D_{1,eq} - 1 + \frac{\varphi_{13,eq}}{\pi}\right) \cdot (I_{13,R,eq} \cdot \sin(D_{1,eq} \cdot \pi + \varphi_{13,eq}) \\ + I_{13,L,eq} \cdot \cos(D_{1,eq} \cdot \pi + \varphi_{13,eq}) + I_{23,R,eq} \cdot \sin(D_{1,eq} \cdot \pi + \varphi_{13,eq}) \\ + I_{23,L,eq} \cdot \cos(D_{1,eq} \cdot \pi + \varphi_{13,eq}))$$

$$c = \frac{R_f}{L_f} + \frac{4L_1}{L_f \cdot (1 - L_a) \cdot T_s}$$

$$d = \frac{1}{C_3 R_{L3}}$$

$$e = \frac{4}{\pi C_3} \cdot \frac{n_1}{n_3} \cdot (I_{13,R,eq} \cdot \sin(D_{1,eq} \cdot \pi + \varphi_{13,eq}) + I_{13,L,eq} \cdot \cos(D_{1,eq} \cdot \pi + \varphi_{13,eq}) \\ + I_{23,R,eq} \cdot \sin(D_{1,eq} \cdot \pi + \varphi_{13,eq}) + I_{23,L,eq} \cdot \cos(D_{1,eq} \cdot \pi + \varphi_{13,eq}))$$

Figure 4.7 compares the Bode plots of the full-order transfer functions (G_{v3} and G_{i1}) calculated from the linearization of system (4.10) to the reduced-order ones (G_{v3_r} and G_{i1_r}) expressed in equations (4.12) and (4.13). As we can notice, the full-order and the reduced-order responses of each one of these two transfer functions are similar at low frequencies (below the switching frequency where the resonance occurs). This proves that the reduced-order model represents the system's slow dynamics appropriately and as expected.



(a)

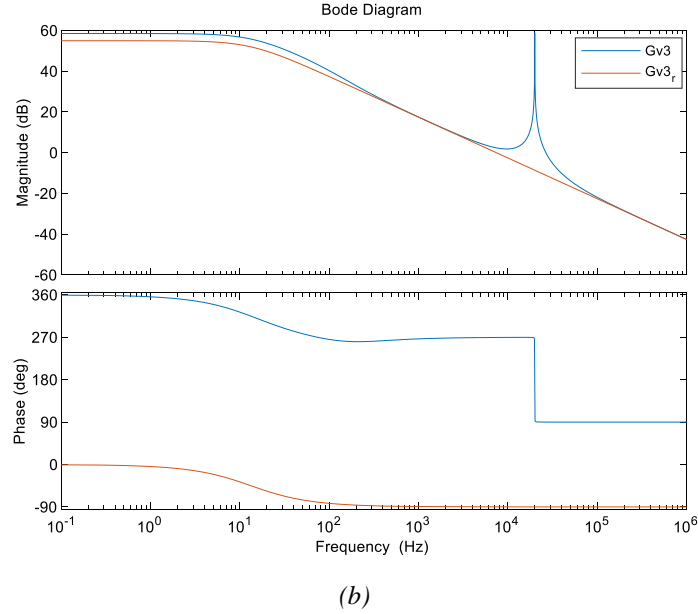


Figure 4.7: Comparison of the Bode plots of the full-order model and the reduced-order model transfer functions of the hybrid-fed TAB converter: (a) Input current I_1 of port #1 controlled by D_1 ; (b) Output voltage V_3 of port #3 controlled by φ_{13} .

Furthermore, transfer function G_{i1_r} can also be reduced by ignoring the dynamics of voltage V_3 , considering that it does not vary a lot around its nominal value. The new reduced transfer function will therefore be a first order transfer function having the following expression:

$$G_{i1_{r2}}(s) = \left. \frac{I_1(s)}{D_1(s)} \right|_{\substack{\hat{\varphi}_2=0 \\ \hat{\varphi}_3=0 \\ \hat{V}_3=0}} = \frac{a}{(s + c)} \quad (4.14)$$

Figure 4.8 compares the Bode plots of the full-order transfer function G_{i1} calculated from the linearization of system (4.10) and the two reduced-order transfer functions of equations (4.12) and (4.14) (G_{i1_r} and $G_{i1_{r2}}$). We can notice that the responses of these three plots are quite similar, proving that the current control's dynamics can also be represented by $G_{i1_{r2}}$, further simplifying the system's order.

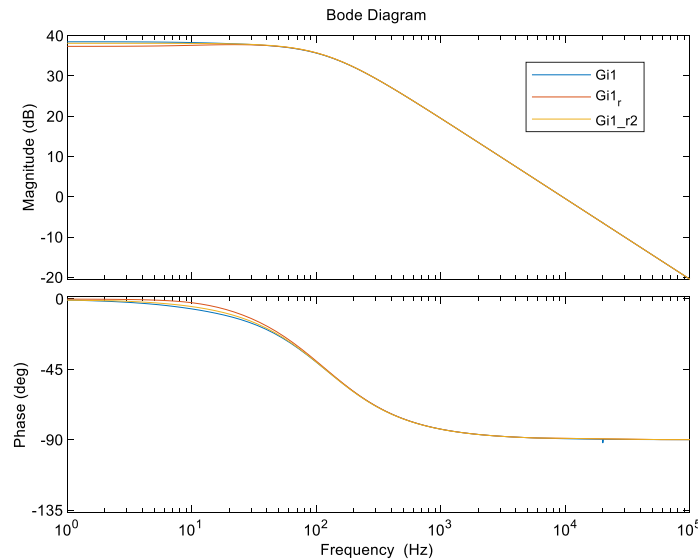


Figure 4.8: Comparison of the Bode plots of the full-order model and the two reduced-order models of the DC current control of port #1.

We deduce from Figure 4.7 and Figure 4.8 that the first order transfer functions $G_{i_{1r_2}}$ and $G_{v_{3r}}$ can be used to study and control the DC current of port #1 and the DC voltage of port #3 of this TAB converter, as their responses are sufficiently close to the full-order model's results.

The order of the reduced transfer functions $G_{v_{3r}}$ and $G_{i_{1r_2}}$ is independent of the number of ports of the TAB converter. Therefore, this developed reduced-order model of the hybrid-fed TAB converter can be generalized to a hybrid-fed MAB converter having n -ports, one of which is current-fed while the $(n-1)$ others are voltage-fed ports. These two reduced-order functions will then still be first order functions regardless of the number of ports of the MAB converter, such that the voltages of the voltage-fed ports do not vary a lot around their average values for a certain operating point. We should note that in this case, it is important to connect at least one of the voltage-fed ports to a stiff voltage source, such as a battery or the grid, in order to impose its voltage value at the current-fed port's side of the transformer. This allows the sign change of its current, which in turn enables the starting of the hybrid-fed MAB converter and the power exchange between its ports.

The reduced-order models developed in this section will be used in the following sections to study the behaviour of this hybrid-fed TAB converter and to design its closed-loop controllers.

4.5. Proposed Control Strategy

Two parameters should be controlled in this system (control output parameters): the DC input current I_1 of port #1 and the DC output voltage V_3 of port #3. As previously stated, the active power value of port #2 will be determined by the law of power conservation. However, the control input parameters are three: D_1 , φ_{12} and φ_{13} . Therefore, at a chosen operating point, an infinity of combinations of the values of $D_{1,eq}$, $\varphi_{12,eq}$ and $\varphi_{13,eq}$ can give us the same desired values of $I_{1,eq}$ and $V_{3,eq}$, as long as the conditions of expressions (4.6) to (4.8) are respected. Additionally, from system (4.10), we can notice that each control output ($I_{1,eq}$ and $V_{3,eq}$) depends on all the control inputs ($D_{1,eq}$, $\varphi_{12,eq}$ and $\varphi_{13,eq}$) of the system. This proves that the studied TAB structure is coupled and a change in one of the control variables will affect all the ports.

One way to control this hybrid-fed TAB converter is by making $D_{1,eq}$ equal to its minimum allowed value expressed in (4.6), necessary to reverse the AC current in port #1, with an added safety margin ϵ at each operating point ($D_{1,eq} = D_{1,min} + \epsilon$). This will allow the maximization of the power transfer time interval. Adding the safety margin ϵ is a way to compensate for parameter inaccuracies and ensure the satisfaction of condition (4.6).

The corresponding values of $\varphi_{12,eq}$ and $\varphi_{13,eq}$ are then calculated from the full-order model expressed in system (4.10) at the chosen operating point. The calculated values of the three control parameters are then fed forward to the system. Adding a feedforward to the control of the TAB converter will lead to the decoupling of its ports' control, as explained in Chapter 1. Then, from (4.7) and (4.8), we get the minimum allowed values of φ_{12} and φ_{13} .

The approximations that were done in the developed mathematical models will lead to a steady state error if only an open loop (feedforward) control is applied. Two PI controllers are therefore added to the control system in order to delete this error at the DC input current I_1 of port #1 and

the DC output voltage V_3 of port #3 (Figure 4.9). Two control parameters are needed for the steady-state error cancellation of the two control output parameters. In this chapter, duty cycle D_1 is used to regulate current I_1 , and phase shift φ_{13} is used to regulate voltage V_3 . The PI controllers are calculated based on the reduced-order model that was developed in the previous section. Adaptable saturation blocks are finally added to the control system in order to ensure that conditions (4.6) to (4.8) are always satisfied. These blocks are also shown in Figure 4.9, where the maximum and minimum allowed values of D_1 and φ_{13} are dynamically calculated.

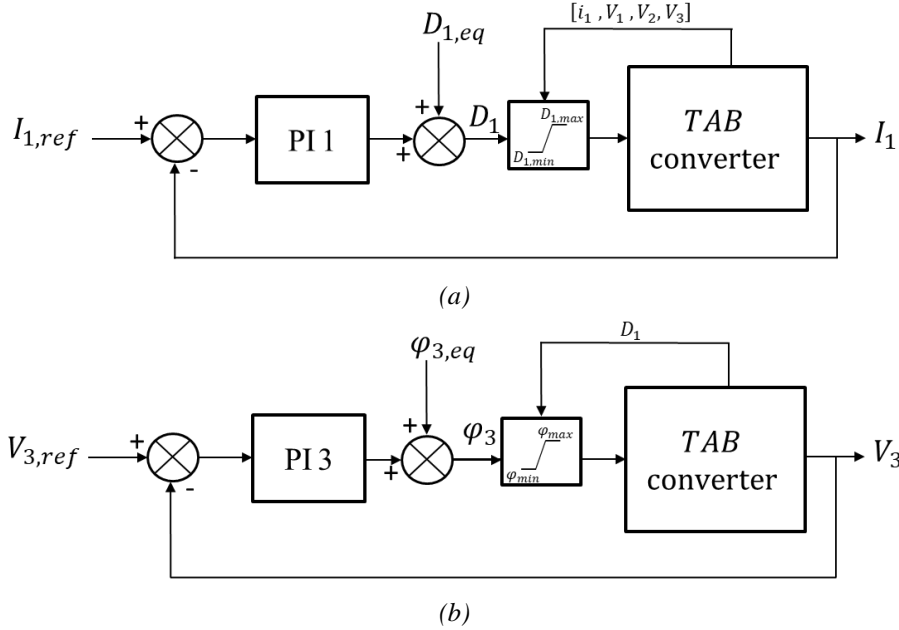


Figure 4.9: Control block diagrams of the hybrid-fed TAB converter: (a) DC current control of port #1; (b) DC voltage control of port #3.

In Figure 4.9, $D_{1,max}$ is the maximum possible value for D_1 and it is equal to one. φ_{max} is the maximum allowed value for φ_{12} and φ_{13} to ensure that the switching of ports #2 and #3 at time instants t_5 and t_6 , respectively, occur before the switching of port #1 at T_s (see Figure 4.4). Therefore, the value of φ_{max} is calculated as follows:

$$t_5 \leq T_s \text{ and } t_6 \leq T_s \rightarrow \varphi_{max} = \pi \cdot \left(\frac{3}{2} - D_1 \right)$$

The controllers PI1 and PI3 have the following expressions, respectively:

$$C_1(s) = \frac{K_{p1} \cdot (T_{i1} \cdot s + 1)}{T_{i1} \cdot s} \quad (4.15)$$

$$C_3(s) = \frac{K_{p3} \cdot (T_{i3} \cdot s + 1)}{T_{i3} \cdot s} \quad (4.16)$$

4.5.1. Input DC Current Control of Port 1

The transfer function G_{i1r2} of equation (4.14) is used to calculate the parameters of the controller PI1 for the input DC current control of port #1. It is a first order transfer function.

We choose $T_{i1} = \frac{1}{c}$. The closed loop transfer function will therefore become:

$$CLTF_1(s) = \frac{C_1(s)G_{i1r2}(s)}{1 + C_1(s)G_{i1r2}(s)} = \frac{K_{p1} \cdot a}{s + K_{p1} \cdot a} = \frac{1}{\tau_1 \cdot s + 1} \quad (4.17)$$

With $\tau_1 = \frac{1}{K_{p1} \cdot a}$ the time constant of the closed loop system.

Considering that the time response value of this closed loop transfer function to get to 95% of the desired current reference is $t_{r1,95\%} = 3 \cdot \tau_1$, the gain K_{p1} is chosen for a desired value of $t_{r1,95\%}$, such that:

$$K_{p1} = \frac{3}{a \cdot t_{r1,95\%}} \quad (4.18)$$

4.5.2. Output DC Voltage Control of Port 3

The transfer function G_{v3r} of equation (4.13) is used to calculate the parameters of controller PI3 for the output DC voltage control of port #3. It is a first order transfer function.

We choose $T_{i3} = \frac{1}{d}$. The closed loop transfer function will therefore be:

$$CLTF_3(s) = \frac{C_3(s)G_{v3r}(s)}{1 + C_3(s)G_{v3r}(s)} = \frac{K_{p3} \cdot e}{s + K_{p3} \cdot e} = \frac{1}{\tau_3 \cdot s + 1} \quad (4.19)$$

With $\tau_3 = \frac{1}{K_{p3} \cdot e}$ the time constant of the closed loop system.

Considering that the time response value of this closed loop transfer function to get to 95% of the desired voltage reference is $t_{r3,95\%} = 3 \cdot \tau_3$, the gain K_{p3} is chosen for a desired value of $t_{r3,95\%}$, such that:

$$K_{p3} = \frac{3}{e \cdot t_{r3,95\%}} \quad (4.20)$$

4.6. Simulated Results and Discussion

The simulation results of the closed-loop control of current I_1 when a setpoint change is applied are presented in Figure 4.10. Table 4.1 shows the parameter values used for the different ports of the simulated TAB converter. The chosen time response to get the parameter values of controller PII from equation (3.29) is $t_{r1,95\%} = 3ms$. We can see from Figure 4.10 that the closed loop time response of the simulated switched model is equal to its chosen value of $3ms$, validating the developed mathematical model and control strategy. The current ripple is dependent on the value of inductance L_f , which can be adjusted based on design requirements and the intended application of the TAB converter (L_f is increased to decrease the ripple).

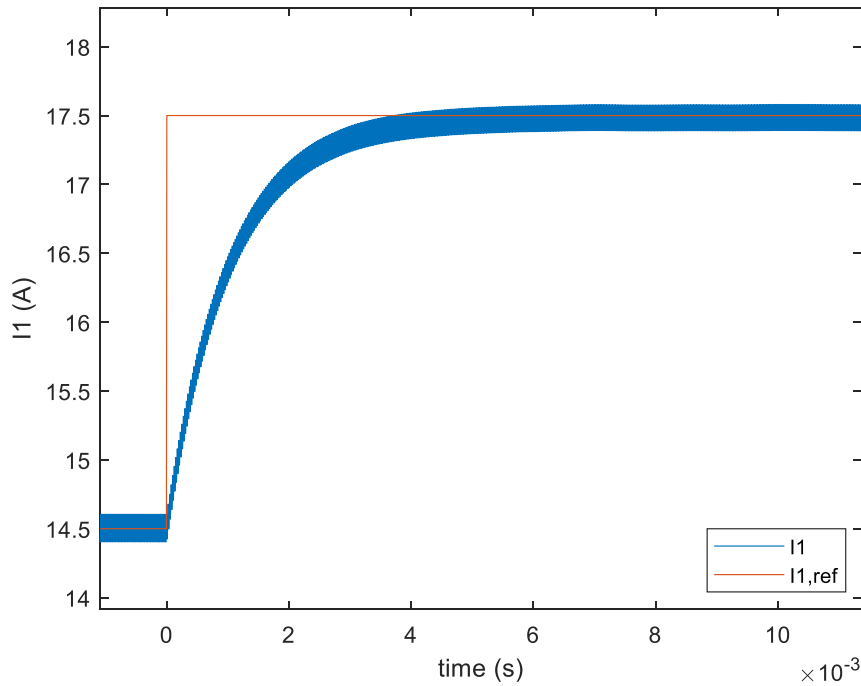


Figure 4.10: Simulation results of the current closed-loop control of port #1 of the hybrid-fed TAB converter.

Figure 4.11 shows the simulation results of the closed loop control of voltage V_3 of this system, when a setpoint change is applied. The chosen time response to get the parameter values of controller PI3 from equation (4.20) is $t_{r3,95\%} = 10ms$. We can see from Figure 4.11 that the closed-loop time response of the simulated switched model is equal to its chosen value (10ms), which validates the developed mathematical model and controller.

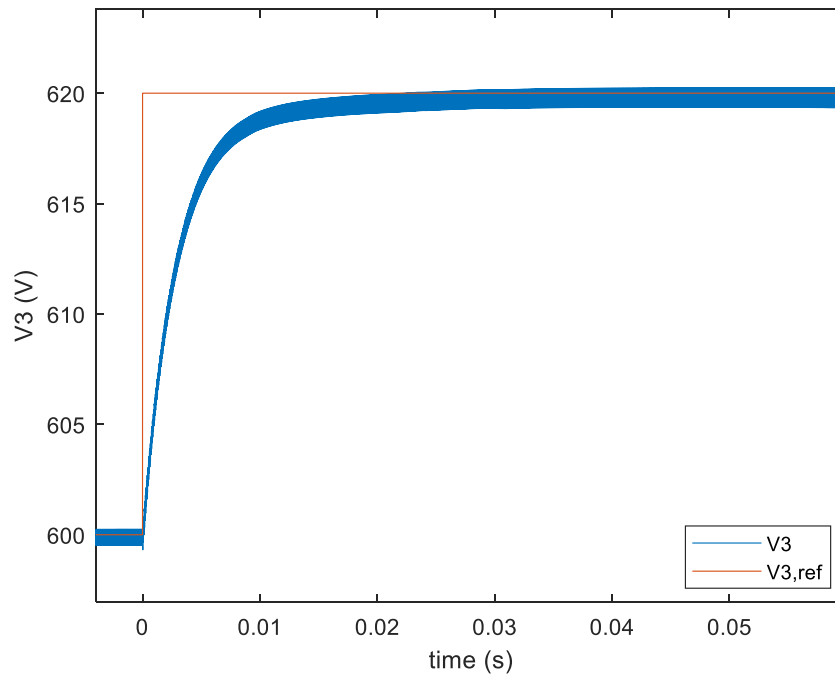


Figure 4.11: Simulation results of the voltage closed-loop control of port #3 of the hybrid-fed TAB converter.

Table 4.1: Parameter values of the simulated hybrid-fed TAB converter.

Parameter symbol	Parameter value
V_1	200 V
V_2	400 V
f_s	20 kHz
L_f	0.016 H
R_f	10 m Ω
L_1	83 μ H
R_1	10 m Ω
L_2	83 μ H
R_2	10 m Ω
L_3	230 μ H
R_3	10 m Ω
C_3	100 μ H
R_{c3}	1 m Ω
L_m	8.3 mH
n_1	100 turns
n_2	83 turns
n_3	124 turns
$P_{3,nominal}$	3 kW (received)
$P_{1,nominal}$	3.5 kW (delivered)
P_{max} (between 2 ports)	4 kW
R_{L3}	120 Ω

The slight mismatch between the characteristics chosen for the calculation of the controller parameters and the characteristics of the simulated responses is due to the simplifying assumptions made during the development of the mathematical model, in particular the first harmonic approximation of the AC signals and the reduction of the model order. To enhance the accuracy of the proposed model, a higher harmonic order can be taken into account. However, this will increase the complexity of the model. The proposed model offers a fair compromise between accuracy and complexity.

Figure 4.12 shows the waveforms of the control input and output parameters of the hybrid-fed TAB converter when the setpoint of current i_1 is changed ($t_{r,1,95\%} = 20ms$). For these results, a safety margin of $\epsilon = 0.01$ for the control of D_1 is taken into consideration ($D_{1,eq} = D_{1,min} + \epsilon$). This value was chosen arbitrarily in this study. As we can notice, current i_1 follows its reference value with the expected response characteristics. DC voltage V_3 also follows its unchanged reference value. The DC current i_2 of port #2 is determined by the law of power conservation such that the sum of the total input and output port powers remains equal to zero. The values of all the control input parameters stay within their allowed intervals.

Figure 4.13 shows the AC voltages at the three transformer windings and the AC current of port #1. No over-voltages have occurred at the current port. Additionally, the waveforms of i_{L1} , v_2 and v_3 shown in Figure 4.13 match their theoretical waveforms drawn in Figure 4.4 and the waveform of v_1 matches its developed expressions in Section 4.2.2. This validates the developed model and the proposed control strategy.

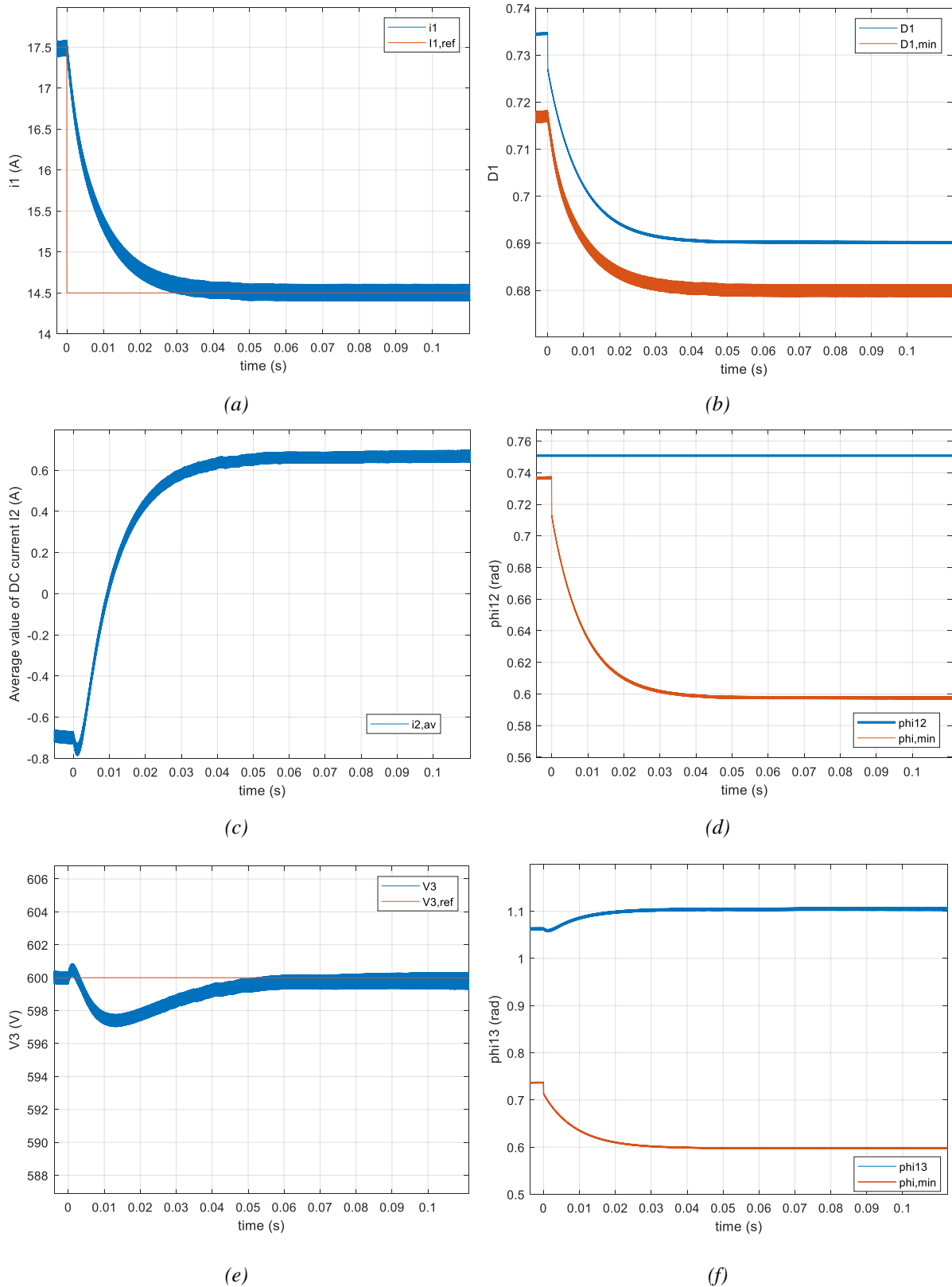


Figure 4.12: Waveforms of the hybrid-fed TAB converter: (a) Input current i_1 of port #1; (b) Duty cycle D_1 of command signal of port #1; (c) Uncontrolled input current i_2 of port #2; (d) Phase shift φ_{12} of command signal of port #2; (e) Output voltage V_3 of port #3; (f) Phase shift φ_{13} of command signal of port #3.

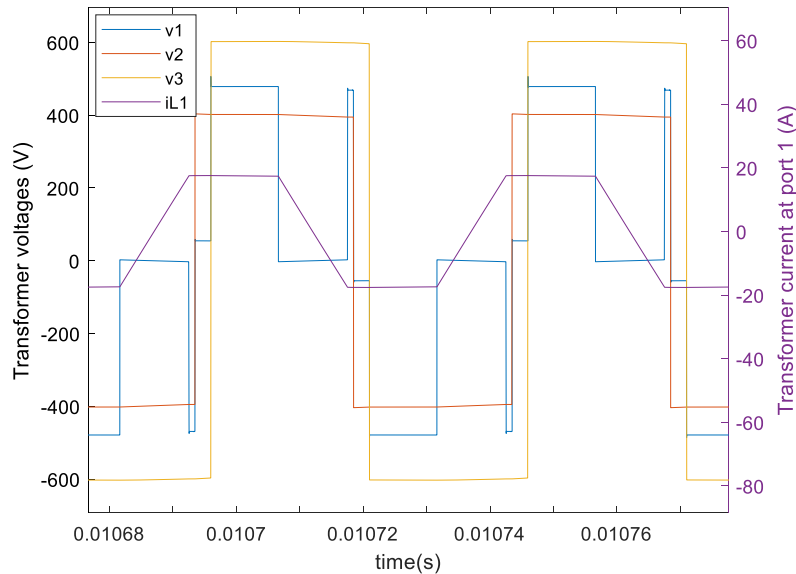


Figure 4.13: Waveforms of the AC voltages of the three ports and the AC current of port #1.

4.7. Conclusion

A hybrid-fed MAB converter is an interesting topology for many applications integrating PV panels and battery storage systems for example. This is mainly due to their soft-switching performances on the whole operation range. However, current-fed ports add operational restrictions to the system, which lead to questioning the feasibility of the closed-loop control of such topologies.

In this chapter, the mathematical modelling and control of a hybrid-fed TAB converter were developed. The working concept of this topology was explained and so were the control conditions that should be respected for a safe functioning without over-voltages and with soft switching. After that, a generalized average model and a reduced-order model of this system were elaborated and compared. A control strategy was proposed based on the developed models and control conditions. The full-order model was used for the calculation of the fed forward control parameters when a setpoint change occurs. This will set the system in a state very close to its desired operating point. The error is then cancelled by PI controllers. The reduced-order model is used to calculate these PI controllers and to simplify the dynamic behaviour study of the system. Adaptable saturation blocks were employed in the control of this TAB converter in order to ensure that the operating conditions are always satisfied, especially when moving from an operating point to another. The mathematical models and the developed control technique were tested and validated using Matlab/Simulink.

The obtained simulation results show the closed-loop response of the input current control of the current-fed port and the output voltage control of one of the voltage-fed ports. Controlling these two variables will allow the control of the power flows between the different ports of the proposed three-port topology. The expected characteristics chosen while calculating the PI controllers' parameters were attained in these responses and no over-voltages have occurred at the current-fed port. This answers the main question of this chapter, proving that the closed-loop control of the proposed topology is possible.

The modelling and control strategy presented in this chapter can be generalized for a hybrid-fed MAB converter with any number of ports, one of which is current-fed. However, the more voltage ports are added, the more control restrictions should be respected and the more complex the system control becomes.

This topology has a number of drawbacks, including additional conduction losses in the series diodes and the voltage oscillations at the switches of the current-fed port. Due to the fact that switching is performed at zero current, it is not possible to properly charge and discharge the parasitic capacitors of the switches, which include both transistors and series diodes. Therefore, the charging and discharging process is achieved by using the transformer current, connecting the parasitic capacitors in series with the link inductance, forming a high frequency resonant LC circuit. This process induces significant voltage oscillations. Compensating for these oscillations through converter control is impossible due to their frequency being much higher than the converter's bandwidth. Therefore, the commonly used method to dampen these oscillations is by adding a snubber circuit, although this results in losses and decreased system efficiency.

In future works, the hybrid-fed TAB converter topology presented in this chapter could benefit from a different approach to determine the three control input parameters (D_1 , φ_{12} and φ_{13}) in order to improve the system's efficiency. For example, reducing the transformer's RMS currents could be achieved by selecting a different combination of control input parameters instead of choosing the combination where $D_{1,eq} = D_{1,min} + \epsilon$. Additionally, using the duty cycles of the voltage-fed ports can also be explored in order to add more degrees of freedom to the system's control. Furthermore, it would be quite interesting to work out an emergency stop strategy for this type of converter.

GENERAL CONCLUSION

The integration of renewable energy sources and energy storage systems into the modern electrical grid is crucial to address the climate change crisis and achieve energy security. To enhance the global electric grid's efficiency, improve power exchanges and guarantee grid ancillary services, multiport converters represent a promising option. They facilitate the interconnection of diverse electrical sources, loads and energy storage systems through a reduced number of conversion stages. Multi-Active Bridge (MAB) converters are multiport converters provided with a full galvanic isolation due to the interconnection of their ports via a high-frequency transformer, which acts as the core of this type of systems. The presence of the transformer also allows the connection of sources and loads with important dissimilarities in their voltage levels.

In general, the primary objective of controlling a MAB converter is to provide each of its ports with its required power value. To achieve this, the correct combination of control inputs needs to be computed and then applied to the system. It is well known that the control system of a MAB converter has more inputs than outputs. Therefore, an infinite number of control input combinations could provide the ports with their required power values. However, most of these combinations would lead to suboptimal system performance. Depending on the control priorities of the application in which the MAB converter is used, and the considered definition of a target performance for that application, at least one of these combinations is optimal.

Chapter 1 of this thesis is dedicated to the mathematical modelling of a MAB converter. First, the selected topology is illustrated and explained. After that, the steady-state model of this topology is developed, first using the First Harmonic Approximation and then the Generalized Harmonic Approximation for higher accuracy. The coupling between the different ports of a MAB converter is discussed, along with several decoupling techniques found in the literature. The dynamic model of the MAB converter is then elaborated based on the Generalized Average Modelling technique to represent the behaviour of the system as it transitions between operating points. The dynamic model is validated through simulation on a three-port MAB converter. Finally, this chapter examines the interaction between the dynamics of a MAB converter and an LC filter connected to one of its ports, and proposes a control-based solution to suppress the instabilities caused by this externally connected resonant circuit.

Chapter 2 details a technique to compute the total conduction and switching losses of an n -port MAB converter. It also proposes a control strategy aiming to minimize these losses while providing the required power values to the ports on the entire operating range. Conduction losses are minimized by cancelling the reactive power exchange between the converter's ports. This additional constraint results in a relation between a number of control input parameters, thus reducing the total number of degrees of freedom of the control. This simplifies the solution of the control optimization problem, allowing it to be executed in real time. Switching losses are minimized by achieving a soft switching on as many switches as possible. The proposed control strategy uses the mathematical model developed in Chapter 1 and the loss calculation model developed at the beginning of Chapter 2 to optimize the performance of the considered MAB converter according to the control priorities set. Two scenarios are considered in this chapter and an optimization algorithm is proposed for each one of them. In the first scenario, the control priority is the minimization of the total conduction and switching losses of the system, regardless of the number of switches operating at ZVS. The second scenario prioritizes

the achievement of a soft switching on all the switches of the converter's ports, while minimizing the total conduction and switching losses as much as possible.

Chapter 3 experimentally validates all the theoretical work presented in the first two chapters. A $4 \times 500W$ MAB converter prototype is built for that purpose. The sizing technique of the prototype is detailed in this chapter. A four-winding transformer is sized and constructed in this thesis in order to complete the developed prototype and to connect its four ports together. The optimization control strategy proposed in this thesis is validated in this chapter, along with the mathematical and loss models. Furthermore, this chapter addresses the potential issue of transformer saturation. An active solution is proposed to eliminate the DC current bias circulating in the transformer, which may eventually lead to its saturation. A special sensor is built in this thesis to properly measure the value of this DC bias, based on a previous work achieved in the G2ELab.

Chapter 4 investigates a new hybrid-fed topology of a MAB converter, mixing both voltage-fed and current-fed ports. Current-fed ports may be interesting in some applications where the behaviour of the source or charge connected to the port can be represented more accurately by a current source. When a current-fed port is added to a MAB converter, soft switching is naturally achieved on all the switches of the ports on the entire operating range. However, the presence of a current-fed port imposes strict control constraints on the system. The proposed hybrid-fed topology is studied and mathematically modelled in this chapter. Additionally, a control strategy is proposed to control the power exchange between its ports while satisfying the control constraints imposed by the current-fed port.

During this thesis, many aspects of the control of a MAB converter have been studied in depth and several new solutions have been proposed for many of its existing problems. However, this work has also led to many other questions and possibilities regarding MAB converters, which were not answered and explored during this three-year PhD project. These questions would be very interesting for future works, as they could lead to further optimization and improvement of the control and the hardware of MAB converters. Some of these aspects are:

- Developing a more accurate loss model, taking into consideration the iron losses of the transformer and its external series inductances, along with the losses in the DC link capacitors and the parasitic capacitances of the system, such as those between the PCB tracks or transformer windings.
- A better understanding of the principles of the magnetic operation, including the coupling and interaction between the transformer's windings, as well as their subsequent impacts on the converter's overall performance. A magnetic model that accounts for this influence and the additional losses that it can generate is necessary for a more effective optimization. This impact should be studied and compared for different winding methods.

- Testing and comparing different methods to carry out the sweep of the control strategy proposed in this thesis, allowing faster convergence with greater precision.
- Extending the proposed optimization control strategy to other MAB converter topologies, such as resonant MAB converters, MAB converters with one or more ports directly connected to an AC power source and hybrid-fed MAB converters. This thesis only considers the connection of DC voltage or current sources to the ports of the MAB converter. However, in some applications, it may be interesting to connect a port to an AC source, such as the grid. This will further allow reducing the number of conversion stages.
- Investigating the interaction of the MAB converter's dynamics with other externally connected systems, such as a rectifier connecting a MAB converter port to an AC voltage source. Adapting the active damping technique proposed in this thesis when an LC filter is connected to a port may be a potential solution to consider.
- Building a more optimized prototype with the aim of reducing its volume and weight while taking into consideration its performance and efficiency. This would give a more accurate picture of the power density of a MAB converter and help to compare different MAB topologies and optimization control strategies.
- Testing the proposed optimization algorithm on a MAB converter prototype with ports featuring higher power ratings, switching frequencies, and voltage and power dissimilarities. In this thesis, this test was only completed through simulation in Chapter 2. However, the experimental validation of this point could be interesting as it brings us closer to actual industrial applications, such as battery chargers or domestic energy hubs.
- Comparing the performance of the proposed hybrid-fed MAB topology with the classical voltage-fed MAB topology in more details, taking into consideration the total system losses of each topology in similar scenarios.
- Building a hybrid-fed MAB converter prototype in order to experimentally validate the theory presented in Chapter 4. This includes validating both the developed mathematical model and the proposed control strategy.

REFERENCES

- [1] A. M. Adil and Y. Ko, "Socio-technical evolution of Decentralized Energy Systems: A critical review and implications for urban planning and policy," *Renewable and Sustainable Energy Reviews*, vol. 57, pp. 1025–1037, May 2016, doi: 10.1016/j.rser.2015.12.079.
- [2] A. Werth, N. Kitamura, and K. Tanaka, "Conceptual Study for Open Energy Systems: Distributed Energy Network Using Interconnected DC Nanogrids," *IEEE Transactions on Smart Grid*, vol. 6, no. 4, pp. 1621–1630, Jul. 2015, doi: 10.1109/TSG.2015.2408603.
- [3] M. Mohammadi, Y. Noorollahi, B. Mohammadi-ivatloo, and H. Yousefi, "Energy hub: From a model to a concept – A review," *Renewable and Sustainable Energy Reviews*, vol. 80, pp. 1512–1527, Dec. 2017, doi: 10.1016/j.rser.2017.07.030.
- [4] A. De, "Optimal sizing and positioning of grid integrated distributed generator: a review," *International Journal of Engineering & Technology*. 9. 299, Mar. 2020.
- [5] "Two centuries of rapid global population growth will come to an end," Our World in Data. Accessed: Oct. 20, 2023. [Online]. Available: <https://ourworldindata.org/world-population-growth-past-future>
- [6] B. K. Sovacool and M. A. Brown, "Competing Dimensions of Energy Security: An International Perspective," *Annual Review of Environment and Resources*, vol. 35, no. 1, pp. 77–108, 2010, doi: 10.1146/annurev-environ-042509-143035.
- [7] "Renewable Energy Statistics 2021: Global Data in the Renewable Energy Sector." Accessed: Oct. 20, 2023. [Online]. Available: <https://www.greenesa.com/article/renewable-energy-statistics>
- [8] U. Nations, "What is renewable energy?," United Nations. Accessed: Oct. 20, 2023. [Online]. Available: <https://www.un.org/en/climatechange/what-is-renewable-energy>
- [9] S. Galeshi, "'Cluster' converters based on multi-port active-bridge: application to smartgrids, Thesis at G2Elab - Université Grenoble Alpes." 2021.
- [10] H. Tao, J. L. Duarte, and M. A. M. Hendrix, "Multiport converters for hybrid power sources," presented at the 2008 IEEE Power Electronics Specialists Conference, Rhodes, Greece, 2008, pp. 3412–3418. doi: 10.1109/PESC.2008.4592483.
- [11] S. Bandyopadhyay, Z. Qin, and P. Bauer, "Decoupling Control of Multiactive Bridge Converters Using Linear Active Disturbance Rejection," *IEEE Trans. Ind. Electron.*, vol. 68, no. 11, pp. 10688–10698, Nov. 2021, doi: 10.1109/TIE.2020.3031531.
- [12] Y. Chen, P. Wang, Y. Elasser, and M. Chen, "Multicell Reconfigurable Multi-Input Multi-Output Energy Router Architecture," *IEEE Transactions on Power Electronics*, vol. 35, no. 12, pp. 13210–13224, December 2020, doi: 10.1109/TPEL.2020.2996199.
- [13] M. Rashidi, N. N. Altin, S. S. Ozdemir, A. Bani-Ahmed, and A. Nasiri, "Design and Development of a High-Frequency Multiport SST with Decoupled Control Scheme," *IEEE Transactions on Industry Applications*, vol. 55, no. 6, pp. 7515–7526, Nov.-Dec. 2019, doi: 10.1109/TIA.2019.2939741.
- [14] C. Zhao, S. D. Round, and J. W. Kolar, "An Isolated Three-Port Bidirectional DC-DC Converter With Decoupled Power Flow Management," *IEEE Trans. Power Electron.*, vol. 23, no. 5, pp. 2443–2453, Sep. 2008, doi: 10.1109/TPEL.2008.2002056.
- [15] M. L. Mendola, M. di Benedetto, A. Lidozzi, L. Solero, and S. Bifaretti, "Four-Port Bidirectional Dual Active Bridge Converter for EVs Fast Charging," in *2019 IEEE Energy Conversion Congress and Exposition (ECCE)*, Baltimore, MD, USA: IEEE, Sep. 2019, pp. 1341–1347. doi: 10.1109/ECCE.2019.8912252.
- [16] U. Abronzini *et al.*, "High Performance Active Battery Management System with Multi-Winding Transformer," IEEE Energy Conversion Congress and Exposition (ECCE), Baltimore, MD, USA, 2019, pp. 1231–1236, doi: 10.1109/ECCE.2019.8912966 2019.

- [17] M. Blanc, Y. Lembeye, and J.-P. Ferrieux, “Dual Active Bridge (DAB) pour la conversion continu-continu,” *Électronique*, Feb. 2019, doi: 10.51257/a-v1-e3975.
- [18] S. Bandyopadhyay, P. Purgat, Z. Qin, and P. Bauer, “A Multiactive Bridge Converter With Inherently Decoupled Power Flows,” *IEEE Trans. Power Electron.*, vol. 36, no. 2, pp. 2231–2245, Feb. 2021, doi: 10.1109/TPEL.2020.3006266.
- [19] F. Krismer, “Modeling and Optimization of Bidirectional Dual Active Bridge DC–DC Converter Topologies, PhD thesis, Power Electronic Systems Laboratory, ETH Zurich.” 2010.
- [20] M. Shujun, G. Zhiqiang, and L. Yong, “Universal Modulation Scheme to Suppress Transient DC Bias Current in Dual Active Bridge Converters, IEEE transactions on power electronics, Vol. 37, No.2.” Feb. 2022.
- [21] G. G. Oggier, G. O. García, and A. R. Oliva, “Switching Control Strategy to Minimize Dual Active Bridge Converter Losses,” in *IEEE Transactions on Power Electronics*, vol. 24, no. 7, pp. 1826–1838, July 2009, doi: 10.1109/TPEL.2009.2020902. Accessed: Nov. 02, 2023. [Online]. Available: <https://ieeexplore.ieee.org/stampPDF/getPDF.jsp?tp=&arnumber=5185352&ref=aHR0cHM6Ly9pZWVleHBsb3JlLmllZWUub3JnL2RvY3VtZW50LzUxODUzNTI=>
- [22] P. Purgat, S. Bandyopadhyay, Z. Qin, and P. Bauer, “Zero Voltage Switching Criteria of Triple Active Bridge Converter,” *IEEE Trans. Power Electron.*, vol. 36, no. 5, pp. 5425–5439, May 2021, doi: 10.1109/TPEL.2020.3027785.
- [23] P. Koochi, A. J. Watson, J. C. Clare, T. B. Soeiro, and P. W. Wheeler, “A Survey on Multi-Active Bridge DC-DC Converters: Power Flow Decoupling Techniques, Applications, and Challenges,” *Energies* 2023, 16, 5927. <https://doi.org/10.3390/en16165927>.
- [24] S. Galeshi, D. Frey, and Y. Lembeye, “Modular Modeling and Control of Power Flow in A Multi-Port Active-Bridge Converter,” *Symposium De Genie Electrique, 3-5 July 2018, Nancy, France*.
- [25] S. Galeshi, D. Frey, and Y. Lembeye, “Efficient and scalable power control in multi-port active-bridge converters,” in *2020 22nd European Conference on Power Electronics and Applications (EPE'20 ECCE Europe)*, Lyon, France: IEEE, Sep. 2020, p. P.1-P.9. doi: 10.23919/EPE20ECCEurope43536.2020.9215905.
- [26] O. M. Hebala, A. A. Aboushady, K. H. Ahmed, and I. Abdelsalam, “Generalized Active Power Flow Controller for Multiactive Bridge DC–DC Converters With Minimum-Current-Point-Tracking Algorithm,” *IEEE Trans. Ind. Electron.*, vol. 69, no. 4, pp. 3764–3775, Apr. 2022, doi: 10.1109/TIE.2021.3071681.
- [27] C. L., L. J., J. X., W. C.S., and L. K.H., “An Immittance-Network-Based Multiport ZVS Bidirectional Converter With Power Decoupling Capability,” in *IEEE Transactions on Power Electronics*, vol. 37, no. 10, pp. 12729–12740, Oct. 2022, doi: 10.1109/TPEL.2022.3172552.
- [28] J. V. N. S. R., S. A., and D. G.D., “Dual-Transformer-Based Asymmetrical Triple-Port Active Bridge (DT-ATAB) Isolated DC–DC Converter,” in *IEEE Transactions on Industrial Electronics*, vol. 64, no. 6, pp. 4549–4560, June 2017, doi: 10.1109/TIE.2017.2674586.
- [29] M. T. Tham, “An introduction to multivariable control,” in *Industrial Digital Control Systems*, K. Warwick and D. Rees, Eds., Institution of Engineering and Technology, 1988, pp. 189–212. doi: 10.1049/PBCE037E_ch8.
- [30] Y. Chen, P. Wang, H. Li, and M. Chen, “Power Flow Control in Multi-Active-Bridge Converters: Theories and Applications,” in *2019 IEEE Applied Power Electronics Conference and Exposition (APEC)*, Anaheim, CA, USA: IEEE, Mar. 2019, pp. 1500–1507. doi: 10.1109/APEC.2019.8722122.

- [31] M. Amari, I. Khelifi, and F. Bacha, "Average Model of Dual Active Bridge Interfacing Ultra-capacitor in Electrical Vehicle," presented at the 2014 5th International Renewable Energy Congress (IREC), Hammamet, Tunisia, 2014, pp. 1-6, doi: 10.1109/IREC.2014.6826984,
- [32] D. D. M. Cardozo, "Novel nonlinear control of Dual Active Bridge using simplified converter model," p. 7.
- [33] H. Bai, C. Mi, C. Wang, and S. Gargies, "The Dynamic Model and Hybrid Phase-Shift Control of a Dual-Active-Bridge Converter," p. 6.
- [34] X. Li, W. Zhang, W. Chen, Y. Huang, and Y. Qiu, "Dual Active Bridge Bidirectional DC-DC Converter Modeling for Battery Energy Storage System," in *2018 37th Chinese Control Conference (CCC)*, Wuhan: IEEE, Jul. 2018, pp. 1740–1745. doi: 10.23919/ChiCC.2018.8482623.
- [35] Hengsi Qin and J. W. Kimball, "Generalized Average Modeling of Dual Active Bridge DC–DC Converter," *IEEE Trans. Power Electron.*, vol. 27, no. 4, pp. 2078–2084, Apr. 2012, doi: 10.1109/TPEL.2011.2165734.
- [36] P. Costa, P. Lobler, L. Roggia, and L. Schuch, "Modeling and Control of DAB Converter Applied to Batteries Charging," *IEEE Trans. Energy Convers.*, vol. 37, no. 1, pp. 175–184, Mar. 2022, doi: 10.1109/TEC.2021.3082468.
- [37] T. L. Nguyen, G. Griepentrog, and V. T. Phung, "Modeling and Control of Dual Active Bridge Converter with Two Control Loops and Output Filter," presented at the IECON 2017 - 43rd Annual Conference of the IEEE Industrial Electronics Society, Beijing, China, 2017, pp. 4683-4689, doi: 10.1109/IECON.2017.8216807,
- [38] P. Purgat, S. Bandyopadhyay, Z. Qin, and P. Bauer, "Continuous Full Order Model of Triple Active Bridge Converter," in *2019 21st European Conference on Power Electronics and Applications (EPE '19 ECCE Europe)*, Genova, Italy: IEEE, Sep. 2019, p. P.1-P.9. doi: 10.23919/EPE.2019.8914897.
- [39] S. Bacha, I. Munteanu, and A. I. Bratcu, *Power Electronic Converters Modeling and Control*. in Advanced Textbooks in Control and Signal Processing. London: Springer London, 2014. doi: 10.1007/978-1-4471-5478-5.
- [40] M. Gierczynski, L. M. Grzesiak, and A. Kaszewski, "Cascaded Voltage and Current Control for a Dual Active Bridge Converter with Current Filters," *Energies*, vol. 14, no. 19, p. 6214, Sep. 2021, doi: 10.3390/en14196214.
- [41] F. Feng, X. Zhang, F. Lin, and H. B. Gooi, "Impedance modeling and stability analysis of dual active bridge converter with LC input filter," *Trans. Electr. Mach. Syst.*, vol. 2, no. 3, pp. 289–295, Sep. 2018, doi: 10.30941/CESTEMS.2018.00036.
- [42] X. Zhang, X. Ruan, and Q.-C. Zhong, "Improving the Stability of Cascaded DC/DC Converter Systems via Shaping the Input Impedance of the Load Converter With a Parallel or Series Virtual Impedance," *IEEE Trans. Ind. Electron.*, vol. 62, no. 12, pp. 7499–7512, Dec. 2015, doi: 10.1109/TIE.2015.2459040.
- [43] J. Riedel, D. G. Holmes, B. P. McGrath, and C. Teixeira, "Active Suppression of Selected DC Bus Harmonics for Dual Active Bridge DC–DC Converters," *IEEE Trans. Power Electron.*, vol. 32, no. 11, pp. 8857–8867, Nov. 2017, doi: 10.1109/TPEL.2016.2647078.
- [44] Y. Eto, Y. Noge, and M. Shoyama, "A Dynamic Characteristic of Bi-directional Dual Active Bridge Converter with Power-Feedback Control," presented at the 2021 IEEE 12th Energy Conversion Congress & Exposition - Asia (ECCE-Asia), Singapore, Singapore, 2021, pp. 1940-1945, doi: 10.1109/ECCE-Asia49820.2021.9479008,
- [45] A. Aldaheri and A. Etemadi, "Impedance Decoupling in DC Distributed Systems to Maintain Stability and Dynamic Performance," *Energies* 2017, 10, 470. <https://doi.org/10.3390/en10040470>.

- [46] Y. Guan, Y. Xie, Y. Wang, Y. Liang, and X. Wang, "An Active Damping Strategy for Input Impedance of Bidirectional Dual Active Bridge DC–DC Converter: Modeling, Shaping, Design, and Experiment," *IEEE Trans. Ind. Electron.*, vol. 68, no. 2, pp. 1263–1274, Feb. 2021, doi: 10.1109/TIE.2020.2969126.
- [47] O. Mo, "Active damping of oscillations in LC-filter for line connected, current controlled, PWM voltage source converters," *SINTEF ENERGY RESEARCH*, p. 11, 2003.
- [48] H. Wang, X. Ge, and Y. C. Liu, "An Active Damping Stabilization Scheme for the Suppression of the DC-Link Oscillation in Metro Traction Drive System," *IEEE Transactions on Industry Applications*, vol. 54, no. 5, pp. 5113–5123, Sept.-Oct. 2018, doi: 10.1109/TIA.2018.2849719.
- [49] T. Langbauer, A. Connaughton, F. Vollmaier, M. Pajnic, and K. Krischan, "Closed-Loop Control of a Three-Port Series Resonant Converter," in *2021 IEEE 22nd Workshop on Control and Modelling of Power Electronics (COMPEL)*, Cartagena, Colombia: IEEE, Nov. 2021, pp. 1–7. doi: 10.1109/COMPEL52922.2021.9646070.
- [50] S. Dey, A. Mallik, and A. Akturk, "Investigation of ZVS Criteria and Optimization of Switching Loss in a Triple Active Bridge Converter Using Penta-Phase-Shift Modulation," *IEEE J. Emerg. Sel. Topics Power Electron.*, vol. 10, no. 6, pp. 7014–7028, Dec. 2022, doi: 10.1109/JESTPE.2022.3191987.
- [51] J. Li, Q. Luo, T. Luo, D. Mou, and M. Liserre, "Efficiency Optimization Scheme for Isolated Triple Active Bridge DC–DC Converter With Full Soft-Switching and Minimized RMS Current," *IEEE Trans. Power Electron.*, vol. 37, no. 8, pp. 9114–9128, Aug. 2022, doi: 10.1109/TPEL.2022.3157443.
- [52] M. Kasper, R. Burkart, J. W. Kolar, and G. Deboy, "ZVS of Power MOSFETs Revisited," *Power Electronic Systems Laboratory, ETH Zurich, Physikstr. 3, 8092 Zurich, Switzerland*.
- [53] G. Lakkas, "MOSFET power losses and how they affect power-supply efficiency," *Analog Applications Journal*, 2016.
- [54] B. Kozacek, M. Frivaldsky, and V. Jaros, "Improving qualitative parameters of LLC converter using a perspective semiconductor and magnetic components," presented at the 2016 International Conference on Applied Electronics (AE), Pilsen, Czech Republic, 2016, pp. 125–129, doi: 10.1109/AE.2016.7577256.,
- [55] PSI Moissan, "Transformateur électrique," 2013. [Online]. Available: <https://psiphysiquemoissan.files.wordpress.com/2014/01/transformateur.pdf>
- [56] Southeast University, L. Shu, W. Chen, Southeast University, Z. Song, and Southeast University, "Prediction Method of DC Bias in DC-DC Dual-Active-Bridge Converter," *CPSS TPEA*, vol. 4, no. 2, pp. 152–162, Jun. 2019, doi: 10.24295/CPSS TPEA.2019.00015.
- [57] S. Han, I. Munuswamy, and D. Divan, "Preventing transformer saturation in bi-directional dual active bridge buck-boost DC/DC converters," in *2010 IEEE Energy Conversion Congress and Exposition*, Atlanta, GA: IEEE, Sep. 2010, pp. 1450–1457. doi: 10.1109/ECCE.2010.5618254.
- [58] G. Ortiz, J. Muhlethaler, and J. W. Kolar, "Magnetic Ear-based balancing of magnetic flux in high power medium frequency dual active bridge converter transformer cores," in *8th International Conference on Power Electronics - ECCE Asia*, Jeju, Korea (South): IEEE, May 2011, pp. 1307–1314. doi: 10.1109/ICPE.2011.5944377.
- [59] A. Pandey, "Magnetic properties of the material," Power Electronics Talks. Accessed: Jan. 09, 2024. [Online]. Available: <https://www.powerelectronicstalks.com/2018/12/magnetic-properties-of-material.html>
- [60] R. Chattopadhyay, U. Raheja, G. Gohil, V. Nair, and S. Bhattacharya, "Sensorless phase shift control for phase shifted DC-DC converters for eliminating DC transients from

- transformer winding currents,” in *2018 IEEE Applied Power Electronics Conference and Exposition (APEC)*, San Antonio, TX, USA: IEEE, Mar. 2018, pp. 1882–1889. doi: 10.1109/APEC.2018.8341274.
- [61] A. Blinov, D. Vinnikov, and V. Ivakhno, “Full soft-switching high step-up DC-DC converter for photovoltaic applications,” in *2014 16th European Conference on Power Electronics and Applications*, Lappeenranta, Finland: IEEE, Aug. 2014, pp. 1–7. doi: 10.1109/EPE.2014.6911013.
- [62] Z. Guo, K. Sun, T.-F. Wu, and C. Li, “An Improved Modulation Scheme of Current-Fed Bidirectional DC–DC Converters For Loss Reduction,” *IEEE Trans. Power Electron.*, vol. 33, no. 5, pp. 4441–4457, May 2018, doi: 10.1109/TPEL.2017.2719722.
- [63] A. Chub, J. Rabkowski, A. Blinov, and D. Vinnikov, “Study on power losses of the full soft-switching current-fed DC/DC converter with Si and GaN devices,” in *IECON 2015 - 41st Annual Conference of the IEEE Industrial Electronics Society*, Yokohama: IEEE, Nov. 2015, pp. 000013–000018. doi: 10.1109/IECON.2015.7392957.
- [64] A. Chub, R. Kosenko, and A. Blinov, “Zero-voltage switching galvanically isolated current-fed full-bridge DC-DC converter,” in *2016 10th International Conference on Compatibility, Power Electronics and Power Engineering (CPE-POWERENG)*, Bydgoszcz, Poland: IEEE, Jun. 2016, pp. 455–459. doi: 10.1109/CPE.2016.7544231.
- [65] S. Kurm and V. Agarwal, “Current Fed Dual Active Bridge based Multi-Port DC/AC Converter for Standalone Solar PV fed Systems with Battery Backup,” in *2020 IEEE International Conference on Power Electronics, Drives and Energy Systems (PEDES)*, Jaipur, India: IEEE, Dec. 2020, pp. 1–6. doi: 10.1109/PEDES49360.2020.9379447.
- [66] Yaow-Ming Chen, Yuan-Chuan Liu, and Feng-Yu Wu, “Multi-input DC/DC converter based on the multiwinding transformer for renewable energy applications,” *IEEE Trans. on Ind. Applicat.*, vol. 38, no. 4, pp. 1096–1104, Jul. 2002, doi: 10.1109/TIA.2002.800776.
- [67] V. Rathore, K. Rajashekara, A. Ray, L. A. G. Rodriguez, and J. Mueller, “A Current-fed High Gain Multilevel DC-DC Converter for BESS Grid Integration Applications,” in *2021 IEEE Applied Power Electronics Conference and Exposition (APEC)*, Phoenix, AZ, USA: IEEE, Jun. 2021, pp. 1964–1970. doi: 10.1109/APEC42165.2021.9487339.
- [68] R. Tarraf *et al.*, “Modeling and Control of a Decoupled Hybrid-Fed Multi-Active Bridge (MAB) Converter,” in *PCIM Europe 2023; International Exhibition and Conference for Power Electronics, Intelligent Motion, Renewable Energy and Energy Management*, May 2023, pp. 1–9. doi: 10.30420/566091242.
- [69] H. Foch, Y. Chéron, R. Arches, B. Escaut, P. Marty, and M. Metz, “Commutateurs de courant,” *Conversion de l’énergie électrique*, Sep. 1993, doi: 10.51257/a-v1-d3171.

APPENDIX

Modeling and Control of a Decoupled Hybrid-Fed Multi-Active Bridge (MAB) Converter

Rebecca Tarraf¹, Baptiste Morel¹, David Frey², Sylvain Leirens¹, Sébastien Carcouet¹, Xavier Maynard¹, Yves Lembeye²

¹ Université Grenoble Alpes, CEA, Leti, F-38000 Grenoble, France

² Université Grenoble Alpes, G2Elab, CNRS, F-38000 Grenoble, France

Corresponding author: Rebecca Tarraf, rebecca.tarraf@cea.fr

Abstract

Multi-Active Bridge (MAB) converters are the extension of the well-known Dual-Active Bridge (DAB) bidirectional DC-DC converter. This multiport structure has attracted a lot of attention recently, especially for applications soliciting renewable energy sources and energy storage systems. Generally, MAB structures are based on voltage converters. However, in some cases, it could be interesting to have a current-fed input port due to load characteristics or operation constraints. This leads to a hybrid MAB structure mixing both current-fed and voltage-fed bridges. In the first part of this paper, the operation of a current-fed DAB converter topology is investigated. Additionally, a continuous-time model is developed for this topology and a control strategy is proposed. In the second part, the elaborated work is generalized to a decoupled hybrid-fed MAB converter. Simulation results using Matlab/Simulink are presented to validate this study.

1 Introduction

The integration of renewable energy sources and energy storage systems in modern power electronics applications drew greater attention to multiport converters in recent years. These structures form an Energy Hub where the production, consumption and storage of electrical energy can be done in one place [1]. Multi-Active Bridge (MAB) converters are multiport converters provided with intrinsic galvanic isolation. This is due to the connection of this topology's ports through a high frequency (HF) transformer. Galvanic isolation is crucial for applications where different energy sources/loads with important voltage dissimilarities should be connected together.

Current-fed DAB converters present several advantages compared to a classical voltage-fed DAB converter such as soft switching on the full operation range and the absence of an input capacitor at the current-fed port. This can be interesting for different applications like connecting a PV panel or a battery system to the current-fed port [2]–[5]. Some previous works addressed different topologies of multiport hybrid-fed converters [6]–[8]. In this paper, a new topology of a fully isolated, decoupled hybrid-fed MAB converter was studied, modelled and controlled.

In the first part of this paper, the continuous-time model of a current-fed DAB converter is developed. The mathematical modeling of a system helps with the study of its dynamic behavior and controller design. The main drawback that the current-fed port introduces into the system is the complexity of its control. In fact, the current inverter will impose control restrictions on all the other ports of the system. The non-compliance of these restrictions may cause brutal over-voltages that could destroy the circuit. A control method is proposed in this paper, based on the elaborated mathematical model and the control constraints. The second part of this paper extends this work for a decoupled, hybrid-fed MAB converter, having any number of ports. Simulation results are displayed to validate the developed model and control strategy.

2 Current-Fed DAB Converter

2.1 Topology and Working Concept

Figure 1 shows the studied topology of a current-fed DAB converter connected to a current source at its primary port and a voltage source at its secondary port.

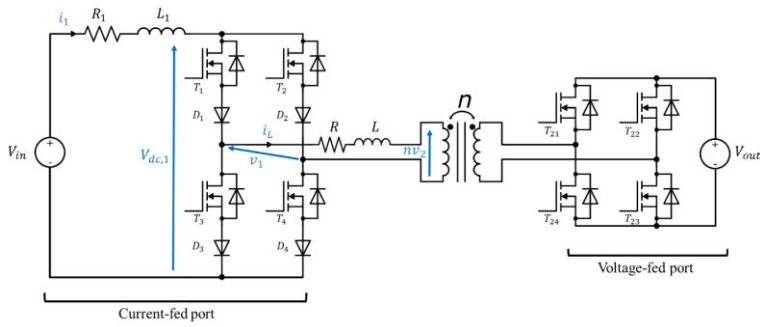


Fig. 1 Current-fed Dual-Active Bridge (DAB) converter topology.

The waveforms of this DAB's AC signals circulating in the transformer are shown in Fig. 2, all along with the command signals of switches T_1 of the current inverter and T_{21} of the H-Bridge. These shapes are an approximation of the real signals' shapes. In reality, the current i_L is not perfectly trapezoidal, as it is slightly affected by the switching of the secondary H-bridge at instants t_1 and t_4 .

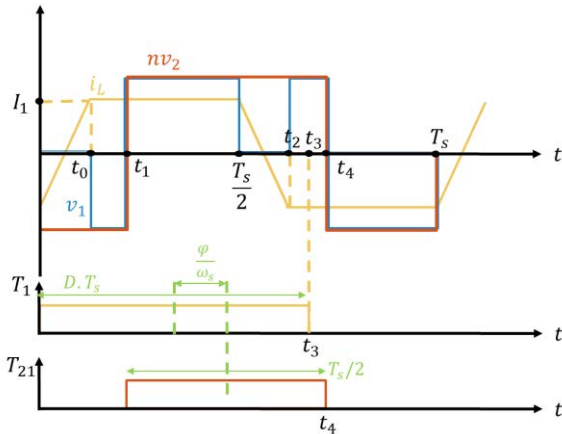


Fig. 2 AC signals at the DAB converter's transformer with the command signals of switches T_1 and T_{21} .

As shown in Fig. 2, D is the command duty cycle of switch T_1 , with $D > 0.5$, and φ is the phase shift angle in radians between the commands of T_1 and T_{21} . T_s is the switching period (f_s is the switching frequency). The command duty cycle of the secondary H-Bridge switches is fixed to 50% on all the operation range, so v_2 is a 2-level voltage as shown in Fig. 2.

The operation cycle of this current-fed DAB converter is divided into the following time intervals:

- $0 \leq t \leq t_0$:

At $t = 0$, switches T_1 and T_4 are turned on. T_2 and T_3 were already ON right before $t = 0$ from the previous cycle. Since all the current i_1 was passing through T_2 and T_3 , the switching of T_1 and T_4 is done at zero current (ZCS), thus decreasing the switching losses. In this time interval, all the current inverter's switches are ON, so the voltage

$v_1 = 0$ (Fig. 3.a). On the voltage port, the AC voltage should be $v_2 = -V_{out} < 0$ in order to reverse the transformer current, so T_{22} and T_{24} are ON. Therefore, the transformer current increases from $-I_1$ to I_1 in this interval and is represented by the following expression (neglecting the value of the transformer's series resistance R):

$$i_L(t) = -\frac{nv_2}{L}t - I_1 = \frac{nV_{out}}{L}t - I_1 \quad (1)$$

Where n is the turn ratio of the transformer and L is the link inductance between the ports. I_1 is the value of the input current at a certain operating point. This current is considered constant at each operating point as it is limited by the input inductance L_1 , which's value is a lot bigger than the value of the link inductance L .

As i_L gets closer to I_1 , the current starts passing more through diodes D_1 and D_4 and less through D_2 and D_3 . At $t = t_0$, D_2 and D_3 are naturally turned off.

- $t_0 \leq t \leq \frac{T_s}{2}$:

In this time interval, the input current passes through T_1 , T_4 , D_1 and D_4 and $i_L = I_1$ (Fig. 3.b). Switches T_2 and T_3 are turned off between t_0 and t_1 at zero current (ZCS) since D_2 and D_3 are blocking the current. At $t = t_1$, the voltage port's H-Bridge is switched at zero voltage (ZVS) since $i_L > 0$ (T_{22} and T_{24} are turned off while T_{21} and T_{23} are turned on). Therefore, $v_2 = V_{out} > 0$ (Fig. 3.c). Ideally, the switching of the voltage port does not affect the transformer's current value since it is imposed by the current source ($L_1 \gg L$). However, it will allow the transformer current to reverse again in the next time interval.

- $\frac{T_s}{2} \leq t \leq t_2$:

At $t = T_s/2$, T_2 and T_3 are turned on at zero current. Therefore, all the current inverter's switches are ON again and the voltage $v_1 = 0$ (Fig. 3.d). The transformer current decreases from I_1 to $-I_1$ since $nv_2 > 0$ in this interval and it is represented by the following expression:

$$i_L(t) = -\frac{nv_2}{L}\left(t - \frac{T_s}{2}\right) + I_1 = -\frac{nV_{out}}{L}\left(t - \frac{T_s}{2}\right) + I_1 \quad (2)$$

At $t = t_2$, D_1 and D_4 are naturally blocked.

- $t_2 \leq t \leq T_s$:

The input current passes entirely through T_2 , T_3 , D_2 and D_3 in this time interval and $i_L = -I_1$. At $t = t_3$, T_1 and T_4 are turned off at zero current. At $t = t_4$, the voltage port's H-bridge is switched with ZVS and $v_2 = -V_{out} < 0$. This cycle is then repeated for each switching period T_s .

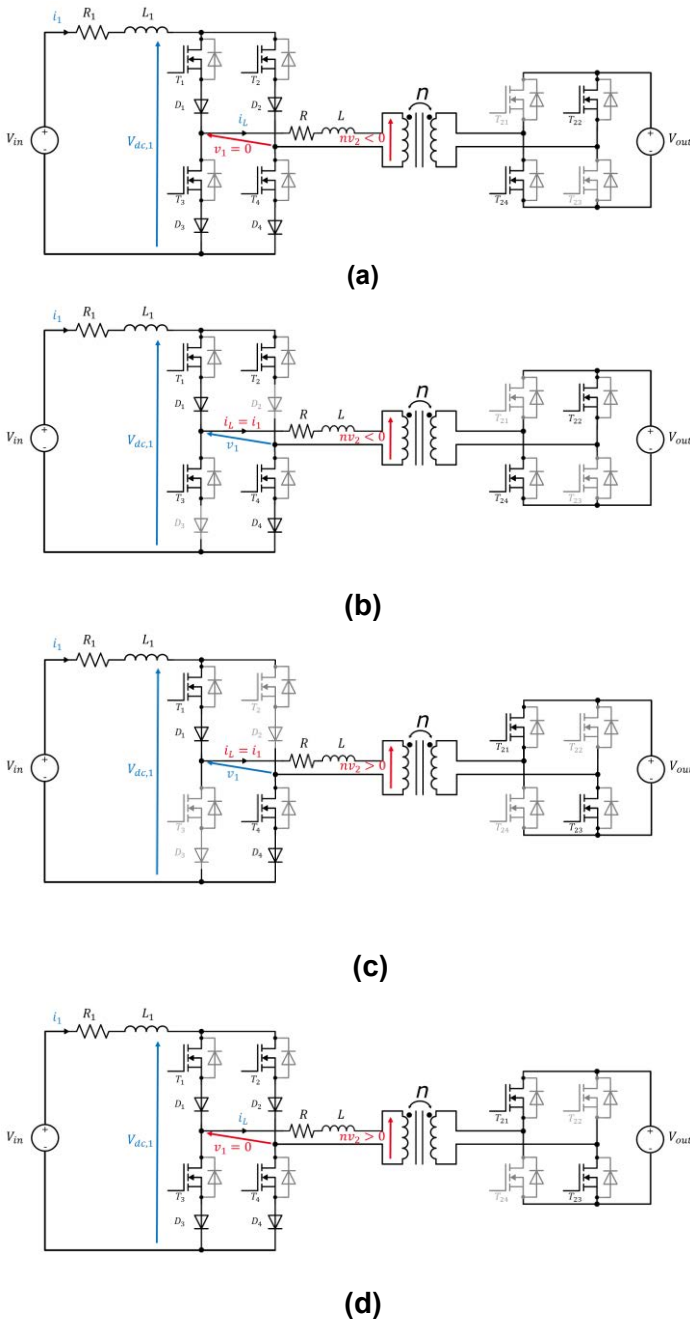


Fig. 3 Equivalent circuits of the DAB converter at: (a) $0 < t < t_0$ (b) $t_0 < t < t_1$ (c) $t_1 < t < T_s/2$ (d) $T_s/2 < t < t_2$.

2.2 Operating Conditions

In order to be able to transfer power from port 1 to port 2 with soft switching on the whole operation range at both active bridges, while avoiding over-voltages at port 1, two main conditions should be respected:

- a) In order to avoid over-voltages and to have a soft switching at the primary side, the switches of the current inverter should not be turned off before the complete reversal of the transformer current and the blocking of their series

diodes. Otherwise, these switches would block an important current in the link inductance, which will cause brutal over-voltages at the current port. This means that:

$$t_3 \geq t_2 \rightarrow DT_s \geq \frac{T_s}{2} + t_0$$

With $t_0 = \frac{2LI_1}{nV_{out}}$ from eq. (1).

Therefore,

$$D \geq \frac{2LI_1}{nV_{out}T_s} + \frac{1}{2} \quad (3)$$

- b) The voltage port's AC voltage v_2 should be reversed after the transformer current's full reversal and the blocking of both the diodes and their series switches. If v_2 is reversed before that, over-voltages will occur at the primary side. Additionally, the current might not be able to reverse, so no power would be exchanged between the two ports. If v_2 is reversed before the blocking of the primary's switches ($t_2 < t_4 < t_3$), the diodes could be turned on again. This condition also ensures a soft switching at the voltage port and it can be written as :

$$t_4 \geq t_3 \rightarrow \frac{DT_s}{2} + \varphi \frac{T_s}{2\pi} + \frac{T_s}{4} \geq DT_s$$

Therefore,

$$D \leq \frac{\varphi}{\pi} + \frac{1}{2} \quad (4)$$

As we can notice, these conditions depend on the operating point of the converter as I_1 , D and φ vary according to the desired input power. This is what makes the control of this topology of a current-fed DAB converter more complex than a DAB converter with 2 H-bridges.

2.3 Mathematical Modelling of the Current-Fed DAB Converter

In general, the mathematical model of a system makes the study of its dynamic behavior easier, giving valuable information about its response characteristics such as stability margins and time response. Additionally, it helps with the design of its controllers. For the proposed current-fed DAB converter, the state space equations are:

- $L_1 \frac{di_1}{dt} = V_{in} - V_{dc,1} - R_1 \cdot i_1$
- $L \frac{di_L}{dt} = v_1 - nv_2 - R \cdot i_L$

We can also write, from Fig. 1 and Fig. 2:

$$V_{dc,1} = \begin{cases} v_1 & \text{for } 0 \leq t \leq \frac{T_s}{2} \\ -v_1 & \text{for } \frac{T_s}{2} \leq t \leq T_s \end{cases}$$

By considering the transformer current perfectly trapezoidal, and by neglecting the transformer resistance R , we can write :

$$V_{dc,1} = \begin{cases} 0 & \text{for } 0 \leq t \leq t_0 \\ -nV_{out} & \text{for } t_0 \leq t \leq t_1 \\ nV_{out} & \text{for } t_1 \leq t \leq \frac{T_s}{2} \end{cases}$$

Therefore, $V_{dc,1}$ has a period of $T_s/2$ and can be written as $V_{dc,1} = S_0 \cdot nV_{out}$ with:

$$S_0 = \begin{cases} 0 & \text{for } 0 \leq t \leq t_0 \\ -1 & \text{for } t_0 \leq t \leq t_1 \\ 1 & \text{for } t_1 \leq t \leq \frac{T_s}{2} \end{cases}$$

The first state equation becomes:

$$L_1 \frac{di_1}{dt} = V_{in} - S_0 \cdot nV_{out} - R_1 \cdot i_1 \quad (5)$$

The state variable i_1 of Eq. (5) is DC. Therefore, in order to have a continuous-time model, i_1 can be represented by its average value, which is the 0th coefficient of its Fourier series representation.

Considering that $\langle x \rangle_k(t)$ is the kth coefficient of the Fourier series of a variable x , we can write:

$$L_1 \frac{d\langle i_1 \rangle_0}{dt} = \langle V_{in} \rangle_0 - n\langle S_0 \rangle_0 \langle V_{out} \rangle_0 - R_1 \langle i_1 \rangle_0 \quad (6)$$

With:

$$\langle S_0 \rangle_0 = \frac{2}{T_s} \int_0^{\frac{T_s}{2}} S_0(t) \cdot dt = \frac{2}{T_s} \left(t_0 + \frac{T_s}{2} - 2t_1 \right),$$

where:

$$t_0 = \frac{2L\langle i_1 \rangle_0}{nV_{out}} \quad (\text{from Eq. (1)})$$

$$t_1 = \frac{DT_s}{2} + \varphi \frac{T_s}{2\pi} - \frac{T_s}{4} \quad (\text{from Fig. 2})$$

Therefore:

$$\langle S_0 \rangle_0 = \frac{4L}{nV_{out}T_s} \langle i_1 \rangle_0 + 2 - 2D - 2\frac{\varphi}{\pi} \quad (7)$$

Equation (6) becomes:

$$L_1 \frac{d\langle i_1 \rangle_0}{dt} = - \left(R_1 + \frac{4L}{T_s} \right) \cdot \langle i_1 \rangle_0 + \langle V_{in} \rangle_0 - 2 \cdot \left(1 - D - \frac{\varphi}{\pi} \right) \cdot n\langle V_{out} \rangle_0 \quad (8)$$

The approximations that were done made the first equation of the state space representation enough to get the relation between current I_1 (the control output) and the control parameters φ and D .

The small-signal model of this system is obtained by linearizing it about an operating point and then applying a perturbation to its variables. The variables will therefore be represented as:

$$\langle x \rangle = x_{eq} + \widehat{\langle x \rangle}$$

Where variables with the symbol “ \wedge ” represent the small signals (perturbations around the operating point) and x_{eq} represents the value of $\langle x \rangle$ at the operating point, also called equilibrium point.

The linearization of Eq. (8) around an operating point is done using Taylor series expansion. The variations of the input and output voltages around their average values can be neglected ($\langle \widehat{V_{in}} \rangle_0 = \langle \widehat{V_{out}} \rangle_0 = 0$) since their dynamics are considered relatively slow. Therefore, we can write:

$$L_1 \frac{d\widehat{\langle i_1 \rangle}_0}{dt} = - \left(R_1 + \frac{4L}{T_s} \right) \cdot \widehat{\langle i_1 \rangle}_0 + \frac{2nV_{out}}{\pi} \cdot \widehat{\varphi} + 2nV_{out} \cdot \widehat{D} \quad (9)$$

At the equilibrium point, where all the dynamics are zero ($\frac{d\widehat{\langle i_1 \rangle}_0}{dt} = 0$), we can write:

$$I_{1,eq} = \left(V_{in} - 2nV_{out} \cdot \left(1 - D_{eq} - \frac{\varphi_{eq}}{\pi} \right) \right) \times \frac{1}{R_1 + \frac{4L}{T_s}} \quad (10)$$

2.4 Control of the Input Current

From Eq. (10), we can notice that, at a certain operating point, the input current I_1 depends on the command duty cycle D and the phase shift φ . An infinity of combinations of the values of D_{eq} and φ_{eq} can give us the same desired input current value $I_{1,eq}$, as long as conditions of Eq. (3) and Eq. (4) are respected.

We can get the expression of φ_{eq} in function of D_{eq} and $I_{1,eq}$ from Eq. (10) as follows:

$$\varphi_{eq} = \pi \cdot \left(\frac{R_1 I_{1,eq}}{2nV_{out}} + \frac{2L I_{1,eq}}{nV_{out} T_s} - \frac{V_{in}}{2nV_{out}} - D_{eq} + 1 \right)$$

By choosing the value of D_{eq} to be equal to its minimum allowed value expressed in Eq. (3), with a certain added safety margin ϵ , we get:

$$D_{eq} = D_{min} + \epsilon = \frac{2L I_1}{nV_{out} T_s} + \frac{1}{2} + \epsilon.$$

Therefore,

$$\begin{aligned} \varphi_{eq} &= \pi \cdot \left(\frac{R_1 I_{1,eq}}{2nV_{out}} - \frac{V_{in}}{2nV_{out}} + \frac{1}{2} - \epsilon \right) \\ &\approx \pi \cdot \left(\frac{1}{2} - \frac{V_{in}}{2nV_{out}} - \epsilon \right) \end{aligned} \quad (11)$$

R_1 has a relatively small value compared to other terms of this equation, so it can be neglected. We notice from Eq. (11) that for $D_{eq} = D_{min} + \epsilon$, the phase shift φ_{eq} does not depend on the operating point anymore. Therefore, to move from a certain operating point to another (in order to change the input current's desired value), we do not need to modify the value of φ (as long as the input and output voltages are constant). Only the modification of the duty cycle D is required, making it easier for conditions of Eq. (3) and Eq. (4) to be respected.

The maximum allowed value D_{max} of D , given in Eq. (4), also becomes independent of the operating point since it is a function of φ . From Eq. (3), Eq. (10) and Eq. (11), we can get the corresponding maximum reachable value of the input current:

$$I_{1,max} = \frac{nV_{out} - V_{in}}{\frac{4L}{T_s} - R_1} \quad (12)$$

The approximations that were done in the developed mathematical model will lead to a steady state error if only an open loop (a feedforward) control is applied. A feedback with a PI controller is therefore added in order to cancel this error.

The closed-loop control block diagram of the input current I_1 is shown in Fig. 4. A safety margin $\epsilon = 0.01$ for the control of D was taken into consideration ($D_{eq} = D_{min} + \epsilon$). This value was chosen arbitrarily in this study. In future works, a more accurate margin value could be calculated by taking into consideration the variations of the voltage sources, the error on the values of the inductances, current and voltage sensors, etc...

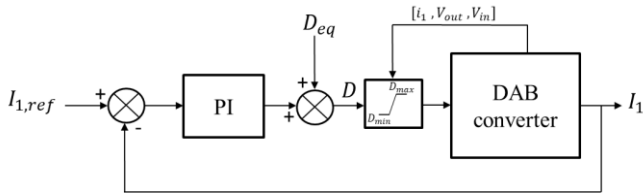


Fig. 4 Block diagram of the input current closed-loop control of the current-fed DAB converter.

The open loop transfer function of this control loop can be calculated from the Laplace transform of Eq. (9) and has the following expression:

$$G_{i1}(s) = \left. \frac{\hat{I}_1(s)}{\hat{D}(s)} \right|_{\varphi=0} = \frac{\frac{2nV_{out}}{L_1}}{s + \left(\frac{R_1}{L_1} + \frac{4L}{L_1 T_s} \right)} = \frac{g}{\tau s + 1} \quad (13)$$

It is a first order transfer function with a gain g and a time constant τ .

The PI controller's transfer function is:

$$C(s) = \frac{K \cdot (T_i \cdot s + 1)}{T_i \cdot s}$$

We choose $T_i = \tau$. The closed loop transfer function will therefore become:

$$CLTF(s) = \frac{C(s)G_{i1}(s)}{1 + C(s)G_{i1}(s)} = \frac{1}{\frac{\tau}{K \cdot g} \cdot s + 1}$$

Consequently, the new time constant would be:

$$\tau_a = \frac{\tau}{K \cdot g}$$

Knowing that the feedback time response to get to 95% of the desired input current value is $t_{r,95\%} = 3 \cdot \tau_a$, the gain K is chosen for a desired value of $t_{r,95\%}$, such that:

$$K = \frac{3 \cdot \tau}{t_{r,95\%} \cdot g}$$

3 Decoupled Hybrid-Fed MAB Converter

In this section, a TAB converter having two voltage-fed ports and one current-fed port is modelled and controlled (Fig. 5). The proposed TAB converter's ports are decoupled using the hardware decoupling technique described in [9]. Therefore, this converter will have a master port and two slave ports. The decoupling is ensured by having a low leakage inductance at the master port and relatively higher leakage inductances (with externally added series inductances) at the slave ports. Ideally, this will make the link inductance between the two slaves big enough so no (or little) power is directly exchanged between them. The link inductance between a port #i and a port #j is calculated from the delta equivalent representation of the system as follows:

$$L_{ij} = \begin{cases} NA, & \forall i = j \\ L'_i + L'_j + L'_i L'_j \left(\sum_{k \neq i,j}^n \frac{1}{L'_k} \right), & \forall i \neq j \end{cases} \quad (14)$$

Where L'_i is the leakage inductance of port #i referred to a chosen reference side of the transformer which is port 1 in this work.

In this study, the master port will be port 2, which is a voltage-fed port. Ports 1 and 3 will be slave ports with port 1 being a current-fed port and port 3 a voltage-fed port, as shown in Fig. 5. The master port should be connected to a stiff voltage source such as the grid or a battery system [9]. Port 1 necessarily generates power so it can represent a PV panel for example, port 2 is bidirectional and port 3 is connected to a load.

Consequently, with $L_2 \approx 0$, we will have:

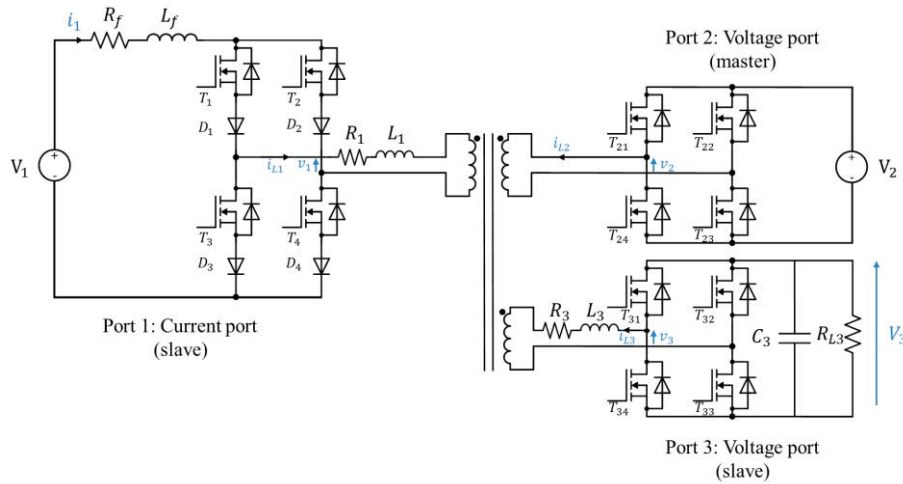


Fig. 5 Decoupled hybrid-fed Triple-Active Bridge (TAB) converter.

$$\begin{cases} L_{12} \approx L_1 \\ L_{23} \approx L_3' \\ L_{13} \approx \infty \end{cases}$$

Controlling the power flows of this converter can be done by regulating port 1's input current i_1 and port 3's output voltage V_3 .

3.1 Mathematical Modelling of the Decoupled Hybrid-Fed TAB Converter

By decoupling the ports of this TAB converter, this Multiple-Input Multiple-Output (MIMO) system is transformed into two independent Single-Input Single-Output (SISO) systems that can be modelled as two DAB converters. Ports 1 and 2 form the first SISO system which is a current-fed DAB converter having the topology described in the previous section. Ports 2 and 3 form the second SISO system, which is a classical DAB converter having two voltage-fed ports.

The modeling of the first SISO system was described in the first section. Therefore, by analogy, we can directly write the following transfer function for the control of the input current I_1 of port 1:

$$G_{i1}(s) = \left. \frac{\widehat{I}_1(s)}{\widehat{D}_1(s)} \right|_{\widehat{\varphi}_2=0} = \frac{\frac{2}{n_2} V_2}{s + \left(\frac{R_f}{L_f} + \frac{4L_1}{L_f T_s} \right)} \quad (15)$$

D_1 is the command duty cycle of port 1's switches and the control parameter of the input current I_1 .

$$G_{v3}(s) = \left. \frac{\widehat{V}_3(s)}{\widehat{d}_{23}(s)} \right|_{\widehat{v}_2=0}$$

$$= \frac{\frac{4b}{\pi C_3} \left(s + \frac{R_3}{L_3} - \frac{a}{b} w_s \right)}{s^3 + \left(2 \frac{R_3}{L_3} + \frac{1}{R_{L3} C_3} \right) \cdot s^2 + \left(\frac{R_3^2}{L_3^2} + w_s^2 + 2 \frac{R_3}{R_{L3} C_3 L_3} + \frac{8}{\pi^2 C_3 L_3} \right) \cdot s + \left(\frac{8R_3}{\pi^2 C_3 L_3^2} + \frac{R_3^2}{R_{L3} C_3 L_3^2} + \frac{w_s^2}{R_{L3} C_3} \right)}$$

n_1/n_2 is the turn ratio of the transformer between ports 1 and 2. The other parameters are represented in Fig. 5.

The same control conditions explained in the previous section apply for ports 1 and 2 of the decoupled hybrid-fed TAB converter. Accordingly, we can write:

$$D_1 \geq \frac{2L_1 I_1}{nV_2 T_s} + \frac{1}{2} \quad (16)$$

$$D_1 \leq \frac{\varphi_2}{\pi} + \frac{1}{2} \quad (17)$$

The mathematical modelling of the second SISO system, which is the classical voltage-fed DAB converter consisting of ports 2 and 3, can be found in many previous works [10], [11]. The generalized average model is used to accurately represent the AC signals of this system. The phase shift φ_{23} between the command signals of ports 2 and 3 is the control input parameter of the DC voltage V_3 of port 3. Equation (18) (shown in the bottom of this page) is the transfer function linking φ_{23} to V_3 in the frequency domain, where:

$$a = \frac{2}{L_3} \cdot \frac{n_3}{n_2} \cdot V_2 \cdot \cos(d_{23,eq} \pi)$$

$$b = -\frac{2}{L_3} \cdot \frac{n_3}{n_2} \cdot V_2 \cdot \sin(d_{23,eq} \pi)$$

with: $d_{23} = \frac{\varphi_{23}}{\pi}$.

3.2 Control Strategy

Port 1 is chosen to be the phase shift reference port of this system, so $\varphi_1 = 0$.

The first SISO system, which is equivalent to a current-fed DAB converter, is controlled as it was described in Section 2.4. Therefore, the command duty cycle D_1 of port 1 is set equal to its minimum allowed value expressed in Eq. (16), with an added safety margin ϵ . The command phase shift φ_2 of port 2 would therefore be fixed to the value given in Eq. (19) (as long as the voltage sources V_1 and V_2 are not perturbed), independently of the chosen operating point (i.e. the values of I_1 and V_3).

$$\varphi_{2,eq} = \pi \cdot \left(\frac{1}{2} - \frac{V_1}{2 \cdot \frac{n_1}{n_2} \cdot V_2} - \epsilon \right) \quad (19)$$

The phase shift φ_{23} between the command signals of ports 2 and 3 is calculated from the well-known power flow expression of a voltage-fed DAB converter, for a desired value of V_3 :

$$P_{23} = \frac{n_3 V_2 V_{3,eq}}{2 n_2 f_s L_{23}} \cdot \frac{\varphi_{23,eq}}{\pi} \cdot \left(1 - \frac{\varphi_{23,eq}}{\pi} \right),$$

where P_{23} is the power received by port 2 from port 3.

The steady state errors of the input current control of port 1 and the output voltage control of port 3 are cancelled by using PI controllers. The parameters of these PI controllers are calculated based on the transfer functions of Eq. (15) and Eq. (18) and the imposed response characteristics (e.g. time response, stability margins ...). The control block diagrams are presented in Fig. 6.

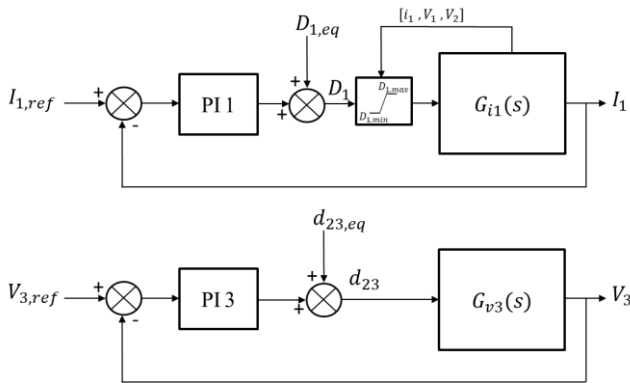


Fig. 6 Control block diagrams of the decoupled hybrid-fed TAB converter.

3.3 Simulation Results

The simulation platform that was used to validate this study is Matlab/Simulink.

The parameter values of the simulated decoupled hybrid-fed TAB converter are shown in Table 1.

Table 1 Parameter values of the decoupled hybrid-fed TAB converter.

Parameter symbol	Parameter value
V_1	200 V
V_2	400 V
R_{L3}	120 Ω
f_s	20 KHz
L_f	0.016 H
R_f	10 m Ω
L_1	83 μ H
R_1	10 m Ω
L_3	230 μ H
R_3	10 m Ω
C_3	100 μ H
R_{C3}	1 m Ω
L_m	8.3 mH
n_1	100 turns
n_2	83 turns
n_3	124 turns
P_{max}^*	4 KW

*maximum power exchanged between 2 ports

The simulation results of the decoupled hybrid-fed TAB converter are shown in Fig. 7.

Figure 7.a shows the response of the input current control of port 1 when a change of setpoint is introduced around its operating point. The chosen time response to get the parameter values of the loop's PI controller is $t_{r1,95\%} = 6ms$. We can see from Fig. 7.a that the simulated closed-loop time response is equal to its chosen value (6ms), which validates the developed mathematical model and control strategy.

Similarly, Figure 7.b shows the response of the output voltage control of port 3 when a setpoint change is applied to it around a certain operating point. The chosen time response for this loop is $t_{r2,95\%} = 60ms$ with an overshoot of 5%. These values are found in the response of the simulated model, thus validating this study.

Figure 7.c shows the AC voltages of the transformer windings at ports 1 and 2 with the AC current of port 1. The simulated waveforms match the theoretical ones in Fig. 2.

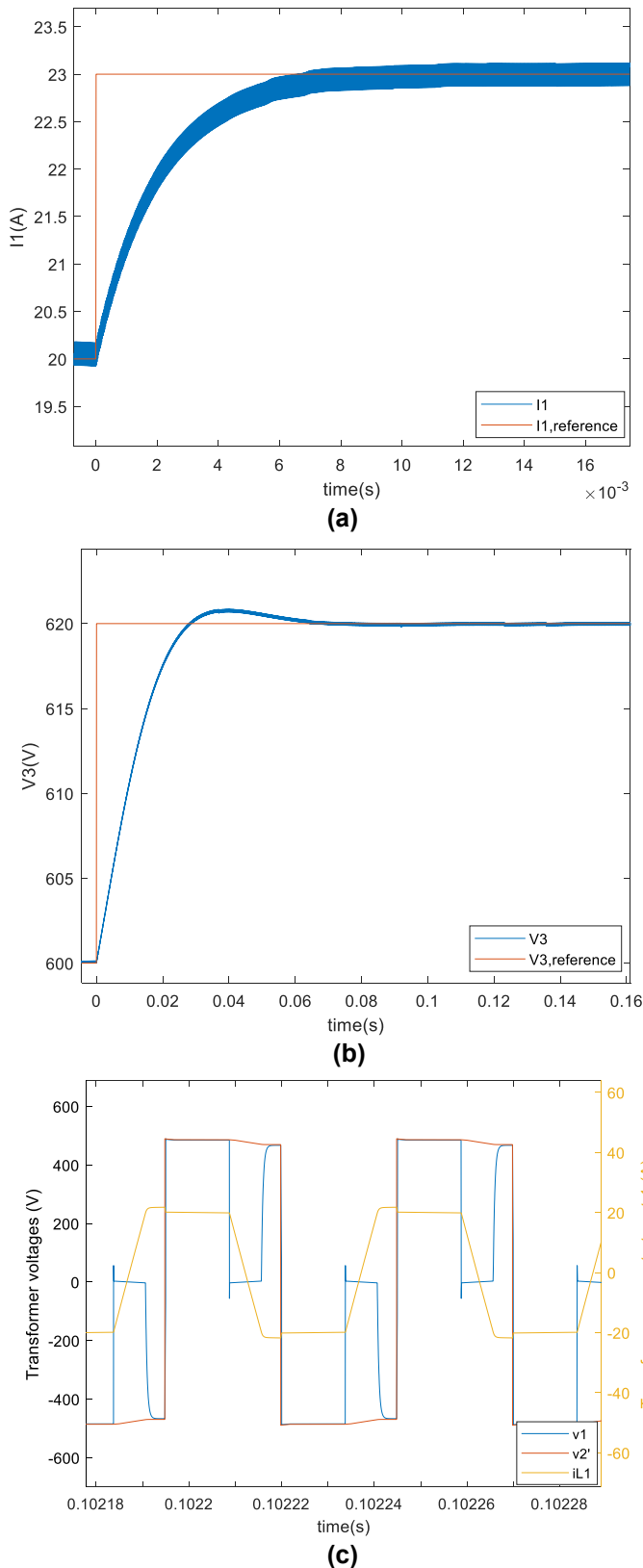


Fig. 7 Simulation results of the control loops developed for the decoupled hybrid-fed TAB converter: (a) input current control of slave current port 1 (b) output voltage control of slave voltage port 3 (c) transformer AC voltages of ports 1 and 2 and AC current of port 1 at the chosen operating point.

4 Conclusion

A hybrid-fed MAB converter is an interesting topology for many applications such as PV panels and battery storage systems. This is mainly due to their soft-switching performances on the whole operation range. In the first part of this paper, the mathematical modelling and control of a current-fed DAB converter topology were developed. The working concept of this topology was explained and so were the control conditions that should be respected for a safe functioning without over-voltages and with soft switching. This work was then extended in the second part for a decoupled hybrid-fed TAB converter. The mathematical model and the proposed control strategy were tested and validated using Matlab/Simulink.

The work presented in this paper can be generalized for a decoupled hybrid-fed MAB converter having a total of n ports, with m current-fed ports and $(n - m)$ voltage-fed ports. The master port should be a voltage-fed port connected to a stiff voltage source. The decoupling of this system allows the addition of as many ports as needed without increasing the complexity of its control.

In future works, a coupled hybrid-fed TAB converter having leakage inductances at all its ports will be investigated. The control restrictions will be reevaluated in order to elaborate a new mathematical model and control strategy for the coupled system.

5 References

- [1] M. Mohammadi, Y. Noorollahi, B. Mohammadi-ivatloo, and H. Yousefi, "Energy hub: From a model to a concept – A review," *Renewable and Sustainable Energy Reviews*, vol. 80, pp. 1512–1527, Dec. 2017, doi: 10.1016/j.rser.2017.07.030.
- [2] A. Blinov, D. Vinnikov, and V. Ivakhno, "Full soft-switching high step-up DC-DC converter for photovoltaic applications," in *2014 16th European Conference on Power Electronics and Applications*, Lappeenranta, Finland, Aug. 2014, pp. 1–7. doi: 10.1109/EPE.2014.6911013.
- [3] Z. Guo, K. Sun, T.-F. Wu, and C. Li, "An Improved Modulation Scheme of Current-Fed Bidirectional DC-DC Converters For Loss Reduction," *IEEE Trans. Power Electron.*, vol. 33, no. 5, pp. 4441–4457, May 2018, doi: 10.1109/TPEL.2017.2719722.
- [4] A. Chub, J. Rabkowski, A. Blinov, and D. Vinnikov, "Study on power losses of the full soft-switching current-fed DC/DC converter with

- Si and GaN devices,” in *IECON 2015 - 41st Annual Conference of the IEEE Industrial Electronics Society*, Yokohama, Nov. 2015, pp. 000013–000018. doi: 10.1109/IECON.2015.7392957.
- [5] A. Chub, R. Kosenko, and A. Blinov, “Zero-voltage switching galvanically isolated current-fed full-bridge DC-DC converter,” in *2016 10th International Conference on Compatibility, Power Electronics and Power Engineering (CPE-POWERENG)*, Bydgoszcz, Poland, Jun. 2016, pp. 455–459. doi: 10.1109/CPE.2016.7544231.
- [6] S. Kurm and V. Agarwal, “Current Fed Dual Active Bridge based Multi-Port DC/AC Converter for Standalone Solar PV fed Systems with Battery Backup,” in *2020 IEEE International Conference on Power Electronics, Drives and Energy Systems (PEDES)*, Jaipur, India, Dec. 2020, pp. 1–6. doi: 10.1109/PEDES49360.2020.9379447.
- [7] V. Rathore, K. Rajashekara, A. Ray, L. A. G. Rodriguez, and J. Mueller, “A Current-fed High Gain Multilevel DC-DC Converter for BESS Grid Integration Applications,” in *2021 IEEE Applied Power Electronics Conference and Exposition (APEC)*, Phoenix, AZ, USA, Jun. 2021, pp. 1964–1970. doi: 10.1109/APEC42165.2021.9487339.
- [8] D. Liu, “Topology, Development, and Control of a Three-Port Triple-Half-Bridge DC-DC Converter for Hybrid Energy Storage Application”.
- [9] S. Bandyopadhyay, P. Purgat, Z. Qin, and P. Bauer, “A Multiactive Bridge Converter With Inherently Decoupled Power Flows,” *IEEE Trans. Power Electron.*, vol. 36, no. 2, pp. 2231–2245, Feb. 2021, doi: 10.1109/TPEL.2020.3006266.
- [10] Hengsi Qin and J. W. Kimball, “Generalized Average Modeling of Dual Active Bridge DC–DC Converter,” *IEEE Trans. Power Electron.*, vol. 27, no. 4, pp. 2078–2084, Apr. 2012, doi: 10.1109/TPEL.2011.2165734.
- [11] P. Costa, P. Lobler, L. Roggia, and L. Schuch, “Modeling and Control of DAB Converter Applied to Batteries Charging,” *IEEE Trans. Energy Convers.*, vol. 37, no. 1, pp. 175–184, Mar. 2022, doi: 10.1109/TEC.2021.3082468.